Cranfield University

M Partridge

Fibre-optic sensors with molecular coatings

Cranfield Health & School of Engineering

PhD Thesis

Academic year 2009 - 2012

Supervisors: Dr Stephen James, Professor Ralph P. Tatam & Professor Séamus Higson

Co-supervisor: Dr Frank Davis

December 2012

Cranfield UNIVERSITY

Cranfield Health & School of Engineering

PhD Thesis

Academic year 2009 - 2012

Matthew Partridge

Fiber-optic sensors with molecular coatings

Supervisors: Dr Stephen James, Professor Ralph P. Tatam & Professor Séamus Higson

Co-supervisor: Dr Frank Davis

Sponsored by Leksing Ltd

Dedicated to my dad

Of all the things I have achieved in my career I know that this would have made him the proudest

Abstract

The intrinsic stability of fibre optic based sensing systems offer a platform that is suited to hazardous waste detection in a wide range of environments. Over the last few years Cranfield University has been working on the development of chemical sensors using optical fibres in combination with a group of chemical recognition molecules called calixarenes. Calixarenes semi-selectively with a range of solvents of interest makes them useful for chemical detection systems. This work has primarily been focused on the use of calixarenes in sensing benzene and other hazardous solvents. However, this approach could potentially be expanded for use in a wide range of chemical and even biological recognition systems.

The initial aim of this project was to build on the previous work in fibre optic sensing at Cranfield and explore approaches to improve and extend the performance of the sensor system. The project first focused on improving the techniques used in the Langmuir-Blodgett (LB) deposition of calixarenes. Initial studies in this area highlighted one critical experimental error associated with the use of dry Wilhelmy plates to monitor the surface pressure of the Langmuir film. Dry filter paper plates take up to 2 hours to give stable data, with a drift of up to 10% in the measured surface pressure. It is shown that this problem can be avoided by using pre-soaked plates. To provide an alternative to the Wilhelmy plate surface pressure senor, an optical fibre surface pressure sensor was developed, measuring changes in the meniscus forming properties of a liquid. The sensor consists of a tapered single mode silica fibre, mounted with a small curvature and positioned with the tapered region of the fibre immersed in the water. The performance of the fibre optic sensor is comparable with that of the conventional Wilhelmy plate surface pressure sensor showing linearity of greater than 0.9.

Following the analysis of the experimental systems used in the construction of the sensors, the project then focused on the chemistry of the materials and their suitability for LB coating. A variety of these materials were spread as Langmuir monolayers and their behavior upon compression measured. Long chain-substituted resorcinarenes gave more stable monolayers than their short chain analogues. The incorporation of long chain surfactants led to large increases in surface area, demonstrating that both resorcinarenes and surfactants are located at the water surface, except for one system where a bilayer structure is potentially formed. Further work on the behavior of the materials involved the alteration of the dipole-dipole interaction of the monolayer materials with the subphase. The modification of this interaction through the introduction of dipole altering additives, including alcohols and hydrogen peroxide, to the aqueous subphase was investigated. The resulting isotherms of

the materials showed a reduction in the surface pressure and area per molecule required in order for the monolayer to reach its point of collapse. This ability to shift the point of collapse has application in the optimisation of Langmuir-Blodgett coating of surfaces.

Within this project the sensing properties of a fibre sensor were also modelled extensively in order to determine the theoretical sensing limits of a fibre optic vapour sensor. The model showed that the sensing goals of 1ppm originally envisaged for this project were unobtainable due to the low number of gas molecules interacting with the sensor. However, this led to the proposal of a new application of the system in sensing contaminants in water, where the same limitations would not apply. The results for the sensor system tested in water show how significantly more sensitive the system is to toluene contamination in water than it is to toluene vapour. These results demonstrate the utility of the developed system for many pollutant-sensing applications, include crude oil detection.

Acknowledgements

Working solidly for 3 years on a single project towards a PhD could not have been done without the support of the people around me. I did want to explain all the contributions that various people made but my original draft of this section was already several pages long when I realised I was only about half way through. Not only that but it was starting to read a lot like an Oscar acceptance speech, so in lieu of my rambling first draft I thought it more appropriate to list those who have been exceptional in their support during my work over the last 3 years. If you're reading this then you know what you did and for that I am amazingly grateful.

Helen, Nathan & Jessica Partridge

Gillian & Nicholas Loake

Thomas Loake

John & Claire Partridge

Sarah Smith-Wightman

Steve James

Tim Richardson

John & Natalie Cartwright

All of my very patient friends

Anyone who asked me "so how's work?" in the last 3 years and then had to endure a long rambling lecture

@_Delver; because he asked

Table of Contents

List of Figures

Unless otherwise stated all figures are produced by the author.

List of Tables

List of Equations

Chapter 1 Rationale and Aims for this Research

Chemical and biological sensing is an area that has expanded over the last fifty years. In many cases, improvements that have been made in electronics, optics and fabrication technologies have quickly been exploited though combination with either chemical or biological recognition systems to create new sensor systems. Despite these new advances in technology, sensing is an area that is still in need of novel approaches to allow improved sensitivity in an ever-widening range of environments.

To put the sensing challenges in some perspective, genetic markers, which are found in concentrations of femtograms (10^{-15} g) per ml of whole blood, is the sensing equivalent of trying to find the sweetness of an Olympic swimming pool to which a single grain of sugar has been added. In addition, European Union legislation lowered the exposure concentrations for many hazardous industrial by-products to levels that are pushing the limits of many existing sensor systems.

Developments in manufacturing techniques are being exploited by both biotech and chemical industries, driven by a growing demand for new sensor technology that can respond faster and more accurately while working in a more flexible environment. Previous work at Cranfield University on fibre optic chemical sensing has focussed on the detection of BTEX (benzene, toluene, ethylbenzene and xylene) gases [1,2]. BTEX gases are a group of gases commonly associated with pollution; either through industrial waste or from domestic use via exhaust products. This group of pollutants are of particular interest both to the environment and to public health. The current recommendations from the European Commission on vapour exposure limits are 1 ppm by mass (average exposure during a 24 hour period) for these volatile organic compounds (VOC) [3]. Alongside these limits, the EU directive goes further and sets out not only the requirement on signatory nations to abide by these limits, but also provides a framework of routine air quality testing at the locations of likely waste release. For industry this means that plants will need to have networks of sensors covering any possible waste leaks points within the plants as well as at the locations of any release of exhaust gases. In addition to industry monitoring, there is also a requirement for sensing at petrol station forecourts and oil handling stations.

One of the most rapidly expanding areas of sensing, which is helping to meet this demand, is that of fibre-optic based sensors. The field of fibre-optics is approximately a century old [4] and the full potential of these flexible glass fibres within sensor technology has yet to be fully

realised. Over the last few years Cranfield University has been working [5] on the development of fibre-optics as a possible sensing platform when used in combination with a group of chemical recognition molecules called calixarenes. Calixarenes are ideally suited for use in chemical synthesis as they form reversible gas-state complexes semi-selectively with a range of solvents of interest [6]. This work has primarily been focused on the use of calixarenes in sensing benzene [1] and other hazardous solvents. However, this approach could potentially be expanded for use in a wide range of chemical and even biological recognition systems.

The initial aim of this project was to build on the previous work in fibre optic sensing at Cranfield and explore approaches to improve and extend performance. First focusing on the combination of fibre-optic sensors with the recognition elements and the Langmuir-Blodgett (LB) film coating technique used to deposit the recognition elements onto the fibres as depicted in Figure 1.1.

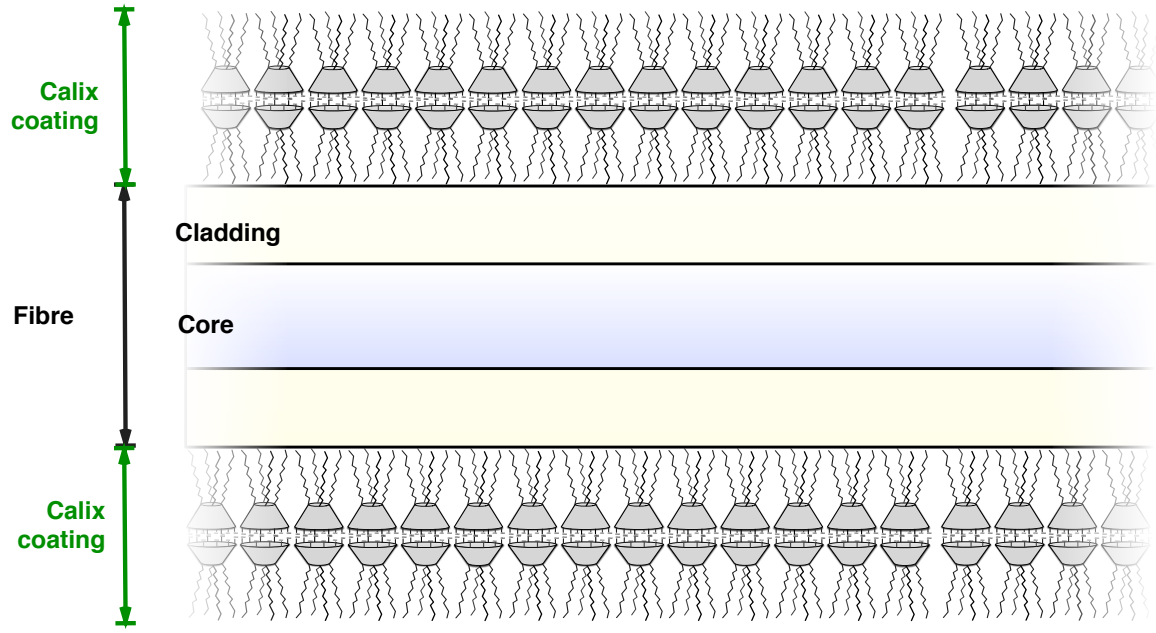

Figure 1.1: Schematic of the overall structure of the sensor design
The sensor consists of two key regions, the fibre sensor and the outer calixarene material

Based on previous observations made during the work by Professor Tatam's group [1] and a series of papers on film defects [7-9], the focus of the project was initially on ways to improve the coating methods and reduce coating defects and variation. As discussed in section 2.7.3, any variation in the surface coating of a fibre optic sensor has an impact on the quality of the results it produces with regard to sensitivity and repeatability. With the aim of exploring

improvements in existing fibre optic sensor systems, the project focussed on the following key areas:

- Optimisation of the LB coating method through isotherm characterisation of calixarene materials (Chapter 5).
- Selection of calixarene monolayers via exposure of the monolayers to target vapours (Chapter 8).
- Use of sub-phase additives to change the properties of Langmuir monolayers (Chapter 9).
- Comparison of coating properties through subphase altered monolayers and solvent enhanced coating (Chapter 10).
- Comparison of coating methodologies using the same fibre optic sensor technology as used in previous work (Chapter 12).

During this initial work, two other areas were discovered and were tested and developed alongside these original aims.

- Fibre optic surface pressure sensor (Chapter 7).
- Monolayer altered vortex rings (Chapter 6).

Chapter 2 Introduction and Literature Review

2.1. Sensors

A sensor by definition is an “element of a measuring instrument or measuring chain that is directly affected by the measurand” [10]. A sensor can be thought of as the recognition element of a measuring device. For example, a pH meter has an electrode (which acts as the recognition element) and the measurement of the change in potential in the electrode allows the transduction of that recognition to a quantitative result. This definition is not clear-cut in the context of biosensors & chemical sensors, where the term sensor often refers to the whole system of recognition and transduction (Figure 2.1). It is this biosensor definition that is more commonly used in relation to fibre-optic sensor systems [10].

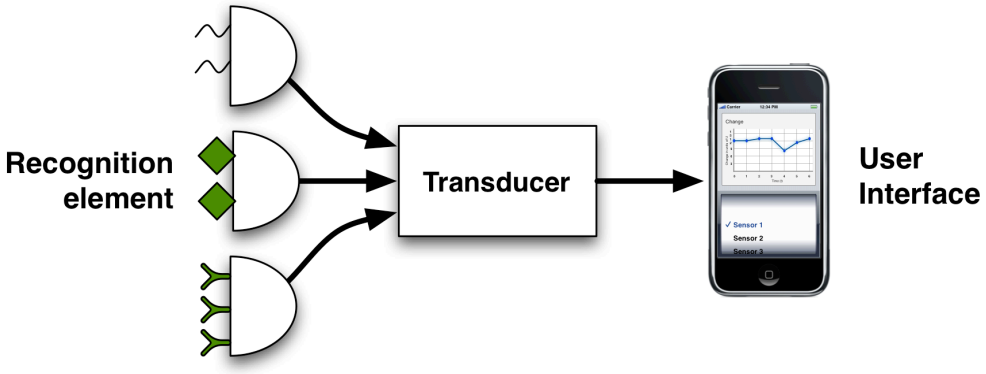

Figure 2.1: Schematic of a biosensor linked to a user interface
This figure shows a generic schematic of a biosensor with distinct recognition and transduction elements.

2.2. Sensing target

Both chemical sensing (the sensing of chemical agents) and biological sensing (the sensing of biological agents) encompass a wide verity of targets and often the line between these two areas of sensing is not clear. The main focus of this project is one sub-set of the broad theme encompassed by the term chemical sensing, namely gas chemical sensing. This group of sensors aims to be specific in targeting either groups or individual chemicals of interest within airborne samples. Gas sensing provides a great number of challenges for chemical sensing, from low sample size, contamination, and high environmental variability. Many of these challenges are met though the myriad of gas detecting techniques available for specific applications. This project focuses on just one small area within gas sensing, the detection of volatile organic compounds (VOC).

2.2.1. VOCs

VOCs are used and produced in innumerable areas within industry and domestic life for people across the globe. Along with this heavy use also comes a significant risk of exposure and leakage in to the environment causing serious personal and ecological damage. One key group of VOCs are the BTEX gases (benzene, toluene, ethylbenzene and xylene), which are common by-products of a number of industrial and domestic activities and which are toxic either though immediate expose or via long-term build-up.

The relatively high health and environmental risk of these compounds is highlighted by tight control on the exposure limits that are constantly being revised as new medical information becomes available. For example, the current EU standard [3] on permissible benzene concentrations in the air is 1 μg m^3 . However, even at this low level the US Agency for Toxic Substances and Disease Registry (ATSDR) estimate [11] that life-time expose of 1ppm will cause an extra 5 cases of leukaemia per 1000 population.

In response to the needs outlined above, a number of sensing solutions exist that are well suited to a range of gas and BTEX sensing, including optical absorbance, mass spectrometry and ion-mobility spectrometry

2.2.2. Mechanical sensing

Chemical analytes, for example, can be small and to measure a mechanical/mass change is a daunting task. As previously discussed, the EU standard [3] on permissible benzene concentrations in the air is 1 μg $m^{3\ -1}$. This is clearly a small amount of mass to measure. However, the sensitivity of microbalances and cantilevers has improved sufficiently for the detection of the change in mass when small quantities of the target molecule is immobilised on the surface. One increasingly common mass detector is the piezoelectric sensor. Exploiting resonant effects in piezo crystals allows accurate (to around 1 ug cm^2) determination of changes in the mass bound to them. When two crystals are placed next to each other and a current is passed through one of them, it will begin to vibrate. At resonant vibration frequency, the complementary crystal will also vibrate. This resonance can be recorded by connecting the second crystal to a meter that records the charge produced by the resonating crystal. Once set up and stable, any increase in the mass of the complementary crystal will change and the resonance frequency and the signal generated will change [12,13]. This technology can be combined with a number of reusable and one-shot recognition methods [12,13].

Other than piezo electric systems, there has also been a significant amount of research into the use of micro cantilevers. These cantilevers are coated with a specific recognition system and then exposed to either a liquid or a gas sample. The target chemical binds or creates a chemical change, which alters the stress on the cantilevers, which can then be measured.

2.2.3. Electrical sensors

Electrical sensors includes any sensor that though interaction with a measurand produces an electrical signal or a change in an electrical property (e.g. resistivity). Electrical based sensors have been a key technology behind the miniaturisation of the glucose test and, since the development of screen-printing; the technology has expanded in diversity and application. One example of an electrical sensor system is the AC impedance sensor. In its most basic form, a pair of electrodes is coated with a specific recognition system. An excitation waveform is applied to the electrodes and the subsequent output is measured. This output can then be linked directly to the concentration of the target molecule [14]. AC impedance sensors have been used with a large number of biological recognition systems, ranging from antibodies [15] to DNA hybridisation [16].

2.2.4. Optical sensors

Optical transduction of a signal covers a range of methods, from visual readings of a device (e.g. Pregnancy test) to sensitive spectroscopic techniques. Optical sensing can be broken in to two sub-groups - indirect through the optical detection of a secondary molecule, and direct though optical detection of a target analyte. This division is not ideal, but provides a simple categorisation to discriminate between the most common optical methods.

Direct optical sensing is an older category of sensors, with spectroscopic techniques dating back as far as 1861 when Gustav Robert Kirchhoff worked with optics to understand the spectrum produced by different optics, and how impurities in the optics induced these changes [17]. This field has now expanded into a vast array of spectroscopic techniques from simple and near-infrared spectroscopy to the more complex ion mobility spectrometry. One of the great strengths of this spectroscopy is the existence of fundamental gas absorption peaks with the spectrum of a material. For simple gases such as CO_2, H_2O and NH_3, these peaks are widely separated [18], allowing clear differentiation and measurement However, these techniques have limited success in the differentiation of larger VOC species, such as benzene, where the measurement is difficult and requires sensitive equipment and data analysis.

Indirect optical sensors have a number of advantages over the direct method, as a result of the availability of a large number of potential recognition or capture methods that can confer selectivity without the need for direct optical measurement. Indirect optic sensors, however, require that the signal generation be more closely linked to the recognition method. Over the last 50 years, a large number of methods for achieving this optically have been presented. Many use a type of evanescent wave detection, which is explained further in section 2.5. One of the most commonly employed is surface plasmon resonance (SPR) [17] (Figure 2.2).

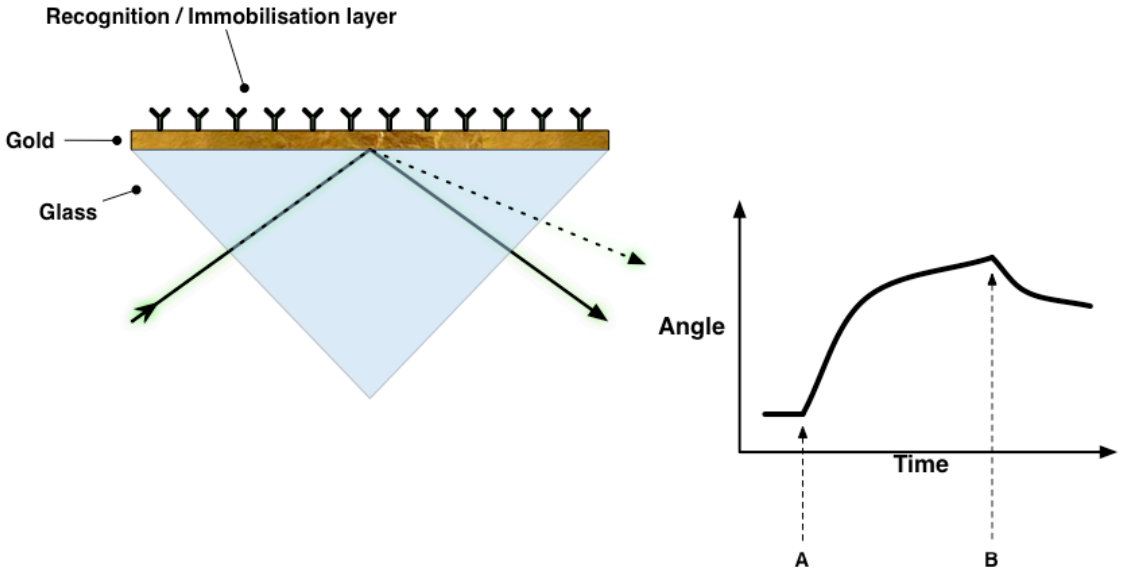

Figure 2.2: SPR sensor
*The top part of this figure shows a schematic for a SPR sensor. Light reflected off the back of the gold layer is altered by any binding to the recognition layer. This is shown in the graph below where **A** is the point at which the target molecule is introduced and **B** is the point at which the target begins to disassociate as it is washed off.*

The discovery of SPR dates back to 1902 [19], although it was not widely used until it was combined with biological recognition methods until 1983 by Liedberg *et al* [20]. Liedberg combined SPR techniques with an antibody based detection method showing how SPR could be used as a biosensor platform [20]. A more recent development in the use of evanescent wave sensing is the development of fibre optic based sensor systems, which work in a similar fashion. These are explained in more detail in section 2.5.

The development of a number of different VOC sensing systems has led to significant investment in finding VOC sensitive recognition systems. When these recognition systems are combined with the versatility of fibre-optics, there is the potential for the development of a flexible and versatile sensors capable of providing sensor information in a wide range of challenging conditions (e.g. deep ocean sensing). In chemical sensing there are a wealth of examples of fibre optic chemical sensors, ranging from a simple ozone sensor made by

stripping the cladding from the fibre [21] to more complex fibre grating based sensors which can detect low concentration vapours [22].

2.3. Calixarene based sensors

This recognition element of a sensor can come in many forms, and new methods are being discovered every day. This project has focused primarily on a group of VOC sensitive molecules called calixarenes. Calixarenes and the related calixresorcinarenes are cyclic oligomers based on phenolic compounds condensed with aldehydes and have been studied widely due to their potential usage within, amongst other applications, synthetic receptors capable of binding a wide variety of guests species including solvents, metal ions and a wide range of other chemicals of interest. It is this receptor quality which is of particular value to this project.

2.3.1. Synthesis

Like many chemical discoveries, calixarenes are the cumulative result of years of research by a number of groups working on phenol-formaldehyde chemistry. Initially, this field was treated with little attention and there was really only further progression in the late 1800s with the work of Johann Friedrich Wilhelm Adolph von Baeyer and a number of other key chemical synthesis scientists who all worked to characterise the structures formed through phenol-formaldehyde chemistry. However, during this period it was difficult to source formaldehyde and to prepare pure products from its reaction with phenols. In 1907, this field was forever altered with the filing of a patent [23] by Leo Hendrik Baekeland for his now famous Bakelite. Baekeland had discovered that, through a carefully refined process, he could create repeatable samples of a hard dark substance, which had a huge range of possible uses. Baekeland did not fully understand this process and even today the exact structural formation of Bakelite is not entirely understood [6], though we are not short of possible explanations. Formed by the reaction of phenols and formaldehyde, creating simple linked phenols joined by a methyl bridge, and once cooled, the final structure sets hard, creating Bakelite plastic (Figure 2.3).

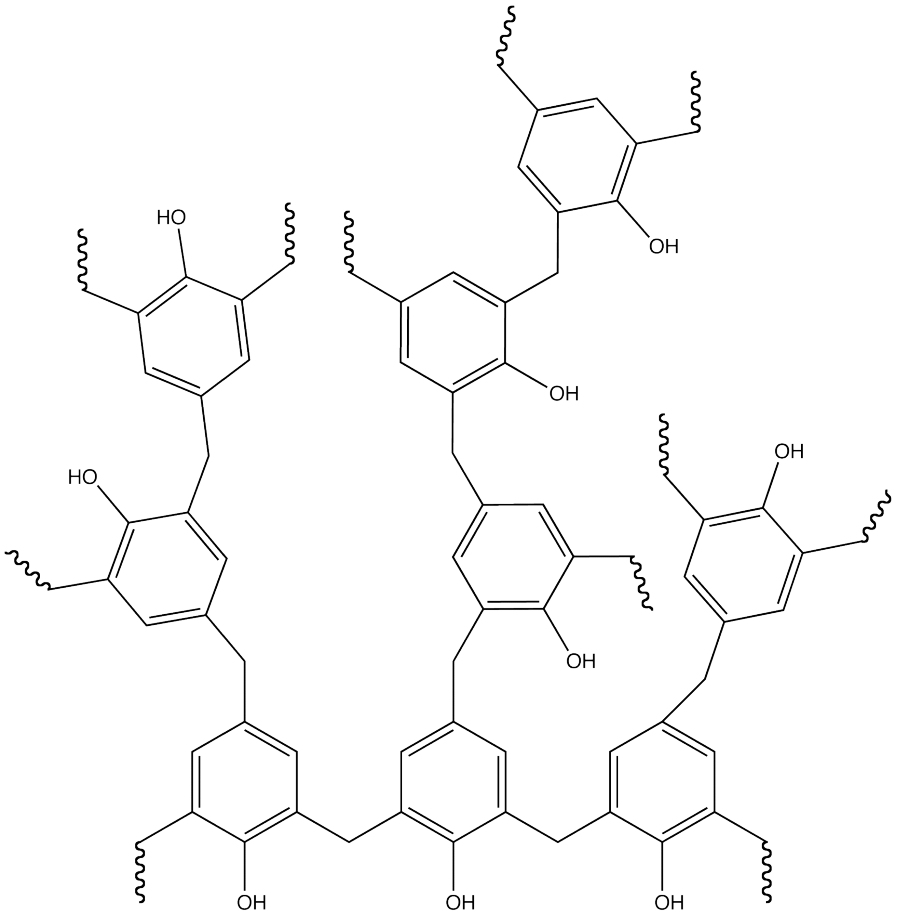

Figure 2.3: Cross linked phenols
This is an expansion of the final stage of the phenol-formaldehyde chemistry where is highly cross linked to create a resin

Baekeland showed that the previously under-invested area of phenol-formaldehyde chemistry had huge potential for producing novel materials with a wide variety of uses. After a short patent squabble between a number of groups with a claim to the Bakelite process, the patent was awarded to Baekeland who quickly exploited his invention. As the first thermo setting plastic, Bakelite was much adopted in a large number of applications and gave prominence to the area of phenol-formaldehyde chemistry.

As discussed, Baekeland plastics form by phenol-formaldehyde reactions cross-linking in a variety of disorganised shapes. In 1941, Alois Zinke [6] sought to develop simple plastics by using phenol-formaldehyde chemistry to create ordered chains, rather than these cross-linked structures. Zinke used para-substituted phenols to force the phenols to react only at the two positions either side of the –OH group (Figure 2.4).

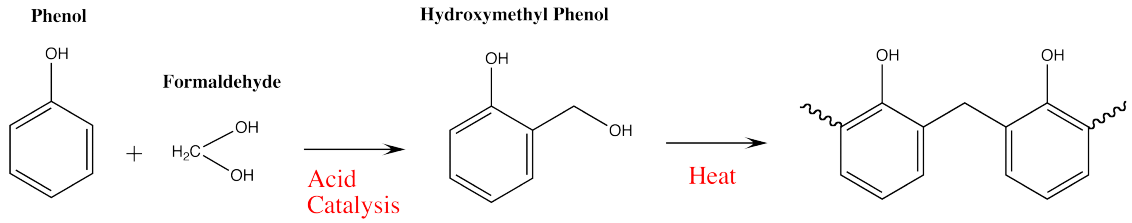

Figure 2.4: Phenol-formaldehyde reaction [6]
The reaction of phenol and formaldehyde to create simple cross-linked phenols.

It was through this reaction that he created what is thought to be the first cyclic tetramer. However, it was not until 1944 that this structure was published as a possible explanation for the results that his earlier experiments had obtained [24]. Over the next thirty years, more work was performed, characterising the structure and diversity possible with cyclic tetramers, but there was little consideration given to the possible use of these structures. In 1972, David Gutchse (in an attempt to unify the nomenclature for these structures), proposed that the similarity of the 3D structure of the cyclic tetramer to a Greek Calyx vase should be used as part of a unified name and termed them calixarenes (Figure 2.5).

Figure 2.5: Calix vs Calyx
On the left is a space fill model of a simple calix-[4]-arene. On the right is a photograph of a Greek calyx-krater wine bowl, currently held at the British museum (reproduced with permission)

As all calixarenes are drawn with the –OH group point down and the p-substitutes pointing up, all calixarenes are said to have a narrow endo rim at the bottom and a wider exo rim at the top [6]. However, this rule is not definitive and, with a number of calixarenes, this orientation is hard to derive.

2.3.2. Other Calixarene applications

These bucket-like calixarene molecules have been put to use in a number of approaches in sensors. By altering the active groups that are presented in either the endo or exo side of the calixarene, they can be made specific to certain agents. For example, a considerable amount of work has been undertaken using ion-specific calixarenes that can be used as part of an electrode sensor system. These ion-specific calixarenes can be tailored to detect a number of ions through modifications of the side chains. A simple Na^+ sensitive calixarene can be made using a calix[4]arene with side chains that, when they come into contact with the Na^+ group, are modified. This modification can be detected either by the electrochemical and, in some cases, optical change [25] in the calixarenes, or by the loss of the Na^+ ions from the solution. In the referenced Benco paper[25], the calix used is a modified calix[4]arene with a

rhodamine B group amino covalently bonded to one of the four benzene rings. The rhodamine B group fluoresces at a wavelength of 535 nm through the action of the Na^+ ions converting the Rodamine B group to an excited state. This kind of chromomeric calixarene is particular useful in sensing due to the signal multiplication that is possible with optical sensors. There are a number of examples of calixarenes that use fluorescent/chromomeric shifts between the free and reacted state, which can be used to determine ion concentrations with high sensitivity [26]. The wide ranging use and potential of modified calixarenes is clear from the number of patents filed for their use in applications ranging from Uranium recovery [27] to ion selective sensors (as previously outlined).

Calixarenes can also be used as molecular 'buckets', enabling them to form temporary solid, liquid and gas state complexes. Depending on the calixarenes used, certain molecules with a particular charge and size will form complexes with calixarenes. These complexes can be formed from a great many types of interaction, from hydrogen bonding to electrostatic. However, this ability of to form complexes only began to be exploited in the early 1990's, when several groups began to study their ability to form solution state complexes. The driving force behind this move to the solution sate was the more applicable re-usable sensor technology for detecting contaminates in solutions.

2.3.3. Calixarene gas state complexes

The movement from solid to solution has continued with the developing field of gas-state calixarenes complexes. This has only recently been explored and currently only a handful of papers document gas-state complex formation. The clearest examples of gas state complex formation have been seen with chemical agents such as acetone [28], benzene [29], ethyleyebenzene [28], toluene [29], xylene [28] and chloroform [29].

The formation of gas state complexes are just one part of the gas sensing properties seen in calixarene coatings. Nabok *et al*. [30] showed how, at higher concentrations (9000-98000 ppm), the calixarenes also show an uptake of solvent via capillary condensation.

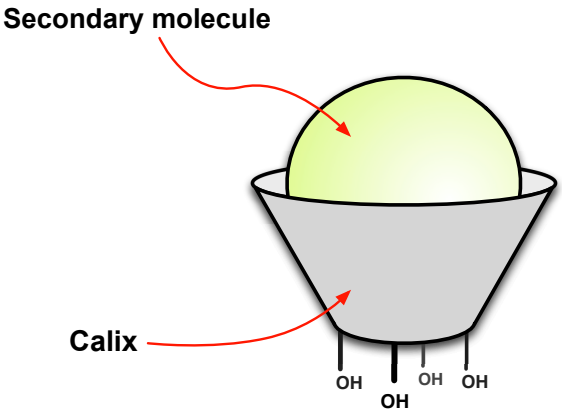

Figure 2.6: Guest-host interaction of a calix[4]arene molecule [31]

As seen in Figure 2.6, calixarenes form a natural cavity from their 3D shape with an approximate diameter of around 1-2 nm. These small cavities encourage the condensation of the target vapour below the natural condensation point of the vapour. In the case of calixarenes it has been shown previously that this can be as low as 0.2 P_s (P_s is the saturated vapour pressure) [30]. This condensation within the film causes a swelling and an optical thickness change, the degree of which correlates with the mobility of the vapour through the calixarene layers [32]. As identified in Topliss (2010) [1], it is the swelling of the film which is being measured by the optical fibre sensors, not the uptake of the analyte into a gas state complex. As capillary condensation can only be sustained at vapour pressures above 0.2 P_S, any attempts to improve sensitivity should be focused on the formation of gas state complexes, and not on capillary condensation uptake into the film. Gas state complexion is a weaker reaction and will result in a smaller proportion of VOCs being held within the sensing region of a fibre or other sensor surface. For optical sensors reliant on measuring changes in refractive index, this small uptake presents a significant sensing challenge. The calixresorcinarene used by Topliss *et al.* has a refractive index of 1.46 [33], whereas pure benzene has a refractive index of 1.49 [34]. Even if the film was entirely saturated with benzene, the largest refractive index change would be just 0.03. This value is the largest possible change within the system and is not reflective of the change that would be estimated for low ppm levels. Nabok *et al.* examined [30] this refractive index change further and found that, the point at which the gas state complex mechanism takes over from capillary condensation, the change in refractive index from the uptake of benzene was just 0.002 [30], with this shift being close to the estimated limit (0.001) of the fibre optical sensing system used within this project.

2.4. Fibre-optics

The story of fibre optics and their use in optical based sensing can be said to have begun with the work of Augustin Jean Fresnel in the early 1800s 4]. Building on the earlier work of Willebrord Snellius and Christiaan Huygens, in the 1820s Augustin-Jean Fresnel showed how total internal reflection (TIR) could be achieved at the interface between two media (Figure 2.7). Fresnel demonstrated that, as the angle of incidence is increased, the amount of light reflected from the interface changes until a critical point at which all light is reflected by the interface, as shown in Figure 2.8. Fresnel also showed how this TIR only occurred when light was travelling from a higher refractive index into a lower refractive index media.

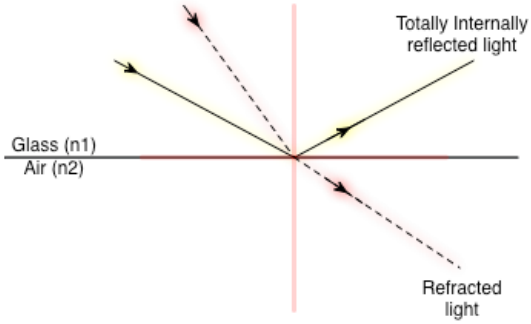

Figure 2.7: Total internal reflectance in glass
Light at a certain angle reflects internally at the interface between two media of differing refractive indexes

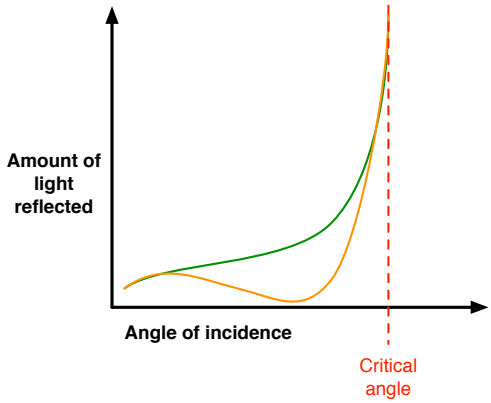

Figure 2.8: Change in reflected light with angle of incidence
The above graph is a diagrammatical example of the relationship between the angle of incidence and the amount of light reflected. The green curve represents s-polarised light and the orange curve, p-polarised light.

The change in the reflection of the light from varies between p and s polarised light, (discussed further in section 3.3) but both polarisations totally internally reflect at the same angle of incidence. These equations can be further simplified by the use of a single equation to predict the angle at which light will begin to totally internally reflect, Figure 2.1.

$$\theta_{crit} = sin^{-1}\left(\frac{n_2}{n_1}\right)$$

Equation 2.1: Calculating the critical angle of TIR
n2 is the refractive index of the less dense material and n1 is the refractive index of the material of the denser material from which the light is being reflected.

Daniel Colladon and *Jacques Babinet,* (working independently) are generally thought of as being the first to discover the use of total internal reflection to guide light. Both scientists produced demonstrations of light being 'carried' through a stream of water pouring out of a hole into a bucket. While *Colladon* had originally produced the flowing water experiment around the same time as *Babinet*, *Babinet* pursued the experiment and shown that the same effect was possible in bent glass rods and quartz fibres [4]. Initially this 'trick' was considered an unarguably attractive but essentially irrelevant property of light. Indeed *Colladon* spent most of his time shortly after discovering the effect of light on water helping to design special effects for the theatre and producing magnificently lit fountains [35].

The first man to realise the possible commercial value of piping light was *William Wheeler* [36]. In 1881 *Wheeler* published the first patent for use of light piping technology which detailed the used of glass tubes which would direct the light from a central light source to all the rooms of a house. Wheeler used glass to act as a light guide using total internal reflection, in the same way used today in thinner glass fibres [36][37].

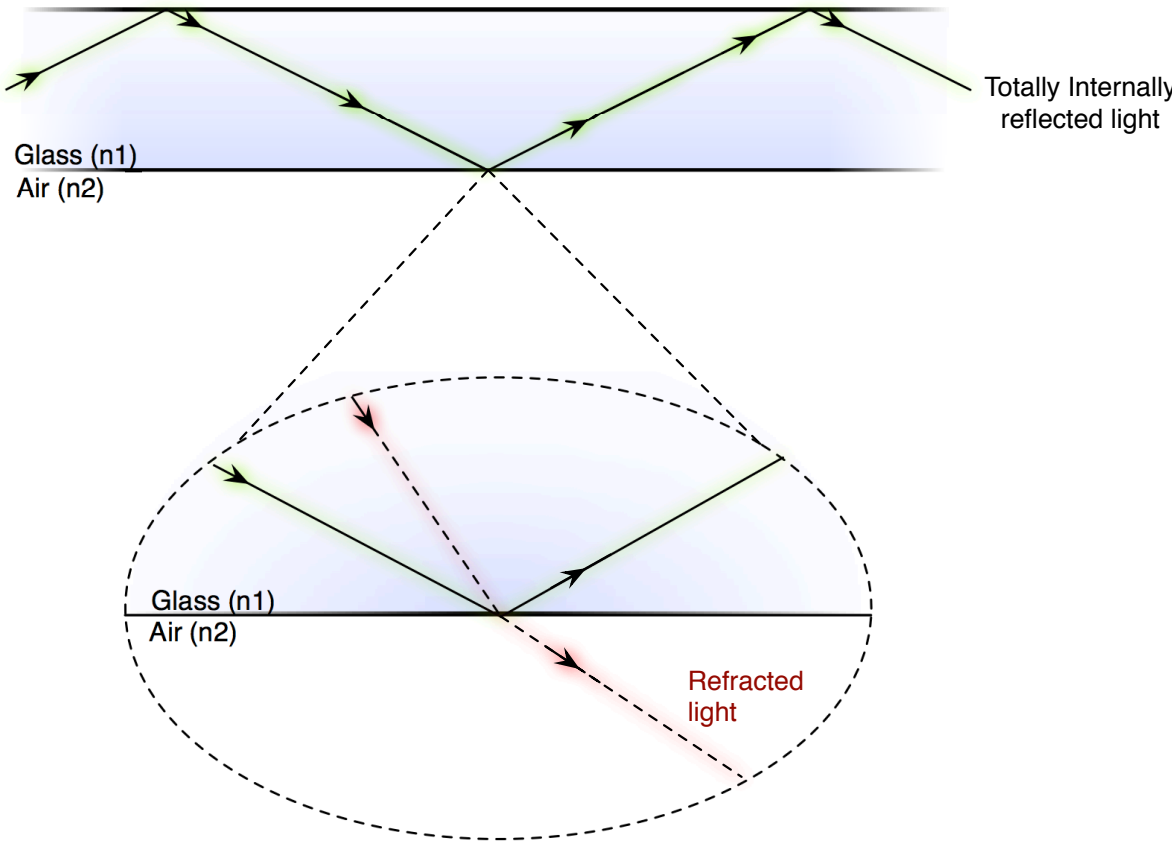

Figure 2.9: Total internal reflectance within an optical fibre
Total internal reflectance occurs when n1 has a greater refractive index than n2

Over the next 60 years, development in the uses of fibre-optics was slow and focused mainly on the use of fibres to guide light to specific locations. For example, in 1898 *David Smith* pioneered the use of a bent glass rod for use in dental operations [38].

The limiting factor in the further development of fibre-optics was not due to a lack of creativity or scientific understanding of total internal reflectance; the problem lay with the poor quality of glass available at the time. Many of the early fibre technologies developed in this period were limited by the large loss of light over relatively short distances of glass or quartz.

2.4.1. Making the fibres

Glass fibres have been produced by a number of methods since they were first made in a course form by ancient Egyptians thousands of years ago, though they were little more than glass rods [4]. Further developments were only pushed forward after the late 1800s, with discoveries in light piping encouraging scientists to look for new methods and materials to exploit this optical effect.

From the late 1800s until the 1950s, there were slow improvements in fibre production methods. One of the first repeatable methods came from Charles Vernon Boys in 1887 [39] and involved firing a bow with an arrow trailing molten quartz across his lab. As the arrow pulled the fibre out across the lab, it pulled out thin fibres that could be easily bent. These methods were then significantly improved when, in 1938, Owens-Illinois demonstrated a repeatable way of mass-producing fibres by pulling continuous strands of glass. All the methods produced in this period suffered from the same problem of loss and interference if the fibre touched another surface.

The previously mentioned, fibre optics used TIR to guide light, relying on the difference between the high refractive index glass and the low refractive index air surrounding the fibre. However one problem with these fibres was that if anything touched the glass fibre then the refractive index immediately surrounding the fibre is changed and the light may then no longer be totally internally reflected. As shown in section 2.4, *n2* must have a lower refractive index that *n1* for TIR to occur, so even particles of dust of other surface contaminates (e.g. grease) would cause significant loss of signal along a fibre. This problem was eventually solved in the 1950s by Brian O'Brian, the then president of the Optical Society of America, who proposed that the best way to prevent this loss was to the coat the fibres in a uniform low index cladding material [4]. This use of low index cladding material ensures that the high index core of the fibre, where the light is confined by TIR, can remain insulated from any contact with other surfaces (Figure 2.10).

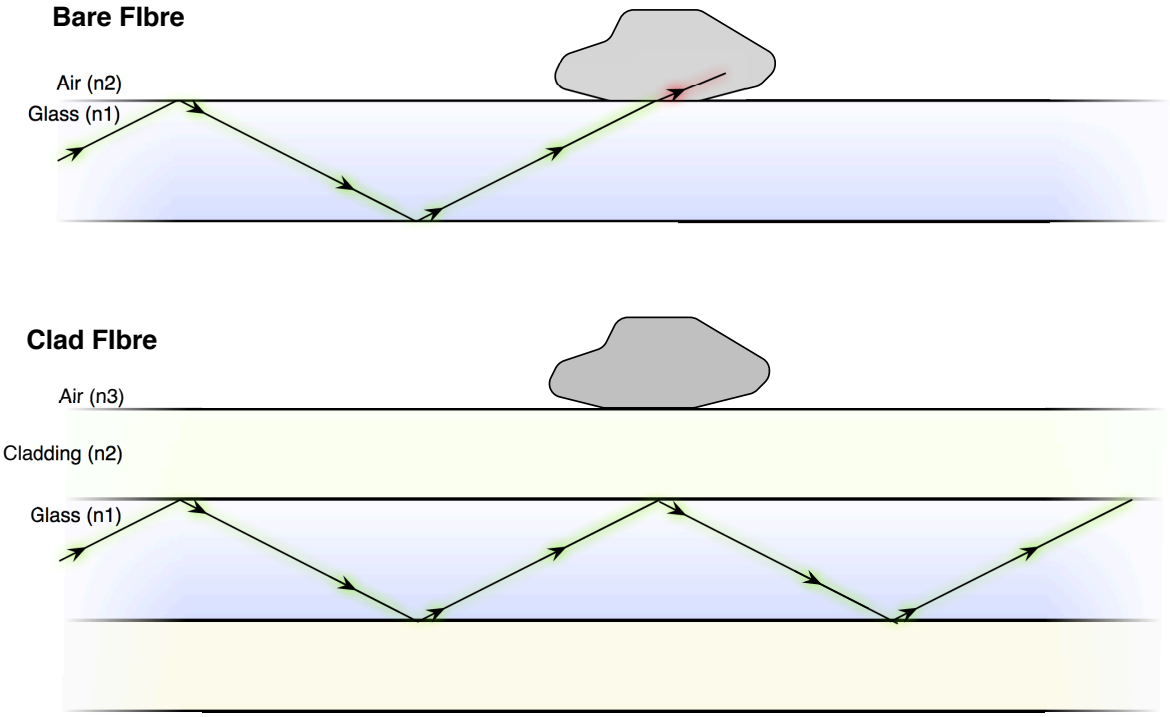

Figure 2.10: Signal loss reduction in fibres
The above pair of diagrams shows bare and clad fibre and the reaction of the fibre to a dust particle.

Modern fibre optics now comprise more than just the simple cladding layer shown in Figure 2.10 and are also protected from mechanical breakage by primary and secondary buffer layers, Figure 2.11.

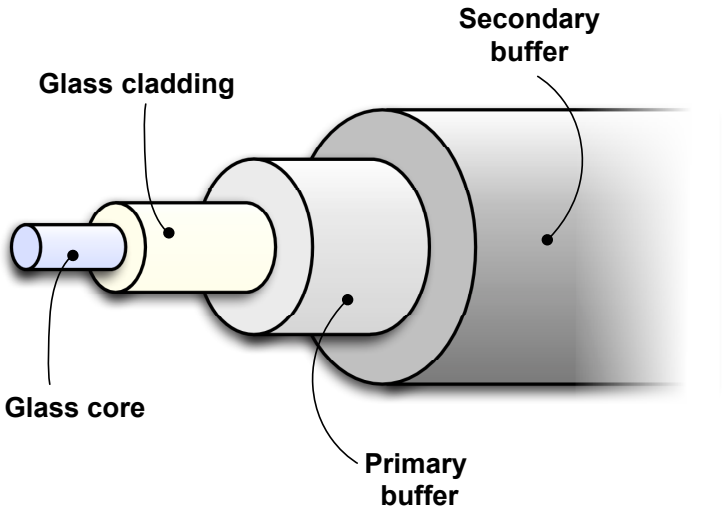

Figure 2.11: Schematic of a stripped fibre
The glass core typically has a diameter of ~5-50 µm, the cladding ~125 µm and the buffers have a combined thickness of around 900 µm.

As previously discussed, an optical fibre exploits total internal reflectance to transmit light. While any light that enters the core of the fibre within the critical angle (also known as the cone of acceptance Figure 2.12) can be totally internally reflected, the light transmitted is reflected within distinct modes. This is better explained by thinking of three different light rays entering a fibre at three different angles (Figure 2.13).

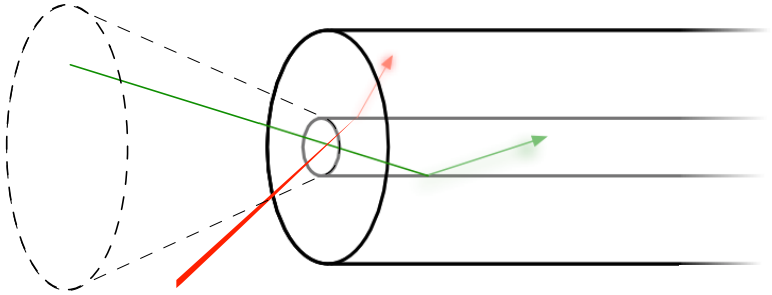

Figure 2.12: Cone of acceptance for light entering a fibre
The above figure shows the effect of the critical angle on light entering the core of the fibre, creating a cone of acceptance.

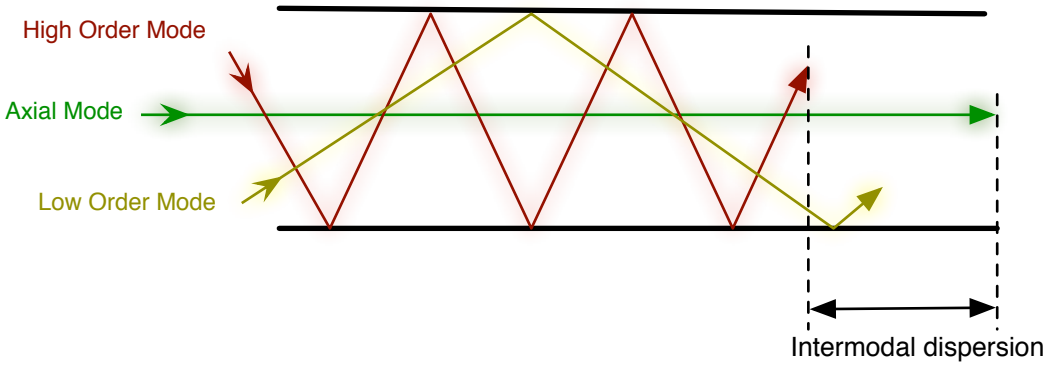

Figure 2.13: Modes and Intermodal dispersion with the fibre core
Depending on the angle at which the light enters the fibre the path length is different. In this figure we can see that the higher order mode has to travel further than the axial due to the extra lateral distance as it reflects off the sides of the fibre optic

The first mode enters the fibre perpendicular to the end of the fibre and is transmitted directly down the core - this is known as the Axial Mode. The second mode enters at a shallow angle, illustrating a low order mode with the third, sharper angle ray illustrating a high order mode. One feature of these modes is the variation in speed at which they pass from one end of the fibre to the other. The axial mode travels in a straight line between one end of the fibre and the other, taking the shortest time possible. By comparison, a lower order mode, which has to travel further as it undergoes multiple reflections as it propagates through the fibre, will arrive shortly after the light that is travelling in the axial mode. This time delay between

modes only worsens with higher order modes, which suffer even more reflections. By the end of a 1 km fibre, this time delay can be as much as 37 ns (which equates to a distance of around 7.4m) although this value depends on fibre type. A fibre with a 200 μm radius can support thousands of modes with varying time delays between them. The result of this time delay can be seen in a series of bursts of light sent down a multimode fibre optic cable (Figure 2.14).

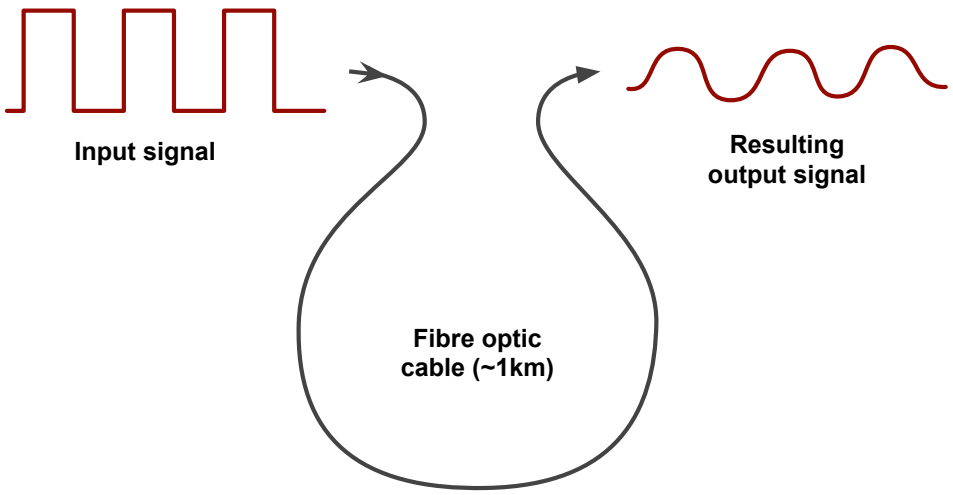

Figure 2.14: Schematic of intermodal dispersion

The variation in the speed of the various modes supported in the cable causes the sharp on/off pulse to be smoothed. This creates two problem - firstly the peak of the output pulse is lower than the input, making it harder to detect, and secondly if two pulses are sent close together, then the light travelling in the axial mode of the second pulse may overlap with the light travelling in the higher order modes of the first pulse. This effect is called 'Intermodal Dispersion'.

The single mode fibres produced by Mosaic Fabrications Inc. solved the problems of multiple modes by creating a fibre so thin it could only support the axial mode (Figure 2.15). This removed the problems of intermodal dispersion and enabled clear transmission of pulses of light. With concurrent research in laser technology throughout the 1960s, a great many people began to see the possibilities of using fibre-optics for use in communication. Subsequently, during the 1960s and 70s, a number of organisations made a series advancements using fibre-optics for communications. This culminated in a demonstration of digital video transmitted over a fibre optic cable, shown to the Queen Elizabeth 2nd at the Institution of Electrical Engineers in 1971 [4].

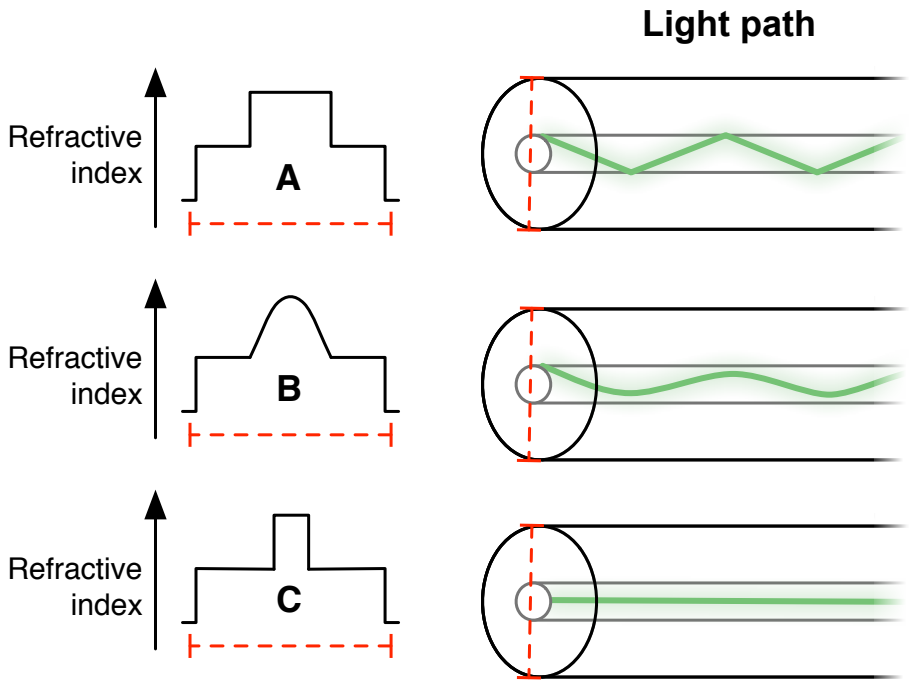

Figure 2.15: Different index fibres compared to single mode fibre
This figure shows the refractive index across two cross sections. Section A shows the early fibre index step between the core and the cladding. Section B shows a graded core, which tapers from high in the centre to the cladding refractive index. Section C shows a single mode fibre.

Driven by consumer demand for high bandwidth optical fibres, the 1970s also saw the emergence of a new type of multimode fibre, which solved many of the early problems with Intermodal Dispersion. In the original multimode fibres, TIR was achieved using a glass fibre with a different refractive index to the cladding surrounding it. This is known as a stepped-Index fibre. To combat the Intermodal dispersions problems with this fibre, a graded fibre was developed that substantially reduced the effects of intermodal dispersion [4]. A graded fibre has a graduated refractive index, which increases towards to the core (Figure 2.15).

In graded index fibres, the low mode and axial modes travel through the lower speed higher refractive index core which is counter balanced to the higher mode travelling mostly through the lower refractive index, higher speed region. The overall effect is a reduction in the time delay between the modes. Further developments in fibre-optics have produced ever-decreasing loss and noise per km of cable through better manufacturing.

2.5. Fibre-optic sensors

While the telecommunication industry has devoted considerable effort into solving many of the problems with transmitting the cleanest signal down fibre-optics, the sensitivity of the

propagating light to external perturbation has provided the sensing world with a wealth of new fibre based techniques.

2.5.1. Intrinsic fibre optic sensors

One of the earliest examples of intrinsic fibre optic sensors is in the use of fibre-optics as sensitive strain [40] and temperature gauges [41]. Changes in the force applied and temperature of the fibre can cause it to expand and contract which changes the critical angle within the fibre. This change can then be detected either by the loss of light that was on the edge of the cone of acceptance or by the change in delay between the axial and higher modes. G. B. Hocker was one of the first people to realise that this could be exploited to form a sensor. In 1978, Hocker assembled an apparatus that measured the change in the interference pattern created by overlapping the outputs from two fibres, which were put under pressure [42]. This change in the interference pattern could then be used to calculate the force applied to the fibres. This type of direct interaction between the measurand and a change in signal within a fibre is categorised as an intrinsic fibre optic sensor. One of the key advantages with this method is that a fibre optic sensor can make measurements over a length of the fibre optic cable. This sensing technique was first developed by the telecommunications industry, with the aim of identifying and locating defects in optical fibre cables. This so-called distributed sensing is one of the key advantages fibre-optics has over other sensing systems. One of the biggest companies in this area is Sensa, which produces a fibre optic sensing system capable of high accuracy (-/+ 0.01 degree celcisu) temperature sensing in fibres up to 30km long [27,43].

2.5.2. Extrinsic fibre optic sensors

Extrinsic fibre optic sensors represent a wider category of optical devices and include any sensor that uses fibre-optics to transmit a signal, but where the measurement principle does not rely on perturbation of the optical fibre. An extrinsic sensor requires a secondary sensor system to act as the interface between the measurand and the fibre. A commonly used example is found in remote spectroscopic equipment. The light is piped to the sample using a fibre optic cable, passed through the sample and then returned via a second fibre optic cable to the spectrometer. The light is modified as it passes through the sample and not within the fibre. This is has a number of advantages for systems such as fibre spectrophotometers, which allows laser and electronics to remain separate from the interface of the light and the sample. Fibre optic based spectrophotometers are particularly useful in oceanic systems, which have to stay immersed for long periods.

2.6. Combination coated fibre optic sensors

Some of the most powerful fibre optic sensors should really be classed as a combination of both intrinsic and extrinsic fibre optic sensors. Combination sensors include any fibre-optic sensor that is modified over a specific sensing region to better detect their target measurand. There are several ways to build a combination sensor, but it is with the understanding of the evanescent field and the development of methods to write gratings into fibres that this area has really developed.

As discussed earlier, the total internal reflection characteristics of a fibre optic are directly related to the difference between the refractive indices of the core and the cladding surrounding it. Further understanding of the importance of this divide led to some of the progress made on low loss optical fibre produced in the mid 1900s. The interaction at the interface between two media of different refractive indices in fibre optics is in fact more complicated than a simple index difference. Within the fibre, at the interface between the core and the cladded an evanescent wave is generated which proper gates into the cladding. (Figure 2.16*)* [44][58].

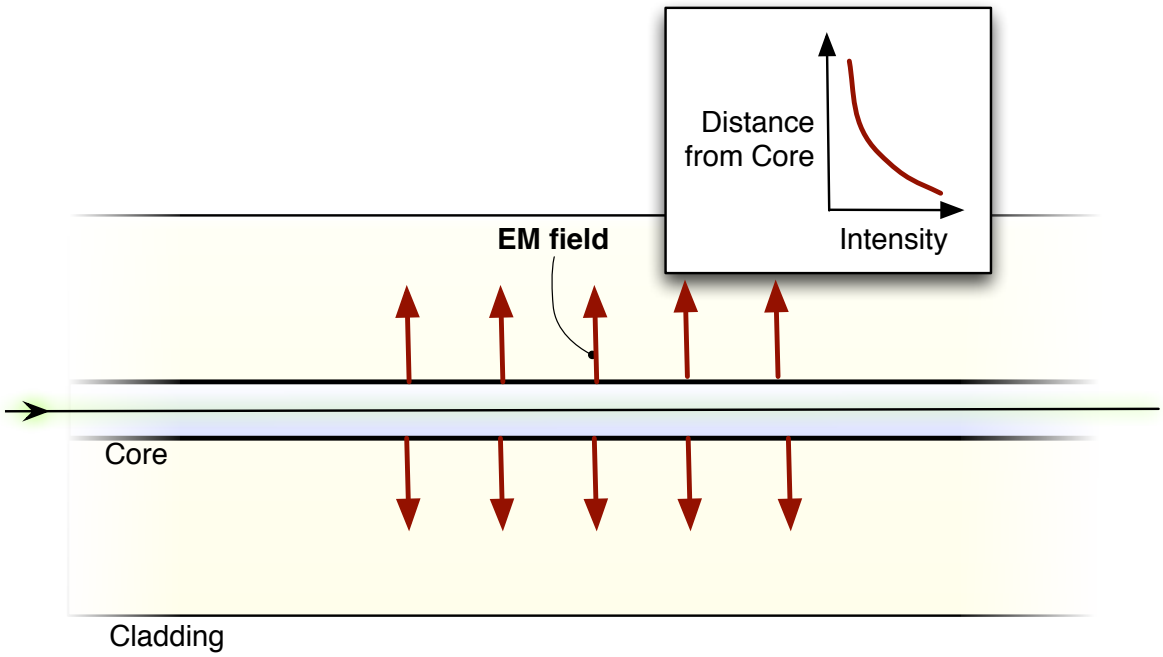

Figure 2.16: Evanescent field within a single mode fibre
A simple diagram to show the propagation from the core of the evanescent field. The field intensity tapers off quickly as it moves from the core.

One feature that makes the optically induced evanescent wave usefully for sensing is that it is coupled with the light that produces it. If the evanescent wave is manipulated, this has an effect on the light within the fibre. This manipulation can often be achieved by modification of the cladding material in which the evanescent wave forms. For example by decreasing the thickness of the cladding to half the distance of the evanescent wave, which is approximately a fraction of the wavelength, results in a fibre in which changes in the optical transmission of the fibre can be induced by interaction with the now exposed evanescent wave. This can be tailored for specific sensing purposes by the selective binding of materials to the outside of the cladding, which will differ from the un-bound state.

Several techniques have been used to modify the penetration depth of the evanescent field. One, as discussed, is the physical modification of the cladding material and core; the other is the chemical modification of the fibre. These modifications are further explained in later sections.

2.6.1. Modified fibre optic sensors

A later development in fibre optic sensing was the discovery of the ability to modify the refractive index of the core of an optical fibre via a number of techniques including irradiation [45], core doping and mechanical bending. This internal modification of the fibre has been put to good use in the production gratings inside the fibre. These gratings have two common

names depending on their scale; long period gratings (LPG) Figure 2.17 and fibre Braggs gratings (FBG) Figure 2.18.

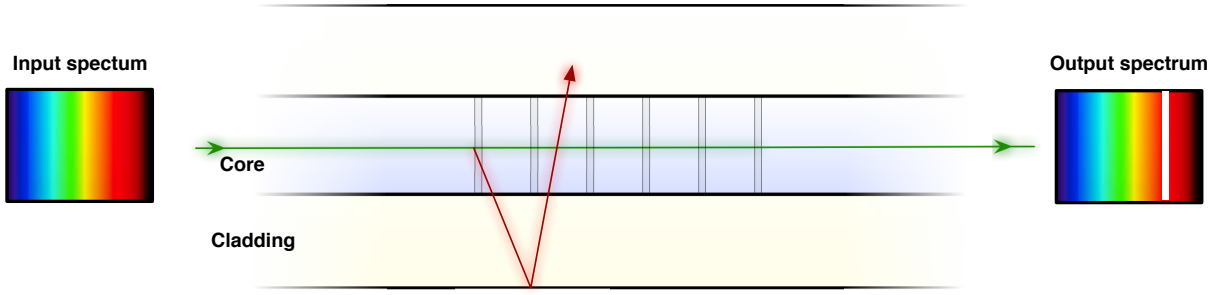

Figure 2.17: Long period grating schematic
The long period grating promotes a specific wavelength of light into the cladding mode.

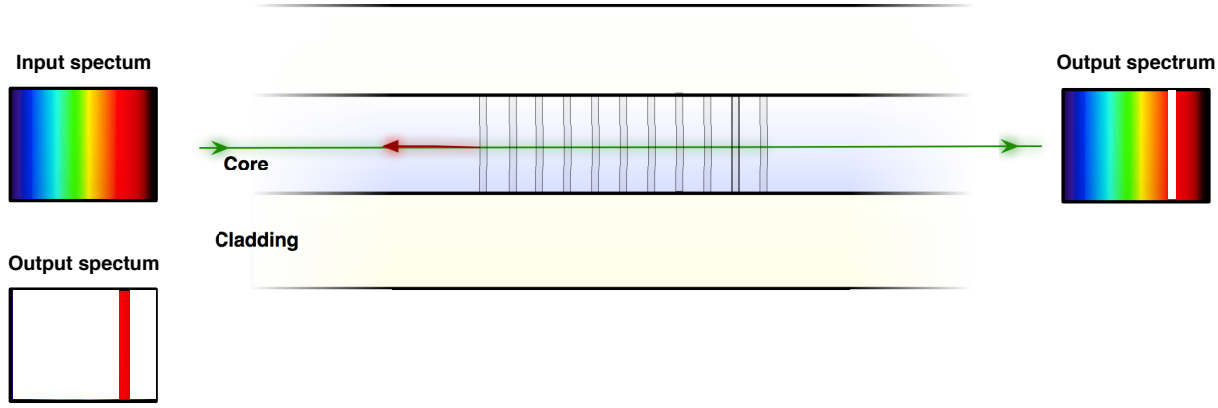

Figure 2.18: Fibre Braggs grating schematic
The FBG reflects a specific wavelength back down the fibre.

LPGs (shown in Figure 2.17) typically have periods that are longer than the wavelength of the input light. These inscribed gratings refract the input light into higher order modes, or modes that are no longer contained within the core of the fibre, at specific wavelengths depending on the period of the grating used [46]. FBGs (Figure 2.18) have periods ~1/2 the wavelength of the input light and do not promote light into the cladding but return a specific wavelength of light down the fibre. There are then a number of complex types of gratings, which are less commonly used, such as chirped gratings, π-phase shifted gratings and a variety of different tapered gratings [47].

In LPGs, the coupling of light from the core into the cladding material effectively sensitises the fibre to external modification through surface interactions which alter the cladding modes of the fibre and in tern affect the transmitted light. The resultant modification of the spectrum also has a secondary advantage; it is technically difficult to measure accurately the change in

the spectrum of a continuous curve, however if this is broken up in to a series of peaks within the spectra then the position and intensity of these peaks can be more easily monitored. For example, a modification of the cladding material may cause the grating to produce output spectrum with the peaks closer together than it would in an un-modified state.

2.6.2. Different shapes of fibres

Tapered fibres come in a variety of shapes and sizes and use changes in the fibre width along its length to modify the transmission properties of the fibre and create a sensing region. Within the available literature some work focuses on modification of the fibre so that the resulting output is modified in the sensing region (Figure 2.19) [48], while others deal with the modification at the tip of a fibre so that the reflected signal is altered [49] (Figure 2.20).

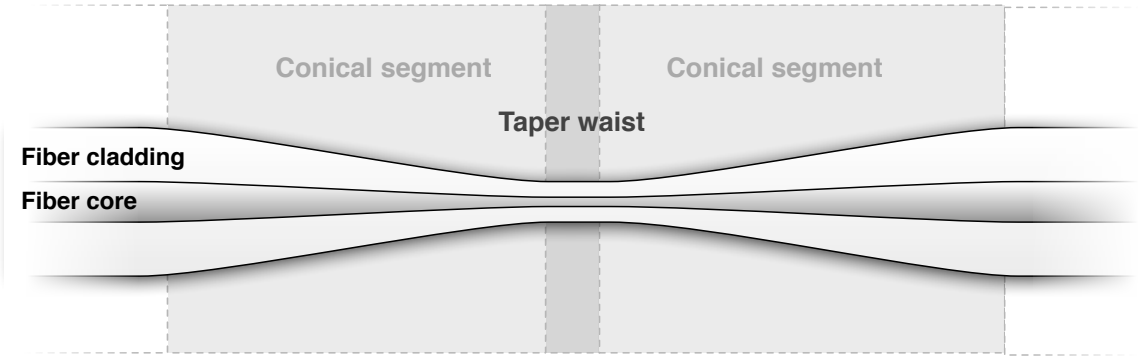

Figure 2.19: Tapered Fibre
This is a schematic of a tapered continuous fibre. The tapered region here would in reality be long and have no clearly defined start and end.

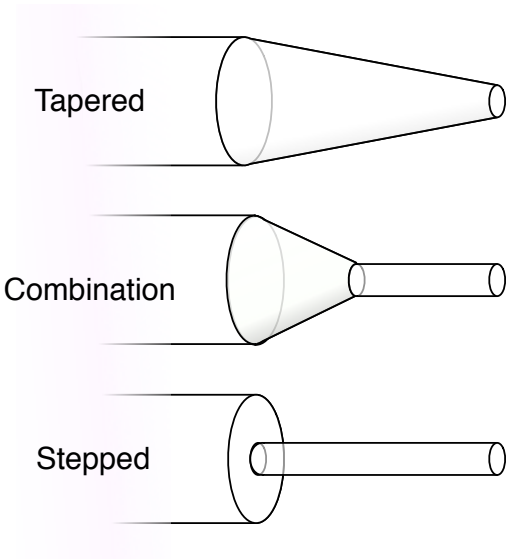

Figure 2.20: Tapered tips
This figure shows 3 possible tip alterations that have been used in fibre optic sensing.

Using long tapered fibres like those in Figure 2.19 can have the same effect on the signal as a fibre grating, without internal modification of the fibre. This mechanical deformation of the fibre promotes the evanescent wave in to the surrounding medium, which, any change in the surrounding medium causes signal modification via interaction directly with this evanescent wave. Taped fibres such as these can be sub-divided into to categories adiabatic [44] and non-adiabatic [50].

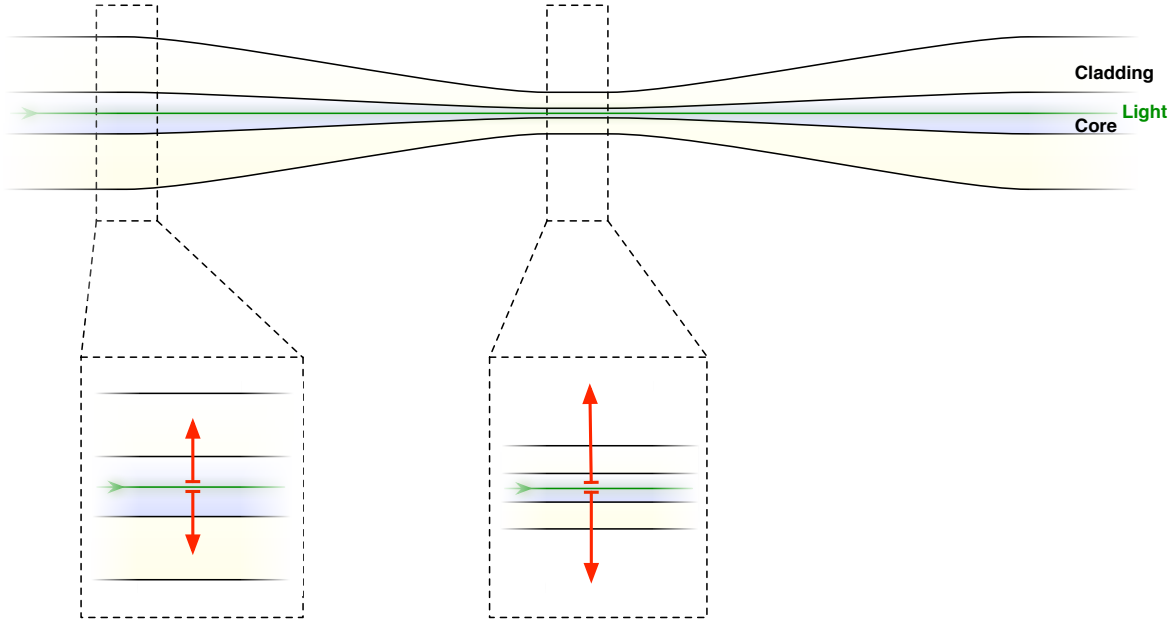

Figure 2.21: Adiabatic tapered fibre
Adiabatic taper supports a single mode through out the tapered section through a gradual change in the fibre thickness along it's length

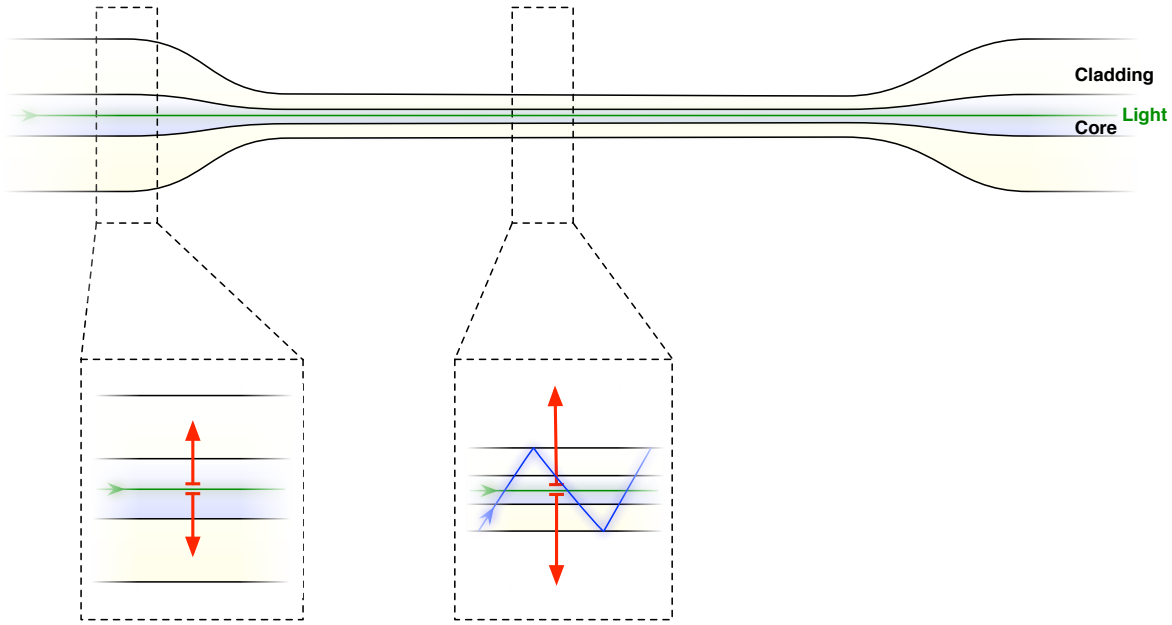

Figure 2.22: Non-adiabatic tapered fibre
The steep change in fibre thickness in the fibre conical sections temporarily induces the formation of cladding modes in the taper waist

These sub-divisions of tapered fibres are defined by the mechanism within the fibre that promotes the evanescent wave into the surrounding medium. Adiabatic tapers typically have a long drawn out conical segment that allows for the gradual promotion of the evanescent wave into the surrounding medium [51]. This type of fibre sustains just a single mode throughout the fibre. Non-adiabatic tapers by contrast have a steeper conical section, which leads to the formation of many cladding modes in the taper waist [52]. The evanescent wave associated with these cladding modes will penetrate into the surrounding medium through the taper waist before re-coupling to the core as the taper re-expands in the second conical section. It is this second type of fibre that is used in this project.

2.6.3. Fibre sensor coating techniques

As previously discussed, one of the growing areas within fibre optic sensing is the combination of intrinsic and extrinsic fibre optic sensors. Much of this interest is being focussed towards looking at fibre modification to enhance the signal generated by specific recognition systems immobilised on the surface of the fibre. It is in this way that these sensitive signal generation systems can be combined with the specificity of biological and chemical systems. One property of light propagating in an optical fibre that can be exploited in chemical and biological sensing is the evanescent wave produced at the interface between the fibre and the cladding.

The first step in harnessing the evanescent field to create a fibre optic sensor system is the modification of the fibre. As discussed in section 2.6, modification of the fibre itself can determine the depth and power of the evanescent field. It is on this fibre that the recognition system then must be deposited.

There are a number of ways that a fibre can be coated with either a chemical or biological sensing recognition agent. The simplest is direct deposition of the agent onto the surface of the fibre. This technique can work on almost any surface; since there is no movement or treatment required after the material has been applied. However, because you cannot accurately determine the amount of material that is bound/immobilised on the surface, this is a highly variable method. An improved version of this direct coating is spin coating. Spin coating is a well-established technique re-purposed for modern applications. Essentially, spin coating consists of a flat rotating disk on to which a substrate is fixed. The coating sample is then applied at the centre of the disk and spun out into a thin film. Film thickness can be controlled by spin speed and solvent used to increase or decrease evaporation as the film is spun out. Once the film has been spread to the desired thickness, the sample is allowed to

dry, which encourages the substrate to bind to the surface. Spin coating has a number of advantages over other methods due to its simplicity. This technique can be scaled to fit a large number of applications from coating glass panels to micro manufacturing of medical devices [53]. However, spin coating is heavily reliant on the material being flat and any significant shape changes across the surface cause an uneven layer to build up. This makes spin coating infeasible for coating small fibres.

Sol-gel is a process by which it is possible to create a large number of uniformly sized particles from a variety of inorganic materials. First understood in the early 1900s through the development of alkoxides and silica-based gels, the technique was advanced further as part of developments in the nuclear fuel industry involving the use of sol gel droplets in reactors. While this technology was never fully realised, other branches of science adopted the sol-gel process for a variety of uses. One such use is the immobilisation of recognition systems and their subsequent attachment to solid surfaces [54]. Sol-gel techniques have been used to coat a number of substrates, including fibre-optics. Sol-gel apparatus allows for simple coating with safe materials at room temperature. However, they also suffer from some of the problems associated with straight layering. The application of the sol gel layer can cause large variations in the thickness of a sol-gel layer. This is a critical flaw when used with fibre-optics, and many complicated gel coating and signal processing methods have to be employed to correct these variations.

2.7. Langmuir-Blodgett (LB) deposition

The development of LB layering technology is of great significance to sensing technology. First designed in the mid 1920s jointly by Irving Langmuir and Katherine Blodgett [55], the technique is a direct descendant of early investigations of the formation of a monolayer on an aqueous surface. By 1920, it had been well understood that when an amphiphilic substance is spread on the surface of water (sub-phase) it organises itself into a monolayer. What Langmuir [56] discovered prior to his work with Blodgett was that when a monolayer is compressed, the amphiphilic substances arrange with the tails pointing away from the sub-phase. He also showed how this monolayer developed as the area per molecule was decreased using equipment now called a Langmuir Trough (Figure 2.23).

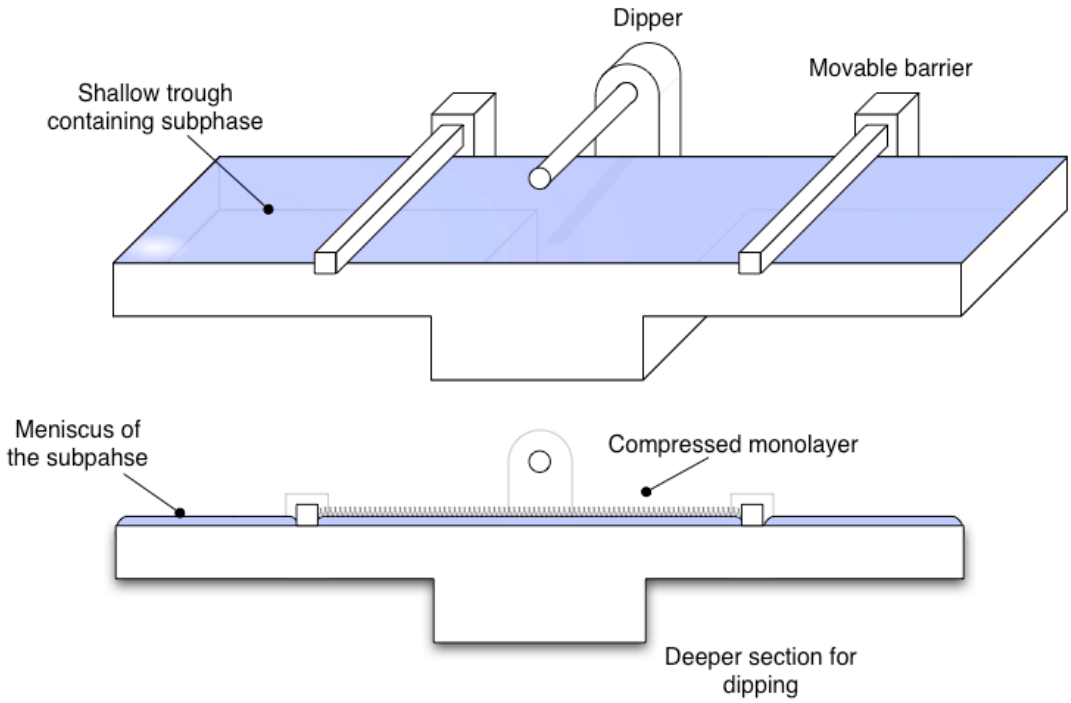

Figure 2.23: Langmuir-Blodgett trough
A diagram showing an over view of a simple LB trough

When an amphiphilic substance is spread on the surface of water, it will form a disperse monolayer. An insoluble amphiphilic material will spread on the aqueous subphase, orientated so that the hydrophilic head, which is able to interface with water, is immersed in or on the surface of the water, with the insoluble hydrophobic tail orientated away from the water. This property of amphiphilic materials ensures that an ordered monolayer always contains molecules with homogenous orientation. In this state, the molecules are well spaced and do not interact strongly. When the surface of the water is compressed, then the area per molecule decreases and the molecules begin to interact. Interaction between the monolayer can be monitored using surface pressure measurement and the greater the interaction of the molecules, the higher the surface pressure. As the surface area is reduced, this pressure increases until the molecules form a stable condensed monolayer. At this point, the surface pressure increases rapidly with further decrease in area. Eventually, the packing of the monolayer exceeds the possible space causing monolayer collapses, typically causing a sudden drop in surface pressure [57] or the development of a plateau in the rate of surface pressure increase [58]. This collapse is governed by the forces applied by the surrounding molecules in overcoming the dipole-dipole interaction of the monolayer material with either the surrounding monolayer molecules or the aqueous subphase [58] (Figure 2.24).

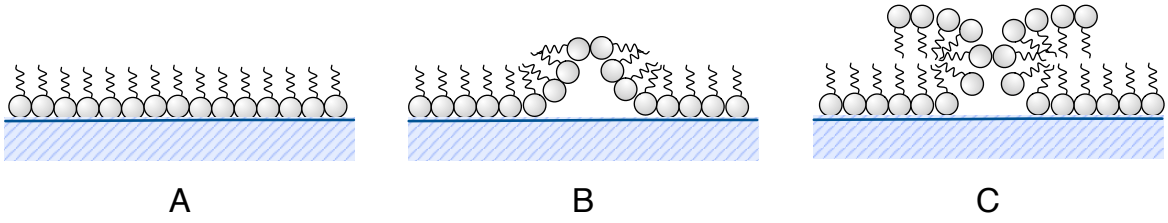

Figure 2.24: LB film collapse
These three diagrams show the stage in the collapse of an LB film. A shows a stable compressed film, B the buckling of the film and finally C, the formation of a bi-layer.

Langmuir and Blodgett built on this monolayer work by investigating the interaction between compressed monolayers and solid surfaces. They found that the monolayer could be deposited onto the surface in its homogenous monolayer form. Initially it looked like they had just discovered the ability to accurately coat surfaces with one-molecule thick layers, but further work by Langmuir and Blodgett showed that not only could they coat one monolayer but that they could repeat the process and coat the solid surfaces with a number of layers by repeat deposition. This build-up of layers allows for increased density of the molecule in a highly ordered structure.

Blodgett showed that, when a substrate was dipped through the subphase, the monolayer followed the line of the water meniscus and that, as the contact angle approached zero, the LB film transferred on to the substrate. As shown in Figure 2.25, as the solid surface is slowly drawn out of the water, the monolayer is deposited on to the surface. If the same surface is then re-inserted into the water, then a second coat can be deposited on top of the first. This can be repeated a number of times to build up a series of monolayers (Blodgett's original paper showed a 200 layer coating deposited on to a silica slide by repeated dipping [59]).

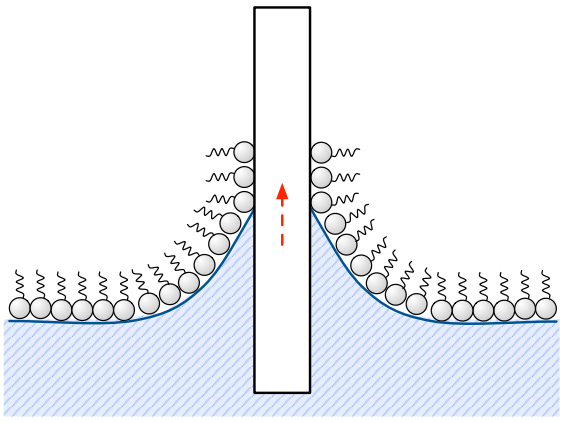

Figure 2.25: Drawing a solid substrate up through an LB film
As the substrate is draw out of the trough the monolayer is deposited on the surface.

The exact structure of the deposited monolayer is highly dependent on the characteristics of the molecule being deposited. The orientation of the molecule and the charge and charge strengths within the molecule all act to determine the orientation of the coated film.

2.7.1. LB Isotherms

As briefly mentioned in the previous section, as the barriers of and LB trough contract there is a change in the surface pressure and molecule organisation. This change is specific to the molecule spread on the surface of the trough and the resulting record of this change is called an Isotherm. A classic example of an isotherm is shown in Figure 2.26.

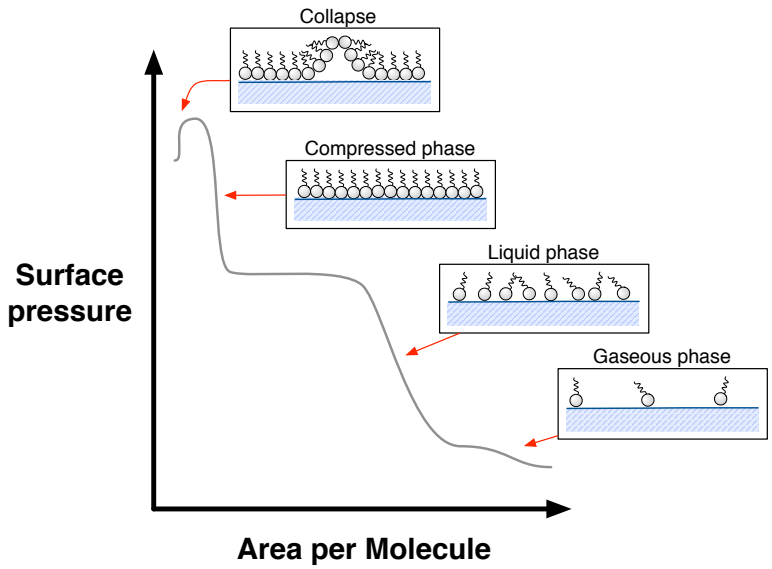

Figure 2.26: Isotherm schematic
This graph is the representation of the phases within a typical isotherm. The shape of this graph is highly dependent of the specific substance spread on the surface to form a mono-layer.

However, it is rare to obtain an isotherm that follows this shape, since each molecule responds differently when put under pressure on the water sub-phase. Spreading solvent, temperature, pH and additives in the sub-phase can also affect isotherms. Assessing the shape of an amphiphilic substance's isotherm is critical in determining the best surface pressure at which to coat a substrate.

2.7.2. LB deposition

Coating surfaces with LB films is a simple process, but it is a difficult process to perfect. For a surface to be coated, it needs to be dipped into the LB trough and drawn out a number of times to build up multiple layers. However, as previously discussed, the structure and amphiphilic nature of the monolayer will have an impact on how the structure of the layers builds up (Figure 2.27).

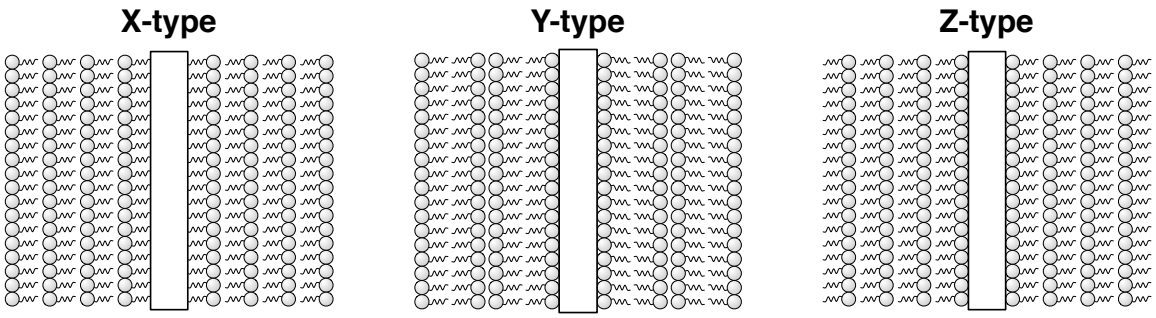

Figure 2.27: Types of LB film layering
The three common types of layering show in substrates coated with LB layering.

There are three key structures found in LB deposition (Figure 2.27). These structures can, to some extent, be predicted through understanding the monolayer. They can also be determined by monitoring the deposition rates on each pass through the monolayer. For example, if there is transfer to the surface as the surface is moved into or out of the sub phase, then it is most likely that the film is arranged as a Y-Type (bi-layer coating). The difference between an X-type and a Z-type coating however is most likely to be the result of the hydrophobicity on the surface, which determines the orientation of the first layer. An X or Z-type film can be forced into Y-type coating though the modification of the layers after each coating changing their hydrophobicity. The LB technique can also be used to deposit composite films by using two dipping tanks containing two different subphases [60].

2.7.3. LB Problems

While the ability to build up multi-layer LB films is a great strength of the technique, this can also represent a key weakness. As the film is uniformly layered on to the surface, with each monolayer deposited any defects can be amplified quickly. Defects can result in pits which, when LB films are combined with sensitive sensor platforms, can create large device-to-device variation. This problem can often be better seen in Atomic Force Microscopy (AFM) studies, which have been used to image the upper layer of LB films [61].

2.8. Calixarene coated fibre sensors

As discussed the initial trials [1] of this combination of calixarenes and fibre optic sensors had produced promising results for VOC sensing and it is a key aim of this project to improve upon this work. As highlighted in sections 2.4 and 2.7 both the production of the fibres and the coating technique are sensitive procedures that require optimisation and characterisation in order to produce a suitably sensitive sensor system attuned to the required analyte, as set out in the aims of this project. As discussed in Chapter 1 this aim of this project is to produce

and optimise system based on this combination sensor and to investigate possible methods of improving their performance further through monolayer modification, and characterisation. It is clear both from the multifaceted VOC sensing capabilities of calixarene (section 2.3.3) and from the sensitive coating techniques (section 2.7.3) that there is wide scope for performance improvements through better understanding of the methods and chemistry involved.

Chapter 3 Materials and Methods

This chapter describes the equipment, methods and materials used during the course of this project.

3.1. Langmuir Troughs

Canfield University has two Langmuir Blodgett troughs in a dedicated clean room within the School of Engineering. Both troughs are designed for simple monolayer work and LB coating using removable dipping rigs and are mounted on vibration isolation platforms. Each trough consists of two independent barriers and a central dipping section, which divides the trough into two separate chambers (Figure 3.1, Figure 3.2, Figure 3.3). These barriers can be independently electronically controlled though a computer control interface and allow for alternate layering of two different materials.

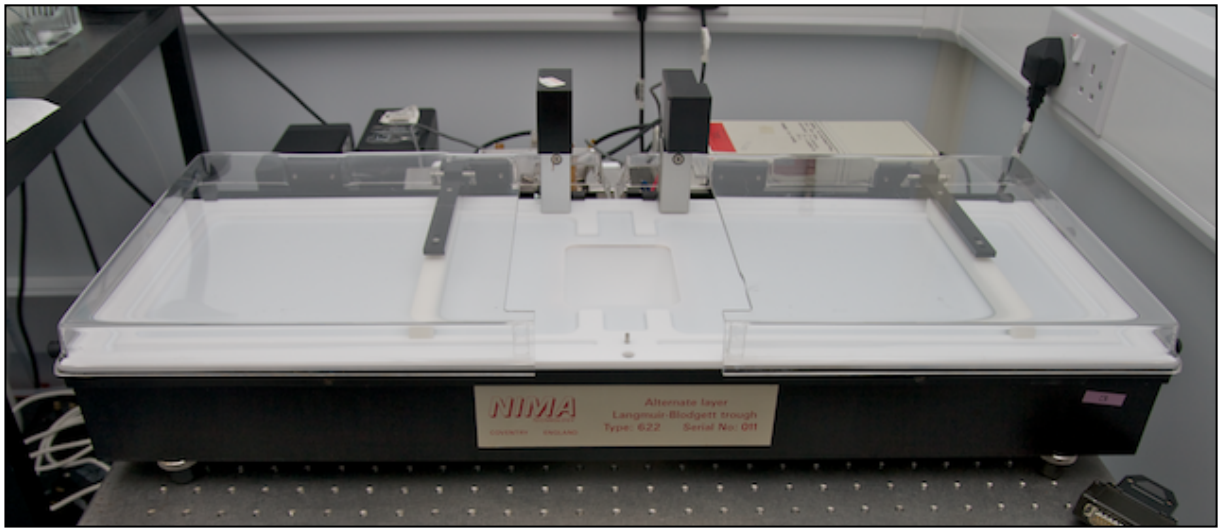

Figure 3.1: Square Nima trough (Type: 622, Serial: 011)
This photograph shows the square Nima trough on it's vibration isolation stage, without a dipping rig

Figure 3.2: Circular Nima Trough (Type: TKB2410A, Serial: 8810)
This photograph shows the top of the circular trough, without a dipping rig. The trough is enclosed by a black wooden box and positioned in the fume hood for use in vapour experiments.

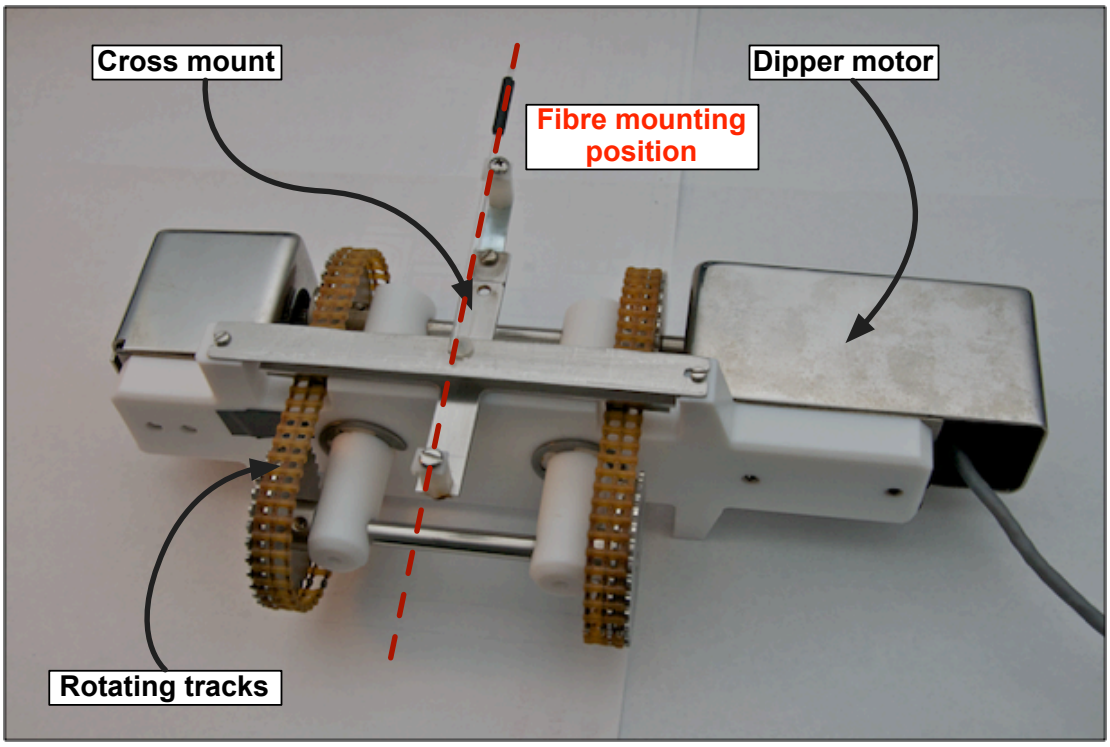

Figure 3.3: Dipping rig used for coating fibres and glass capillary tubes
The above dipping rig fits into the central cavity of both Nima troughs and is controlled by the Nima software

For smaller scale monolayer work, a smaller Langmuir trough designed with no dipping mechanism was re-built from parts (Figure 3.4). This trough was purchased as part of a pervious project and was re-assembled as part of this project. Unlike the Nima troughs, the single barrier is manually controlled via a screw thread with no feedback mechanism for maintaining surface pressure.

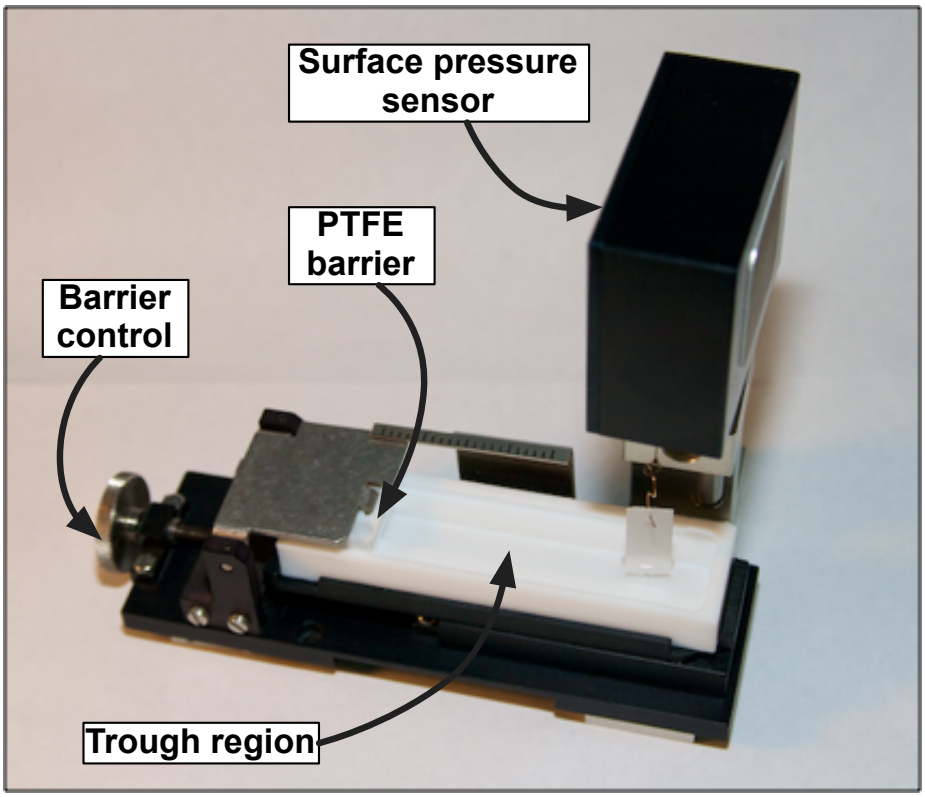

Figure 3.4: Mini Langmuir trough
This is a photograph of the mini trough. The pressure sensor is the same as used in the Nima troughs.

The methodologies for using the LB troughs had previously only been shared between students from notes in lab books. To ensure that a consistent procedure was used during this project, these notes were prepared into a single standard operating procedure for all troughs, this procedure is summarised in the following section.

3.1.1. Trough Cleaning

Ensuring that the troughs are clean and free of impurities is critical in any monolayer work. Trace impurities can create defects in the monolayer, which can cause poor quality LB coating or monolayer collapse. Any cleaning procedure needs to include the removal of dust and particulates that may have collected on the trough, as well as contamination from previous experimental samples.

The exterior of the trough was first wiped down with isopropyl alcohol (IPA) using clean room grade filter paper (Primo 100). Following this, the interior of the trough was wiped using a small amount of acetone and then again using IPA, after which the trough was allowed to dry for 5 minutes. The troughs used in this project were cleaned before and after each experiment to limit the chance of contamination.

3.1.2. Preparing a monolayer

To prepare the trough for monolayer spreading, it was filled with high purity (18 MOhms/cm resistivity) de-ionised water until the meniscus was 'bulging' over the top of the trough. A small 1 cm x 2 cm piece of filter paper was then hung from a Wilhelmy balance and positioned so that the tip was immersed to a depth of 2 mm in the water. The output from the balance was monitored using Nima's proprietary software running on dedicated computer that was connected, to the balance via a Nima control box. All three troughs used Wilhelmy balances for the surface pressure measurements.

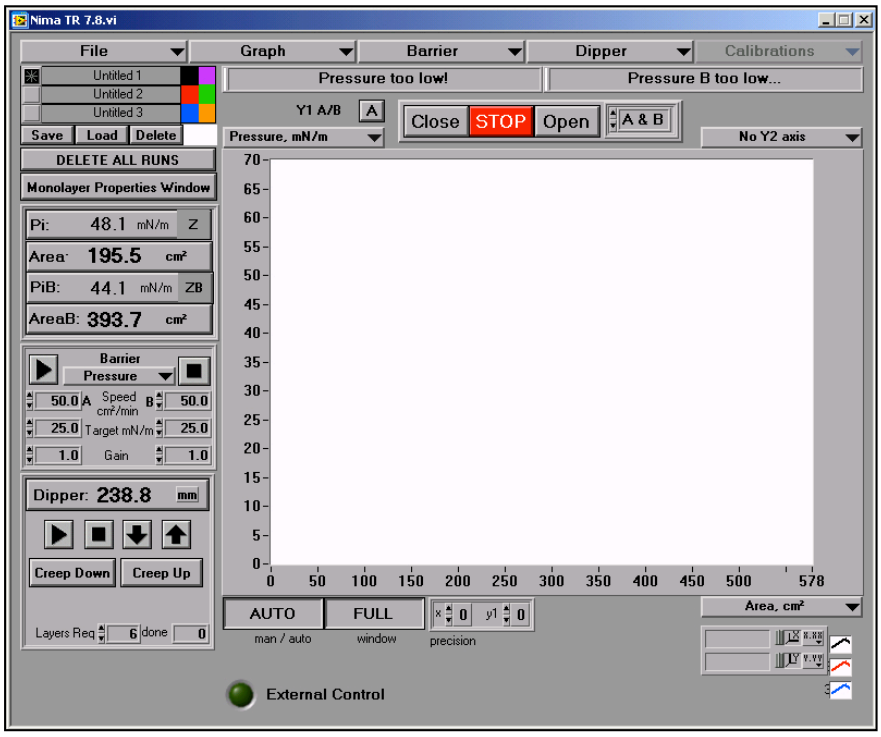

Figure 3.5: Nima 7.8 software
This is a screen shot of the software used to run the Nima brand troughs and the pressure sensor for the Mini trough. This software allowed for a range of customisation and control over the monolayer surface.

Before any pressure readings were taken, the barriers of the trough were closed and the surface was cleaned using a vacuum pump. This step ensured that any monolayer forming contaminates had been removed. Following this, the barriers were re-opened and the pressure sensor was 'zeroed'.

Each monolayer material was applied from free falling drops, produced using a 100 µl glass syringe, in several places across the subphase. Each free-falling drop was applied as close to the surface as possible to prevent any disturbance of the subphase. Once applied, the

surface was left for 30 minutes to ensure that all of the spreading solvent had evaporated, leaving a disperse layer of calixarene on the surface of the water.

Depending on the exact nature the experiment, this monolayer was then compressed to a specific pressure (or series of pressures) either via the Nima software, or in the case of the smaller trough, the manually controlled wheel.

3.1.3. Langmuir-Blodgett Coating

Coating a monolayer onto a substrate is, in principle, a simple process of moving the substrate through the monolayer, as described in section 2.7. However, there are a great number of parameters that can affect this process and alter the quality of the coating. Parameters such as dipping speed, surface pressure and monolayer modification techniques all require careful optimisation before a substrate can be coated effectively.

During the course of this project, two types of substrate were coated using the LB troughs, small silica capillary tubes and prepared fibre optic devices (also made from silica). Both materials were mounted on a single motor dipper with a ‘cross’ holder.

Capillary tubes were mounted using just the top screw to hold loosely the tube in a vertical position. A small piece of tape was wrapped round the top end to prevent the tube from dropping into the subphase. This set up is shown attacked to the alternate layer dipper in Figure 3.3.

Optical fibre substrates were mounted using both top and bottom screws and required careful handling to ensure that they were positioned without breaking. It was critical that during the mounting process they were pulled taut between the top and bottom screws; this ensured an even coating and a clear transmission signal though the fibre.

Once mounted on the dipper mechanism, the whole unit was positioned in the trough, which was then filled and prepared as in section 3.1.2. Depending on the experimental design, the monolayer was compressed to a fixed pressure and the software was switched to automatic barrier control. This automatic control ensured that the pressure was maintained even when material was transferred to the substrate. Using the Nima software, the dipper was instructed to move the ‘cross’ holder up and down through the monolayer at a fixed speed and for a pre—programmed number of times.

3.1.4. Method changes & development

During the course of the work described in this thesis, the procedure described in section 3.1.3 was altered, with the modifications driven by observation of the coating process and quality.

The alterations to the software were the result of collaboration with Chris Harling, Managing Director at Nima Technology. In return for helping to develop and beta test their new software Chris serviced both troughs, replaced the pressure sensors and provided support for combining their new software with the spectrophotometer systems used to monitor the transmission of the optical fibre devices during the coating procedure.

3.2. Spectrophotometers

The transmission of the optical fibre devices were monitored in real time during the coating deposition process using an Ocean Optics (Geograaf 24, 6921 EW Duiven, Netherlands) S2000 spectrophotometer (serial number: 00131). The S2000 has a wavelength range of 200 to 1100 nm and a resolution of ~0.3nm. The spectrometer was interfaced to a PC via a USB cable and the spectra recorded using Ocean Optics' software.

There are three versions of the software that runs the Ocean Optics spectrophotometer. The first is provided by Ocean Optics and produces a live graph of the transmission spectrum within a fibre. The second is a custom piece of software written using Labview 2009, as part of this project to link the spectrophotometer to the Nima troughs. This second software allows the transmission spectrum of the fibre to be recorded and saved at particular stages of the coating process and was the version predominantly used in this project. Through further development, this software was eventually expanded to include a number of additional functions to control the Nima trough; this version of the software was eventually made open source and is now being tested by other groups using the Nima trough systems.

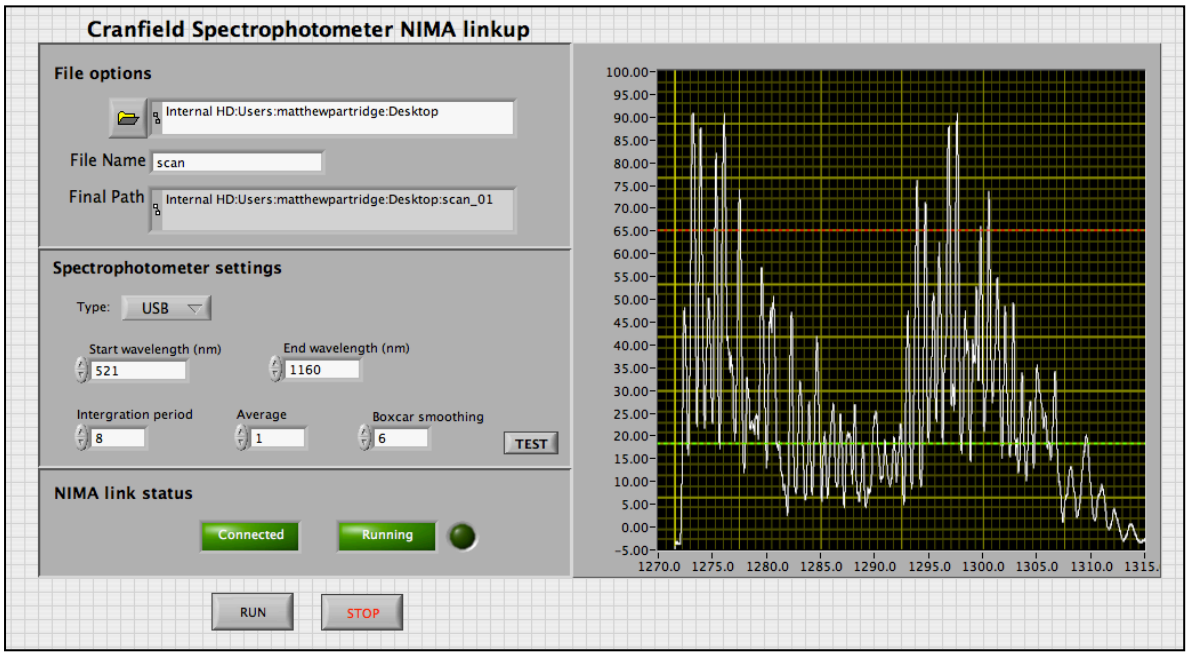

Figure 3.6: Screen shot of the Nima-Spectrophotometer link software
The screen shot above shows the software used to link the Nima trough controls to the Ocean Optics spectrophotometer. When run, the software saves each spectrum to a sequentially numbered file for later analysis. The recording of the spectra is synchronised with the movement of the dipper mechanism, so that spectra were recorded at the top and bottom of the stroke.

3.2.1. Further spectrum processing

The individual spectra recorded during coating or subsequent vapour measurement experiments are of little value without being combined into an overall picture of the change in transmission. As part of this project, software was written with algorithms for tracking the position and intensity of spectral features over time. Throughout the course of this project, the software was updated and the algorithms improved to enable higher-resolution feature tracking. During the development of the fibre optic pressure sensor, the software was also updated to allow large data set handling which enabled the processing of 0.5 GB of data in under a minute.

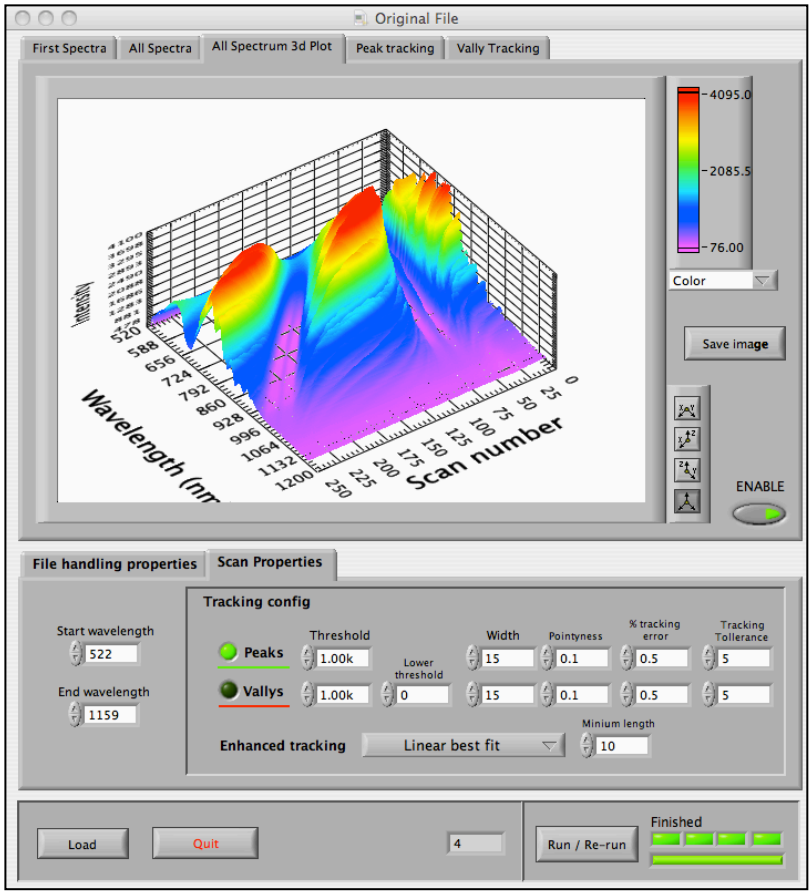

Figure 3.7: Screen shot of the customer built peak tracking software (version 2)
The above figure is a screen shot of the software produced as part of this project to track the position of peaks within series of transmission scans. The above screenshot is from one part of the software showing a 3D plot all scans.

The software shown in Figure 3.7 was also used to prepare 'grey-scale plots' of successive spectra in order to show the evolution of the transmission spectrum of the optical fibre device as the coating thickness increase, or as the characterisation of the coated fibre sensor progressed. A grey-scale plot is a 2D intensity plot produced by combining all the spectra collected during an experiment. A schematic of the processing required to generate a grey-scale plot is shown in Figure 3.8.

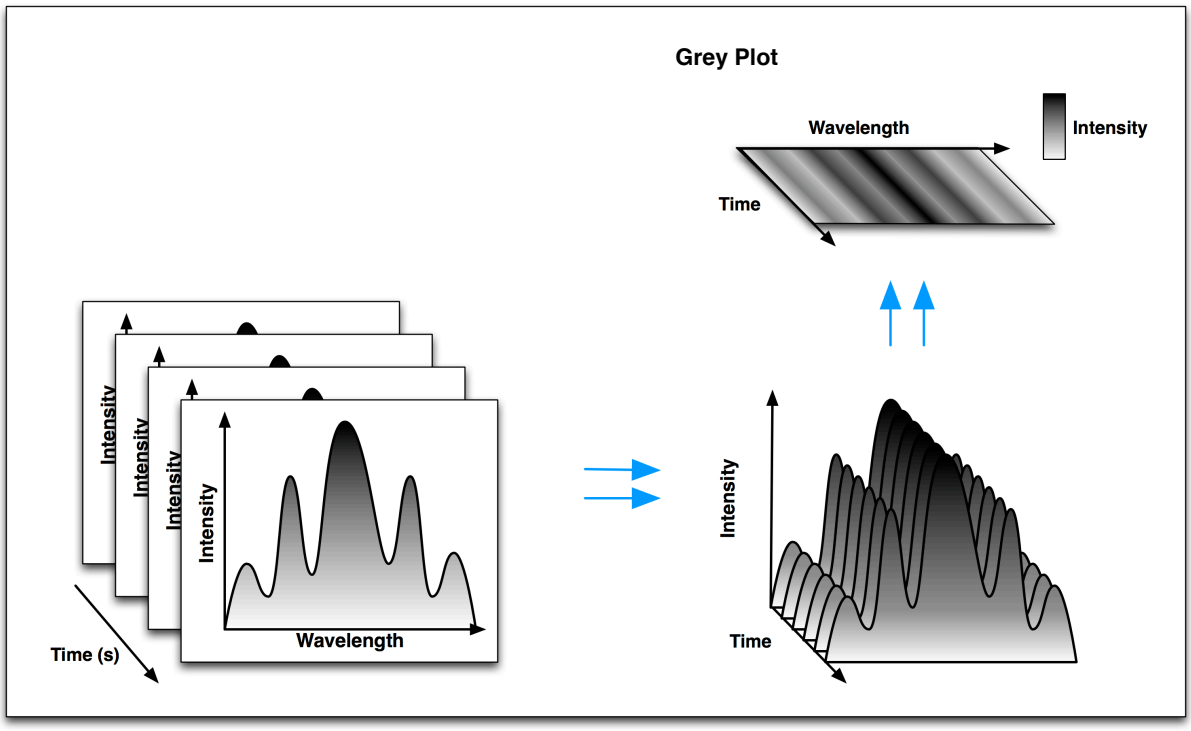

Figure 3.8: Schematic of the production of a grey-scale plot

As shown in Figure 3.8, each spectra is plotted on a 3-axis graph, this 3D interpretation is then presented as a 2D intensity plot by converting the intensity of the light to a grey scale indicator. Converting the data in this manner allows for the clear visual identification of patterns and shapes within successive spectra. The software developed for this peak tracking and data presentation is under further development to enable its use with a large variety of spectral data.

3.3. Brewster angle microscope (BAM)

In an attempt to better visualise defects within Langmuir monolayers, there was a need for the development of a microscope to view the surface of the subphase. Previous work reported by other groups had used a Brewster Angle Microscope to achieve this. Brewster's angle is the angle at which light of a certain phase will not reflect off the boundary between two materials with different refractive indices. This essentially splits the light into two phases, one reflected, and one transmitted into the material Figure 3.9.

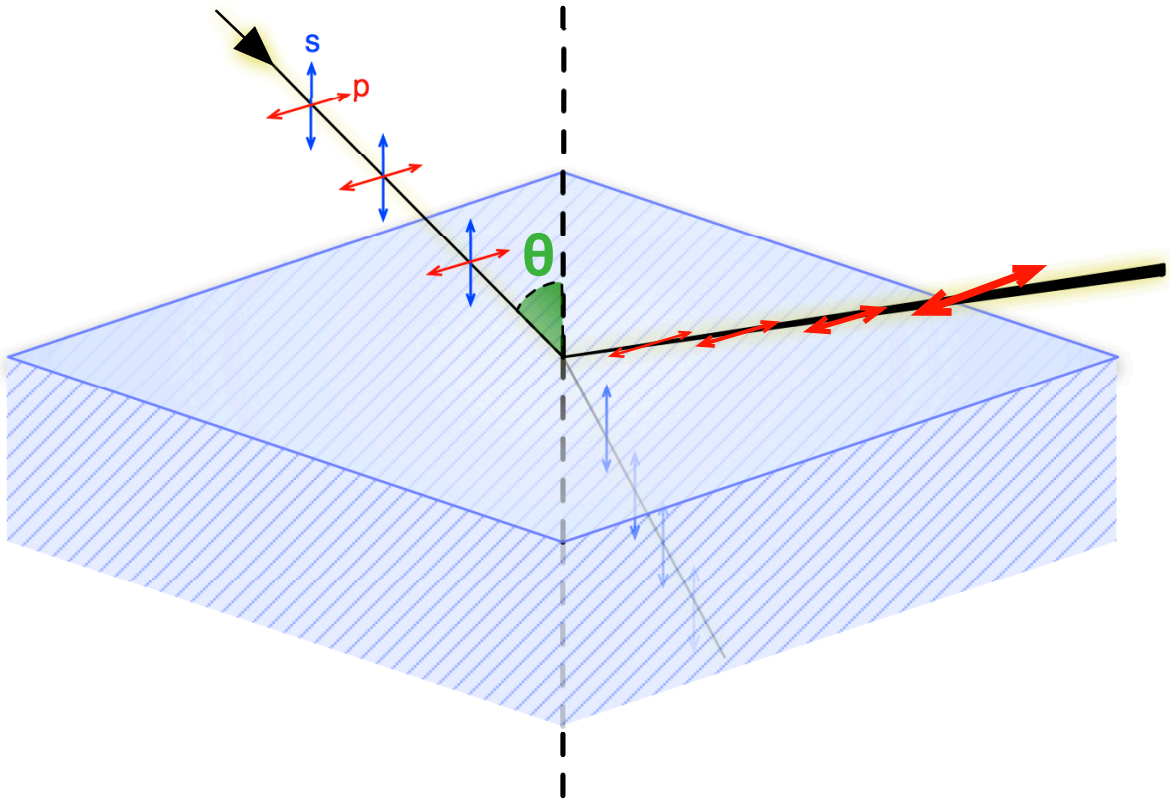

Figure 3.9: Principle behind a Brewster angle microscope
As the figure shows, light of mixed p & s-phase splits at the interface between air and water. s-phase light is refracted into the water while p-polarised light is reflected. The angle at which this effect occurs (shown in green) is known as the Brewster Angle (θ).

Brewster's angle can be calculated for the interface between two given materials using Equation 3.1;

$$\theta = \arctan\left(\frac{n2}{n1}\right)$$

Equation 3.1: For the calculation of Brewster's angle

The above equation provides the angle at which s-phase light will be totally refracted at the interface between two interfaces with a refractive index n1 (e.g. air) and n2 (e.g. water). According to Brewster's equation, if the surface of the water is illuminated at an angle 53.1° only one plane of polarised light will be reflected. If the refractive index of the water changes through the addition of a monolayer then the reflected light will no longer be perfectly polarised, as the Brewster angle will shift away from 53.1°. A BAM utilises this in one of two ways. More sophisticated equipment can monitor the change in the polarisation of the light

across the field of view and build a detailed picture of the surface based on those measurements. A basic setup relies solely on the contrast created by the refractive index change. By blocking out all of the perfectly p-phased light reflected off the surface with a polarising lens, it is possible to observe the light reflected by the refractive index change of the monolayer.

While most BAMs are large pieces of specialist equipment, using this second simpler method, it was possible to build a smaller version suitable for this project using a number of low cost components. A simple proof of principle BAM was constructed by mounting a inexpensive USB microscope (VMS-001, Veho, UK) and a 1 mW green laser pen (SP31, SP3Plus Ltd, UK) on a frame, each with a 49mm linear polarising filters (Hama (UK) Ltd, Hampshire, UK) positioned in front of them. The frame was constructed to allow small changes in the angle of the component optics.

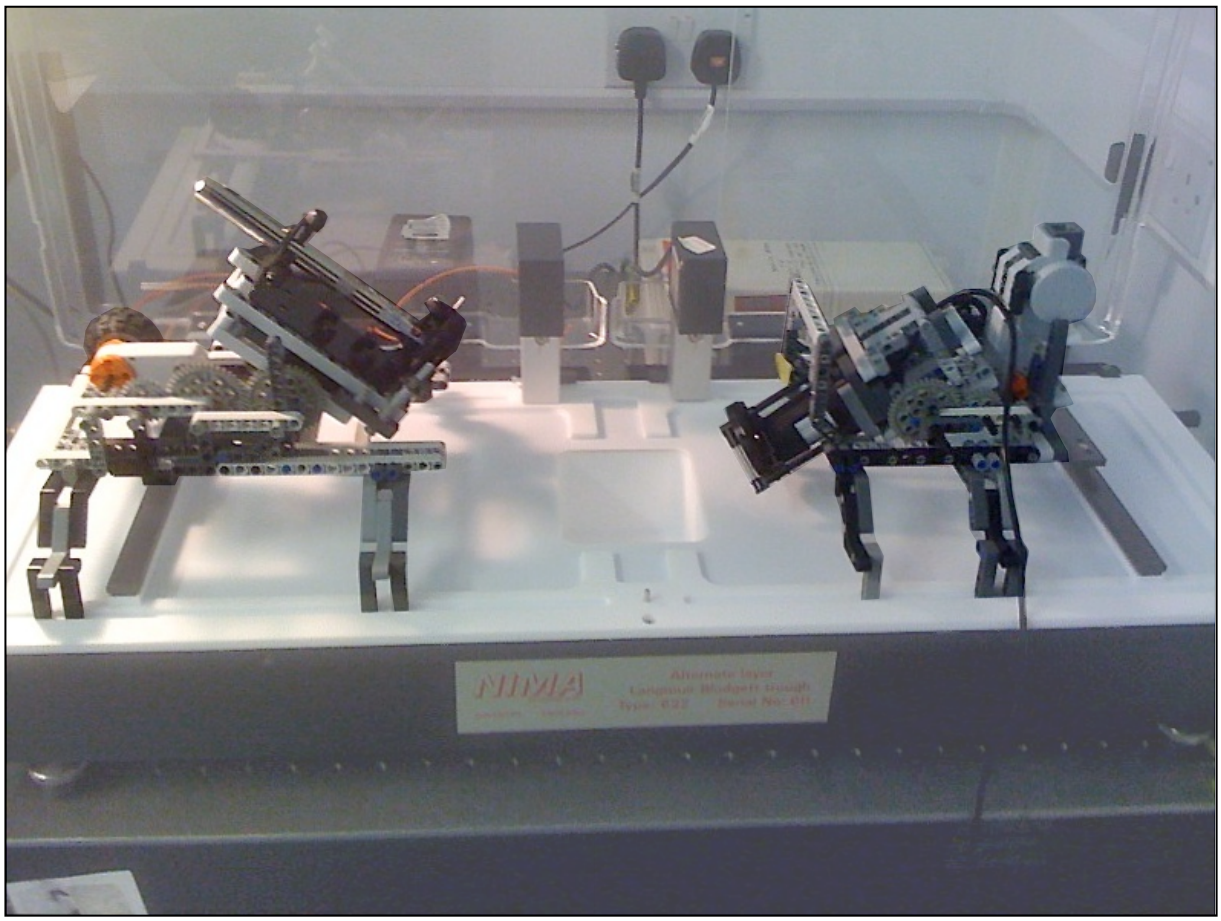

Figure 3.10: Photograph of the BAM mounted on the square Nima trough
This photograph shows the two units of the BAM, the laser on the left and the camera on the right, mounted on the square Nima trough.

This simple set up was able to record live video of the monolayer surface at 30 frames per second.

3.3.1. Trial images

As an initial trial of the BAM, we chose to image a well-known calixarene monolayer (calix[4]res C11). calix[4]res C11 has been previous used in in elipsometry studies (a similar technique to BAM), which showed that calix[4]res C11 has refractive index (when coated onto a substrate) of 1.46 [30]. By using Equation 3.1 we can calculate that calix[4]res C11 has a Brewster's angle of 55.6°, which is 2.5° larger than water. This difference in Brewster's angle provides contrast between the water and a monolayer of calix[4]res C11.

The trough was prepared as in the standard procedure. The Wilhelmy balance was set up using pre-soaked filter paper (as discussed in Chapter 4). 250 µl of 0.1 mg ml^{-1} calix[4]res C11 was spread on the subphase. The monolayer was then compressed to surface pressures of 5 mN m^{-1} and 15 mN m^{-1} and filmed for 30 s using the BAM connected to a computer. Still images from these videos are shown in Figure 3.11.

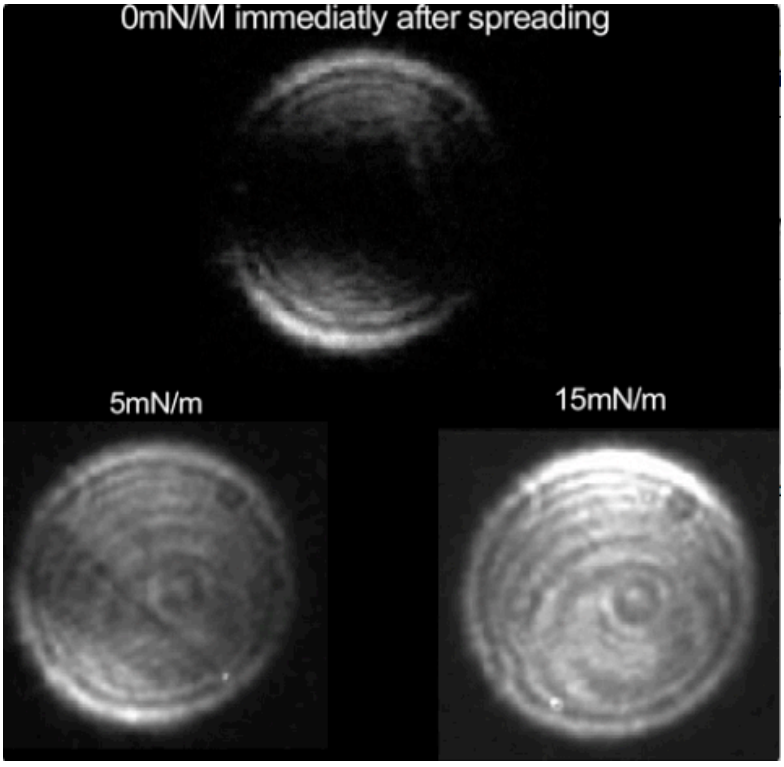

Figure 3.11: BAM image of one film at three different pressures
This figure is the amalgamation of 3 stills of a single Calix[4]res C11monolayer held at 3 different pressures. The rings visible in all 3 images are the result of optical artefacts and dust.

The three images in Figure 3.11 show that the microscope was successful in picking out some of the details required for examination of the monolayer structure. At 5 mN m^{-1} there is clear striping of the monolayer, which disappears as the monolayer is compressed to

15mN/m. The static images fail to convey the shapes and structures apparent when the video is viewed.

In order to improve the image quality shown in Figure 3.11, the camera was refocused and a second monolayer was prepared in the same manner as the previous experiment. The monolayer was initially compressed to a pressure of 5mN m^{-1} and then the barrier was opened fully. The compression and relaxation of the monolayer created moving areas of monolayer on the surface of the sub-phase, which passed though the small viewing window of the camera. From the video recorded captured during the relaxation of the monolayer the image shown in Figure 3.12 was selected.

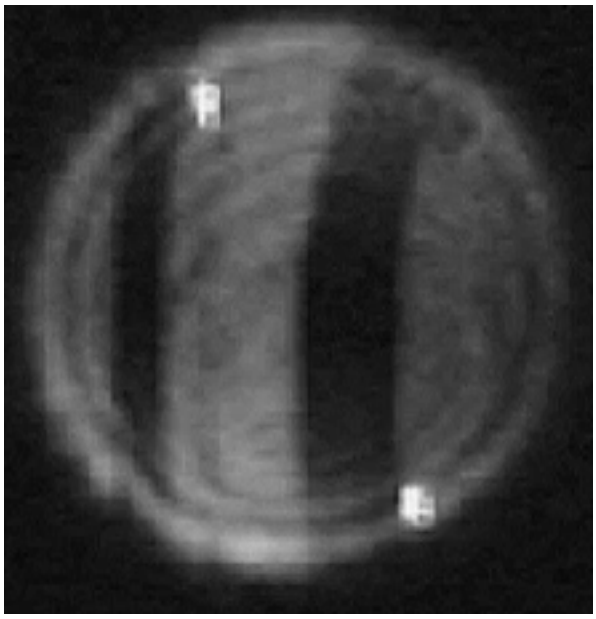

Figure 3.12: Single image of a Calix[4]res monolayer
A still image taken from a video recorded during the relaxation of a monolayer from 5 mN m^{-1} to 0 mN m^{-1}. The white bands are monolayer whereas the dark is the water surface

3.3.2. Limitations of the BAM

Whilst this low cost BAM can certainly visualise the monolayer, it is not capable of the resolution or image quality of that is required for the clear examination of variability in a compressed monolayer. The main limitation was the use of low cost optical components that can create optical artefacts and prevent clear focussing on the monolayer. Because of this limitation, the BAM work was not taken any further and it was decided that the quality of the coating method could be determined in other ways, such as transfer ratios and changes in

the transmission spectrum of coated fibre optic devices. It is hoped that a future project will develop this low cost approach further, with improved optics.

3.4. Vapours

During the course of the project, two methods were used for solvent vapour generation.

3.4.1. Evaporation method

This method is the same as that discussed in Topliss 2010 [1]. The sensor was enclosed in a sealable container (a bell jar when optical fibres were used, a wooden box when the trough itself was used as the sensor) of known volume. A measured volume of solvent was added to the chamber (which was then sealed) and allowed to evaporate at room temperature and atmospheric pressure. It is possible to calculate the vapour concentration (ppm by volume) based on the assumption that the solvent fills the container evenly. The benefit of this method is that it is quick and achievable using basic lab equipment. However, the difference between density of the solvent vapours that are generated and the air in the chamber creates one flaw in this method when employed to characterise the response of fibre optic sensors. As the optical fibres were suspended at the top of the bell jar and the solvent was injected into the bottom. As the solvent evaporated, without any airflow or movement, the vapour did not distribute evenly through the jar, preferentially localising at the bottom. A sensor suspended at the top of the bell jar is potentially analysing a lower concentration of vapour than that calculated from the volume of solvent added.

3.4.2. Owlstone vapour generator

The Owlstone OVG-4 vapour generator is an incubation based vapour generator that can produce a flow of vapour with specific vapour concentration. The vapour generator consists of a small oven (permeation oven) into which a PTFE tube (containing the target solvent) is placed and held at a fixed temperature. During calibration, the permeation of the solvent through the PTFE tube is calculated and, by varying the flow rate of the air into and out of the chamber, a range of concentrations can be achieved.

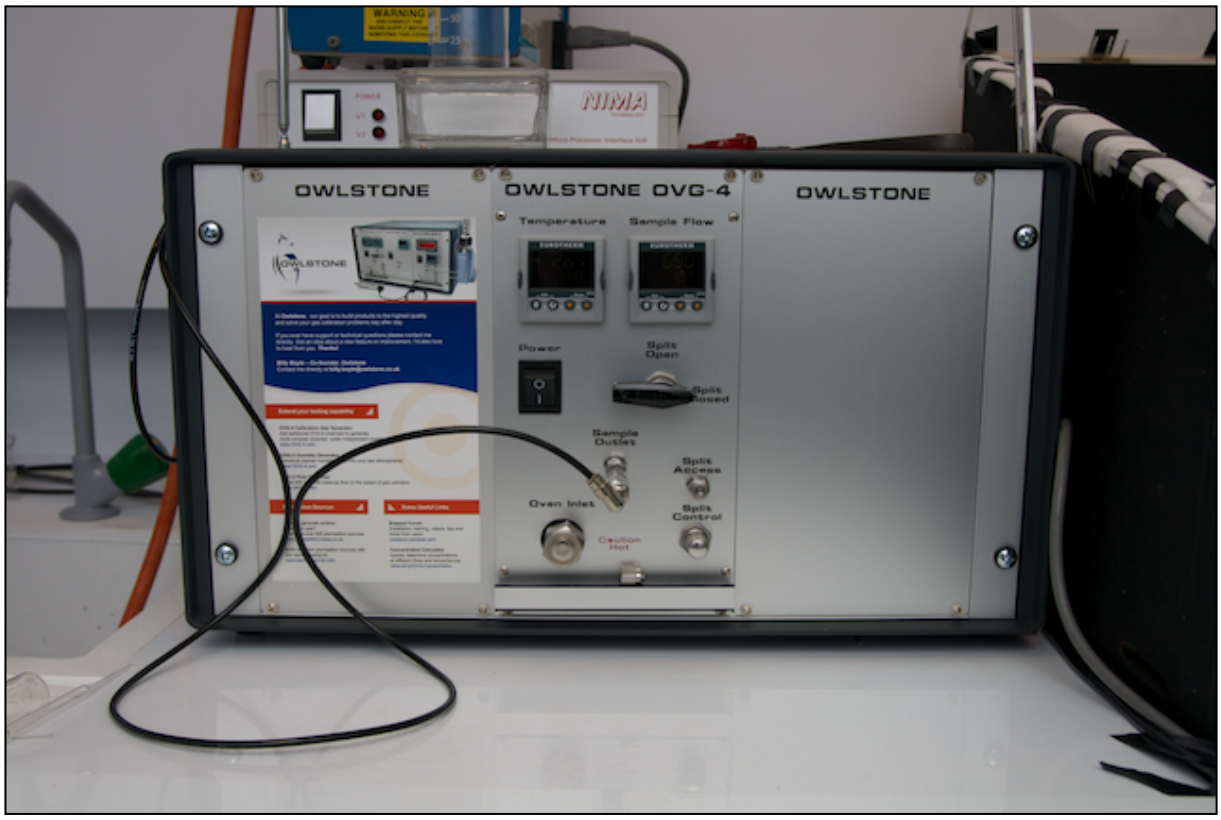

Figure 3.13: Owlstone OVG-4 Vapour generator
This photograph shows the installed OVG-4 vapour generator with sample outlet connected to a long PTFE tube.

The permeation tubes were created using 16 cm lengths of PTFE tube (provided by Owlstone), which were filled with solvent and sealed at both ends using hard PTFE plugs secured by metal collars (both also provided by Owlstone).

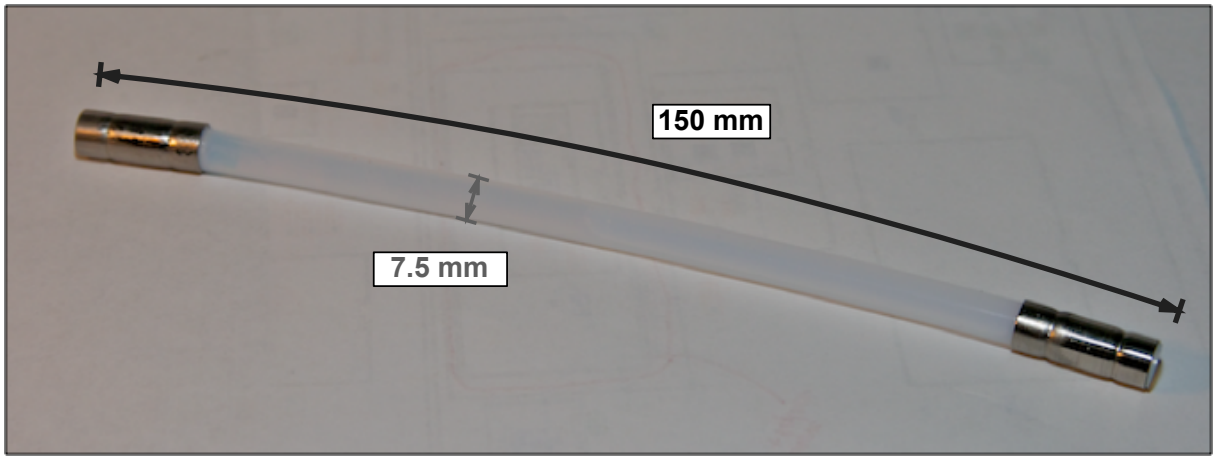

Figure 3.14: Owlstone permeation tube, assembled at Cranfield
An ethanol filled permeation tube, which fits into the Permeation oven on the front of the OVG-4 unit.

Each tube was calibrated using Owlstone's own gravimetric method [62]. The tube was baked at a fixed temperature in the OVG-4's oven for a number of days depending on the solvent used. At random intervals, the tube was removed and weighed. The overall weight

loss of the tube is proportional to the permeation rate of vapour through the walls of the PTFE tube.

Once calibrated, the permeation rate of each tube can converted into a ppmv. The conversion to ppm is carried out by software written as part of this project, using equations and constants provided by Owlstone [62,63]. This software proved so useful in the operation of the OVG-4 that Owlstone purchased the rights to this software (OVG-live) in exchange for a second OVG-4 unit.

3.5. Calix compounds

Dr Frank Davis of Cranfield Health kindly provided the calixarenes investigated in this project. These materials have been shown previously [31] to have some sensitivity to BTEX compounds. The structures of the calixarenes are shown below in Figure 3.15. They are all based on a calix[4]resorcarene structure and have a wide variety of side chain modification and inclusion of surfactants. Calixresorcarene is the term given to resorcinol-derived calixarenes with two –OH groups branching off the rings.

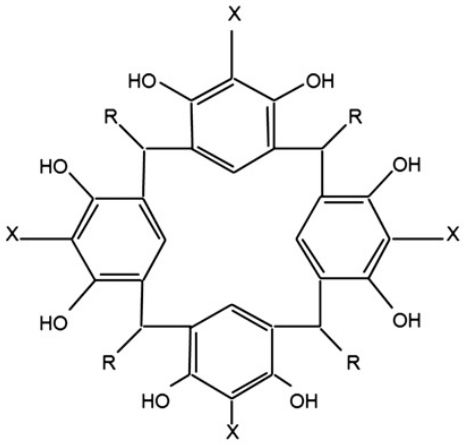

Resorcinarene

Res-A1	$R=C_{11}H_{23}$	$X=H$
Res-A2	$R=C_{11}H_{23}$	$X=CH_2N(C_2H_5)_2$
Res-A3	$R=C_{11}H_{23}$	$X=CH_2N^+(C_2H_5)_2CH_2CH_2OH\ Br^-$
Res-A4	$R=C_{11}H_{23}$	$X=CH_2SO_3^-Na^+$
Res-A4C16	$R=C_{11}H_{23}$	$X=CH_2SO_3^-\ (C_{16}H_{33})_2N^+(CH_3)_2$
Res-A4C18	$R=C_{11}H_{23}$	$X=CH_2SO_3^-\ (C_{18}H_{37})_2N^+(CH_3)_2$
Res-B1	$R=C_6H_5$	$X=H$
Res-B2	$R=C_6H_5$	$X=CH_2N(C_2H_5)_2$
Res-B3	$R=C_6H_5$	$X=CH_2N^+(C_2H_5)_2CH_2CH_2OH\ Br^-$
Res-B4	$R=C_6H_5$	$X=CH_2SO_3^-\ Na^+$
Res-B4C12	$R=C_6H_5$	$X=CH_2SO_3^-\ (C_{12}H_{25})_2N^+(CH_3)_2$
Res-B4C16	$R=C_6H_5$	$X=CH_2SO_3^-\ (C_{16}H_{33})_2N^+(CH_3)_2$
Res-B4C18	$R=C_6H_5$	$X=CH_2SO_3^-\ (C_{18}H_{37})_2N^+(CH_3)_2$
Res-C1	$R=CH_3$	$X=H$
Res-C2	$R=CH_3$	$X=N{=}N$-C$_6$H$_4$-$SO_3^-\ Na^+$
Res-C2C18	$R=CH_3$	$X=N{=}N$-C$_6$H$_4$-$SO_3^-\ (C_{18}H_{37})_2N^+(CH_3)_2$

Figure 3.15: All calix[4]resorcarene used in this project

Resorcinarenes calix[4]res A1 (C11), calix[4]res B1 and calix[4]res C1 were synthesized by the acid catalyzed condensation of resorcinol with dodecanal, benzaldehyde or acetaldehyde respectively according to methods published previously [64-66]. Resorcinarenes can be substituted by a variety of reactions at the 2-position due to the activating effects of the hydroxyl groups. Condensation of resorcinarenes with formaldehyde and diethylamine gave resorcinarenes calix[4]res A2 and calix[4]res B2 and these could be substituted by reaction with 2-bromoethanol to give calix[4]res A3 and calix[4]res B3 [67]. Resorcinarenes could also be substituted with formaldehyde and sulphite ions at the 2-position to give the tetrasulphonated resorcinarenes [68,69]. Simple mixing of aqueous solutions of these resorcinarenes with a fourfold excess of a dialkyl dimethyl ammonium compound led to precipitation of a 1:4 complex that could be extracted with chloroform and purified [68].

Attempts were also made to synthesize resorcinarenes with deeper aromatic cavities and therefore resorcinarene calix[4]res C1 could be condensed with sulphanilic acid to give the tetrasulphonate salt [70] calix[4]res C2 which could then be complexed with dioctadecyl dimethyl ammonium bromide to give the complex calix[4]res C2C18. Attempts were also made to synthesize similar analogues from calix[4]res B1 and calix[4]res B2 but these were unsuccessful.

Resorcinarenes calix[4]res A4, calix[4]res B1, calix[4]res B4, calix[4]res C1 and calix[4]res C2 could not be dissolved in suitable solvents for monolayer formation and could not be studied. However both substitution of the resorcinarenes or complexation with ammonium surfactants increased their solubility.

3.6. Other materials

Cyclohexane (UN 1145) and n-Hexane (UN 1208) were purchased from BDR laboratory supplies, which is now part of VWR (Lutterwoth, UK).

Acetone (UN 1294), Toluene (UN 1294) and Chloroform (UN 1888) were purchased from J.T.Baker which is a now part of Mallinckrodt Baker (London, UK).

Isopropyl Alcohol (UN 1219) was purchased from H K Wentwoth Ltd (Ashby park, UK).

Ethanol (UN 1170) was purchased from Fisher Scientific (Loughborough, LE11 5RG).

Methanol (UN 1230) was purchased from Fisher Scientific (Loughborough, LE11 5RG).

2- Propanol (UN 1219) was purchased from Fisher Scientific (Loughborough, LE11 5RG).

Chapter 4 Wilhelmy plate wetting

Dynamic measurement of the surface pressure is of particular interest in the field of Langmuir monolayers, where the change in surface pressure throughout an experiment can provide information on the properties of the monolayer forming material [71], or on the reaction kinetics of the monolayer's interaction with other materials [72].The Wilhelmy method has been the mainstay of dynamic surface pressure measurement since its invention in the 1800s by Ludwig Wilhelmy [73]. The Wilhelmy method measures directly the change in the force acting upon a plate held at the interface between a liquid surface and the surrounding environment. When the plate is held at this interface, a combination of forces act upon the plate; gravity, which pulls the plate into the liquid surface, the natural buoyancy of the plate in the liquid and the surface tension of the liquid, which pulls the plate into the water [55] (Figure 4.1).

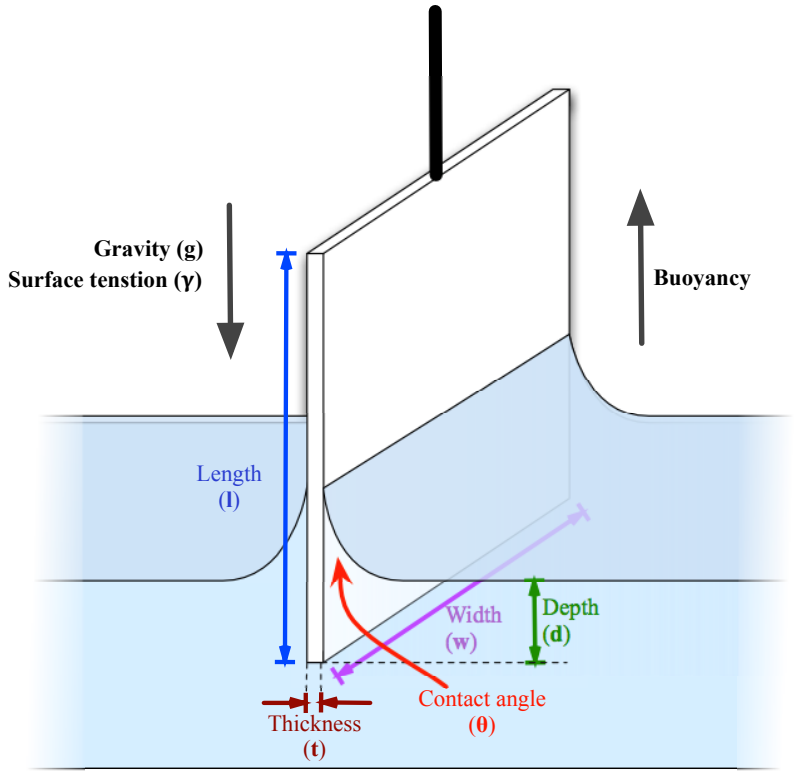

Figure 4.1: Wilhelmy plate
A schematic of the forces acting on a Wilhelmy plate, illustrating the parameters required for the determination of surface pressure

The Wilhelmy plate measures changes in surface pressure through the change in the upward force exerted upon it by the liquid. As the surface tension decreases, the force acting on the

plate becomes less, and thus weight of the plate is reduced. The force acting on the plate is given by Equation 4.1 [55].

$$F = Density_{plate}\ g\ l\ w\ t + 2\gamma\ (t + w)\ cos\theta - Density_{liquid}\ g\ t\ w\ d$$

Equation 4.1: Force on a Wilhelmy plate

Where the plate is defined by its thickness (t), width (w), length (l) and depth (d). The surface tension (γ) can be determined by rearranging Equation 4.1, by assuming that the forces of gravity (g) and buoyancy acting upon the plate remain constant throughout the experiment and by assuming that the contact angle (θ) between the water and plate is zero (i.e. the plate is fully wet),

$$\Delta\gamma\ = \frac{\Delta F}{2\ (t + w)}$$

Equation 4.2: Change in surface pressure from change in force

A Wilhelmy plate comprises either a piece of filter paper or a small plate of non-reactive material (often platinum). Platinum plates, while non-reactive to most monolayer materials, are difficult to clean and often require sonication and other treatments. This is partially due to the roughened surface of the platinum plates, which is required to encourage a zero degree contact angle between the plate and the liquid [74]. Many laboratories opt for the cheaper, disposable alternative of a filter paper plate. The filter paper is naturally absorbent and so forms a reliable zero contact angle, though this absorbency can also lead to a 'wicking' effect causing the monolayer material to move up into the pad over time.

The use of filter paper Wilhelmy plates introduces another, less frequently reported, problem, which until now has not been understood fully. At the start of an experiment, the Wilhelmy plate is mounted on the balance with the plate immersed in the liquid. The plate is commonly left in this state for several hours while the system stabilizes. During this stabilisation period, the readings recorded by the plate may drift downwards until a plateau is reached. Through informal communication it has been established that this effect is well known within the Langmuir community, and is accepted as a necessary stage in the setup of an experiment (Tim Richardson & Alexi Nabok – private communication). However, the cause of the drift in surface tension is not clear, and it is often attributed to contamination of the water in the trough, or to stabilisation of the response of the Wilhelmy plate and balance. In this chapter a

series of investigations aimed at developing an understanding of the origin of the drift, quantifying the problem and providing a solution are presented.

4.1. Characterisation of the problem

The initial study focused on quantification of the drift in the readings taken with the Wilhelmy plate method. This was critical to understanding the problem and its effect on monolayer characterisation. For the initial characterisation, the trough was filled with distilled water and a new piece of filter paper was hung on the Wilhelmy balance. Once the water had visibly saturated the filter paper, the sensor was 'zeroed' - this data point was used as t = 0. The surface pressure was then recorded over a 3-hour period. The experiment was repeated three times, on three consecutive days. The data collected during the three experiments are shown in Figure 4.2.

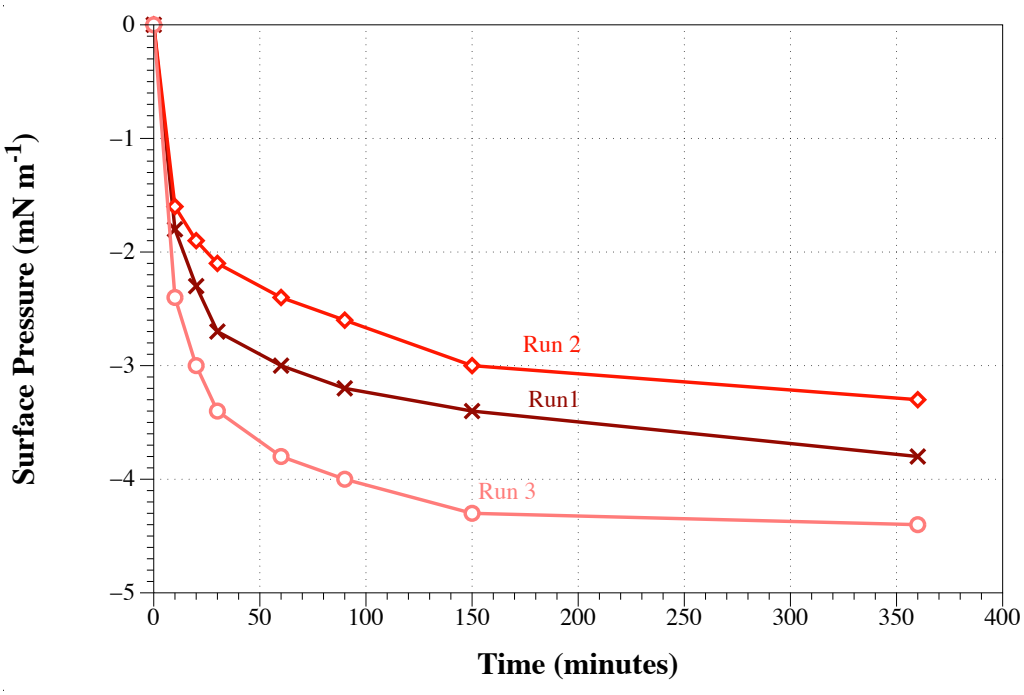

Figure 4.2: Slow change in surface pressure readings in a static water surface
The results of three consecutive experiments in which the surface pressure of water in a Langmuir Blodgett trough was recorded over time (from trough setup) using a filter paper Wilhelmy plate

Figure 4.2 shows that the form of the drift is repeatable, with the measured surface pressure taking approximately 150 minutes to reach equilibrium. There is a clear variation between each run, with the average drift equating to approximately 10% of the surface pressure that would be typically used (~30 mN m^{-1}) during transfer of a monolayer onto a substrate during Langmuir Blodgett deposition.

As the drift was observed to approach a stable plateau, it was assumed that this problem was caused by one or more parts of the system requiring time to equilibrate. Given that the system is comprised of water and a sensor, this limits the number of possible causes. The two key hypotheses considered were the presence of contamination at the liquid surface that causes the surface pressure to take time to equilibrate, and instabilities in the Wilhelmy balance mechanism.

4.2. Cause

Firstly, the possible contamination of the liquid surface was considered. A control experiment was undertaken to ensure that the measured surface pressure had reached equilibrium. The filter paper was then removed and replaced with a new piece. This replacement of the filter paper was undertaken carefully to minimize disturbance of the water's surface. Once fully wetted, the Wilhelmy sensor was again 'zeroed' and the resulting drift in the surface pressure readings were recorded. The data collected are shown in Figure 4.3.

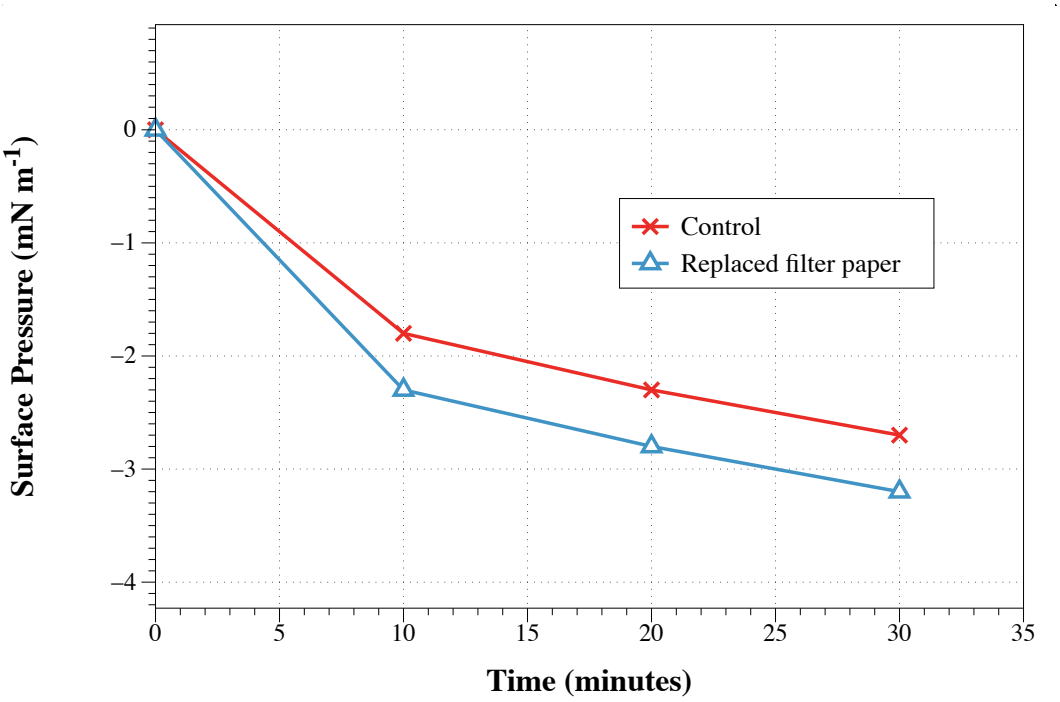

Figure 4.3: A comparison of control and replaced filter papers
Showing changes in the measured surface pressure, with x and Δ representing data from two different filter paper Wilhelmy plates, recorded sequentially without changing the water in the trough

Figure 4.3 shows little difference in the magnitude of the drift in the surface pressure readings between the two experiments. If the water (or contamination thereof) was the cause

of the drift, Figure 4.3 should have shown a decrease in the drift once a new plate was hung on the Wilhelmy balance. This indicates that the drift is a property of the Wilhelmy sensor system and not of the water.

To investigate the properties of the sensor system, the water in the trough and the filter paper Wilhelmy plate were replaced and the surface tension monitored over a 120-minute period. The trough was then emptied, cleaned and re-filled without disturbing the Wilhelmy plate. Once re-filled, the sensor was again 'zeroed' and the change in surface pressure was recorded at ten-minute intervals. Finally, the filter paper was removed from the Wilhelmy balance, the trough emptied, cleaned, refilled and a new filter paper plate (which had been soaked in de-ionized water for 2 hours) was hung on the balance. The results from the three experiments are shown in Figure 4.4.

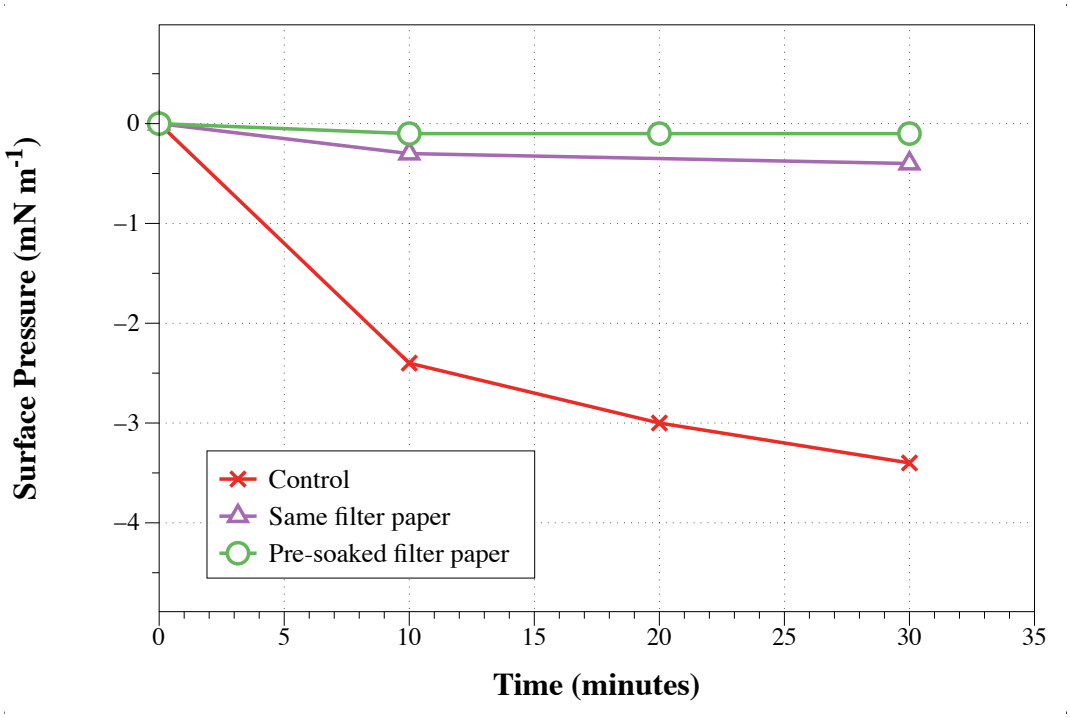

Figure 4.4: Comparison of Wilhelmy plate treatments
Plot of the surface pressure measured using a Wilhelmy balance with a filter paper Wilhelmy plate. x represents the data from the first plate, O the data from the same filter paper plate, but with the water in the LB trough changed, while Δ represents the data obtained after changing the water in the trough and replacing the plate by a new filter paper plate that was pre-soaked in de-ionised water for 2 hours

Figure 4.4 shows a reduction in the magnitude of the drift of the Wilhelmy surface pressure when the filter paper plate had been pre-soaked in water. As discussed, the Wilhelmy plate measures the weight of the plate to determine the surface pressure of the water. The drift observed after the filter paper Wilhelmy plate has been wetted suggests that the filter paper

is increasing in weight. It is suggested that they reason for this effect is that, although appearing fully wetted, the filter paper continues to absorb more water when immersed in the trough, increasing the overall weight, which is recorded by the pressure sensor.

To test the swelling theory, the change in weight of the filter paper was measured using an Ohaus GA200D balance (+/- 0.2 mg precision). Three filter paper plates were wetted in a small vial of distilled water and weighed immediately. Once weighed, the plates were returned to the vial of distilled water, where they were allowed to soak for 30 minutes. During this period the plates weighed at intervals to record any change in the wetted weight. Prior to weighing, they were removed from the water and 'dabbed' dry to remove excess water and after weighing they were immediately returned to the water to soak. The results are shown in Figure 4.5.

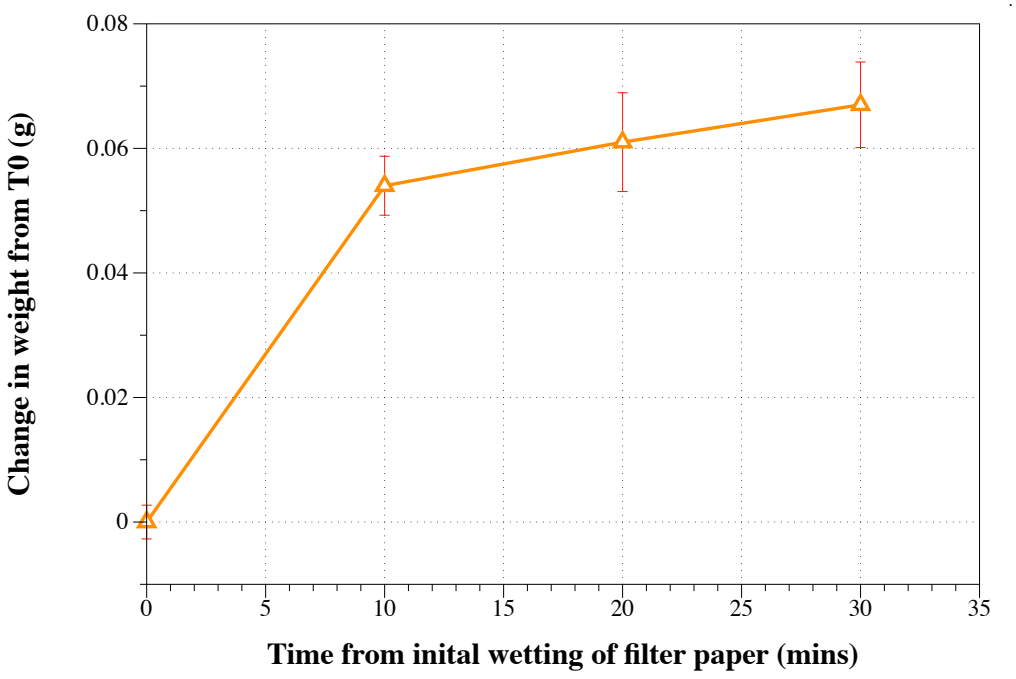

Figure 4.5: Plate wetting by weight
Change in the average weight of three filter papers, measured using an Ohaus GA200D balance. The error bars represent the standard deviation of the three measurements at each time point.

Figure 4.5 shows that the plates gain weight at a similar rate to the drift observed in the measurement of surface pressure by the Wilhelmy balance, indicating that the surface pressure measurement drift is caused by the filter paper plates slowly gaining weight.

4.3. Summary

The use of dry filter paper causes a drift in the readings taken from a Wilhelmy surface pressure sensor for up to two hours after initial setup. The slow increase in the water holding capacity of the filter paper has an influence on the weight of the plate and subsequently the measurements obtained from the Wilhelmy balance. The soaking of filter paper in water prior to use as a Wilhelmy plate reduces the time taken for the surface pressure measurements to stabilize. All future experiments using the Langmuir troughs used filter paper that had been soaked for a minimum of 2 hours before the experiment and included a short 10 minute stabilization step to ensure that the sensor was stable before any spreading solution was applied.

Chapter 5 Surface pressure isotherms

The work described in this chapter has been published as:

"Monolayer behaviour of calix-4-resorcinarenes and their surfactant complexes"
Matthew Partridge, Frank Davis, Steve W. James, Ralph P. Tatam, Charl F. J. Faul, and Séamus P. J. Higson

Thin Solid Films **520** (2012) pp. 6989–6993

The first stage in using new molecules with LB coating techniques is the analysis of the monolayer-forming characteristics of the molecules. As mentioned previously in section 2.7, different amphiphilic molecules respond in different ways when spread on the surface of water. It is important to understand their particular behaviour since it has an impact on the parameters used in coating a surface.

5.1. Calix[4]res isotherms

Each of the calix[4]resorcinarenes (section 3.5) were prepared by dissolving them initially in 2-3 ml of chloroform, before being made up to 10 ml in a volumetric flask to the final concentration (~0.1 mg ml^{-1}). All isotherm experiments were carried out using the square Nima trough, which was prepared as described in section 3.1 with the use of pre-soaked filter papers for the Wilhelmy balance. Each isotherm was run by decreasing the area of the trough at a rate of 50 cm^2 s^{-1}. The surface pressure was recorded at 0.5 s intervals throughout the compression. The isotherms are compared in Figure 5.1, where the isotherms have been grouped by their structural similarities.

Molecular models show that the cross-sectional area of the resorcinarene headgroup is larger than the combined area of the four-alkyl sidechains, and this is confirmed by X-ray crystallography structures [75]. Figure 5.1 shows the isotherms of the tetraundecyl and tetraphenyl resorcinarenes substituted with diethylamine groups and their quaternised derivatives.

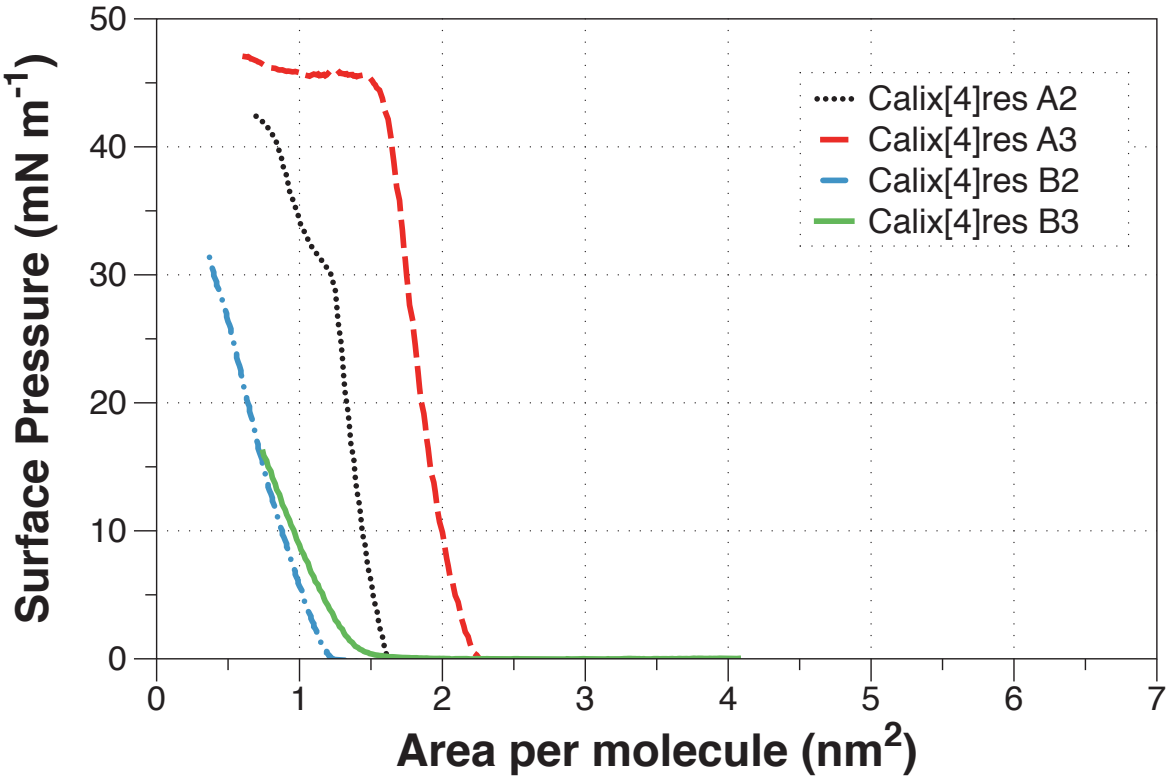

Figure 5.1: Isotherms of the amine and ammonium substituted resorcinarenes.

As can be seen when compared with the unsubstituted calix[4]res C11 (Figure 5.1), which has been extensively investigated in previous work and other workers [76,77], the similar material substituted with diethylamine (calix[4]res A2) has a smaller surface area per molecule, indicative of closer packing of the resorcinarene head groups. This could potentially be because the amine groups and the hydroxyls of adjacent resorcinarenes could hydrogen bond to each other, leading to a more tightly packed monolayer. There is also a kink at a surface pressure of 30 mN m^{-1}, followed by final collapse just above 40 mN m^{-1}, somewhat lower than observed in the parent material. This 'kink' could possibly be the result of the formation of a bi-layer which has a second collapse pressure although without additional data this could not be confrimed. In contrast, the quaternary ammonium salt (calix[4]res A3) has a higher surface area, indicating a more dispersed monolayer, which can be explained by repulsion between the positively charged substituents. The collapse pressure is also higher than for calix[4]res A2, indicating stronger interaction between the resorcinarene and the subphase. The two phenyl-substituted compounds appear to form less stable monolayers with smaller surface areas and, in fact, it is debatable whether a true monolayer is what is being formed, with perhaps the resorcinarenes being aggregated in some manner. However calix[4]res B3 does form a stable film at 22.5 mN m^{-1} and has been previously deposited as an LB film and utilised as a sensor for organic vapors [69]. These isotherms indicate that the presence of the longer undecyl chain is required for the formation

of monolayers. No comparison could be drawn between calix[4]res A1 and calix[4]res B1, since the latter compound is insoluble in any suitable spreading solvent. Since the sulphonate compounds were insoluble in any commonly used spreading solvent (chloroform or ethyl acetate) and could not be utilised, complexes with various ammonium surfactants were studied. Monolayers of calix[4]res B4 complexed with three ammonium salts with differing lengths of alkyl chain had their isotherms measured (Figure 5.2).

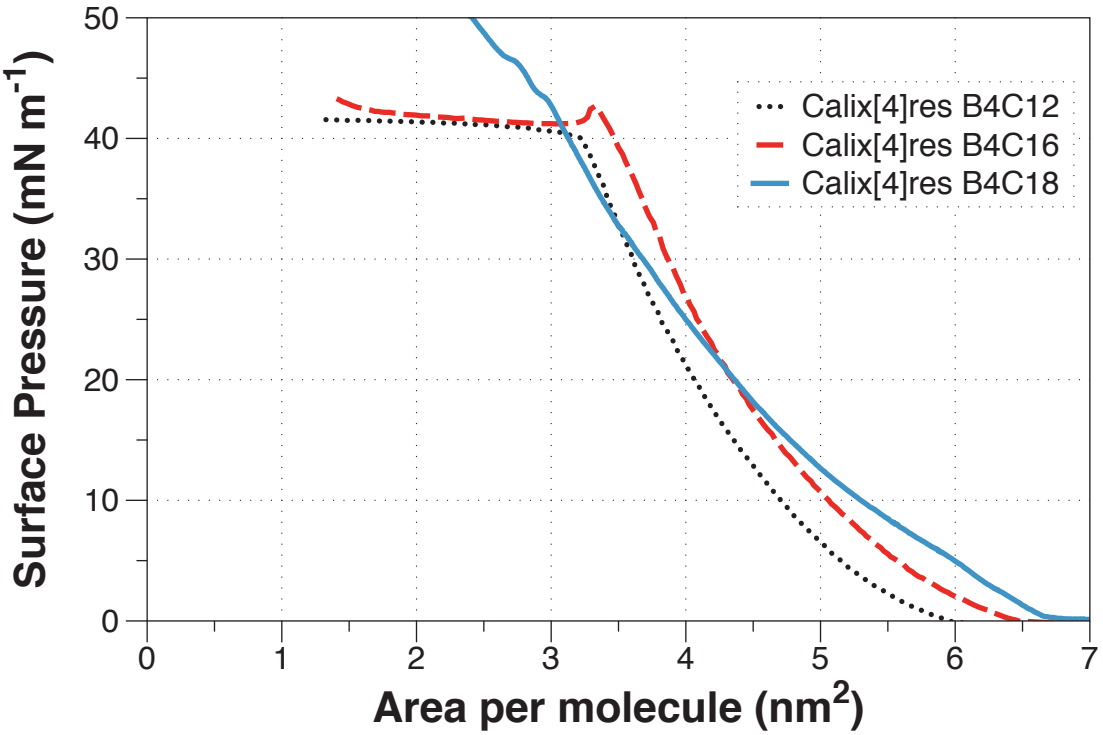

Figure 5.2: Isotherms of the undecyl sidechain resorcinarenes and their complexes with ammonium surfactants.

As can be seen in Figure 5.2, all three complexes gave monolayers that were stable at pressures up to at least 40 mN m^{-1}. Longer chains tended to give more expanded monolayers. However there is an interesting contrast between the C18 containing calix[4]res B4C18 and the other surfactants, in that it initially has the larger surface area but its isotherm is not as steep and it actually crosses over the other two isotherms. Calix[4]res B4C18 also appears to have a higher collapse pressure. Calix[4]res B4C12 and calix[4]res B4C16 are similar in behavior with almost identical isotherms, except that calix[4]res B4C12 has a slightly lower area per molecule.

Since the study of the calix[4]res B4 complexes was successful, complexes of the surfactants with a sulphonated tetraundecyl resorcinarene (calix[4]res A4) and also a tetraazo-substituted resorcinarene with a larger, deeper cavity were also synthesized. Comparison of calix[4]res A4C16 and calix[4]res A4C18 (Figure 6.5) shows, once again, the

crossover effect, where the C18 containing material initially has a larger surface area than the C16 but a less steep isotherm.

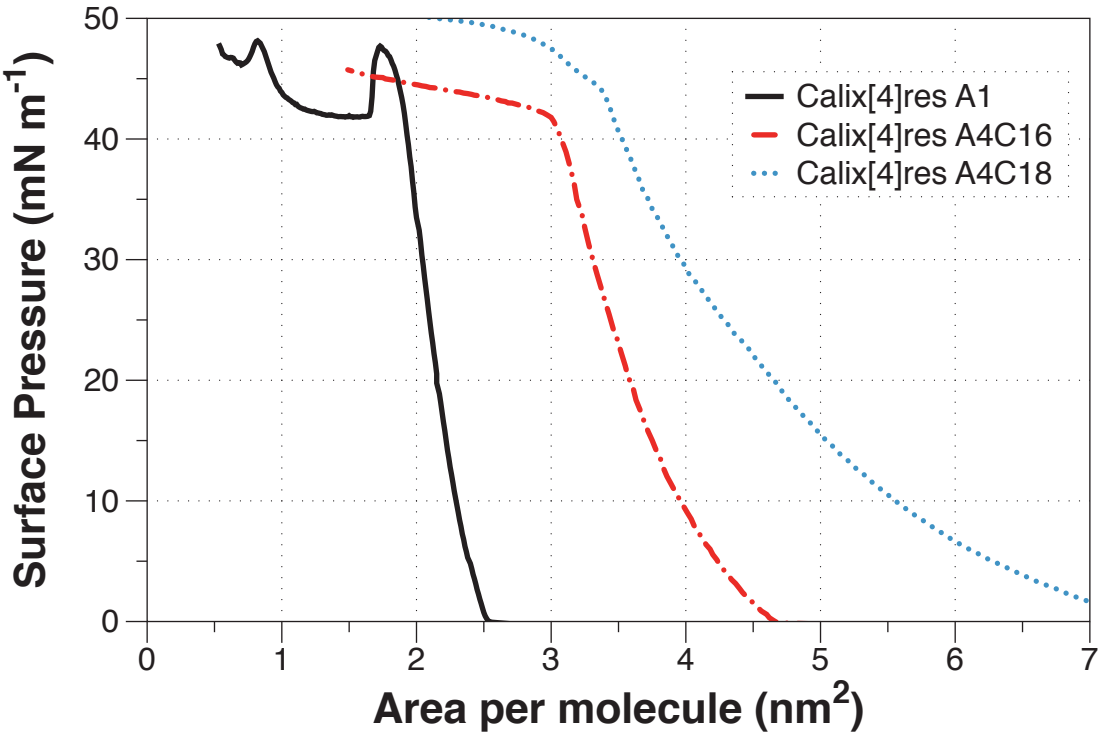

Figure 5.3: Isotherms of the undecyl sidechain resorcinarenes and their complexes with ammonium surfactants.

Both the resorcinarenes have appreciably smaller surface areas per molecule than their tetraphenyl analogues, especially at low pressure. This indicates that the calix[4]res A4 derived monolayers are more tightly packed and probably have a higher degree of order within the film; this could be due to favorable Van der Waals interactions between surfactant and resorcinarene side chains, which is absent in the calix[4]res B4 complexes.

The areas per molecule for calix[4]res A4C16 and calix[4]res A4C18 are higher than the parent resorcinarene (calix[4]res A1) and, in this context for example, although the calix[4]res A4C16 isotherm is of a similar shape and has a similar collapse pressure to calix[4]res A1, the area per repeat unit (1 resorcinarene plus four surfactants) is about 2 nm^2 greater. From these results we can deduce that the use of organic cations allows the formation of stable monolayers from the sulphonated resorcinarenes. Other workers have studied monolayers of the dioctadecyl dimethyl ammonium surfactant on water [78] and shown it to form monolayers with a collapse pressure of approximately 50 mN m^{-1} at a surface area per molecule of 0.50 nm^2. The monolayer is however dependent on the presence of counterions and, in this case, this will be the resorcinarene. If we assume the four surfactant chains take

up a total area of 2 nm^2 at high pressures, as indicated by their isotherm [79], this gives, in the case of the calix[4]res A4 complexes, areas of approximately 1.3 nm^2 for the tetrasulphonated resorcinarene unit (at 30 mN m^{-1}), which corresponds with molecular models. The phenyl substituted calix[4]res B4 derivatives display somewhat larger areas, especially at lower pressures. From these results it appears that the surfactant and resorcinarene are both located within the monolayer side by side, due to the necessity for charge neutralization. This side-by-side formation is shown diagrammatically in Figure 5.4.

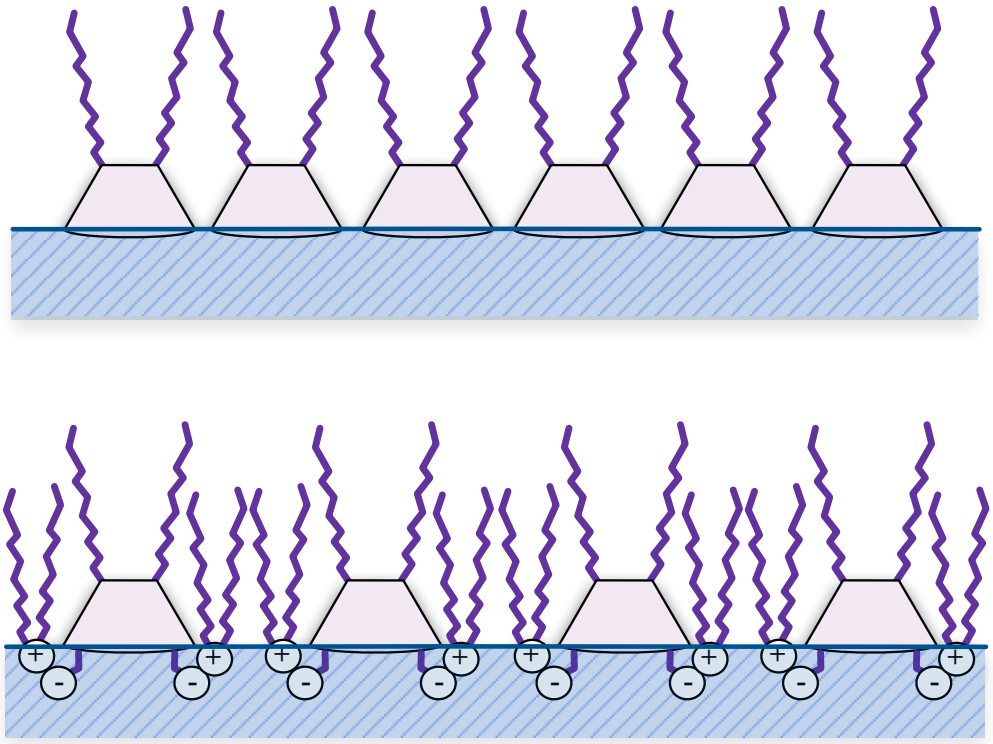

Figure 5.4: Schematic of calix[4]res spreading on a water subphase
Topmost diagram shows the likely orientation of calix[4]res C11, bottom diagram shows the same for calix[4]res A4

When the resorcinarene contains the longer undecyl sidechains, the monolayer appears to be more compact, especially at lower pressure, indicating closer association between the resorcinarene and its surfactant counter ions, whereas phenyl substituted resorcinarene films appear to show appreciable surface pressure at higher areas, indicating a more disperse monolayer.

The tetraazo resorcinarene calix[4]res C2 is of interest because of its potential ability to give colorimetric responses to the presence of metal ions [80]. However it proved too insoluble in anything except water and therefore a complex with a surfactant was made. Calix[4]res C2C18 gave a stable monolayer, collapsing at just over 40 mN m^{-1}, similar to many of the

other complexes and in fact had the smallest area per molecule of this series of materials (Figure 5.5).

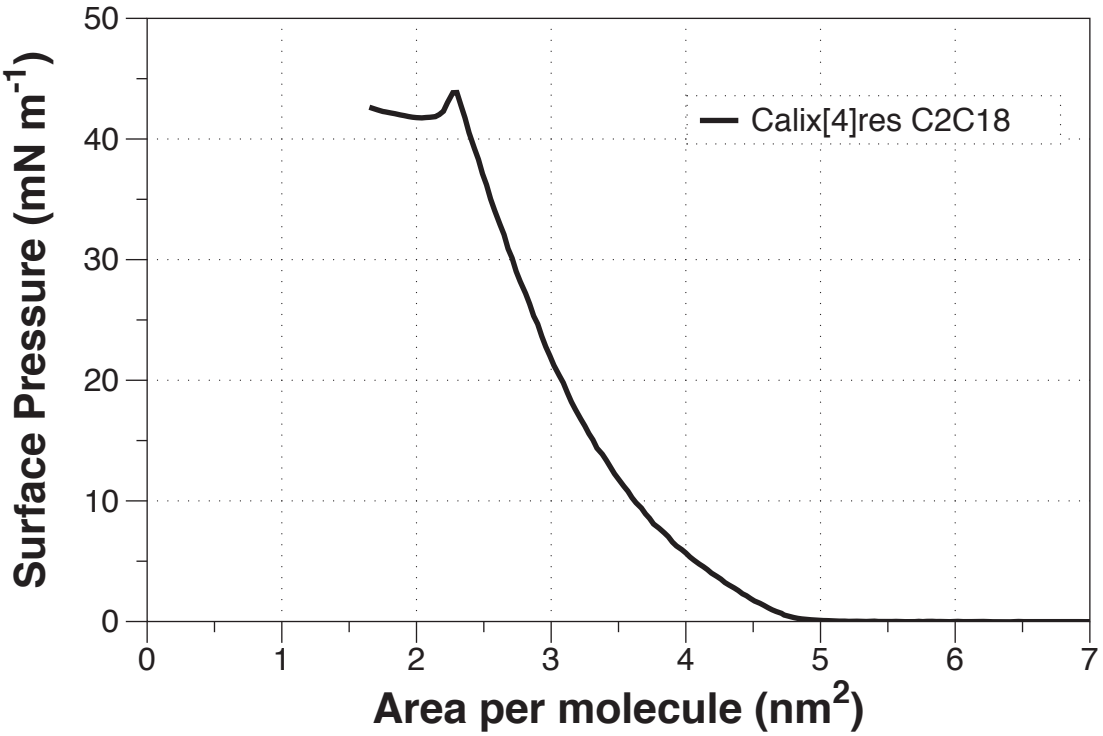

Figure 5.5: Isotherm of the tetra-azo resorcinarene complex with dimethyl dioctadecyl ammonium surfactant

A possible explanation for calix[4]res C2C18, which just has a methyl sidechain, having a lower total area per molecule is that the lack of a long alkyl or phenyl sidechain allows the resorcinarene to flip over on the water surface and, instead of existing side by side with the surfactant, actually sits underneath it. Since the surfactant would therefore be on top of the resorcinarene rather than beside it in the monolayer, the total surface area in this arrangement would be lower.

5.2. Conclusions

Within this work it has been demonstrated that a series of resorcinarenes can form monolayers on water with clearly defined features such as monolayer collapse points. A series of amine and tetralkyl ammonium substituted resorcinarenes were studied and it was showed that the presence of undecyl sidechains in the resorcinarenes gave higher quality monolayers than those with phenyl sidechains.

Resorcinarene surfactant complexes were also studied and were shown to form monolayers on water. Resorcinarenes with undecyl sidechains gave tighter packed monolayers than their

phenyl analogues and also longer surfactants tended to give tighter packing, probably due to favorable interactions between alkyl chains. Areas per molecule studies indicate that the surfactants and resorcinarenes are side by side in the monolayers. A resorcinarene with an extended cavity but a shorter methyl sidechain possibly adopts a different structure, where the resorcinarene turns over and exists below a surfactant monolayer.

Further investigation should focus on analyzing the behaviour of these materials, not just in the monolayer but also in LB multilayers. One advantage of utilising resorcinarene/surfactant complexes is that, to develop sensors, it is often necessary to incorporate a number of chemical units within the same system; a sensing molecule for example could contain a binding site (such as a resorcinarene) and then a transduction unit (such as an fluorescent dye or redox active moiety) which could demonstrate whether or not binding had occurred. This can prove problematic in that this may require the synthesis of a complex molecule that not only contains both the required units but also must be capable of forming stable monolayers and of being deposited on a solid substrate. The synthesis and deposition of such molecules could well be simplified if it is possible to incorporate one of the desired units into one system e.g. a resorcinarene and the other into the surfactant and then simply combine the two by mixing them in solution and isolating the complex. The intimate mixing which must occur to facilitate charge neutralization, and which has been seen in solid phase structures of these types of materials [68], could well allow a high level of interaction between such units.

.

Chapter 6 Mono-Layer Vortex rings

The contents of this chapter have been submitted for publication to Fluid Dynamics Research;

“The effect of surface pressure modification on the speed of vortex rings”

M. Partridge, F. Davis, S. W. James, R. P. Tatam, and S P J Higson

At time of writing this paper is currently under review by the journal.

It has long been known that as a spherical drop of dye falls through the surface of water it creates a ring like pattern with a long tail [81-83]. This “vortex ring” formation is the result of the drop of water coalescing with the larger body of water. The ring shape is a consequence of the movement of the drop through the water and the influence of the resistance of the water acting on it before it disperses into the solution [81,84]. The water resistance acts to 'spin' the edges of the drop inwards, creating the observed ring shape (Figure 6.1). In pure water these rings are relatively slow moving and their progression through the water is thought to be simply the result of gravity and the capillary attraction of the bulk water acting on the drop as it combines with the bulk from its position on the surface of the bulk [85]. The capillary attraction results in capillary waves that propagate across the surface of the bulk as well as over the coalescing drop. It has been seen that the convergence of the capillary waves on the coalescing drop is critical to the formation of full or partial coalescence [86].

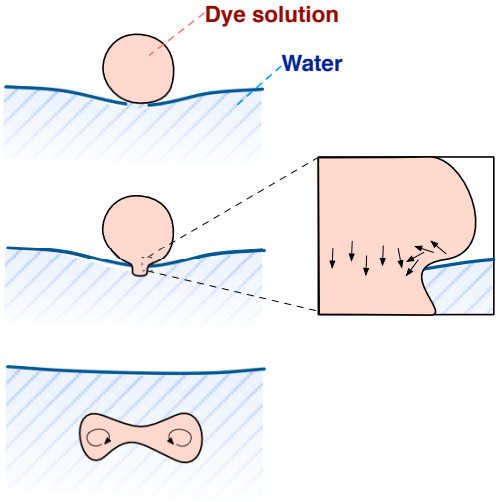

Figure 6.1: Vortex ring formation
A diagrammatic interpretation of the formation of vortex rings. The arrows represent the flow of the dye solution.

The formation of vortex rings in water is thought to play a crucial role in the oxygenation of water by rain [83]. Understanding this role is of particular importance in helping determine the effect of pollutants on the oxygenation process. However, our initial interest in this subject arises from the potential of this method to help expand our understanding of monolayer materials. By exploring the relationship between the formation of vortex rings and a monolayer material, it may be possible to determine properties of the monolayer material. Pikhitsa *et al.* [87] proposed that the formation of vortex rings might be the product of three monolayer properties; the longitudinal surface viscosity, surface elasticity and surface tension. If, through knowledge/control of two of these variables, it is possible to use a vortex ring to determine the third, then this would be of great use in the study of monolayers. The surface pressure/tension of a monolayer can be measured simply using a Wilhelmy plate system [73]. Elasticity can be measured using cycling compression of a monolayer, as described by M Blank *et al.* [88], and viscosity can be measured by a viscometer [89]. The aim of the part of the project was to determine if the formation of vortex rings could be used as a quick method for surface pressure or elasticity; it was not possible to measure viscosity due to the lack of available viscometer.

When a drop falls from the tip of a pipette, it will, given sufficient fall time, form a spheroid shape. Initially the drop will be deformed by its release from the pipette. It will then oscillate between the deformed state and the spherical state until it finds an equilibrium [90]. The formation of clean vortex rings (with no breakup) occurs only when the drop meets the water surface in this spherical shape, enabling it to coalesce partially or fully with the bulk liquid and to create the pressure pattern required to form a vortex ring [90][91].

Previously it has been seen that vortex rings can be affected by the introduction of polar surfactants on to the surface of the bulk water [92], by the doping of the bulk water with alcohol [84] and by the doping of the vortex ring-forming drop. Saylor *et al*. [92] showed that the speed at which the vortex ring moves through the water increases with changes in the concentration of the surfactant Triton X-100. It was suggested that the damping of the capillary waves [93] caused this, although it was also noted that this could not be supported by the work presented [90,94].

The series of experiments described in this section are designed to investigate the various explanations proposed in this earlier work [92]. Through the use of an alternative drop method, combined with along with improved control over the spreading of the monolayer material, we expand on the original experiments while ruling out a number of the variables that could confuse the interpretation of the results. One key aspect that is of particular interest is the influence of the structure and chemistry of the monolayer material. If the characteristics of vortex rings are linked to one or more properties in the monolayer, it would provide a new tool in the exploration of monolayers and their properties without the need for specialist equipment that can be both costly to source and maintain.

6.1. Monolayer preparation and elasticity method

The monolayers were created using a simple setup consisting of a Nima Alternate layer Langmuir-Blodgett trough, filled with deionised H_2O (18 MOhms) and mounted on a table on an anti-vibration stand, as described in section 3.1. During this work the central section of the trough was removed, creating a single large monolayer between the two controllable barriers.

One question highlighted in the work done by Saylor *et al*. [92] concerned the influence of the monolayer material upon the speed of the rings. To investigate the influence of the monolayer material on the speed of the vortex rings, four materials with distinct properties were investigated: stearic acid, tricosanoic acid, 4-tert butyl calix[4]arene and calix[4]resorcarene (C11). Stearic acid is a saturated carboxylic acid with a clear hydrophilic head group and long (C17) hydrophobic tail, while tricosanoic acid has a 22-hydrocarbon chain. 4-tert butyl calix[4]arene (Figure 6.2) was selected due to its short chain length, larger size and less regular packing dynamics when spread as a monolayer. When spread on a water sub-phase, 4-tert butyl calix[4]arene forms a cup-like structure with the benzene domains forming the sides of the cup (Fig. 3). Calix[4]resorcarene (C11) was used as it forms a similar 3D shape to 4-tert butyl calix[4]arene, but has similar hydrophobic chains to the carboxylic acids. Calix[4]resorcarene also has the benefit of producing monolayers that were

stable at high (>25 mN m^{-1}) surface pressures, allowing measurements to be performed over a large surface pressure range. The other three materials cannot sustain surface pressures of this magnitude for the duration of the experiment and collapse to form uneven multi-layers. The differences in the structure of the materials chosen will also confer differences in their monolayer elasticity. These differences in elasticity have been examined previously [81], although no elasticity data could be found for the calix monolayers. To account for this lack of prior data, each monolayer's elasticity was assessed at the surface pressures used for the vortex ring experiments. It has been shown in previous work that stearic acid, tricosanoic acid [95], 4-tert butyl calix[4]arene and calix[4]resorcarene (C11) [96] are all insoluble in water.

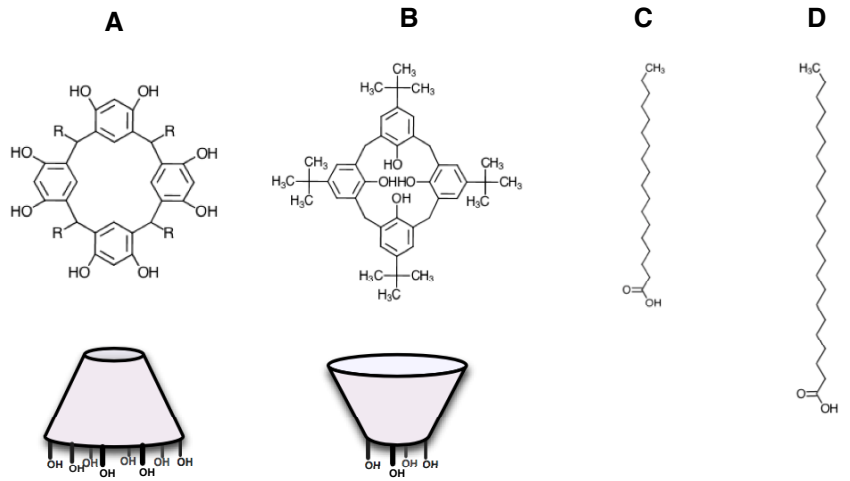

Figure 6.2: Monolayer materials used in vortex ring experiments
The structures of (A) calix[4]resorcarene C11 (R: -$C_{11}H_{23}$), (B) 4-tert butyl calix[4]arene, (C) stearic acid and (D) tricosanoic acid, along with a 3D diagram of how the calix[4] molecules orientate when spread on a water sub-phase. The cone represents the tilted benzene ring.

Monolayers of stearic acid, tricosanoic acid, calix[4]resorcarene C11 and 4-tert butyl calix[4]arene were prepared by the drop-wise addition of 1 mg ml^{-1} solutions of the monolayer material in chloroform to the surface of the water. For each monolayer material, a volume of 100 µl was spread on the surface, and for all materials the initial surface pressure was 0 mN m^{-1}. Once prepared, the monolayer was allowed to spread for 1 hour before starting the experiment. Following this relaxation time, each of the monolayers was compressed at a rate of 50 cm^2 min^{-1} using the surface skimming barriers linked to the Nima trough control software. Initially, the layers were compressed until the surface pressure increased to 1 mN m^{-1}. Once they had reached this pressure, the monolayer was again left for 1 hour to ensure the presence of a uniform film.

In order to determine the elasticity of materials at a range of surface pressures, each compressed monolayer was periodically compressed and expanded by the opening and closing of the barriers. This compression and expansion was carried out at a rate of 4 cycles per minute with an amplitude of 2 cm^2 in a sinusoidal pattern. As discussed in Pingsheng *et al.* [81], this cycling of the area of a monolayer (A) produces a change in the surface pressure (Π) which, though the use of Equation 6.1, can be converted into the elasticity (E) of the monolayer. The values for the change in the surface pressure were derived as the average change across 10 cycles.

$$E = \frac{\Delta \Pi}{\left(\frac{\Delta A}{A}\right)}$$

Equation 6.1: Elasticity derivation from surface pressure measurements[81].

Following the elasticity measurement undertaken at 1 mN m^{-1}, the monolayer was compressed sequentially to 10 mN m^{-1}, 20 mN m^{-1} and, for calix[4]res C11, 30 mN m^{-1} and 40 mN m^{-1}. After each compression, the monolayer was allowed to equilibrate for a minimum of 1 hour. Following these elasticity tests, the trough was cleaned and a new monolayer was prepared for vortex ring testing.

To create the vortex rings, drops of 0.1% dye (Oetker, Natural Red colouring, 643308) mixed in distilled H_20 were added to the water in the trough using an Eppendorf pipette set to dispense 5 µl volumes of liquid. The addition of this low concentration of dye had no measureable effect on the surface tension of the distilled water, ensuring that the surface tension of the solution remained at 72 mN m^{-1} (+/- 0.1 mN m^{-1}). As has been reported by other groups [82,83,90], the method of addition of the solution was critical to the formation of the vortex rings. If the drop is not spherical when it makes contact with the water or monolayer surface, it will not fully coalesced to produce a clean vortex ring [84,90]. It has been shown that when a drop falls its shape oscillates between a sphere and an ellipsoid. To ensure that in these experiments the drops were spherical at the point of contact with the water, they were not allowed to fall, but were manually 'touched' to the surface of the water/monolayer. When touched, the drop is not perfectly spherical but forms a pendant shape with a hemispherical bottom [97]. This ensures that the initial contact was with a spherically curved surface, which allows for the formation of clear vortex rings. Addition of the drop to the water or monolayer in this manner also reduced the disturbance of the surface, decreasing the formation of capillary waves induced by the force of a falling drop. As the drop was not being evacuated from the tip of the pipette, not all of the 5 µl volume was

deposited on to the liquid layer. Analysis of these drops showed that the actual volume was 4.3 µl with a standard deviation of 0.3 µl. Drop size analysis was carried out using a balance to weigh the addition of material during the formation of vortex rings; a total of 75 successive vortex rings were weighed in order to generate an accurate figure for this analysis.

A CCD camera, operating at 30 frames per second, was mounted above the water surface at an angle of approximately 45 degrees to record the evolution of the drops as they travelled into the water (Figure 6.3 and Figure 6.4).

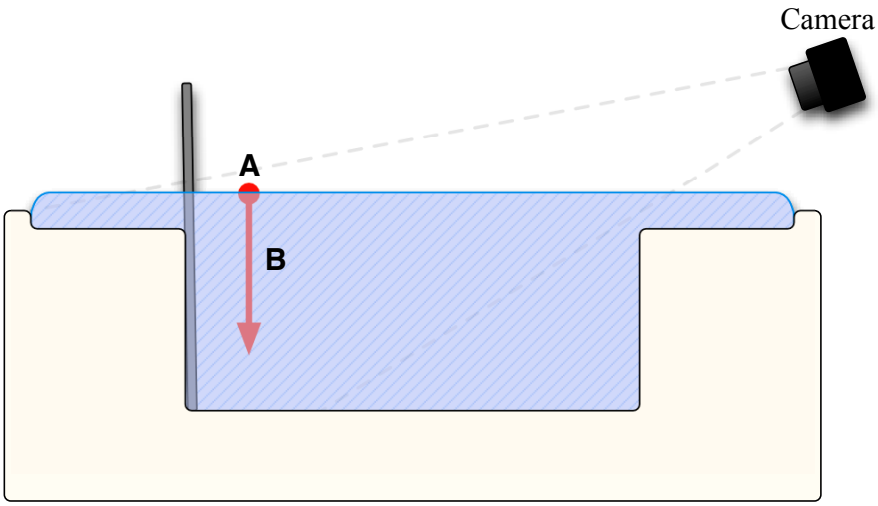

Figure 6.3: Tracking vortex rings in a trough
A cross section of the LB trough showing the camera setup used. The vortex rings move from point A downwards along path B

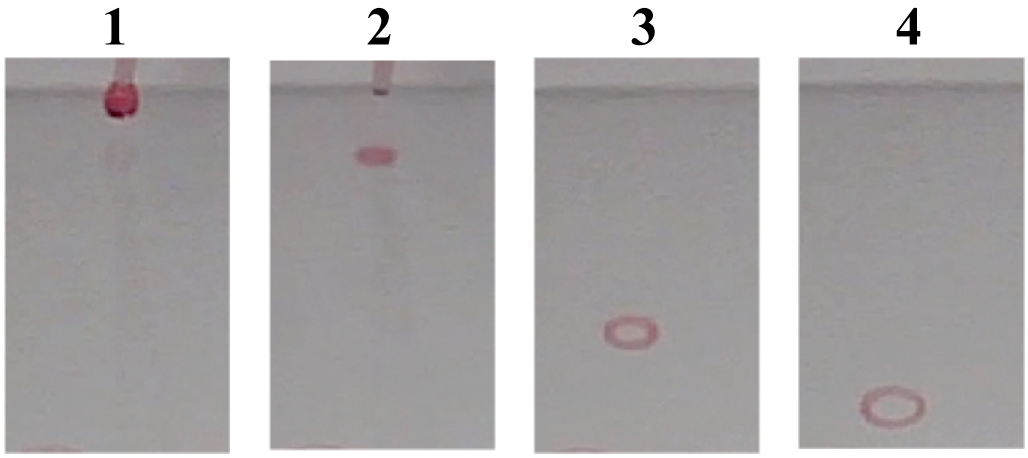

Figure 6.4: Vortex ring photographs
A series of still images showing the formation of a vortex ring during the first 2 seconds. The vortex ring in image 4 has a diameter of 4.5 mm. The images 1,2,3 and 4 were taken at the intervals t=0, t=0.06, t=1 and t=2 respectivly

The correction of perspective distortion of the off-axis recorded images was carried out using the Tracker video analysis and modelling software package (http://www.cabrillo.edu/~dbrown/tracker), which also, following calibration of the camera by recording the image of a ruler, allowed the position, and thus from knowledge of the camera frame rate, the velocity, of the rings to be measured. Each ring was filmed for 5 seconds and allowed to dissipate into the water subphase before the next repeat drop was added. Between monolayer experimental groups, the trough was left to rest for a minimum of 1 hour, as described in the description of the monolayer preparation. The analysis of each ring was possible only for as long as the contrast between the ring and the background was sufficient for the software to track accurately its position. The length of time for which the ring was tracked varied from 1.3 to 4 seconds. Following testing at a surface pressure of 1 mN m^{-1}, the film was then further compressed to surface pressures of 10 mN m^{-1} and 20 mN m^{-1}, and drops were added to the surface. For each surface pressure, a minimum of five vortex rings were created. Once all experiments using a particular monolayer were complete, to ensure no contamination of the monolayer, the trough was emptied and cleaned with acetone and iso-propyl alcohol before being re-filled with distilled water ready for the next monolayer material.

6.2. Monolayer vortex ring modification

Prior to the assessment of vortex ring formation, an experiment was conducted to examine the stability of the monolayer when a drop of dye solution was added. The results of this experiment are shown in Figure 6.5.

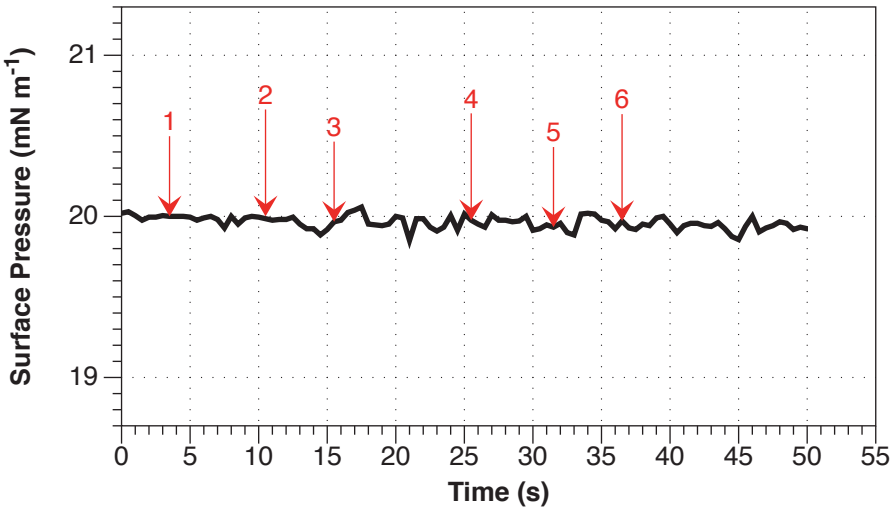

Figure 6.5: Vortex ring surface pressure change
A plot of the change in surface pressure of a calix[4]resorcarene film during the sequential addition of 5µl drops of dye solution to produce vortex rings (each addition labelled 1-6).

The lack of any significant features in the data shown in Figure 6.5 indicates that the repeated addition of dye drops does not affect the stability of the monolayer. There is no loss of material, which would have been characterized by a drop in surface pressure and area, nor is there an increase in surface pressure, which would have indicated the introduction of monolayer contamination from the dye solution. This matches the study by Saylor on a wider range of materials [98].

An example of the data produced by analysis of the videos of the evolution of the vortex rings is shown in Figure 6.6 for three surface pressures and using a monolayer of stearic acid.

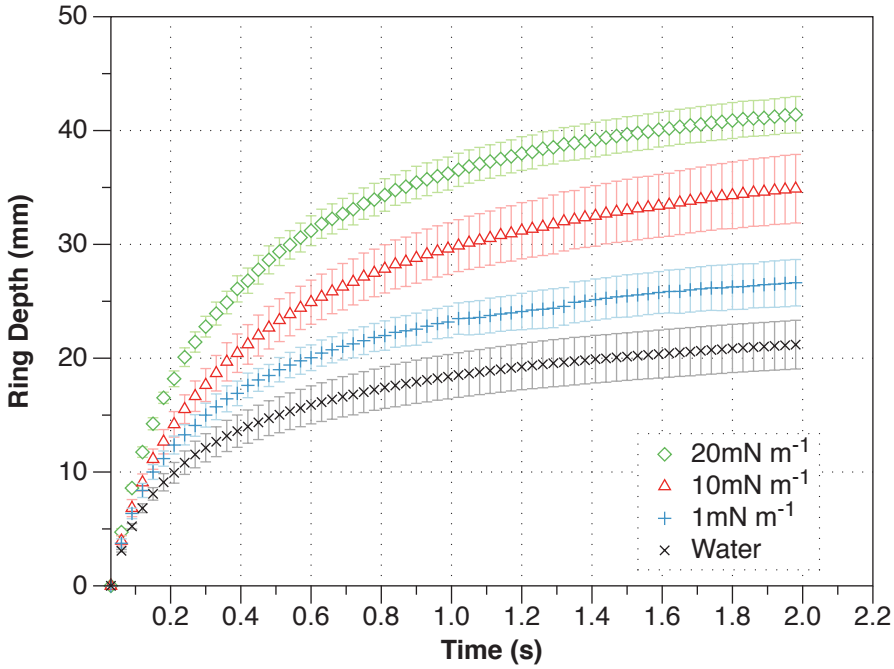

Figure 6.6: Vortex ring evolution at 4 surface pressures
A series of scatter plots showing the average (n=5) position of each of the vortex rings as they were propelled into the sub-phase with a range of surface pressure conditions. The error bars represent a 95% confidence interval.

Figure 6.6 shows that, after initial formation, the vortex rings decelerate sharply before plateauing at a fixed depth. The variation between drops is thought to be a result of an error in quantifying the exact starting point of the drops. To assess the influence of the monolayer upon the vortex rings, the average position of the vortex rings after 1 second (as determined by the camera time stamp with +/- 0.05s accuracy) is plotted in Figure 6.7 as a function of surface pressure for each material. The average speed of the vortex rings over this period can be calculated as the ring depth at 1s divided by time taken (1s), for example as shown in Figure 6.6 where the vortex rings in water have an average speed of 18.5 mm s^{-1}.

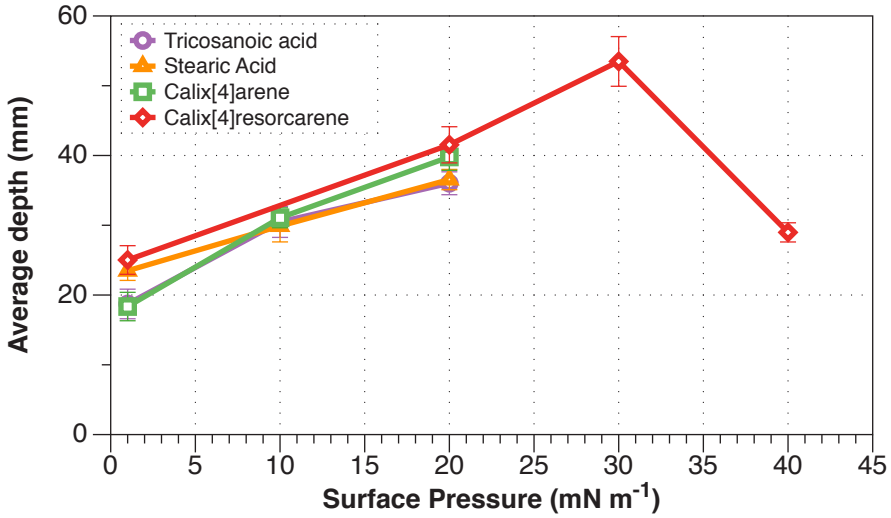

Figure 6.7: Comparison surface pressure to vortex ring depth
Comparison of the depth of vortex rings produced through 4 different monolayer materials. The depth was measured 1 second after the drop left the pipette. The error bars represent a 95% confidence interval.

Figure 6.7 shows that, for surface pressures below 20 mN m^{-1}, changing the monolayer material has little influence on the depth of the vortex ring, measured 1 second after the drop left the pipette, and that there is a correlation between ring depth and surface pressure. It can also been seen that the plots for all of the materials have the same gradient and degree of change. Given the differences between the properties of the materials, this suggests that the formation of the vortex rings is initially material independent. At higher surface pressures, using calix[4]resorcarene C11 as the monolayer material, this relationship appears to break down, with a significant decrease in ring penetration depth. Saylor *et al*. [92], using Triton X-100 as the monolayer material, reported a correlation between ring speed and surface pressure, but this broke down at 5 mN m^{-1}. It was suggested that this matched similar previous data [93] obtained with Triton X-100 and that it was thought to be associated with capillary wave dampening effects.

The ring depth data collected in Figure 6.7 was also compared to the surface elasticity measurements, and this is shown in Figure 6.8.

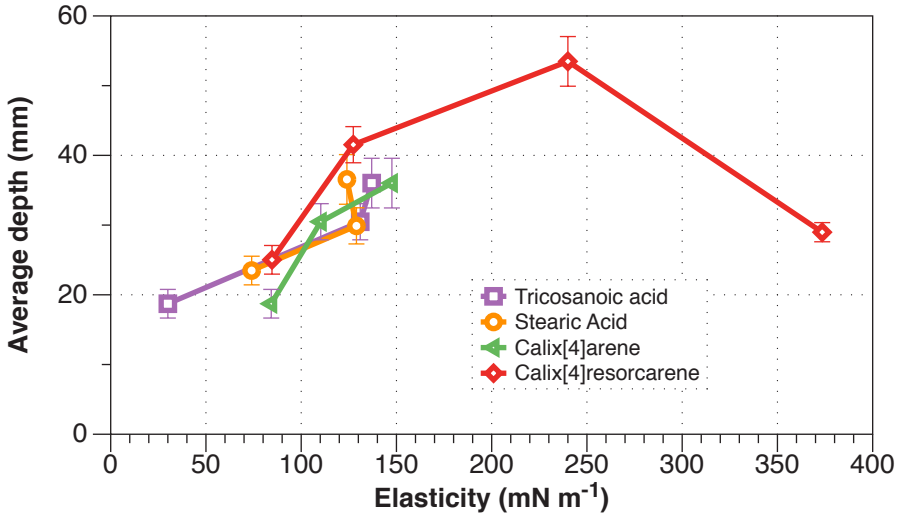

Figure 6.8: Comparison of elasticity to vortex ring depth
Comparison of the depth (measured 1 second after the drop left the pipette) of vortex rings produced through 4 different monolayers at varying surface pressure with varying surface elasticity. The error bars represent a 95% confidence interval.

Figure 6.8 shows a limited correlation between the surface elasticity and the depth of the vortex rings produced. Unlike the data recorded for varying surface pressure, there are many data points across the materials that do not show a linear relationship with the vortex ring depth. There is however, an overall trend, when looking at all materials, with an the increase in ring depth with elasticity of the monolayer, which breaks down at 240 mN m^{-1} for the calix[4]resorcarene monolayer.

6.3. Alcohol vortex ring modification

To examine variations in the vortex ring speed independently of monolayer or surface effects, the trough was cleaned and filled with 5 and 10% alcohol solutions. The results of these experiments are shown in Figure 6.9 and are compared with the data shown in Figure 6.7, which was obtained with a calix[4]resorcarene (C11) monolayer.

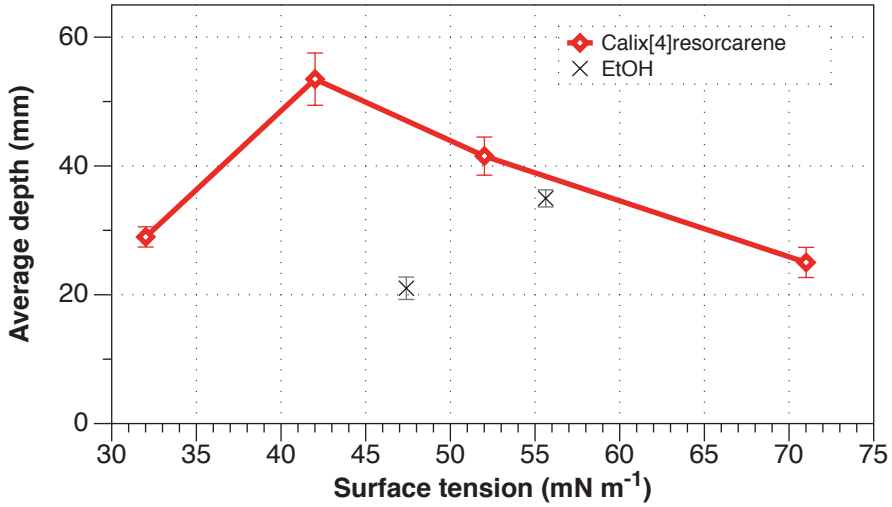

Figure 6.9: Comparison of alcohol altered subphase to vortex ring depth
Comparison of the depth (measured 1 second after the drop left the pipette) of vortex rings produced in subphases containing 5 and 10% ethanol. The error bars represent a 95% confidence interval.

Figure 6.9 shows that the speed of the vortex rings observed in a 5% ethanol solution, which has a surface tension of 16 mN m^{-1} (16 mN m^{-1} lower than pure water) matches the measurements made when using the monolayers to facilitate control of the surface pressure/tension. In the 10% ethanol solution, with a corresponding surface pressure of 25 mN m^{-1}, the speed of the rings decreases sharply. The pressure at which the speed of the ring falls is higher than that reported when a monolayer of Triton X-100 was used to control surface pressure, but is considerably lower than the 30-40 mN m^{-1} seen for the calix[4]resorcarene. The surface pressure values shown in Figure 6.7 were converted to surface tension by simply subtracting the surface pressure from the surface tension of pure water.

6.4. Conclusions

Building on the data provided in Saylor *et al*. [92], this work indicates that there is only limited correlation between surface pressure and vortex ring penetration depth/speed. Up to a surface pressure of 20 mN m^{-1}, the exact nature of the monolayer material has no significant influence on the depth/speed of the vortex ring. This correlation is indicative of what we would expect if the cause of this phenomenon were solely governed by the capillary wave dampening effect caused by a change in surface tension. This can be related closely to the work undertaken by Saylor *et al.* where the relationship between the surface concentration and dampening effects closely matches the shape of the surface pressure isotherm that would be expected for the materials used [99].

However, the work with calix[4]resorcarene and ethanol suggests that the correlation breaks down as the surface pressure increases above 20 mN m^{-1}. Between 30 and 40 mN m^{-1} the presence of the calix[4]resorcarene monolayer causes a distinct decrease in ring depth/speed, in contrast to the observation of the rings formed in ethanol solutions, where a similar drop in vortex ring depth was observed at lower surface pressures between 16 and 25 mN m^{-1}. Saylor *et al*. [92] reported that the vortex ring speed measured when Triton X-100 was used as a monolayer decreased at a surface pressure between 8 and 15 mN m^{-1}. The discrepancy between the speed measured at the same surface pressures - but which were achieved using different materials - indicates that the influence of surface pressure on the speed of vortex rings is most likely secondary to the actual mechanism that regulates their speed, and this will be explored in the following discussion.

Surface pressure has a close relationship to the propagation of capillary waves. It has been shown that, when applied correctly, the intensity of capillary waves can be directly related to surface pressure and in one case this was proposed as a non-contact alternative to the Wilhelmy plate for surface pressure measurement [100]. Devices for performing measurements in this way on liquid or surface films have also been patented [101]. However, Garrett *et al.* [102] showed that the damping co-efficient was not related to the surface pressure and a number of maxima and minima in the damping effect are seen as the surface pressure changes during compression of an insoluble monolayer [102]. This could suggest a reason for the sudden decrease in the ring speed observed at surface pressures that are dependent upon the monolayer material. It might also suggest why there is correlation at lower surface pressures, where the monolayer materials may have a similar influence on the formation of the rings. However, Garrett`s work was centred on the influence of a more complex monolayer material, and it follows that the results may not be directly comparable to those presented here.

One explanation that pulls together the previous and present surface pressure investigation is the impact of the elasticity of the film on the damping of capillary waves. Daillant *et al.* [103] theorized that the surface damping of capillary waves is a function of the elasticity of the film, while Cinbis *et al.* [100] noted that differences in the elasticity of the film caused a relative error of between 0.03 and 6% in their surface pressure calculations from capillary wave measurements. This theory also appears unlikely, as the work presented here shows no clear link between the elasticity of the monolayer and the depth/speed of the rings. Unlike surface pressure, the elasticity of the monolayer shows poor correlation in the range 0 to 20 mN m^{-1} and cannot be used to explain the sudden drop above 30 mN m^{-1}. However, monolayer elasticity is often closely related to monolayer viscosity, which, as suggested by

Pikhitsa *et al.* [87], may be a possible cause of the change in vortex ring formation shown here.

While this work has added to the understanding of the properties of vortex ring formation, it is clear that there is not sufficient published data within this field to show clear causation. Suppression of capillary waves is possible, although conflicting data on the variability or correlation to surface pressure make it difficult to establish this without further study. Further experiments are needed to examine a range of different materials and record not only the speed of the vortex ring, but also the formation and intensity of the capillary waves alongside monolayer viscosity data. This should provide clear evidence on the capillary dampening effect. As Cranfield does not currently posses the equipment required for the measurement of these properties it was not possible to expand this aspect further within this project.

Chapter 7 Fibre optic surface pressure sensor

As discussed in Chapter 4, the Wilhelmy plate is the gold standard for dynamic surface pressure measurement [55], and is used widely in the preparation and monitoring of Langmuir–Blodgett films. The technique relies upon lowering a thin plate in to the surface of a liquid and measuring the downward force exerted on the plate by the contact with the liquid using a microbalance. The plate must be completely wetted before the measurement to ensure that the contact angle between the plate and the liquid is zero. Thus the sensor is sensitive to small vibrations and appropriate preparation of the plate.

Surface tension (the inverse of surface pressure) influences the ability of the liquids to form a meniscus. The higher the surface tension, the higher is the meniscus that can form at the interface with a solid surface. Optical fibre sensors that exhibit sensitivity to the refractive index of the surrounding medium, for example, long period gratings [104], polished or etched Fibre Bragg gratings (FBGs) [105,106] and tilted FBGs [107], have been used to form liquid level sensors but their sensitivity would not be appropriate for measuring the changes in the height of the meniscus, which are typically on the order of micrometers for surface pressure changes in the range 0 to 75 mN m^{-1}. The transmission spectrum of a tapered optical fibre is known to be sensitive to the properties of the surrounding environment [108]. Using optical fibres as surface pressure sensors may provide a wealth of new information on the monolayer and could provide new insights into its potential for coating.

7.1. Experimental setup

Tapering a single mode optical fibre allows the creation of a short section of fibre in which the evanescent field of the propagating modes extends into the surrounding medium. This causes the effective refractive index and the attenuation characteristics of the fibre to exhibit sensitivity to the optical properties of the surrounding material, which has been exploited in the demonstration of a number of chemical and refractive index sensors.

A biconical fibre taper consists of a conical segment where the diameter of the fibre decreases, a taper waist section with uniform diameter and a second conical segment where the fibre diameter increases (Figure 7.1). The taper angle controls the coupling of light between the propagating mode of the single mode fibre and the modes of the tapered section. For non-adiabatic tapers, where the angle of the conical section is large, coupling can occur to a number of modes of the tapered region. When these modes recombine at the second conical section, they interfere, producing a modulation in the transmission spectrum.

The interaction between the modes of the tapered section and the surrounding environment results in a sensitivity of the transmission spectrum to changes in the surrounding refractive index.

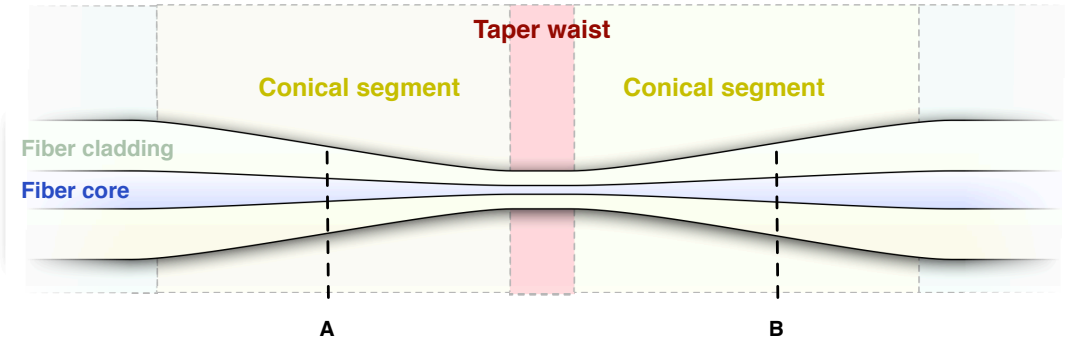

Figure 7.1: Taper regions

Diagram of a tapered fibre showing the different regions. Points A and B relate to the position of the meniscus when the fibre is mounted as a surface pressure sensor

Two tapered optical fibres were prepared for the experiment by Renata Jarzebinska (Research Associate, Department of Engineering Photonics, Cranfield University) using using a heat and pull approach [109]. Single mode optical fibre (Fibercore SM750) was suspended between two motorized rotating stages. The central region to be heated had been stripped of its protective polyacrylate cladding to prevent the coating from melting/burning during the tapering process and contaminating the tapered surface. The central section was heated using a butane-propane burner (65%-35% mix), which produced a 6 mm wide flame with an estimated temperature of 1970°C[110]. The rotation stages were set to rotate in opposite directions to pull the fibre with a constant velocity of 100 μm s^{-1} for ~80 s, producing a taper of length 20 mm. This was repeated with the two separate fibres to produce fibres with tapers of diameter 10.16 μm and 17 μm measured by microscopy.

As described in section 2.7 and 3.1, Langmuir troughs are commonly used for the study and manipulation of monolayers of material on the surface of a liquid. This is typically undertaken within a large PTFE vessel filled with water. A material of interest can then be spread on the surface of the water, forming a monolayer. One or more PTFE 'barriers' that skim the surface of the water are used to change the surface area available for the monolayer, thus controlling the surface pressure/tension. The introduction and subsequent manipulation of the monolayer material is monitored by measuring changes in the surface tension of the water. In previous work these monolayers have been used as a sensor surface, or have been coated on to other surfaces via the Langmuir-Blodgett technique [55].

Monolayers of stearic acid and calix[4]res C11 were created in an Nima Alternate Layer trough (Type: 622). In each experiment the trough was filled with 1250 ml of deionised water (18 MOhms cm^{-1} resistivity) and the surface pressure was monitored using a pre-soaked filter paper Wilhelmy plate attached to a Nima PS-3 Wilhelmy sensor. Stearic acid monolayers were prepared by spreading 50µl of a 1 mg ml^{-1} chloroform (99% Ethanol stabilized) solution of stearic acid. Calix[4]res C11 monolayers were prepared by spreading 40 µl of a 1 mg ml^{-1} chloroform solution of calix[4]res C11. Compression of the monolayers was carried out at 50 mm s^{-1}.

Each sensor was mounted in a small U shaped plastic holder designed to deploy the taper in an arc of large radius of curvature, such that the small contact angle between the fibre and the meniscus amplifies changes in the meniscus height that occur in response to surface tension changes, as illustrated in Figure 7.2. The fibre was mounted such that the menisci were positioned half way between the start of the conical tapering region and the taper waist; these positions are shown in Figure 7.1 as A and B. It was not possible to measure accurately the contact angle achieved with this apparatus, but it was estimated to be approximately 20° to the water's surface.

Changes in the transmission spectrum of the fibre during the subsequent experiments were measured by coupling the output from a tungsten light bulb into the optical fibre and monitoring the output from the fibre using a CCD spectrometer.

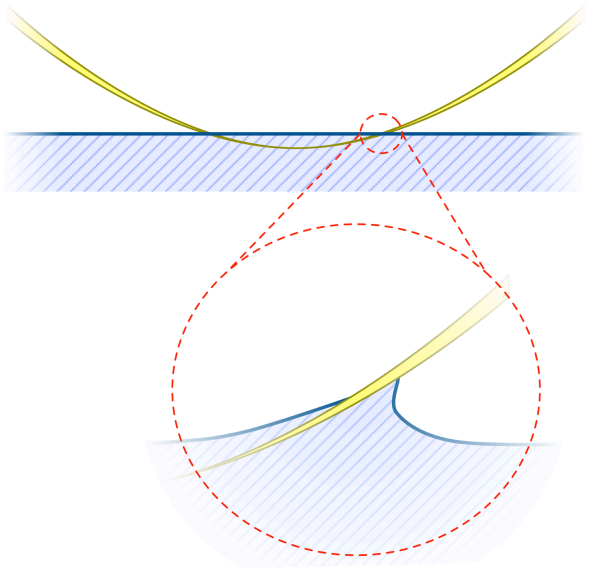

Figure 7.2: Diagram of the curved tapered fibre

7.2. Comparison of methods

The response of the curved tapered fibre surface pressure sensor was compared with that of Wilhelmy plate method. The fibre sensor with a 17 μm taper diameter was mounted in the trough, alongside the Wilhelmy plate system. To examine the influence of the surface pressure on the transmission spectrum of the tapered fibre, monolayers of stearic acid and calix[4]resorcarene were prepared and compressed to a series of increasing surface pressures (as recorded on the Wilhelmy plate). The transmission spectra recorded during the compression of the stearic acid monolayer are shown in Figure 7.3, exhibiting a complex relationship between the transmission spectrum and the surface pressure, with features that show changes in intensity and/or wavelength. Similar effects were observed for the calix[4]resorcarene monolayer.

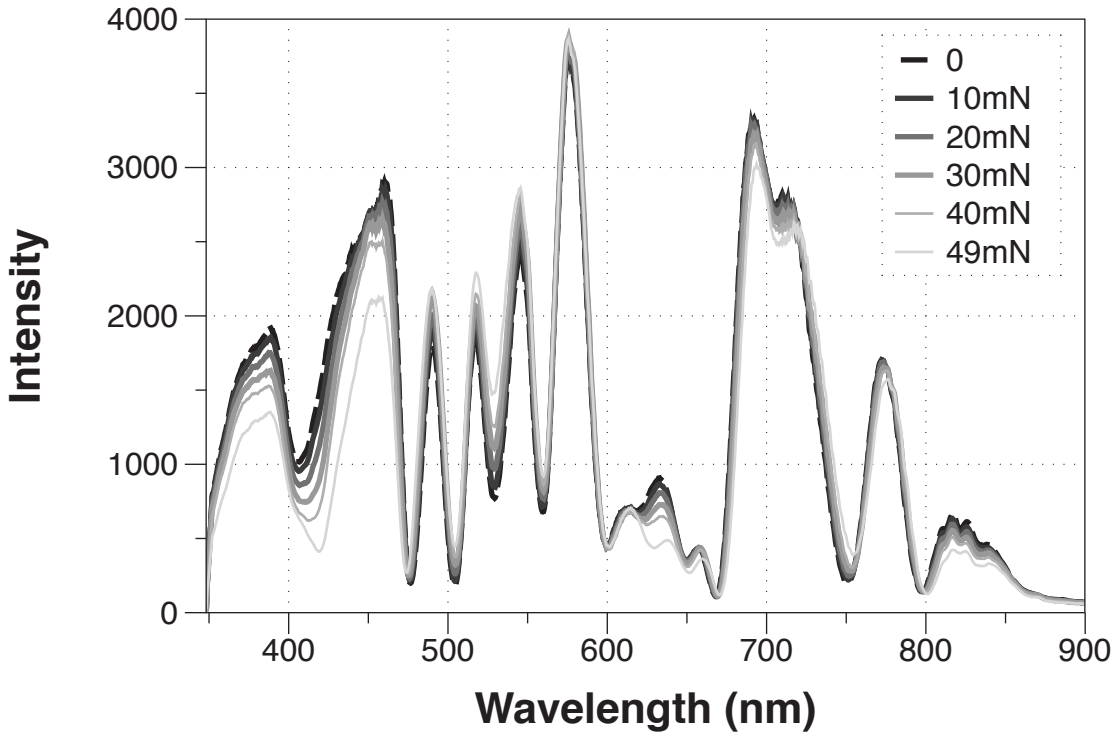

Figure 7.3: Curved fibre full spectrum change
Evolution of spectrum within a 17 µm tapered fibre, at a range of surface pressures of a stearic acid monolayer on the surface of water. The legend indicates the surface pressure recorded by the Wilhelmy plate.

A second series of experiments were conducted in which the monolayers were compressed continuously at 50 cm^2 min^{-1}, during which the transmission spectrum of a 10.16 µm diameter tapered fibre was continuously recorded. This type of monolayer compression is known as an isotherm and monitoring the surface pressure allows the identification of the phase and degree of order of the monolayer. For the LB thin film deposition process, the aim is to identify the pressure at which a packed monolayer of the material is formed on the water's surface, at which point the film may be transferred to the surface of a suitable substrate. When the pressure is increased further the packing density reaches a critical point where the monolayer breaches, so causing rapid formation of a bilayer and a concomitant change in surface pressure.

The recorded spectra were analyzed using a feature tracking system that enabled the comparison of multiple spectral features to the Wilhelmy surface pressure sensor readings. Figure 7.4 (stearic acid) and Figure 7.5 (calix[4]res C11) show the change of the intensity of a peak/feature in the spectrum at 538 nm (chosen for its high signal to noise ratio) along with the measured change in surface pressure.

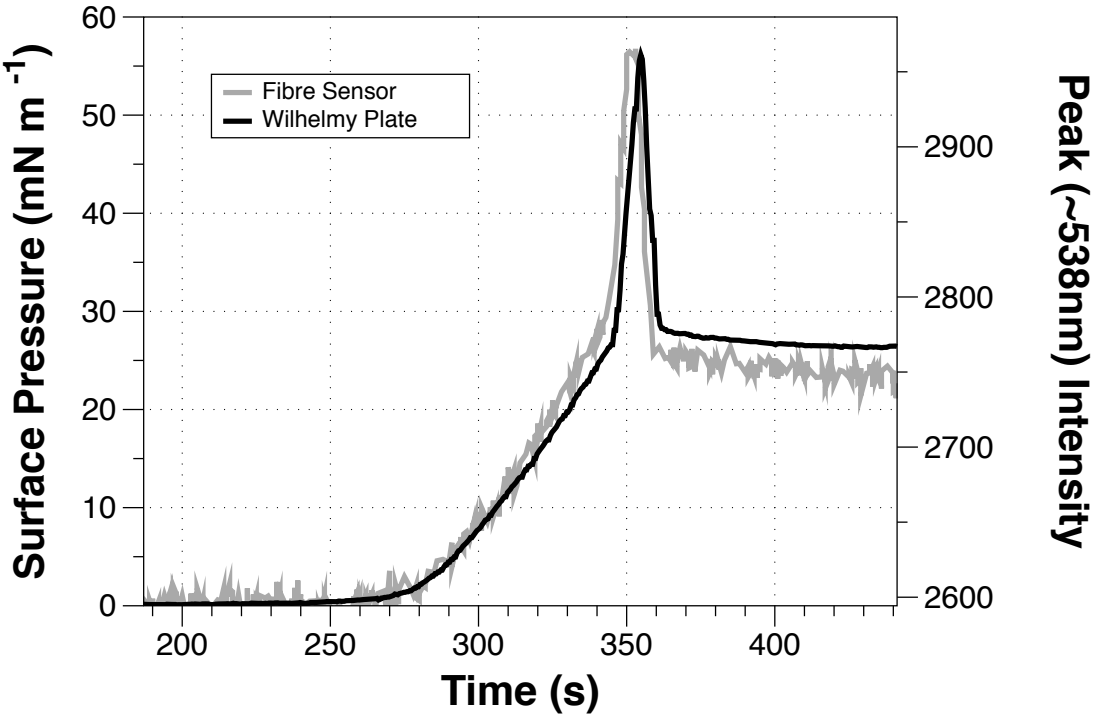

Figure 7.4: Stearic acid isotherm comparison
Stearic acid isotherm, comparison of the tapered fibre sensor with the Wilhelmy plate sensor

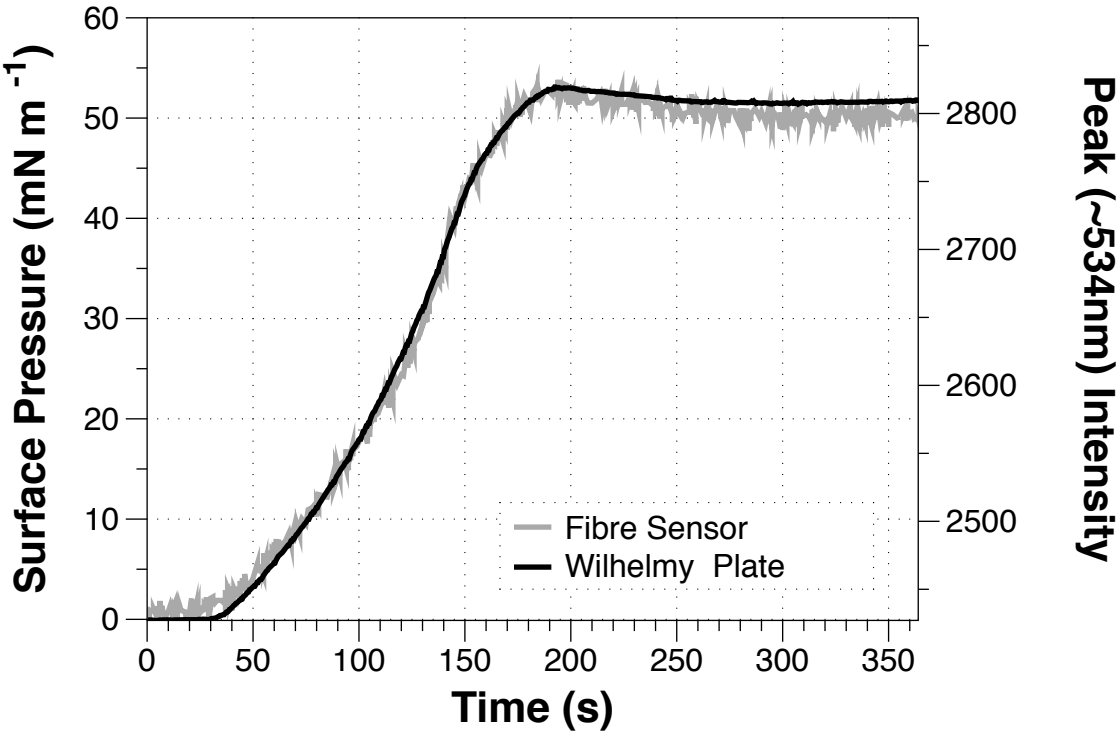

Figure 7.5: Calix[4]res C11 isotherm comparison
Calix[4]res C11 isotherm, comparison of the tapered fibre sensor with the Wilhelmy plate sensor

Figure 7.4 and Figure 7.5 show that for both monolayer materials there is clear correlation between the two different sensor systems. This correlation was further explored by plotting the change in the intensity of the peaks as a function of surface pressure, Figure 7.6.

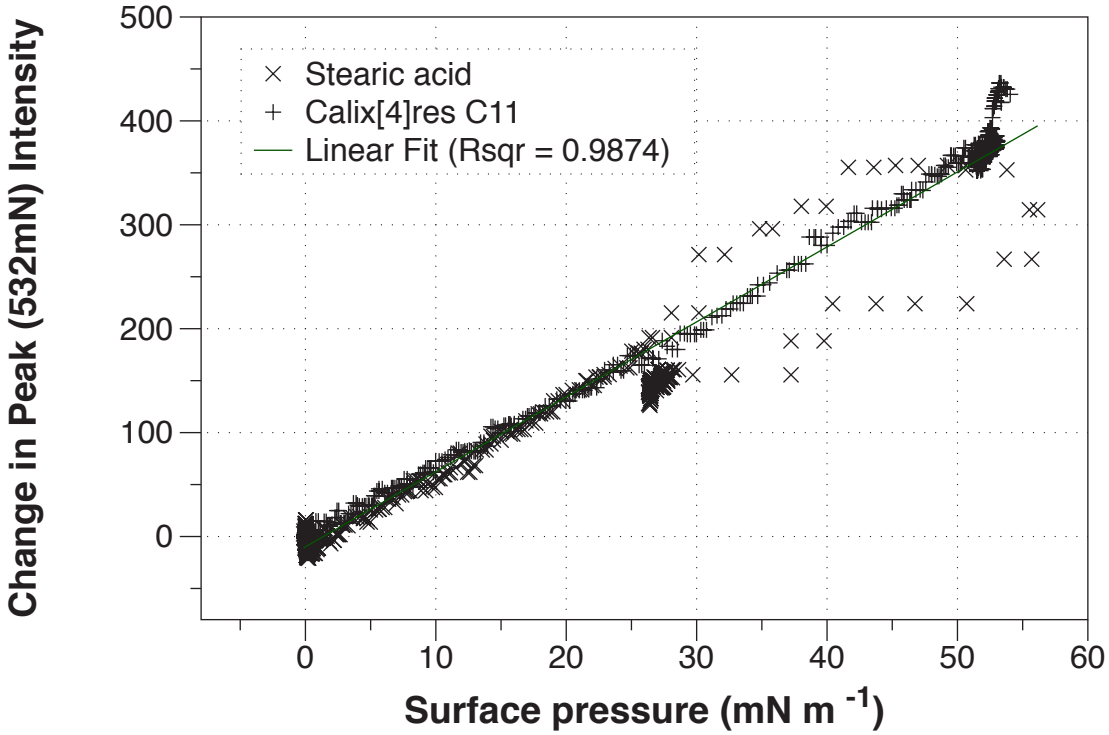

Figure 7.6: Combined plot of peak intensity to surface pressure
Correlation between the changes in the intensity of features in the transmission spectrum of the tapered optical fibre with the surface pressure measured by the Wilhelmy plate. The Linear fit is off all data.

Figure 7.6 shows that the method is not material specific and has a high correlation to the existing Wilhelmy plate method, with a combined R-squared of 0.9874. This correlation is higher with calix[4]res C11 than stearic acid. This is due to the spike in the surface pressure that is characteristic of the stearic acid isotherm. The discrepancies in the response of the tapered fibre may be a result of deposition of stearic acid onto the surface of the fibre during the increase in surface pressure, which then changes the response of the transmission spectrum to further change in the height of the meniscus, or to localized differences in the surface pressure of the monolayer during the rapid surface pressure change.

The results were further analysed to identify features of high and low correlation to the surface pressure. Each of the recorded wavelengths within the spectrum were separated out and compared to the Wilhelmy data using a linear best-fit model. This produced a map of the linearity (Figure 7.7), and slope (Figure 7.8) across the spectrum (overlaid on both figures).

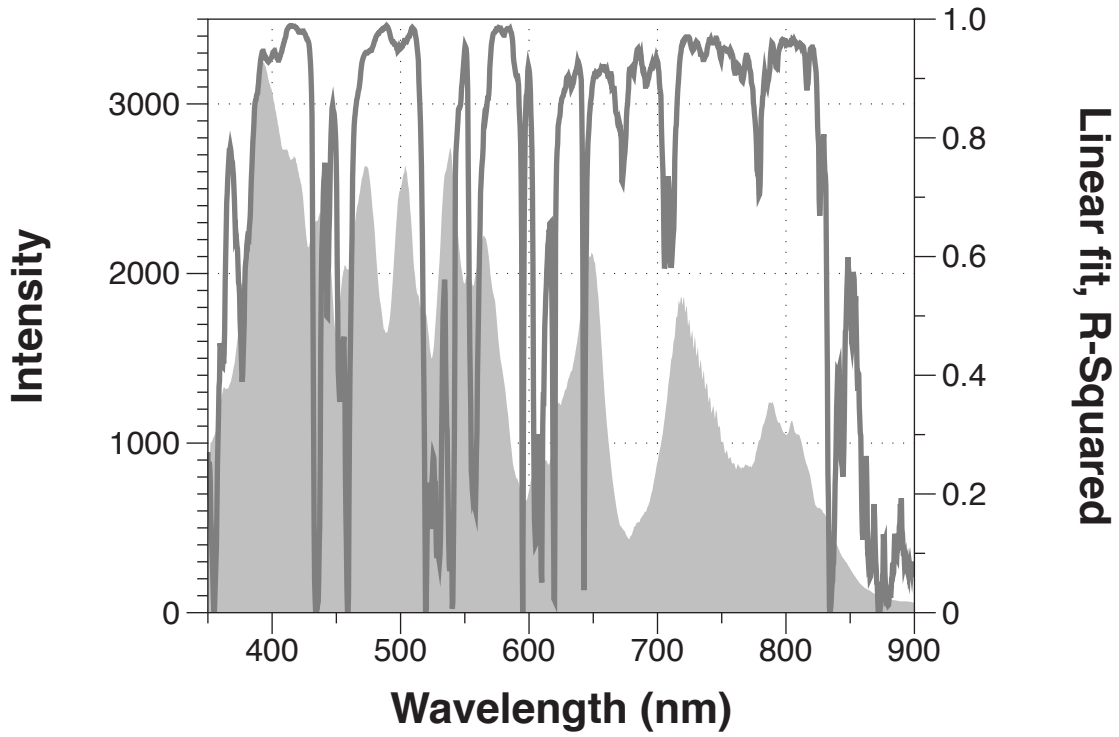

Figure 7.7: R-squared change across the transmission spectrum
Plot of R-square (Y2 axis) overlaid with the wavelength (Y1 axis) against wavelength

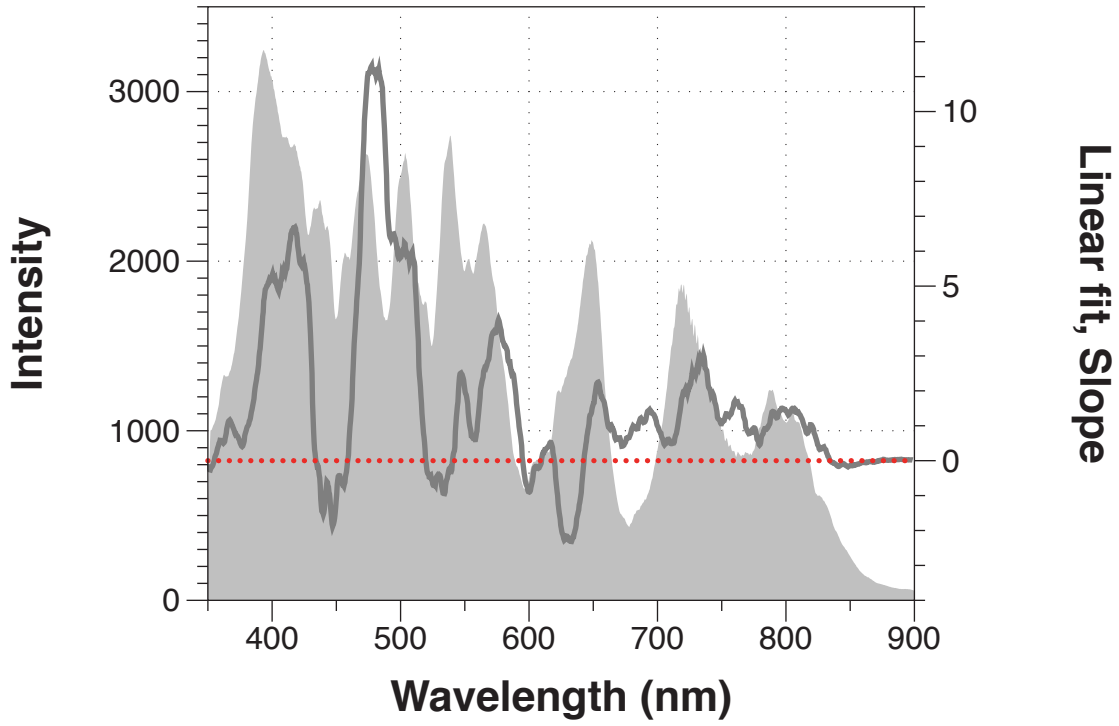

Figure 7.8: Slope across the transmission spectrum
Plot of the slope (Y2 axis), overlaid with the wavelength (Y1 axis) against wavelength. The red dotted line denotes the 0 line on the Y2 axis.

The results from Figure 7.7 and Figure 7.8 show a pattern of correlation to the surface pressure across the spectrum. The R-squared data has a complicated array of peaks and troughs, which show little relationship to any features within the spectrum. This relationship is directly compared in Figure 7.9.

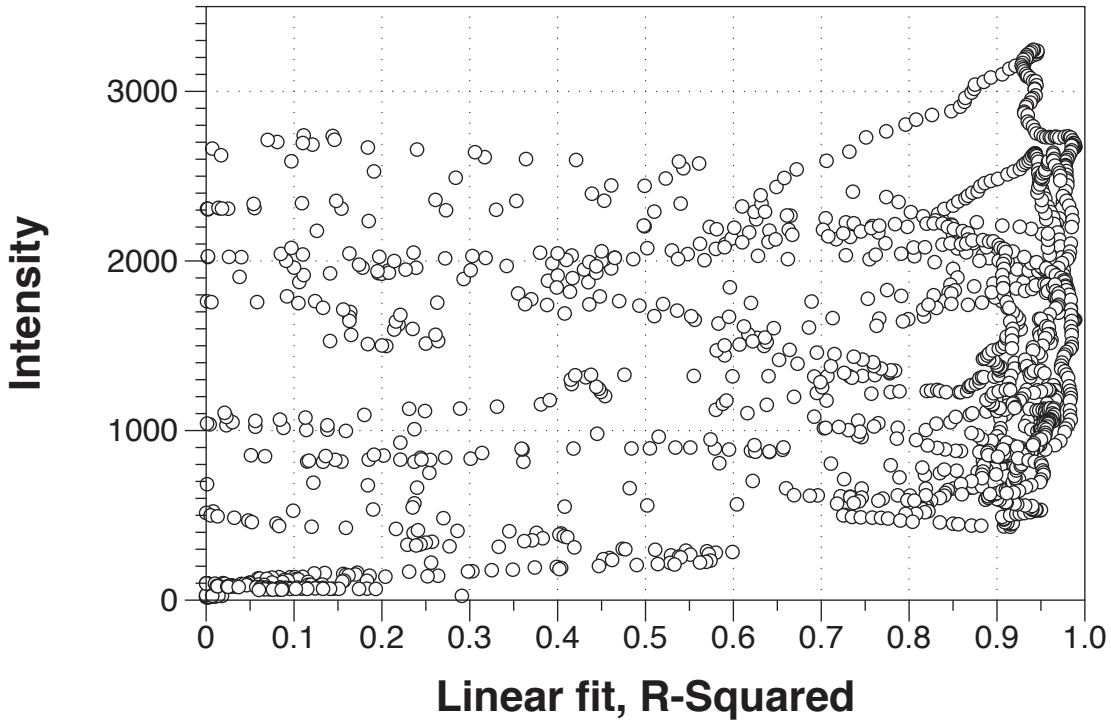

Figure 7.9: Intensity vs R-Squared
Comparison of the R-Squared data to the intensity of the transmission spectrum

Figure 7.9 shows how regions of high R-squared have little correlation with the intensity at any given wavelength. There is a drop in the R-squared values at wavelength with intensities below 500, which indicates that there may be a threshold intensity required to achieve a measurable level of sensing.

Unlike the R-squared plot, Figure 7.8 (slope), shows evidence of periodicity in the form of a wave pattern that switches from a positive to negative slope many times across the spectrum. It is suggested that this periodicity is related to the coupling of modes of the fibre into the surrounding medium. While this pattern shows little relationship to the intensity of the spectrum, the change in the slope can be seen to have a significant relationship with the R-squared plot. This can be more clearly seen in Figure 7.10.

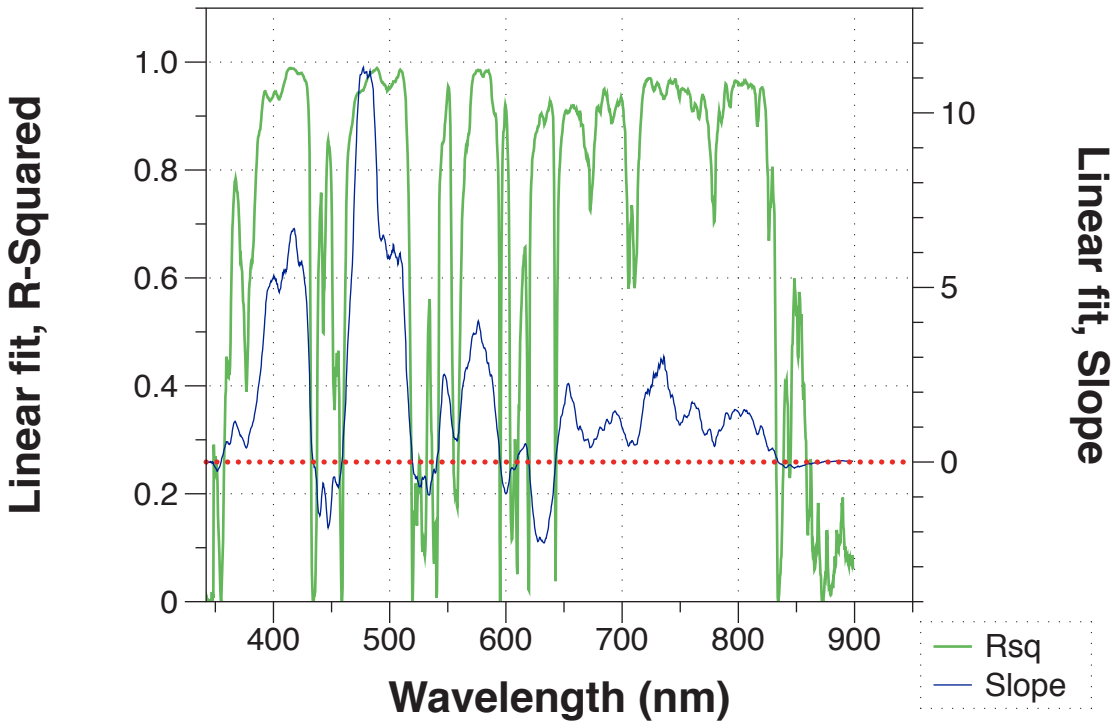

Figure 7.10: Comparison of R-squared to slope
Overlay of R-squared (Y1) and slope (Y2) of a linear fit between intensity and surface pressure at multiple wavelengths.

It is to be expected that the slope has a strong influence on the R-Squared value. However, it can been seen that, when compared in Figure 7.10, the chaotic pattern of peaks and troughs in the R-squared plot correlate closely to the magnitude of slope. Every drop in the R-squared is coupled with a change in the slope from positive to negative.

When the R-squared map is coupled with the slope we can use this data to find the optimal point in the spectrum to provide the best comparison to the Wilhelmy plate. Using this method for both monolayer materials showed that, rather than tracking the largest peak (Figure 7.6), a position halfway down this peak gave a higher linearity: slope ratio and produced a final r-squared of 0.994. It was also noticed that the difference in the transmission spectrum between stearic acid and calix[4]res C11 were also reduced at the same wavelength.

The surface pressure sensing results indicate that the curved tapered optical fibre is a highly sensitive water level sensor. The fibre was mounted in the trough such that it was immersed in the water with the entire taper, including the conical tapering regions, completely under the surface. Once mounted, the trough was then emptied using a pump at a constant rate during which the transmission spectrum of the tapered optical fibre was recorded every 150 ms. The

effect of the movement of the meniscus along the fibre on the transmission spectrum is shown in Figure 7.11.

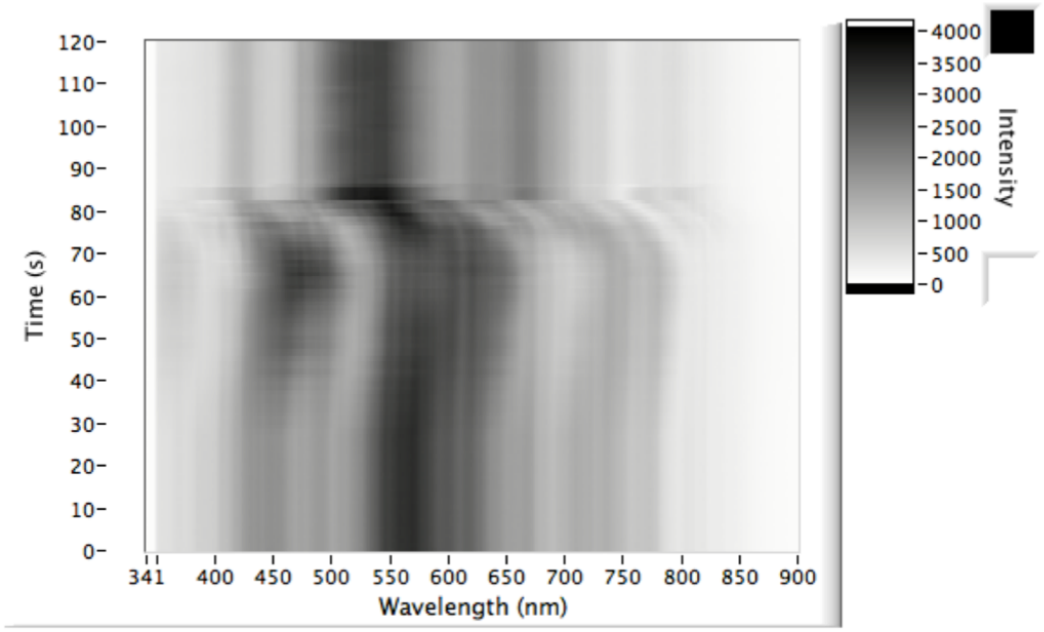

Figure 7.11: Grey scale plot during water level change
Evolution of the transmission spectrum of the curved tapered optical fibre as the water level reduced

Figure 7.11 shows a region of high sensitivity between 70 and 80 s, where the spectral features shift in wavelength. This is a result of the differential responses of the interfering modes to the change in surrounding refractive index caused by the decreasing water level, which influences the spectrum [108]. The high sensitivity is observed as the menisci move in towards the centre of the taper and across the central tapered region, just before the taper is fully removed from the water. Before this transition there is a change in the overall intensity of many of these features. This intensity change (starting at ~40 s) begins as the menisci move down the conical tapering region of the fibre.

7.3. Summary

The use of a curved tapered optical fibre to measure surface pressure has been demonstrated and the performance of the sensor compared to that of a conventional Wilhelmy plate, showing a high degree of correlation. The operation of the sensor is based upon a high sensitivity to change in the position of the meniscus when the meniscus is in contact with the tapering sections. The tapered fibre is capable of measuring changes in the

position of the meniscus on the order of 15μm, which is the change in the height observed for a 1 mN m^{-1} change in surface pressure. With further optimisation this technique may be a significant improvement on the existing Wilhelmy plate sensor.

Chapter 8 Vapour sensitive monolayers

Previous work determining the sensitivity of calixarenes to vapours has relied on combining the calixarene with a suitable sensor platform to measure any physical or chemical change in the calixarenes as they form gas state complexes. In the context of this project, this would require each calixarene to be coated on to optical fibres to allow them to be assessed for vapour sensitivity. This is not ideal since modified fibres are difficult to produce repeatable and can in for some cases can only be used a limited number of times due to their fragile nature.

To allow for quicker method of study of the sensitivity of calixarenes to vapours an alternative method was proposed. Nabok *et al.* [30] showed that calixarenes expand when they form gas state complexes. Given this shape change, it was proposed that the expansion of the calixarenes could be monitored by the increase in surface pressure caused by greater interaction between the expanding molecules.

8.1. Multiple vapour testing with calix[4]res C11

Calix[4]res C11 is the calixarene that was studied in previous work [1] and which has been shown to have sensitivity and to be specific to aromatic hydrocarbon solvent vapours. This previous data suggests that calix[4]res C11 is a good material with which to demonstrate the viability of this method.

The trough was prepared as described in the standard procedure (using pre-soaked filter paper) and 300 µl of a 0.1mg/ml calix[4]res C11 solution was spread on the surface of a water subphase. The film was then compressed to 15 mN m^{-1} and allowed to equilibrate for 2 hours. Between each run, the film was relaxed (the barriers were re-opened) for 1 hour and then re-compressed.

The exposure of the monolayer to solvent vapour was carried out using the following method.

- A glass Petri dish was placed inside the enclosure (with a volume of approximately 0.1 m^3 containing the trough on a small stand holding the dish approximately 5 cm from the surface.
- A calculated volume (Table 8.1) was then pipetted into the Petri dish as per the evaporation method detailed in section 3.4.1. This range of concentrations were used to provide a range of possible sensitivity.

Table 8.1: Volumes of solvent used to achieve the chosen ppmv

Solvent	Volume of solvent used (ml)	~ppmv
Chloroform	**1.8**	6000
	0.9	2000
	0.3	1000
Toluene	**2**	5000
	1	2500
	0.4	1000
n-Hexane	**4.1**	8000
	1.5	3000
	0.5	1000
Ethanol	**3.4**	15000
	0.7	3200
	0.2	900

- The trough was quickly sealed and the surface pressure was monitored for change.
- The trough was then opened and the vapour was allowed to disperse before the next run.

The surface pressure was maintained at 15 mN m^{-1} during the exposure to solvent so that any expansion in the molecules will result in a surface area change so as to maintain this pressure. The reaction to the solvent exposure is measured so as the change in area between its pre-exposure state and it's maximum-area change during exposure, this is plotted in Figure 8.1.

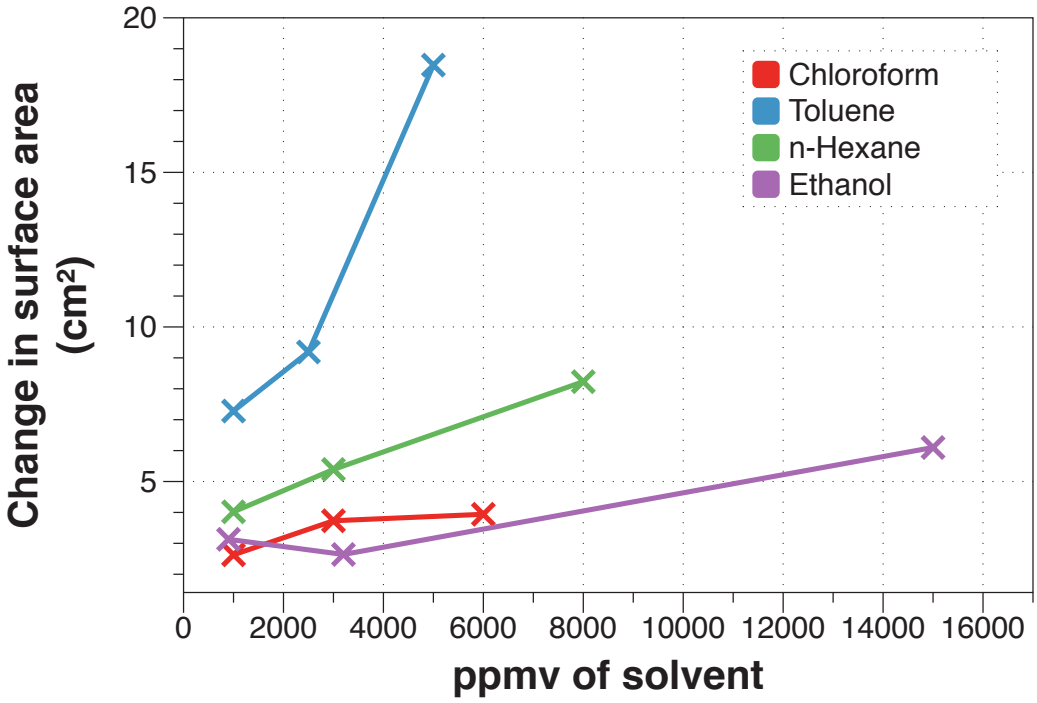

Figure 8.1: Effect of solvent vapour on a monolayer of Calix[4]res C11
The above graph shows the difference in response of a Calix[4]res C11 film to 4 different solvents at 3 different concentrations.

To ensure that this reaction to solvents was not an effect of high concentrations of solvent acting of the sub-phase or pressure sensor, one concentration for each of the solvent was repeated with a stearic acid monolayer, which was chosen as a negative control as stearic acid is well known to have no chemical or physical reaction to VOC gases, these results are shown in Table 8.2.

Table 8.2: Reaction of a monolayer of stearic acid to solvent vapour

Solvent	PPM	BaseLine (cm^2) (+/- 0.01)	Max Area of monolayer (cm^2) (+/- 0.01)	Delta
Chloroform	3000	356.63	356.67	0.04
Toluene	2500	357.36	357.57	0.21
n-Hexane	3000	357.05	357.33	0.28
Ethanol	3200	357.3	357.49	0.19

The results in Table 8.2 and Figure 8.1 indicate that a monolayer of Calix[4]res C11 will responded selectively and quantitatively on exposure to vapours. The variation in the

reaction to different vapours also matches the results from calix[4]res C11 coated fibres in earlier work [3].

8.1.1. Further analysis of sensitivity

A Langmuir film was prepared by spreading 200 µl of the Calix[4]res C11 solution on the surface of a water subphase in the LB trough. The film was then compressed to 15 mN m^{-1} and allowed to equilibrate for 2 hours. Between each run the pressure of the film was maintained.

To expose the film to the appropriate level of toluene vapour the follow procedure was followed.

1. A glass Petri dish covered with four 1 cm x 5 cm strips of filter paper was placed inside the box with the trough (a small stand held approximately 5 cm above the centre of the trough).
2. The appropriate volume of toluene was then pipette into this Petri dish.
3. The volumes chosen were based on reaching certain vapour concentrations within the trough:
    - 800 µl ~ 2 k ppmv
    - 400 µl ~ 1 k ppmv
    - 200 µl ~ 0.5 k ppmv
    - 100 µl ~ 0.25 k ppmv
4. The trough was quickly sealed and the surface pressure was monitored as an indicator of film swelling.
5. This was left to swell until a stable level of swelling was observed.

The trough was then opened and the toluene vapour was allowed to disperse for a minimum of 1 minute before being closed again to check the regeneration of the monolayer.

Unlike the previous experiment, pressure readings were taken every 0.5 s throughout the experiment to ensure a full picture of the way the monolayer reacts to the toluene vapour; these readings are plotted below in Figure 8.2.

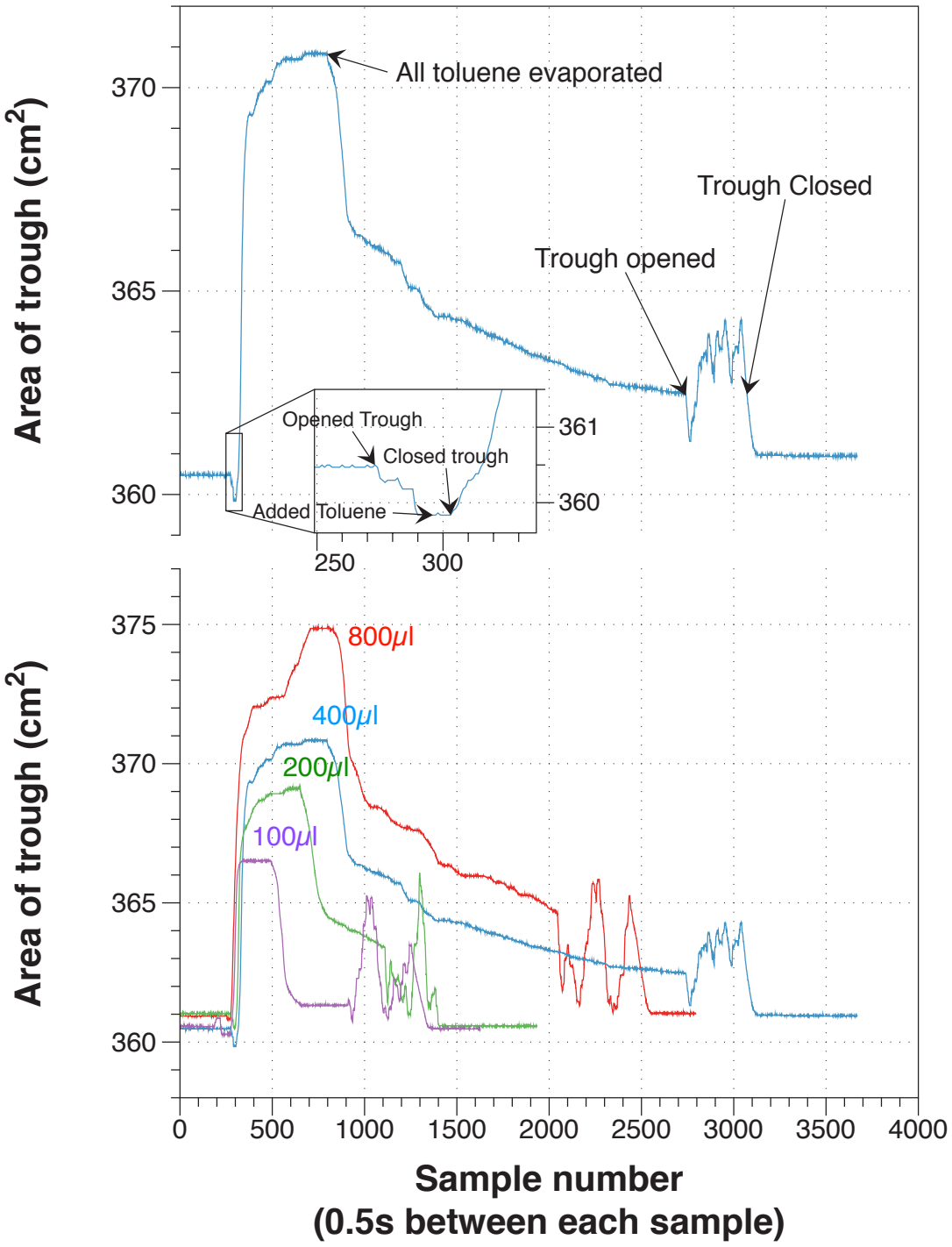

Figure 8.2: Reaction of a Cal[4]res C11 monolayer to toluene vapour while maintain a surface pressure of 15 mN m^{-1}
The above plots show the reaction of Calix[4]res C11 to toluene vapour. The lower plot is the comparison of the reaction of the film to the addition of 4 different amounts of toluene to the chamber. The top plot is the 400 µl graph, which has been annotated to explain the features.

Initially the film reacted strongly but this sharply tapered off once all of the toluene had evaporated. A likely explanation for this is that the toluene vapour (which is heavier than air) cascaded out of the Petri dish on to the film creating high, localised concentration during evaporation. Once the toluene has all evaporated, the monolayer is only left with the ambient

vapour concentration. This ambient level could also be significantly reduced as the toluene may sit around the base of the trough and not encounter the monolayer.

8.1.2. Calix[4]res C11 reactions using a vapour generator

In an attempt to overcome the evaporation problems encountered in the experiment described in 8.1.1, the OVG-4 vapour generator was used. This generator can create a small jet (up to 500 ml s^{-1}) of a specific ppm of vapour, which can be directed towards a sensor surface.

Unfortunately, to achieve the high concentrations used in the previous experiment the vapour generator had to be run with a slow flow rate of around 50 ml s^{-1} to produce a concentration of 480 ppm toluene vapour. At this rate, it would have taken 15 hours to fill the enclosure around the circular trough (used in the previous vapour sensing experiments), and this was not practical. To address this problem, the mini Langmuir trough was used while enclosed within a smaller glass chamber with an approximate volume of 10000 ml.

Because of its small size, a single drop of 0.1 mg ml^{-1} calix[4]res C11 was sufficient to form a monolayer on the subphase in this smaller trough. Once the calixarene had been added, the surface was compressed to a pressure of approximately 17 mN m^{-1} and allowed to settle for 2 hours.

Once stable, the monolayer was then exposed to 100, 200 and 400 ppm toluene vapour concentrations using the OVG-4 generator. Each concentration was delivered to the chamber though a small PTFE tube which injected the vapour into a hole in the top of the enclosure. The trough was exposed to the first two concentrations for 30 minutes. The final concentration was left for a longer time to see if a plateau in the monolayer response could be reached. As the mini trough has no automatic barrier control system, the reaction of the monolayer was measured by the change in surface pressure of the calix[4]res C11 monolayer. The pressure is plotted as a function of time in Figure 8.3.

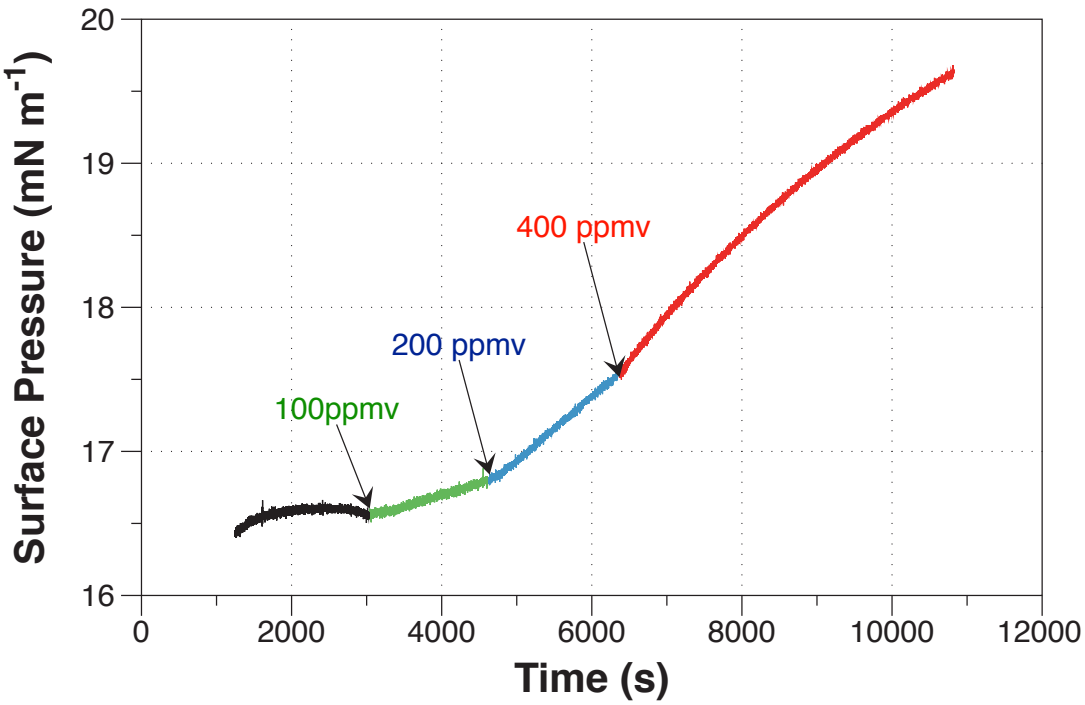

Figure 8.3: Reaction of a Cal[4]res C11 monolayer to varying toluene vapour
The plot shows the change in surface pressure of a Calix[4]res C11 monolayer (held at 17 mN m^{-1}) during exposure to increasing concentration of toluene.

The data shown in Figure 8.3 indicates that a monolayer of calix[4]res C11 does respond to increasing levels of toluene vapour at low ppm concentrations. With increasing concentration there is a concomitant change in the rate of increase of the surface pressure of the calix[4]res C11 monolayer. Unlike previous experiments, the film never reaches a stable plateau during exposure within the time frame allowed for. This lack of a plateau may be a result of a difference in the exposure method; the Owlstone generator will take longer to build up a stable concentration within the chamber whereas the evaporation method is quicker. This problem may be alleviated by examining higher concentrations of solvents using the Owlstone equipment however, the system is limited to lower range ppm vapour production so at this early stage in sensitivity testing the Owlstone system was found to be too limited to examine a wide range of high ppm vapour concentrations.

8.2. Mini trough sensor

Building on the experiments described in 8.1.2, the next stage in testing the use of Langmuir films as sensor surfaces was to build a repeatable system for testing the sensitivity of monolayers to a range of vapours independent of a sensor platform. The glass-based design used in section 8.1.2 was replaced with a sealable plastic container. This allowed for the inclusion of an air suction system which was used to empty the chamber after every run. As with the experiments described in 8.1.2, a monolayer of calix[4]res C11 was prepared on the

mini trough, which was situated in the centre of the chamber. The surface pressure of the monolayer was monitored using a Wilhelmy balance. Once spread, the monolayer was manually compressed using the mechanical barrier on the mini trough to produce a surface pressure of ~15 mN m^{-1}. Once prepared, this monolayer was exposed (via the evaporation method) 5 times to a 3300 ppmv vapour of toluene. Unlike the previous experiments, the solvent was placed in a petri dish next to the trough, which it was hoped would prevent the localised high concentration problems encountered in 8.1.1. The results from the 5 exposures are shown in Figure 8.4.

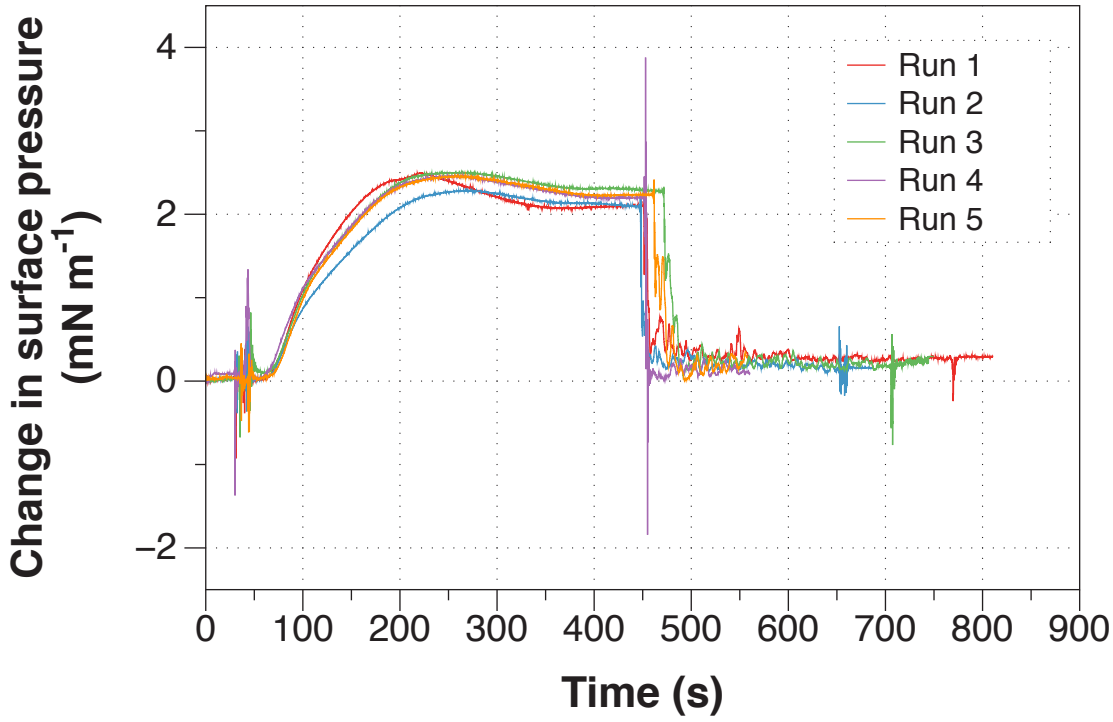

Figure 8.4: Repeat exposures of calix[4]res C11 to toluene
Repeat exposures (n=5) carried out in a sealed box with air-flow control. This addition of the solvent and flushing of the chamber are clearly evident from the sudden change in the surface pressure of the monolayer.

When compared to the exposure profiles shown in Figure 8.2, the profiles in Figure 8.4 show clear improvement in the form of the response. Instead of a sudden increase, there is now a slow build up in film reaction. This slow build up is indicative of the evaporating solvent reaching its final vapour concentration.

8.2.1. Curves

Using the improved Langmuir monolayer vapour testing method described in section 8.2, a number of monolayer-forming materials were tested for their sensitivity to several solvents at a range of vapour concentrations. The materials chosen were calix[4]res C11 (Figure 8.5),

which as discussed has previous shown sensitivity to a range of solvents, stearic acid (Figure 8.6) which is known to be insensitive to solvent vapours and TB calix[4]arene (Figure 8.7) for which there is also no known reaction to solvent vapours. These materials were chosen to show the specificity of the method.

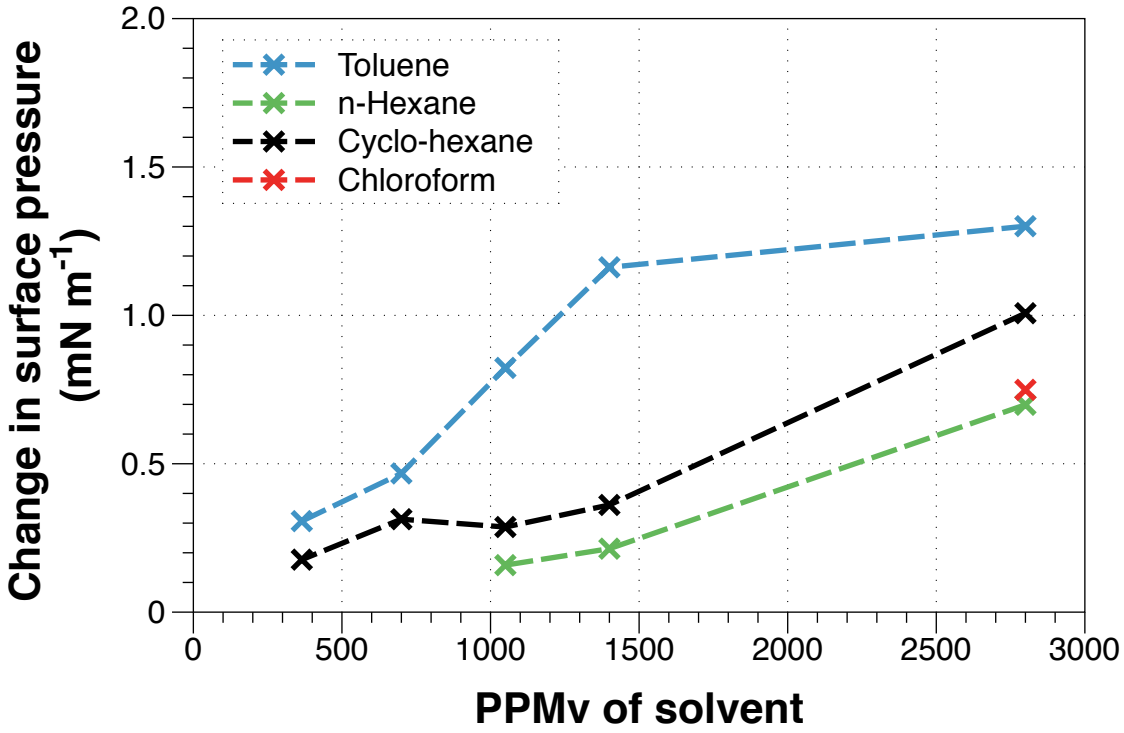

Figure 8.5: Monolayer of calix[4]res C11 with several solvents
The above graph shows a range of ppm for each solvent with the exception of chloroform which, was initially run at a range of concentrations but a computer error meant that the data was lost. The scale of this graph is set to match the other two accompanying monolayer runs shown in Figure 8.6 and Figure 8.7.

The data shown in Figure 8.5 agrees well with previous reports on the investigation of the reaction of calix[4]res C11 to solvents in the literature and in the preliminary work described in section 8.1. Previous experiments had shown a more linear relationship with no plateau during exposure to toluene at a concentration of 2800 ppmv. Given the significantly higher surface pressure change seen in Figure 8.4 at 3300 ppm, the most likely explanation for this difference is experimental error. Additionally, it is interesting that chloroform produces such a strong reaction. There is no previously published data calix[4]res C11 to chloroform, as it had been thought too small a molecule to substantially affect the material[64].

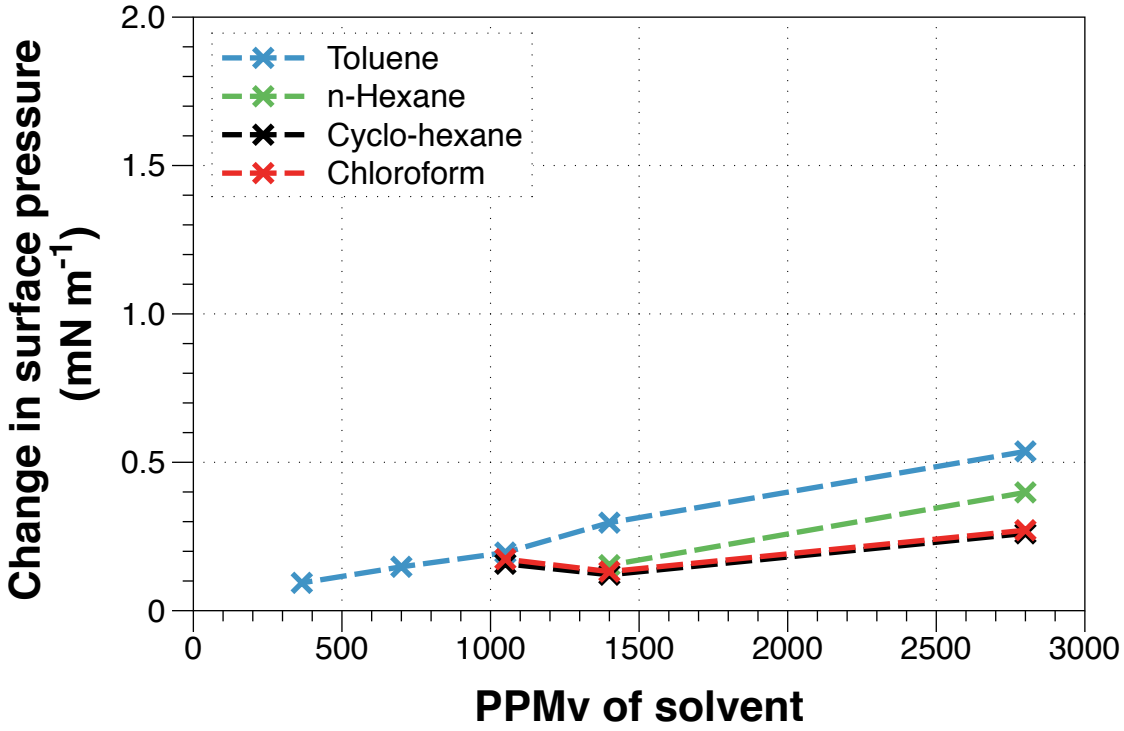

Figure 8.6: Monolayer of stearic acid with several solvents
(Note: The scale of this graph is set to match the other two accompanying monolayer runs shown in Figure 8.5 and Figure 8.7).

Figure 8.6 shows that stearic acid exhibits little or no response to exposure to organic vapours. There is a trend upwards with all the solvents tested which is beyond what would be expect with the variation shown in Figure 8.4, although compared to calix[4]res C11 this reaction is small.

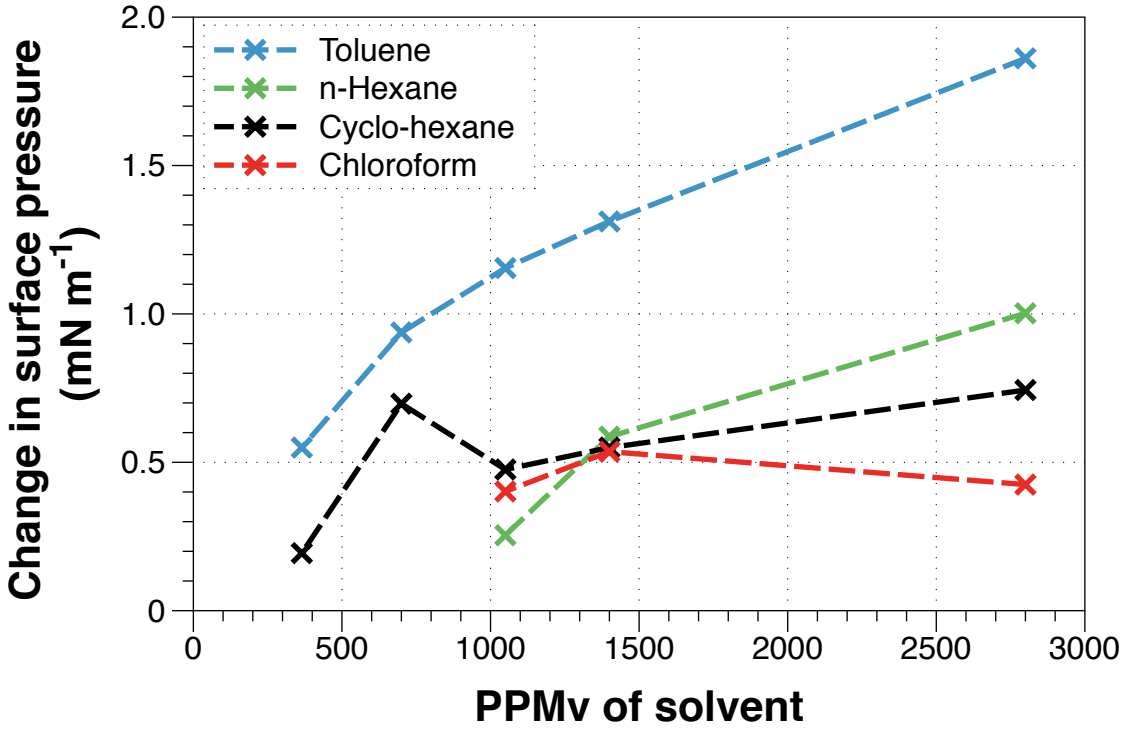

Figure 8.7: Monolayer of TB calix[4]arene with several solvents
The scale of this graph is set to match the other two accompanying monolayer runs shown in Figure 8.5 and Figure 8.6.

TB calix[4]arene has been used for a number of sensing systems, but it was not possible to find any examples of studies of the sensitivity of TB calix[4]arenes to vapours. Given the structural differences between TB calix[4]arene and calix[4]res C11, TB calix[4]arene was also not expected to show any response to exposure to vapours. TB calix[4]arene has also been previously tested for solvent sensitivity using a LPG fibre optic sensor and was found to be unreactive in un-published data from a previous project within the group (Steven Topliss – Private communication). Given these observations and our understanding of the molecular recognition involved, the results shown in Figure 8.7 could not be adequately explained as being the result of TB calix[4]arene having previously undiscovered sensitivity to this range of vapours. The only explanation is that another mechanism was responsible for this reaction to solvents.

8.2.2. Water control

In previous experiments (section 8.1) stearic acid was used to form the monolayer in the control experiment subsequently used to show selectivity of the Langmuir monolayer's sensitivity to vapours. It was felt that this was an suitable control as it was well documented and produced a reliable and repeatable monolayer. However, given the results shown in Figure 8.7, it was realised that stearic acid may not be a suitable control material. Following

the un-explainable results in the section 8.2.1 it was suggested that monolayer exposure reactions had not been characterising the sensitivity of materials to solvents but rather their porosity to solvents. Calix-based molecules are large molecules that pack in an irregular manner as a monolayer material; they also have central cavities which, from molecular modelling[6], can be seen to be large enough to allow the passage of small solvent molecules. It was suggested that stearic acid, with it's regular packing and small size, was acting as an effective barrier to the solvent vapour, preventing it from interfering with the surface pressure of the subphase surface. Calix[4]res C11 and TB calix[4]res however do not pack in this manner and may allow the passage of the solvent vapour. In order to test this theory, a further panel of solvents were run using the mini trough with no monolayer; the results are shown along with equivalent data from the monolayer runs from section 8.2.2 in Table 8.3.

Table 8.3: Comparison of the changes in surface pressure at 2800ppm with multiple solvents

Solvent	Change in surface pressure (+/- 0.1) (mN m^{-1}) at 2800 ppmv			
	Calix[4]res C11	Stearic acid	TB calix[4]arene	Plain water subphase
Toluene	1.3	0.5	1.9	1.5
n-Hexane	0.7	0.3	1.0	0.4
Cyclo-hexane	1.0	0.2	0.7	0.4
Chloroform	0.7	0.2	0.4	0.6

As predicted by the proposed porosity theory, a plain water subphase has a strong reaction to each of the solvents. This indicates that the majority of the reactions seen in the previous experiments are not a reaction of the material but a reaction of the subphase. However, the reaction is often higher in the presence of a calix monolayer, which does suggest that, while a substantial proportion of the observed response is due to the reaction of the subphase, there may be an additional contribution from the sensitivity of the monolayer materials. This sensitivity could be simply that the material acts to concentrate the vapour close to the subphase and so increase the reaction. Alternatively it could be a secondary specific reaction.

8.3. Conclusions

While initially appearing promising as a method for quickly screening a number of materials for vapour sensing, it is clear that the effect seen in monolayers spread on the surface of the

subphase is not solely due to the solvent-vapour interaction with the monolayer material, as the majority of the response can be attributed to a subphase reaction. The reaction of water to these non-polar solvents is un-expected and an extensive literature search did not produce any published evidence of this effect. It is possible to explain this as being due to the slow absorption of a low concentration of solvent in to the subphase, which would be expected to alter the surface pressure. However, this would not explain the almost instant recovery seen on venting the chamber at the end of each experiment. It is more likely this the effect occurs as a the result of a change in the hydrogen bonding potential of the air-water interface, causing a change in the surface tension of the liquid as a reaction to a change in the composition of the surrounding air.

Separate to the cause of the surface pressure change in the water, these results have suggested that this technique may be adapted to look at the porosity of amphillic molecules to solvent vapours. While the evidence here is far from conclusive, it has demonstrated the possibility that the reaction can be linked to the structure and packing of the material. Despite this initial promise, it was felt that the number of questions raised in this chapter would require more work than was possible within the scope of this project, and so it was not developed further.

Chapter 9 Dipole altered Isotherms

Studies on Langmuir monolayers have encompassed a wide range of effects and properties of the monolayer materials. Thanks to a number of new developments in microscopy [111], spectroscopy [112] and range of other analytical techniques, the field has widened to produce a number of models and theories of the ways that monolayers behave and how they react [113]. One area that has received little attention is the modification of the interaction between the monolayer material and the subphase on which it is spread. The solubility of the head group is known [95] to be determined by the dipole moment of any groups it contains. The difference in dipole moments between the monolayer material and the subphase determines the degree of attraction/solubility [114]. This interaction has been explored in a variety of ways, including characterisation using surface potential measurements [115].

9.1. Solvent drops

While working on the vortex rings (see Chapter 6), it was observed that the monolayer material behaved differently during the addition of solvents. It has been reported widely that adding a drop of chloroform to the surface of a stearic acid monolayer results in a 'skipping' drop of chloroform that appears to 'eat' the monolayer until the drop becomes saturated with stearic acid. However, when this was repeated with a similarly chloroform- soluble monolayer of calix[4]res C11, it was observed that the drop had no effect on the monolayer and simply evaporated. In order to investigate the effect described further, monolayers of stearic acid, calix[4]res C11 and TB calix[4]arene, were prepared by spreading 100 µl of a 1 mg ml^{-1} solution of each material in chloroform onto a clean distilled water sub-phase. Once prepared, each monolayer was compressed to a surface pressure of 20 mN m^{-1}. This pressure was chosen as it is high enough to ensure ordered packing of the monolayer with few defects, without causing monolayer instability and possible collapse [116]. To further ensure film quality, the monolayer was held at this pressure for 1 hour before any further experiments were performed. During this hour, the control software for the Nima trough automatically increased and decreased the area of the monolayer surface via mechanical barriers to maintain the required surface pressure. This feedback circuit was designed to ensure that the pressure never deviates from the set value by more than +/- 0.2 mN m^{-1}, both during this stabilisation period and during the subsequent experiments.

Following the 1-hour stabilisation period, a 5 µl drop of chloroform was added to the monolayer's surface. Care was taken during the addition of the drop to ensure that the drop floated on the surface, rather than sank through it. During the addition and subsequent

evaporation of the drop, the change in monolayer area was recorded. The addition of drops was repeated three times for each monolayer and the resulting data is shown in Figure 9.1.

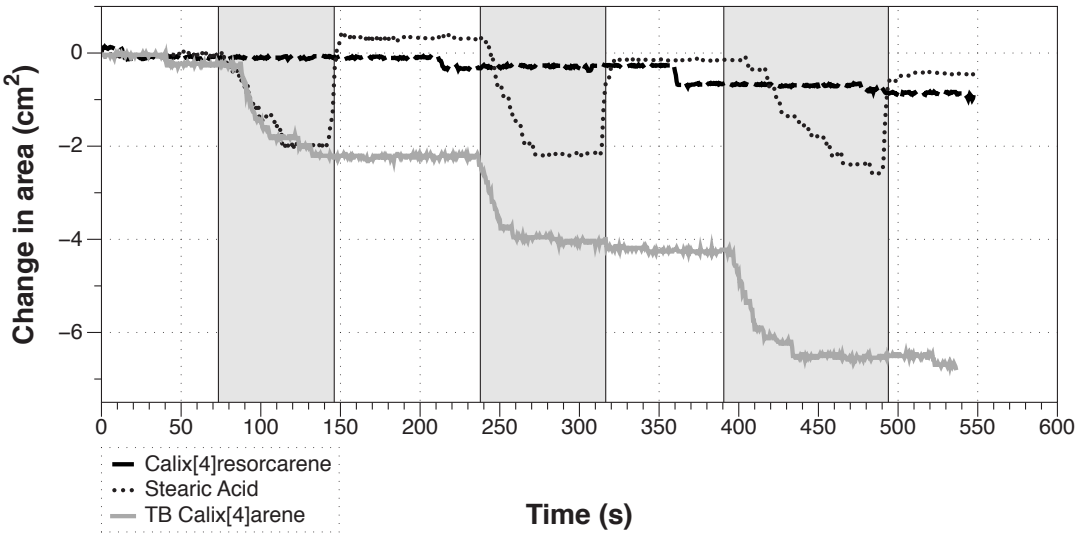

Figure 9.1: Monolayer change during chloroform drop addition
The presence of the chloroform drop on the monolayers is show by the gray bands

The results obtained from all three monolayer materials are superimposed in Figure 9.1 to highlight the differences between the materials. Stearic acid and TB calix[4]arene show clear loss of monolayer on the addition of chloroform to the monolayer surface. The surface area of the stearic acid monolayer shows a quick return to its original monolayer area with the small increase seen after the first addition being due to sensor variation. This indicates that, as the chloroform evaporates, the stearic acid dissolved is quickly reconstituted into the monolayer. The surface area of the TB calix[4]arene monolayer, on the other hand, does not return to its initial value, indicating that material is lost from the monolayer, presumably forming a multilayer in the area that the drop acted upon. Lastly, the calix[4]resorcarene shows no reaction to the addition of chloroform. However, there are two small features independent of the addition of chloroform. These are thought to be the result of variation in the surface pressure sensor, which can change +/- 0.1 mN m^{-1} due to noise and external interference. The change in the solubility of monolayer materials indicates how strong the dipole-dipole interactions at the monolayer surface can be in some materials.

9.2. Shifting Isotherms

As discussed in section 2.7, when the monolayer is compressed, the area per molecule decreases and the molecules begin to interact. This close packing of the monolayer can be monitored using surface pressure measurement; simplistically, the greater the density of the molecules, the higher the surface pressure. As the surface area is reduced, the pressure

increases until the molecules form a stable condensed monolayer. Continued compression past this point causes the monolayer to collapse into a bi-layer or multi-layer. The force required to cause the collapse of the monolayer is related closely to the forces required to encourage the coating of materials onto a substrate passed through the subphase during the Langmuir-Blodgett (LB) coating process. In LB coatings, the packing of molecules must be sufficient to enable the transfer of the material to a solid surface. Experimentally this means that the monolayer is compressed to a surface-pressure near to the point of collapse to ensure that the material is nearing the force required to lift off the subphase and on to the substrate. The point at which the best quality coating (highest coating ratio) is achieved is fixed for a given material and so the density of the coating is similarly influenced by this property [55].

If the isotherm of the monolayer material is linked both to the molecule-molecule interaction within the monolayer and the dipole-dipole interaction of the monolayer material to the subphase, then it was proposed that alteration of the molecule–subphase reaction would cause a change in the shape of the isotherm.

9.2.1. Isotherm doping

The primary route chosen to modify the potential dipole-dipole capacity of the monolayer-water interaction was to interfere with the potential of the water to hydrogen bond, both to itself and to any monolayer material. It is well understood that introduction of alcohols to water disrupts the hydrogen bonding and lowers its boiling point. This disruption is due to the interference of the hydrocarbon tails of these simple alcohols. This effect is clearest in the influence that alcohols have on the surface tension of water; concentrations as low as 10% can cause a 20 mN m^{-1} reduction in surface tension [117]. Similarly, it is also known that the hydrogen bonding potential of water can be increased by the addition of materials with greater hydrogen bonding capacity, such as hydrogen peroxide. Increasing the hydrogen bonding potential of the subphase in this manner will change the overall dipole-dipole forces at the interface between the subphase and the monolayer. Through addition of low concentrations (200 mM) of these chemicals to the subphase, their effect on the monolayer spread on the surface can be monitored.

All experiments were performed using a Nima alternate layer Langmuir trough (Type: 622). All surface pressure measurements were recorded with a Wilhelmy plate system using a pre-soaked filter paper plate. The trough was cleaned between each experiment with acetone and IPA to remove any contaminants. The trough was filled with distilled water (18 MOhms cm^{-1} resistivity). For experiments using doped subphases, the distilled water was combined

with either methanol (99.8%, Fisher), ethanol (99.5%, Sigma), 1-propanol (99.7%, Sigma) or hydrogen peroxide (30% wt. in H_2O, Sigma).

A list of the monolayer materials used is shown in Table 9.1. All of these materials are amphiphilic and will orientate in a similar fashion with their hydrocarbon chains held away from the subphase. The number of dipole interacting groups is included in this table in order to indicate the range of potential dipole-dipole interactions that each molecule is capable of with respect to the subphase. The materials were used were chosen in order to demonstrate the effect with a wide variety of hydrophilic groups.

Table 9.1: Isotherm structures
All the materials run on doped sub-phases along with the number of hydrogen bonding sites available at subphase interfering head group of the molecule.

Name	Hydrogen Bonding	Structure
Stearic Acid	2 acceptors 1 donor	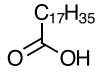
Calix[4]resorcarene (C11)	8 acceptors 8 donors	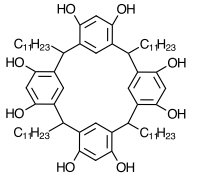
Tertbutyl (TB) calix[4]arene	4 acceptors 4 donors	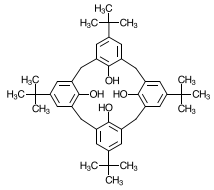
Chloresterol	1 acceptor 1 donor	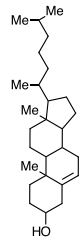
4-Hexadecylaniline	1 acceptor 1 donor	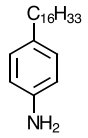
Octadecanol	1 acceptor 1 donor	

Monolayer materials were obtained from Sigma-Aldrich as detailed in section 3.5. Monolayers of each material were prepared by spreading 50 µl of a 1 mg ml^{-1} cholorofrom solution on the surface of a subphase, which consisted of either deionized water or a 200 mM solution of either methanol, ethanol, 1-propanol or hydrogen peroxide. After application, each material was left to spread for 30 mins. Isotherms were defined by slowly compressing the monolayer at 50 cm^2 s^{-1}. All stearic acid isotherms are compared in Figure 9.2, the calix[4]res C11 isotherms are compared in Figure 9.3, TB calix[4]arene in Figure 9.4, cholesterol in Figure 9.5, 4-hexadecylaniline in Figure 9.6 and octadecanol in Figure 9.7.

9.2.2. Isotherms

An isotherm contains several key sections that demonstrate certain properties of the monolayer material. As explained in section 2.7.1, the initial slow compression of a monolayer in its 'expanded' state is followed by a sharp increase in surface pressure when the material reaches its 'condensed' state. This in turn is followed by the collapse of the monolayer and, in the case of stearic acid, a plateau that represents the surface pressure at which the material continues to be pushed up into a collapsed state after the initial 'breach' in the monolayer [118].

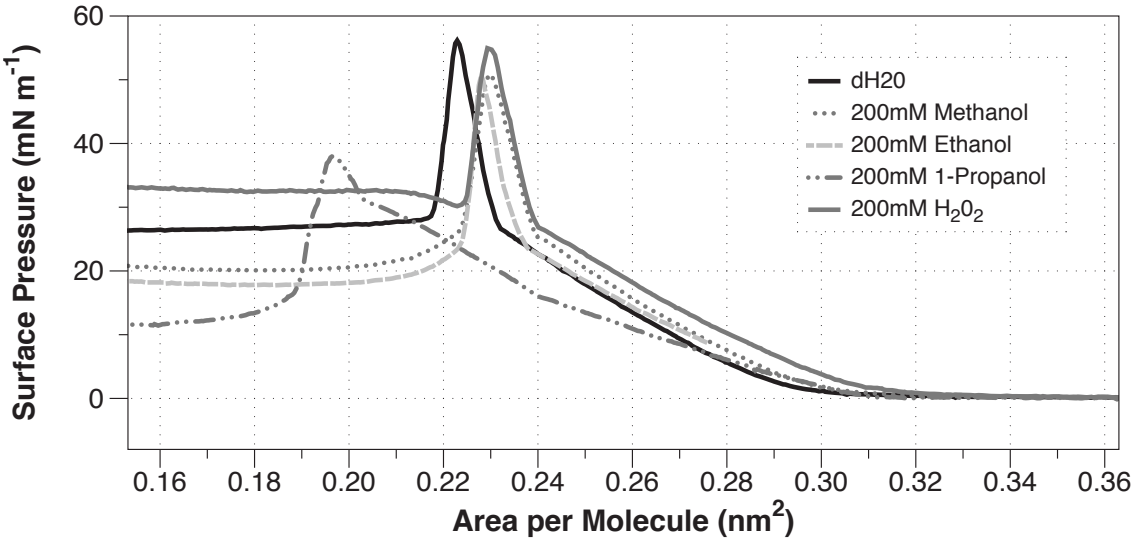

Figure 9.2: Altered stearic acid isotherms
Five isotherms undertaken on subphases containing different additives. The legend indicates the constitution of the subphase.

The stearic acid isotherms shown in Figure 9.2 produce an interesting pattern across the different types of subphase doping. The most striking difference between each subphase is that the surface pressures measured after the initial collapse of the monolayers order themselves in the manner we would expect if the collapse of the monolayer were governed by the molecule's dipole attraction to the water. As the length of the hydrocarbon tail increases, the surface pressure after the collapse decreases, with 1-propanol requiring a surface pressure of just 10 mN m^{-1} in order to continue to collapse. It can also be seen that 1-propanol has a different shaped isotherm than the other alcohol materials. It is suggested that this is because its effect on the subphase causes stability problems in the monolayer early in the compression cycle, prior to it reaching collapse.

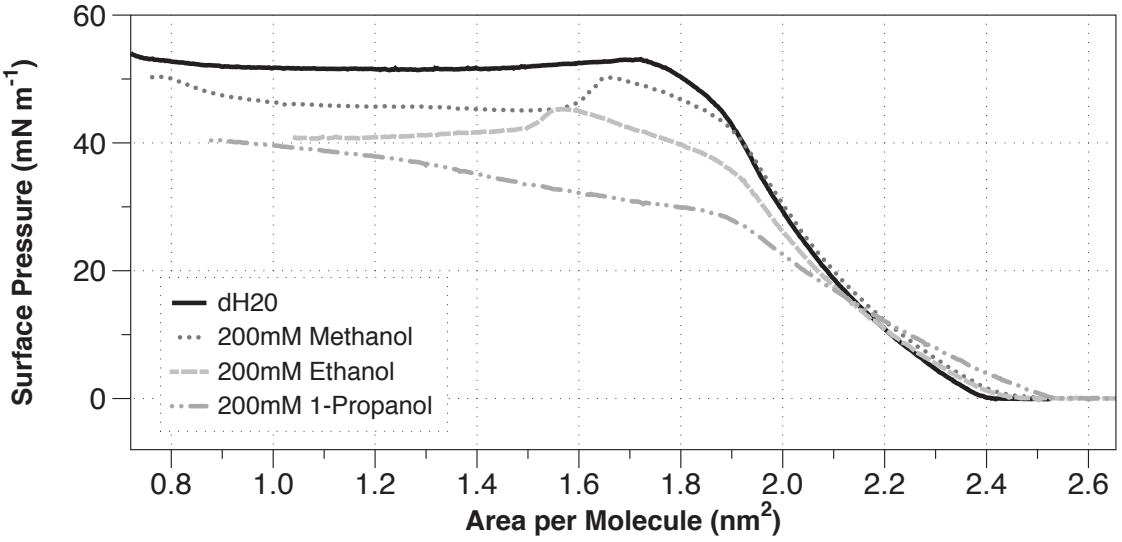

Figure 9.3: Calix[4]res C11 isotherms
Five isotherms undertaken on subphases containing different additives. The legend indicates the constitution of the subphase

The isotherms as shown in Figure 9.3 for with the calix[4]res C11 have a similar trend to those obtained for stearic acid. The isotherms of Calix[4]res C11 do not exhibit the same sharp peak in surface pressure prior to collapse. However, post collapse of the monolayer the material does show a steady plateau at the surface pressure required to lift the material from the surface into a multilayer. As for stearic acid, with the stearic acid monolayers, the surface pressure of this plateau is closely associated with the alcohol additive in the subphase. Again, the longer the hydrogen bonding interfering hydrocarbon chain, the lower the surface pressure of collapse. A monolayer was also prepared on a subphase containing hydrogen peroxide. This data is not included here, since a stable monolayer could not be achieved due to the required surface pressure exceeding the capabilities of the trough.

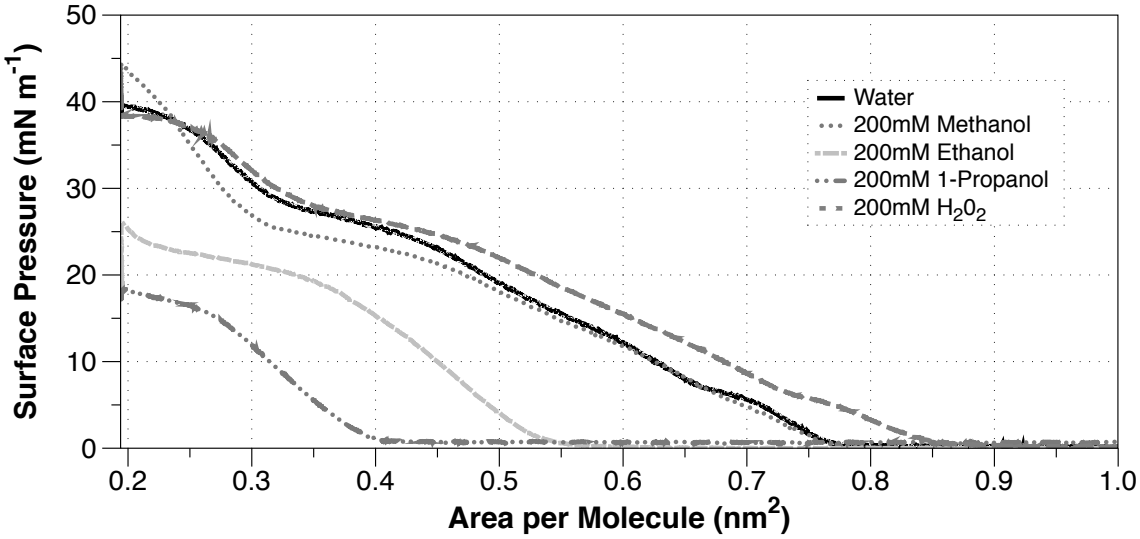

Figure 9.4: TB calix[4]arene isotherms
Five isotherms on subphase containing different additives. The legend indicates the constitution of the subphase

Unlike stearic acid and calix[4]res C11, TB calix[4]arene shows little reaction to either hydrogen peroxide or methanol, but does however show a significant change in the area per molecule when the subphase contained longer chain alcohols. The area per molecule change is likely due to the increased solubility of TB calix[4]arene in the doped subphase. Loss of monolayer material to the subphase should however only affect the position of the isotherm and not the overall shape. As before, when comparing the location of the plateau in each of the isotherms, there is a similar pattern of reduction in the surface pressure required for monolayer collapse, with an increase in the alcohol chain length.

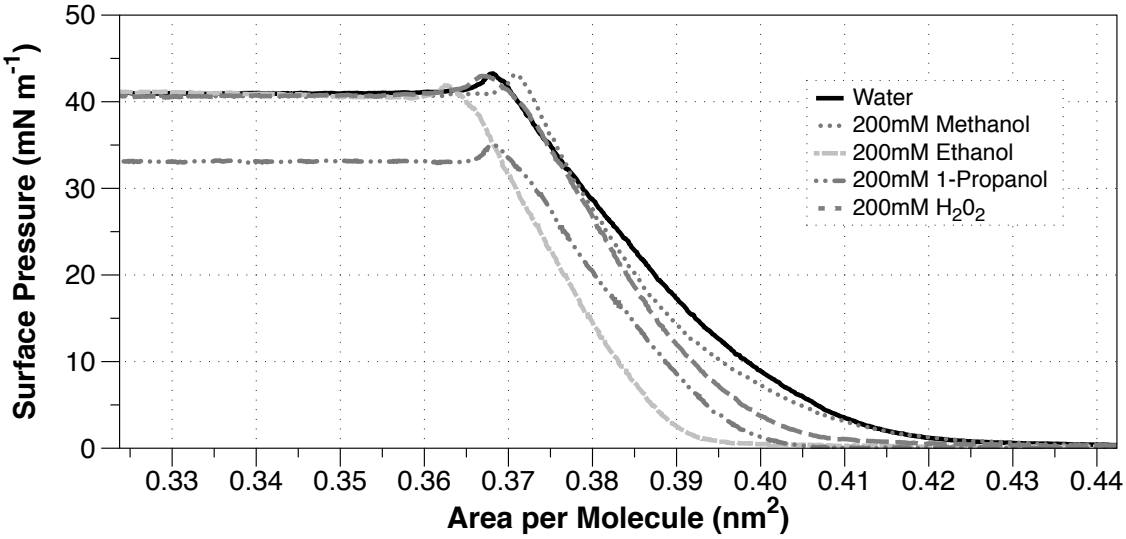

Figure 9.5: Cholesterol isotherms
Five isotherms on subphase containing different additives. The legend indicates the constitution of the subphase

The cholesterol isotherms shown in Figure 9.5 show little or no change to any subphase doping other than 1-propanol. The isotherm run on a subphase containing methanol does show some area loss but this is thought likely to be a result of experimental variation in the addition of the monolayer material. This limited reaction to the changes in the subphase is thought to be due to the relatively low dipole moment of cholesterol (1.51) when compared to stearic acid (1.76). This difference would reduce the effect of the subphase alteration on a monolayer of cholesterol.

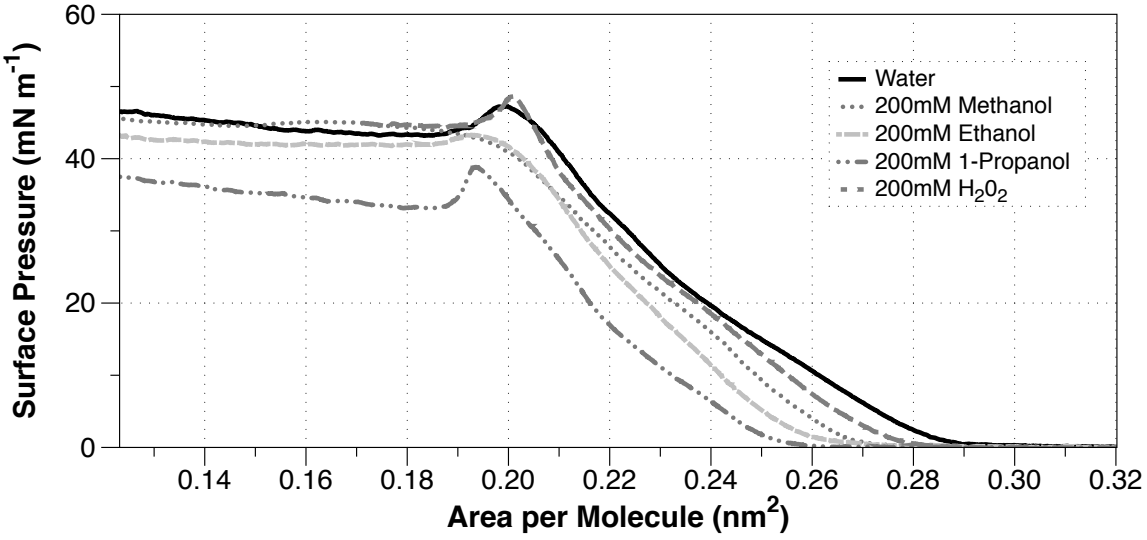

Figure 9.6: 4-Hexadecylaniline isotherms
Five isotherms on subphase containing different additives. The legend indicates the constitution of the subphase

4-Hexadecylaniline is distinctly different form the other materials as its dipole interactions with the subphase are from the $–NH_2$ group and not =O or –O-H groups. Dipole interactions with amine groups are of a lower energy than oxygen based interactions and so will form and come apart more easily. 4-Hexadecylaniline shows the same pattern of response to subphase doping, however, like cholesterol, change with shorter chain alcohols and H_2O_2 is limited, possibly due to the relatively weak interaction with the subphase.

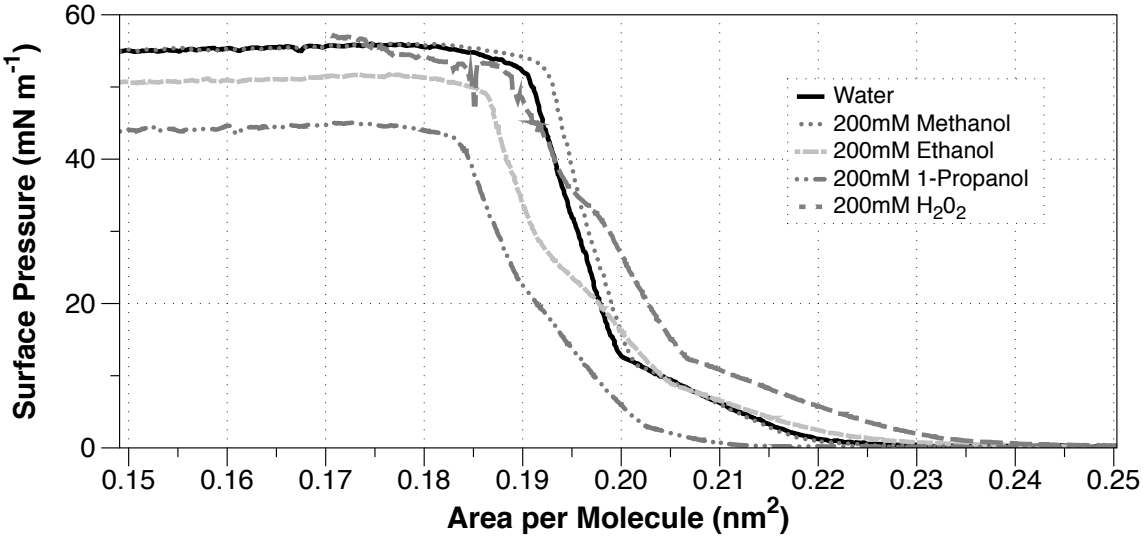

Figure 9.7: Octadecanol isotherms
Five isotherms on subphase containing different additives. The legend indicates the constitution of the subphase

The octadecanol isotherms contain a number of features that show a decrease in surface pressure with the introduction of alcohol to the subphase. After the initial shallow slope, the isotherm rapidly increases in surface pressure (at around 0.2 nm^2 with water). As predicted, the point at which this rate of increase occurs changes with increase in alcohol chain length. However, when the final plateau position is considered, it can be seen that only methanol and 1-propanol are substantially different from water. There is no clear difference between an H_2O_2 doped subphase and a water subphase.

The results presented here show both the strength of the dipole-dipole interaction between monolayers and an aqueous subphase, and the potential for modification of this interaction. This modification of the monolayer's properties through the addition of alcohol shows a clear trend, with a reduction in the dipole moment and in the hydrogen bonding potential of the material. The reduction of the hydrogen bonding potential changes the interaction of the monolayer material with the subphase and allows the release of the material at a lower surface pressure without altering the overall shape of the isotherm. This shift means that the density of the material is lower, which in some applications is desirable in order to obtain the optimal packing that may be application dependent. However, it has also been shown that

the degree or sensitivity to the modification of this interaction varies between materials. It is suggested that this is either due to properties conferred by the interacting tail groups of the monolayer materials or, as suggested in this data, it may be linked to the degree of the interaction between the material and the subphase.

Though not as well characterized, it has also been demonstrated that the packing density can potentially be increased by increasing the dipole forces acting on the monolayer through the addition of hydrogen peroxide. Increasing the density of coated molecules is often desirable in sensing applications [1], since the number of sensitive molecules directly corresponds to the saturation point of a given sensor system. As hydrogen peroxide has a relatively small effect on the subphase when compared to alcohol doping, further work is needed to look at the effect of higher concentrations.

9.3. Doped subphase solvent drops

As indicated in section 9.1 the strength of the dipole-dipole interaction is such that it can affect the solubility of the monolayer material. As will be shown in Chapter 10, this relationship can be manipulated in order to lower the energy required to 'lift-off' the monolayer material. The final stage of this work was to re-visit the solubility experiments and examine the effect of additives to the subphase on the solubility of the monolayer materials.

As described in section 9.1, a monolayer of calix[4]res C11 was prepared by spreading 100 µl of a 1 mg ml^{-1} solution, in chloroform, onto a range of doped subphases. The monolayer was compressed to 20 mN m^{-1} before adding drops of chloroform. Calix[4]res C11 was used as it had previously shown no solubility in chloroform on a water subphase. Monolayers were prepared on subphases consisting of 200 mM, 400 mM 1-propanol as well as a deionised water control. The results for each of these subphases are shown below in Figure 9.8.

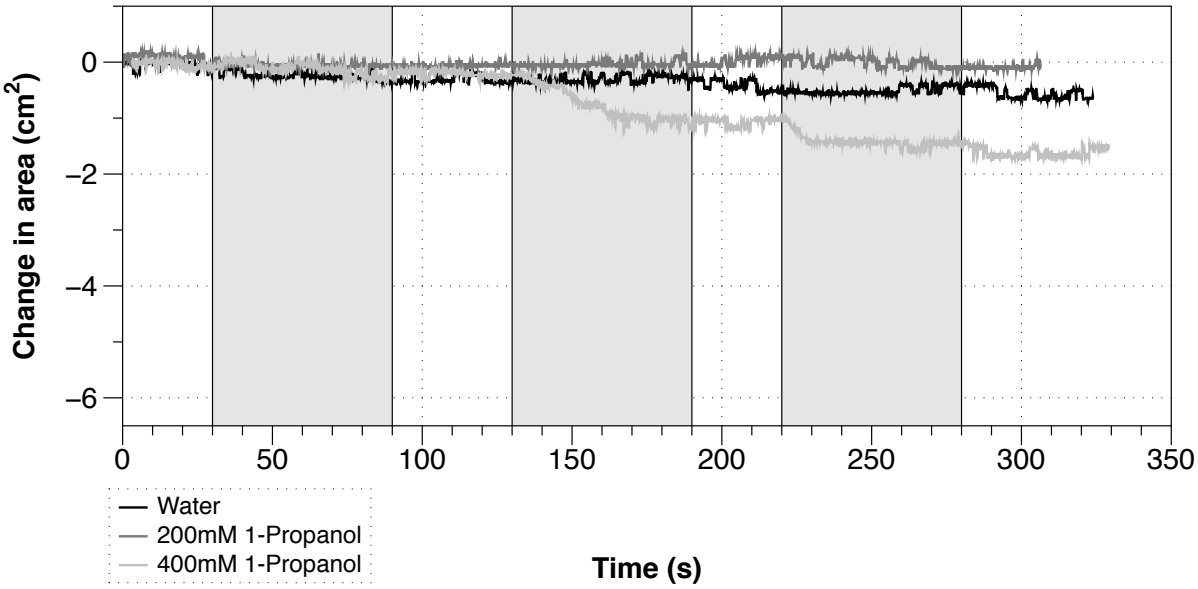

Figure 9.8: Calix[4]resorcarene C11 monolayer solubility with 1-propanol doped subphase
The presence of the chloroform drop on the monolayers is show by the gray bands

As before (section 9.2), a monolayer of calix[4]res C11 spread on a water subphase showed no reaction to the addition of drops of chloroform (Figure 9.8). There was also no observable change with 200 mM 1-proanol. However, 400 mM 1-propanol showed some change that appeared to relate to the addition of chloroform drops to the surface. Of the three drops added to the monolayer spread of 400mM 1-propanol, two showed a related drop in surface area. It is not clear why only 2 out of 3 chloroform drops showed a loss in area however; it is likely that the small area loss (relative to stearic acid) is because 400 mM 1-propanol only allows for partial solubility. Despite this small reaction, the result is interesting and supports the theory that sub-phase additives can be used to weaken the dipole-dipole interaction of monolayers.

Chapter 10 Langmuir coating conditions

As discussed in section 2.7.2, the coating speed and pressures used to form LB films need to be optimised before a repeatable coating can be achieved. The previous work [1] used parameters originally derived from work carried out at Sheffield University [77], which had studied extensively the coating characteristics of calix[4]res C11, along with other calixarenes. However, when researching these parameters for use in this project it was discovered that the figures from the original work had been misinterpreted. The original paper [77], indicated that calix[4]res C11 forms only Y-type bi-layers when coating with a surface pressure of 40 mN m^{-1}; this figure was determined from work carried out by the same group but the results are not presented. However, further work by the same group, presented in Hassan 1999 [33] and Topliss 2010 [1] cite this paper as evidence of bi-layer formation at lower coating pressures of 25 to 35 mN m^{-1}. The only conclusion that could be drawn from this is that previous parameters could not be relied upon and each calixarene should be fully assessed for its optimum coating properties.

10.1. Sample coating

In order to examine changes in the coating method, the first step was to determine the basic coating conditions previously used. Coating conditions were assessed for 3 monolayer forming materials, calix[4]res C11, TB calix[4]arene and stearic acid. For each material, the trough was prepared according to the standard procedure (section 3.1). Each material (made up in chloroform) was applied to the surface of the trough, allowed to spread for 30 mins and compressed to the appropriate surface pressure. Once at pressure each film was left for 1 hour in order to ensure that it had stabilised. Between each run the trough was emptied and cleaned according to the standard method.

The surface used for coating was a single silica glass capillary tube, which had been sealed at both ends. The capillary tube (diameter 2 mm) was mounted on to the LB dipper and positioned to allow for a 32 mm long section in the middle of the tube to be coated; the tube had a total coated surface area of 2.01 cm^2. Prior to coating and in between each coating experiment, the capillary tube was cleaned ultrasonically in de-ionised water and 50% ethanol for 10 minutes and wiped repeatable with clean room filter paper soaked in chloroform. For each dip, the capillary tube started in the submerged position and was moved through the monolayer at a rate of 15 mm min^{-1}. The results for each monolayer material are shown below in Figure 10.1, Figure 10.2 and Figure 10.3.

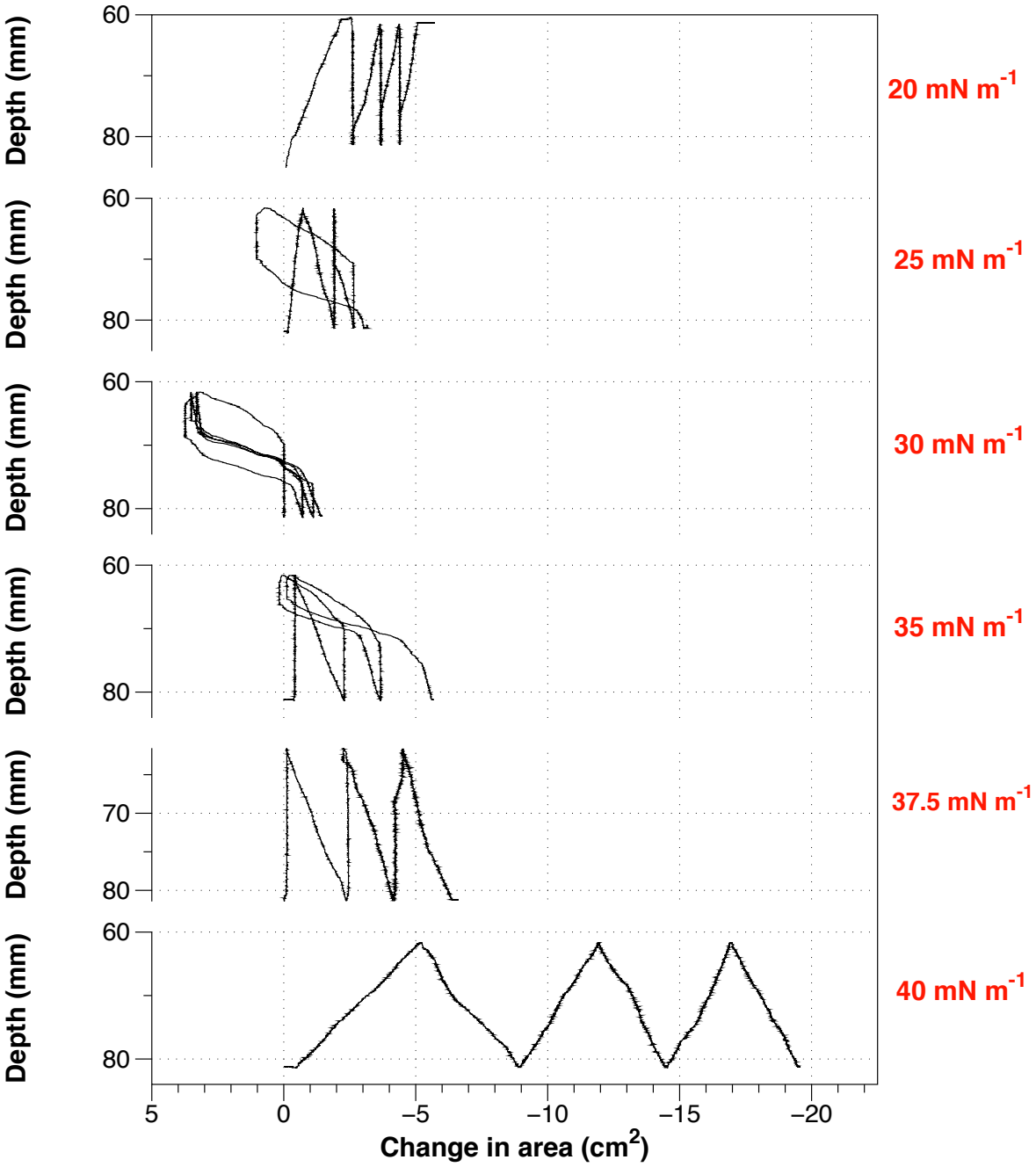

Figure 10.1: Coating of calix[4]res C11
Calix[4]res C11 dip profiles at 20, 25, 30, 35, 37.5 and 40 mN m^{-1} onto a glass capillary tube. Initial capillary tube position was submerged in the subphase.

As shown in Figure 10.1, calix[4]res C11 shows poor coating at surface pressures lower than 35mN m^{-1}. This poor coating is typified by unevenly spaced area changes with each successive layer and sudden gains in surface pressure as the coating detaches from the substrate. This cut off of >35 mN m^{-1} agrees with previously published data by Davis *et al.* [77], and not value referenced by Topliss *et al.* [1]. The coating study presented here goes further than Davis *et al.* [1] and studied lower surface pressures (20 – 30 mN m^{-1}), which appears to show both coated monolayer degradation with sudden jumps in surface area and

more notably the formation of X-type coating on the down stroke only at 20 mN m^{-1}, which has not been previous observed. For the purposes of sensor preparation however, further work will focus on the higher surface pressure range.

Given the total coatable surface area of 2.01 cm^2 (+/- 0.01cm), it is interesting to note that, from the area loss, we can calculate that at 40 mN m^{-1} there is approximately a 160% transfer ratio of material to the surface. It has been observed previously that at high pressure, calix based monolayers take time to find their equilibrium position/state. This means that the initial area loss may be a result of an over reaction of the barriers to the loss of monolayer material. The true transfer ratio is likely to be less than 100%.

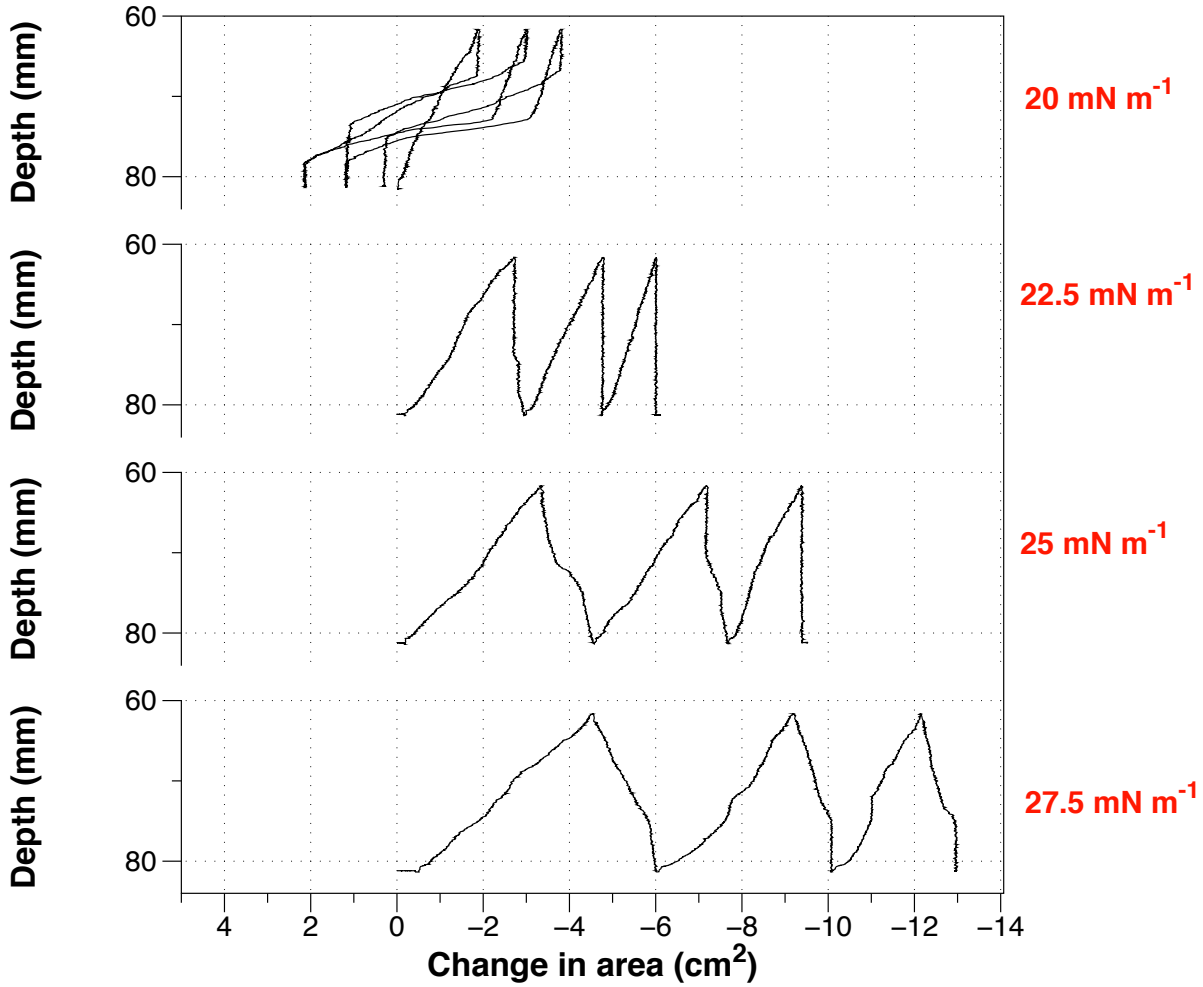

Figure 10.2: Coating TB calix[4]arene
TB calix[4]arene dip profiles at 20, 22.5, 25 and 27.5 mN m^{-1} onto a glass capillary tube. Initial capillary tube position was submerged in the subphase.

TB calix[4]arene shows coating at lower surface pressures than calix[4]res C11, which may be predicted from the difference in isotherm shape (section 5.1). At all surface pressures (excluding 20 mN m^{-1}), there is an higher degree of coating for the first layer of material. This

may be an artefact of the monolayer stabilising with the loss of material, or potentially an increased binding of the TB calix[4]arene directly to the substrate.

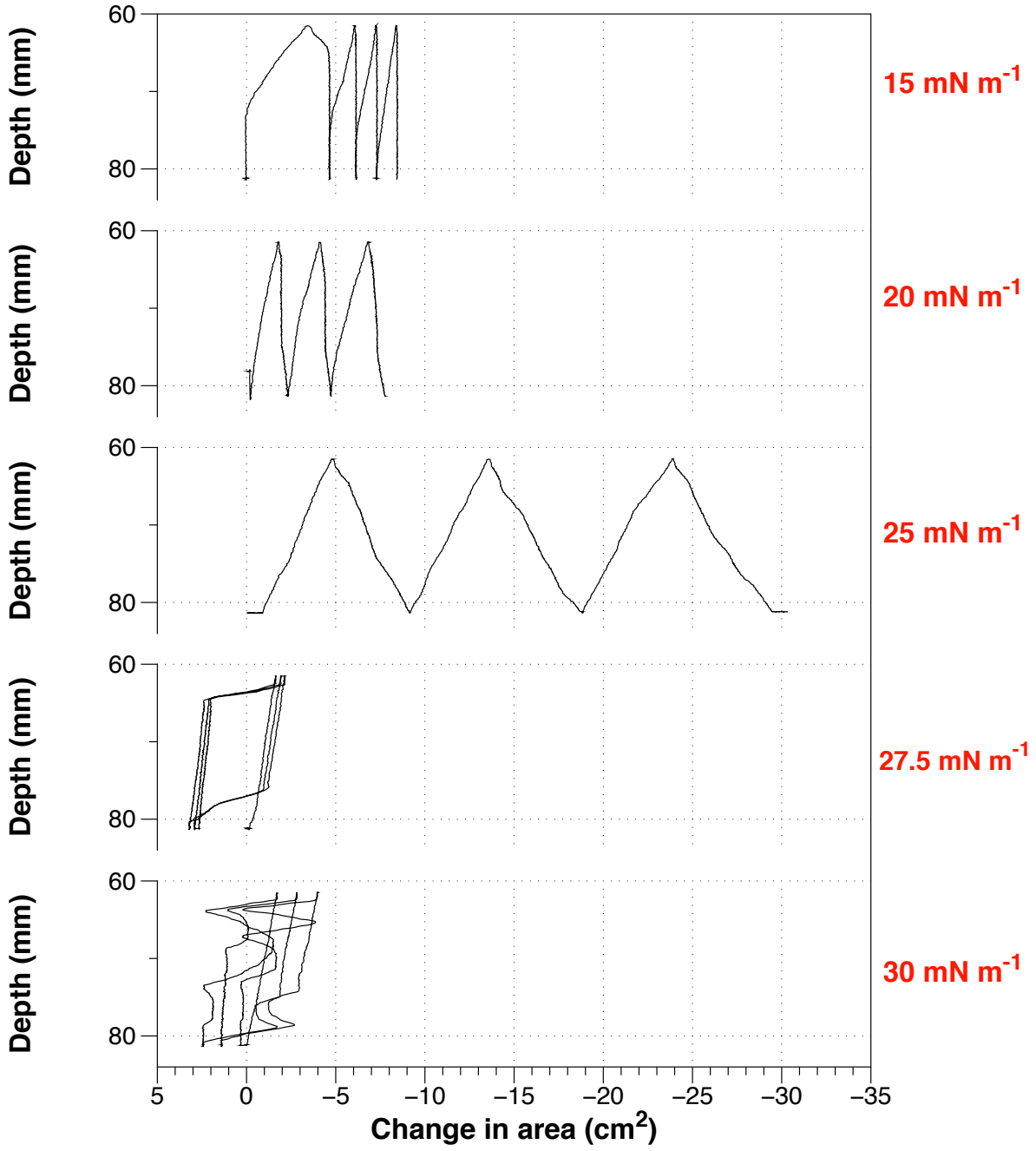

Figure 10.3: Coating stearic acid
Stearic acid dip profiles at 15, 20, 25, 27.5 and 30 mN m^{-1} onto a glass capillary tube. Initial capillary tube position was submerged in the subphase

Stearic acid coating has a cut off at 25 mN m^{-1}; coating at surface pressures greater than this produces little to no coating onto a glass substrate. Unlike both calix[4]res C11 and TB calix[4]arene, stearic acid shows little 'build up' to its optimum coating pressure (25 mN m^{-1}), and there is no clear difference in coating quality between 15 and 20 mN m^{-1}. This appears

to indicate that successful coating of stearic acid only occurs at the change between a liquid and solid monolayer phases (Chapter 5). At 25 mN m^{-1}, stearic acid is coating with a 200% transfer ratio. Like calix[4]res C11, this could be related to film instability. Stearic acid also shows none of the initial coating differences seen in the calix-based materials. This could be because of the calix specific monolayer stabilisation or simply related to the chemistry of the substrate-monolayer interaction. More commonly, stearic acid at higher surface pressure is achieved with dissolved salts (such as cadmium chloride), which stabilises the stearic acid [119].

10.2. Solvent enhanced coating

Once of the key outcomes of study of the alteration of the dipole-dipole interaction presented in Chapter 9 was the potential of using the technique to alter the coating conditions of a monolayer material. Using the same protocol as described in section 10.1, dip profiles for calix[4]res C11 and stearic acid were prepared using a subphase containing 200mM EtOH. 200mM EtOH was chosen as it produced a change in the shape of the isotherm, but the change was not as significant as that caused by 1-propanol, which altered both the position and shape of the isotherms. The dip profiles at each of the surface pressures tested are shown in Figure 10.4 and Figure 10.5, with the data being presented alongside the data from the section 10.1 in order to show the changes in coating conditions.

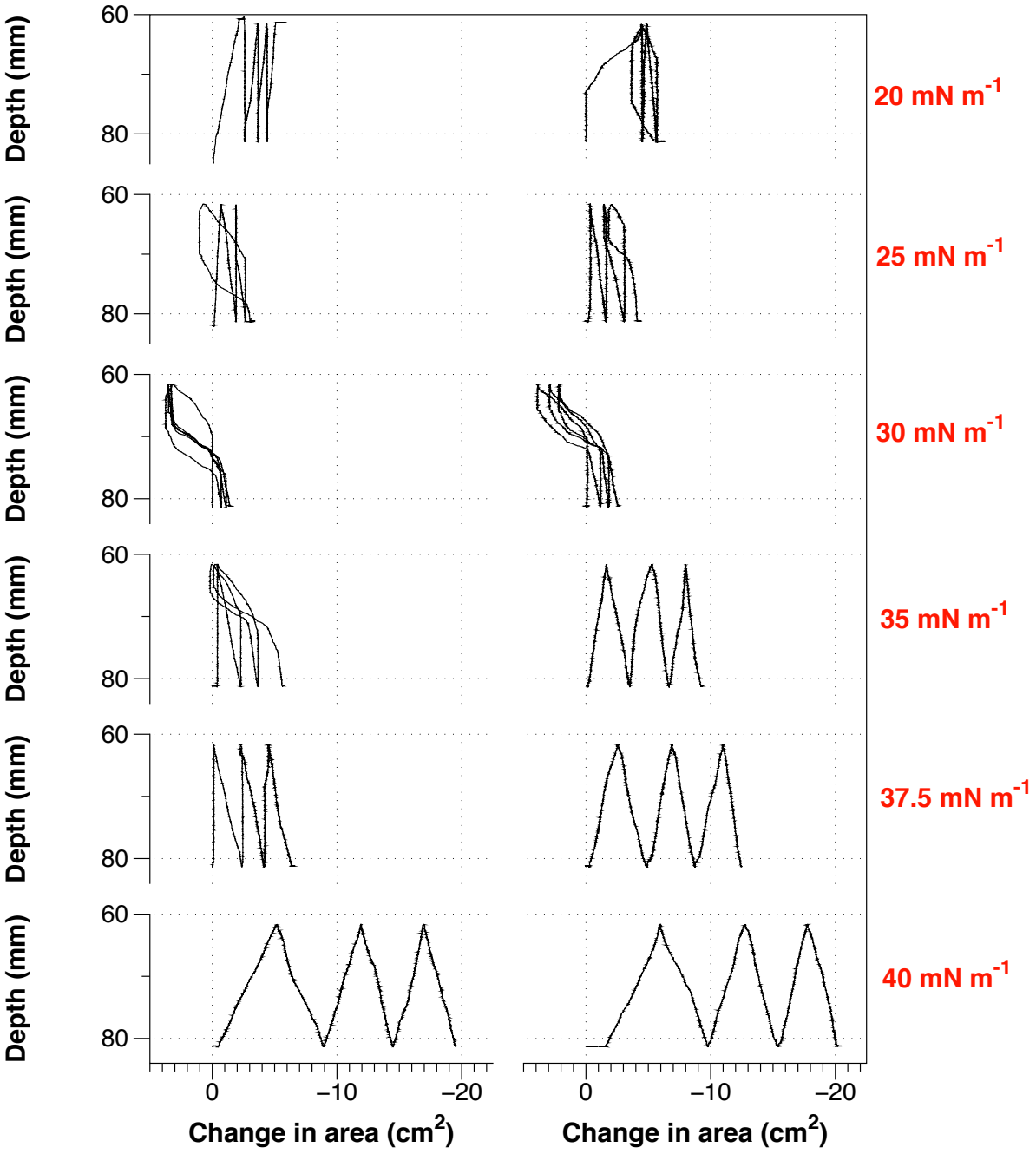

Figure 10.4: Calix[4]res C11 coating with (right) and without (left) EtOH
Calix[4]res C11 dip profiles at 20, 25, 30, 35, 37.5 and 40 mN m^{-1} on a subphase containing 200 mM EtOH (left) and a subphase of pure water (right) onto a glass capillary tube. Initial capillary tube position was submerged in the subphase.

Calix[4]res C11 shows a marked change when comparing the coating profiles obtained with water and 200 mM EtOH substrates. At 35 mN m^{-1}, there is a 90% transfer ratio of the calix[4]res C11 to the substrate on both the up and the down stroke, compared to 0% on the upstroke and 90% (with occasional loss) on the downstroke on water. This difference in coating may be predicted by considering the shift in isotherms (seen in Chapter 9).

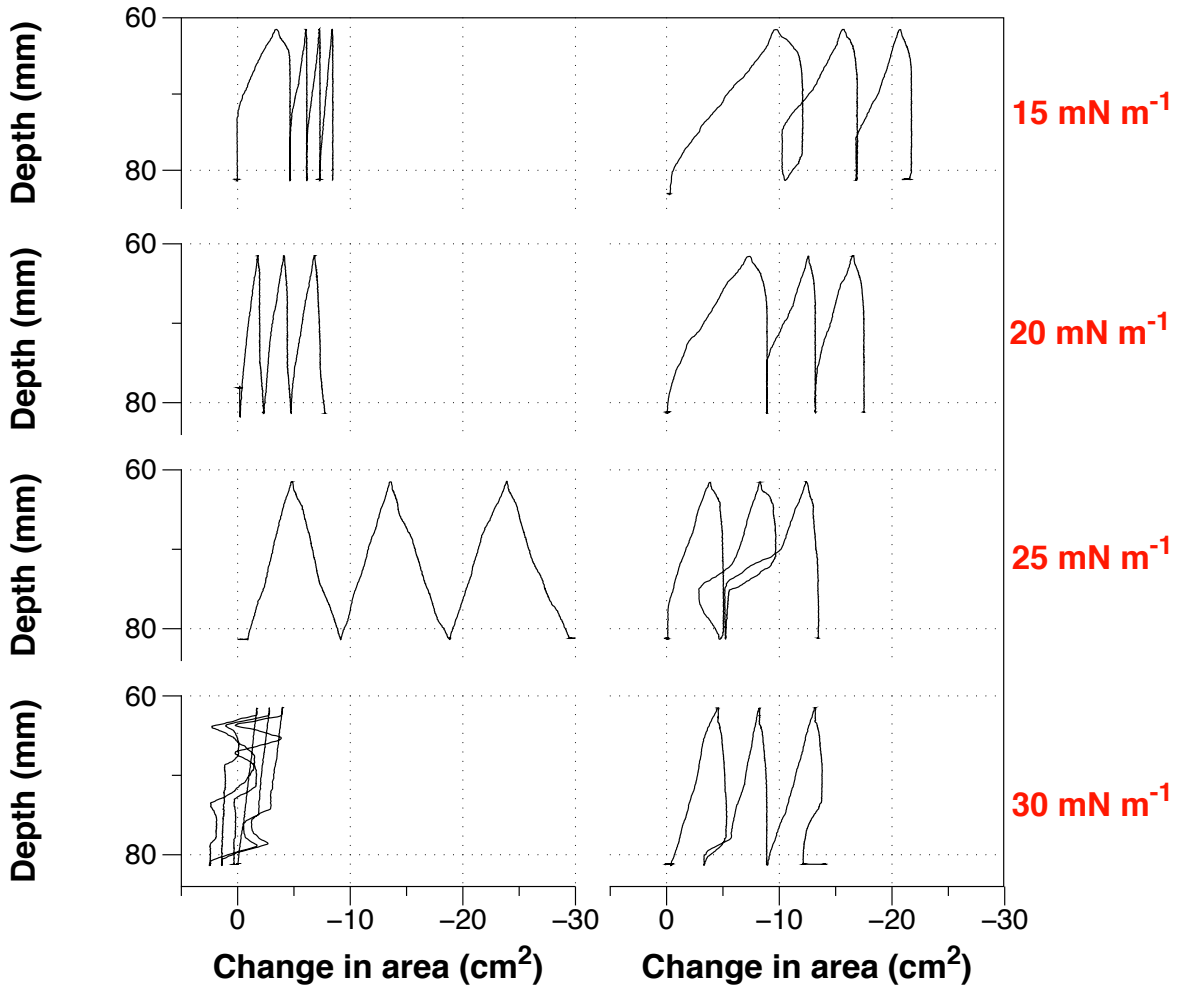

Figure 10.5: Stearic acid coating with (right) and without (left) EtOH
SA dip profiles at 15, 20, 25 and 30 mN m^{-1} on a subphase containing 200 mM EtOH (left) and a subphase of pure water (right) onto a glass capillary tube. Initial slide position was submerged in the subphase

Stearic acid (Figure 10.5) does not show a clear change in coating properties for the two subphases. Rather than only coating at 25 mN m^{-1} in water, stearic acid on 200 mM EtOH appears to coat best at lower pressures and there is a clear trend in the degradation of this coating with increasing surface pressure. Interestingly, the coating is not as unifrom at 15 mN m^{-1} as the best coating achieved on water (25 mN m^{-1}) and it may be that the ideal coating from a 200mM EtOH subphase is actually achieved at pressures less than 15 mN m^{-1}. Ideally the range of this experiment should be expanded.

10.3. Fibre optic coating

The dip profiles described in section 10.2 provide a simple method of assessing coating quality and, as discussed, show clear changes with subphase modification. However, it is also possible to monitor the coating properties of a material through its interaction with a fibre optic device. There are two types of fibre optic device used in this work; long period gratings (LPGs) and tapered optical fibres. Both devices have a sensing region approximately 2 cm in length, located in the middle of a 60 cm length of optical fibre. In tapered fibres the sensing region is defined as being the section of the fibre that has undergone tapering, this includes the 'cone' shaped tapering regions. In LPG fibre the sensing region is defined as the section of the fibre that has undergone modification and contains the LPG. The fibres were provided by Renata Jarzebinska and Rebecca Wong from the Department of Engineering Photonics. The process used for coating optical fibres in the trough is similar to that described for the capillary tube; the optical fibre was mounted on a cross bar that held the fibre at 90 degrees to the surface of the water. The fibre was held by two small screws, approximately 6 cm apart, mounted on the cross bar. The cross bar was then attached to a Nima alternate layer dipping rig which is able to move the fibre straight up and down through the monolayer's surface (Figure 3.3). The free ends of the fibre were connected to a tungsten-halogen bulb light source and spectrophotometer, which were used to facilitate the monitoring of the transmission spectrum throughout the coating experiment.

Once mounted, the fibres were left in place for several dipping experiments and were wiped with acetone and IPA between each coating run. Each fibre was coated using the same methodology as described in section 10.1, with minor variations as described for each sensor.

10.3.1. Tapered fibres

A 6 µm diameter tapered fibre was mounted in the trough as described and filled with water. The trough was then spread with 10 µl of 2 mg ml^{-1} calix[4]res C11 which was allowed to equilibrate for 30 mins before further manipulation. The monolayer was then compressed to 30 mN m^{-1} and allowed to stabilise for 2 hours. This pressure was chosen as it is the coating pressure used in [1], and for this first set of vapour sensing experiments it was important to show that the previous work [1] could be repeated.

The fibre was coated with 15 cycles (one cycle consists of up and down coating) of calix[4]res C11 at a speed of 15 mm s^{-1}. During this process, the transmission spectrum of the fibre was recorded at the top (in air) and bottom (in water) of each dipping cycle. Due to

the change in the refractive index of the surrounding medium, the transmission of the fibre changes significantly between water and air. This change is not related to the coating of the fibre however, to avoid any discrepancy when processing data, only the transmission spectra recorded in air were analysed.

In order to examine the coating quality, three peaks from the transmission spectra in the wavelength range from 800 to 950 nm (Figure 10.6) were selected and their position and intensity was recorded on every cycle (Figure 10.7). Only three peaks were tracked, because the data was sorted manually and each peak took time to sort from the other peaks in the data.

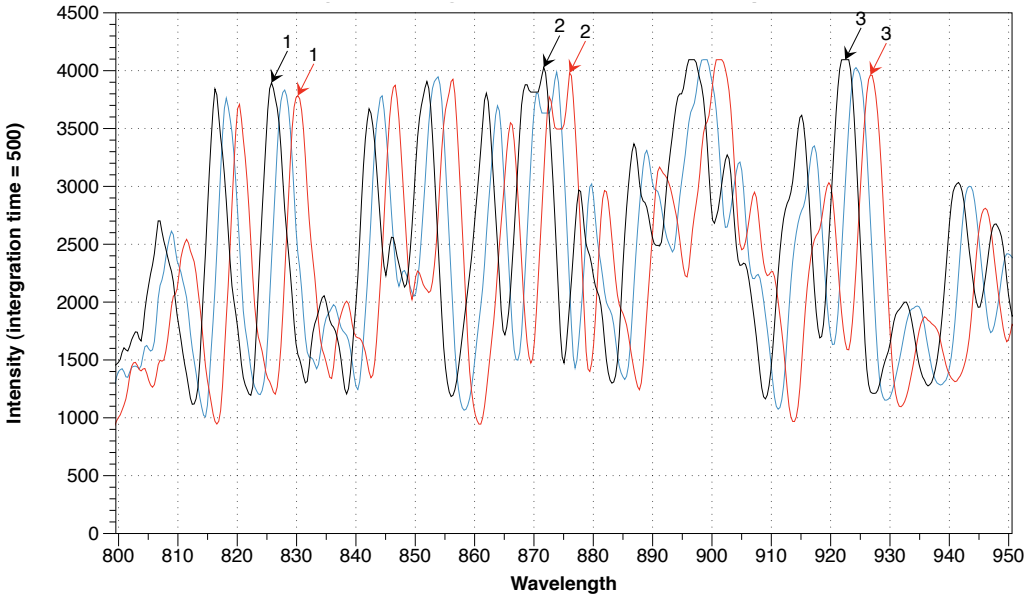

Figure 10.6: Progression of the transmission signal during coating with 15 coating cycles of calix[4]res C11
The graph above is a plot of 3 transmission spectra taken at the beginning (black), middle (blue) and end (red) of the coating process. Highlighted are 3 peaks that were tracked to demonstrate the progression of the signal between each coating.

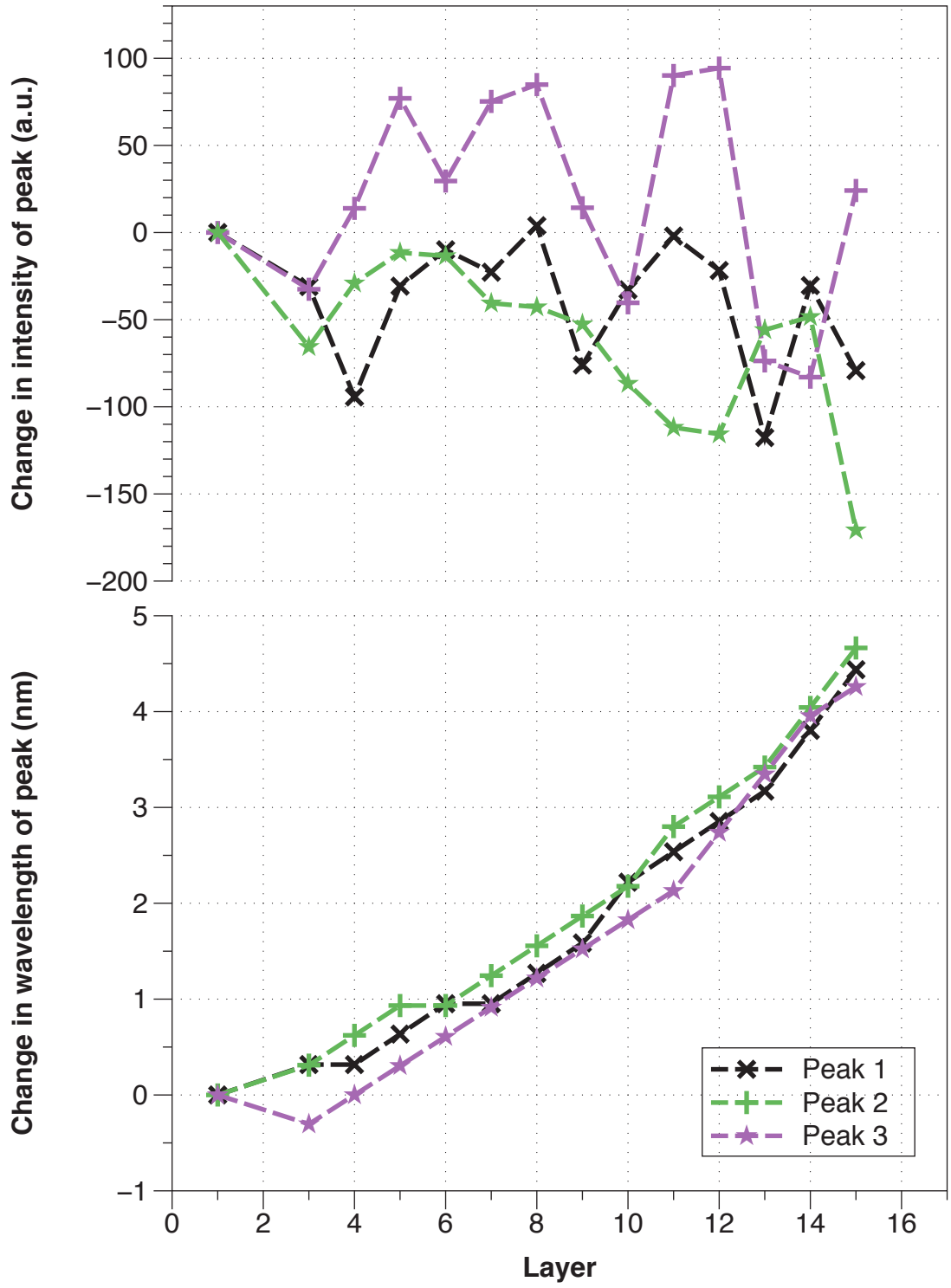

Figure 10.7: Tracking the intensity and position of 3 peaks during 15 coating cycles with calix[4]res C11
The top graph shows the change in the intensity of each peak with each layer. The bottom graph shows the overall change in the wavelength position of the peak with each layer.

As the coating layers build up there is a clear change in the position of the transmission peaks. The shift in the peaks is a result of a change in the phase of the interference of the modes propagating in the tapered region, as reported in [108]. This confirms that the chosen coating method is depositing a measureable amount of material on the surface. This initial

coating experiment demonstrates that calix[4]res C11 can be deposited on the surface of a fibre and cause a change in the spectra.

In order to improve on the results from the 15 cycle coating described above, the fibre was wiped using optical tissue soaked in acetone and then IPA, the experiment above was then repeated with 30 coating cycles. The data from this experiment was processed using upgraded software (see section 3.2.1), which allowed analysis of multiple peaks; the output from this software is shown in Figure 10.8 along with the first spectra, this data is then compared in Figure 10.9.

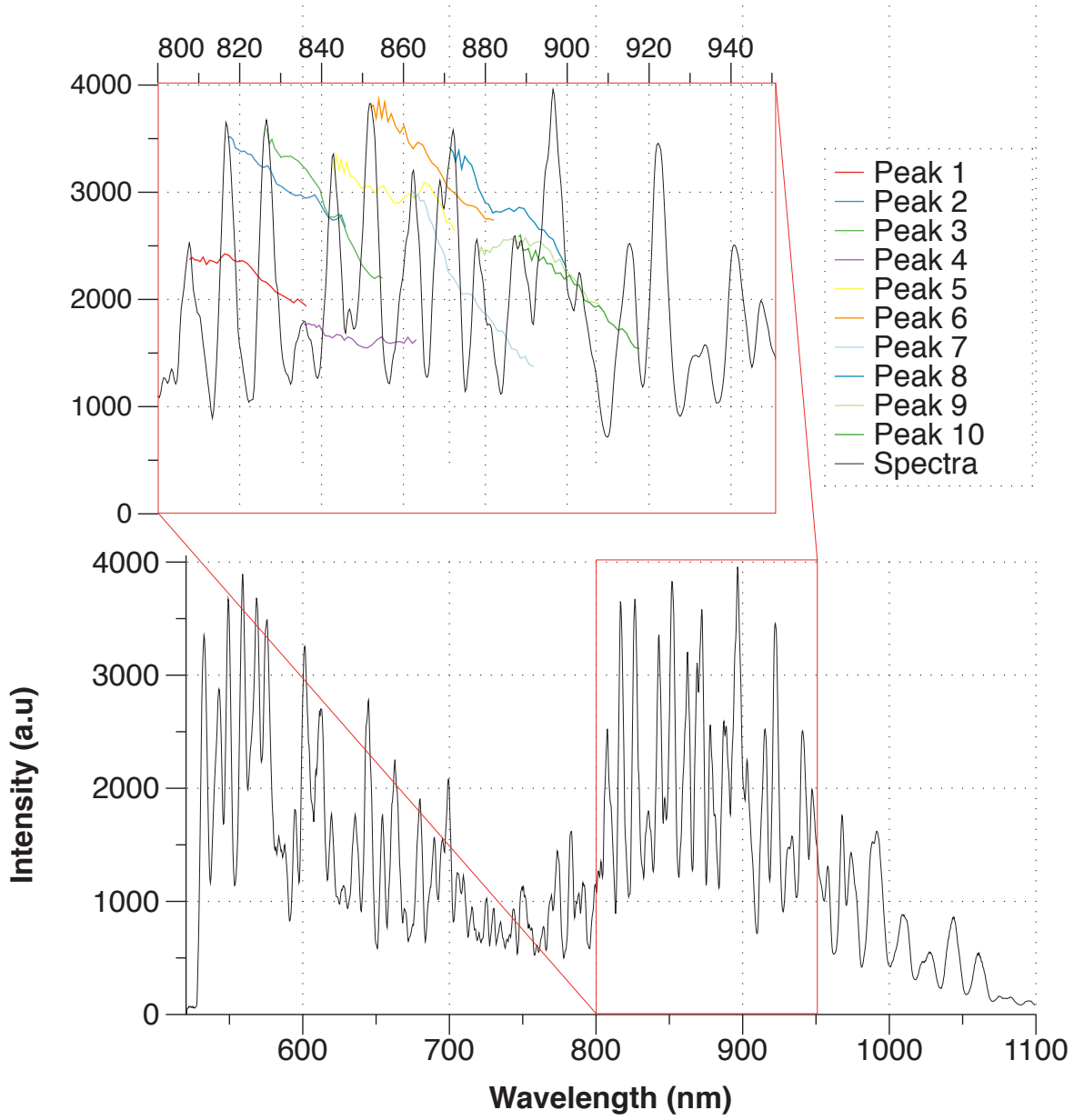

Figure 10.8: Full spectrum plot of the 30 cycle coating of calix[4]res C11 on a 6 µm diameter 20 mm long tapered fibre
The above plot is the full transmission spectrum recorded before the first layer was coated on to the 6 µm fibre. The magnified section shows the 10 peaks tracked and the evolution of those peaks during the coating process.

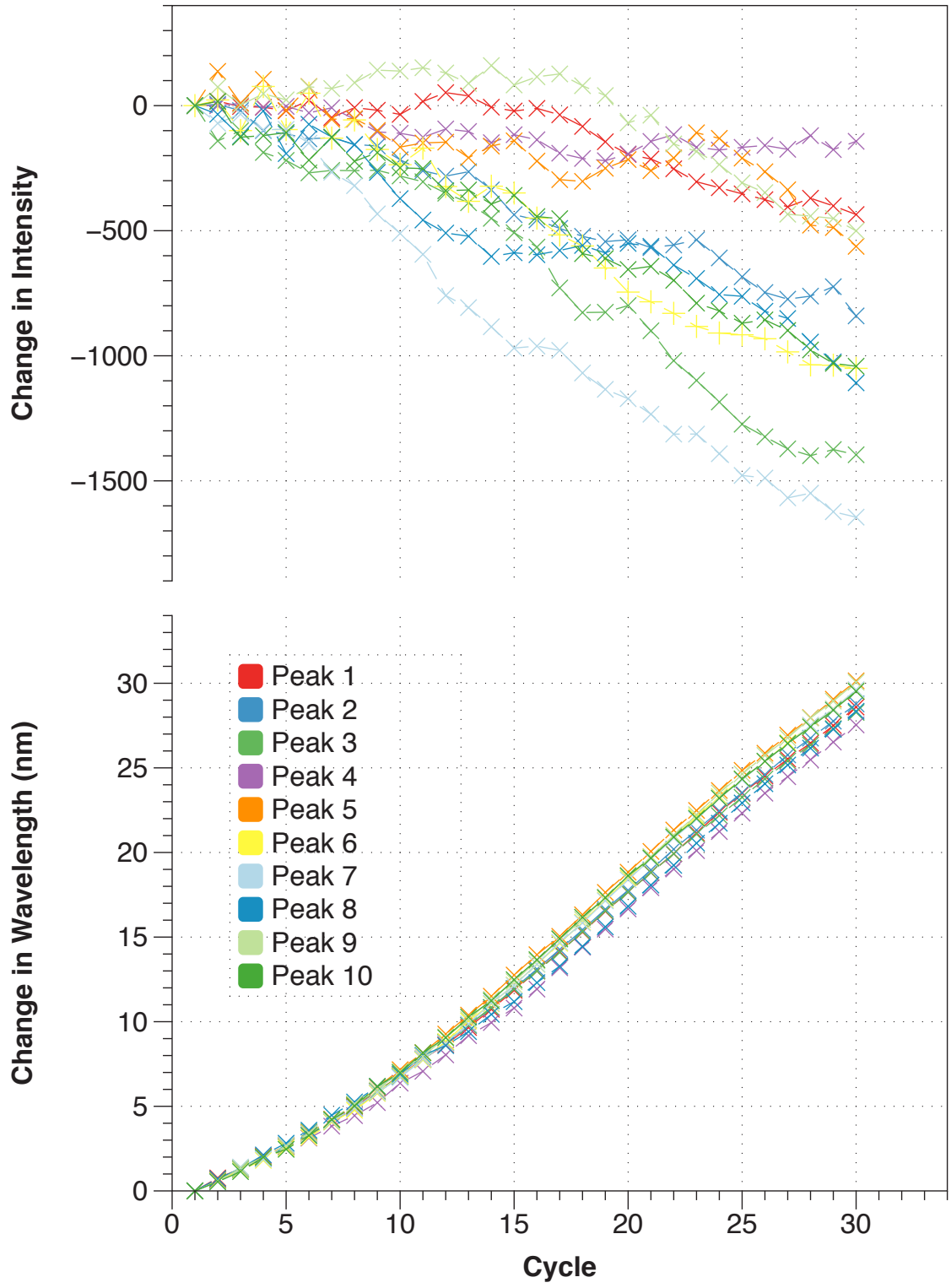

Figure 10.9: Tracking of the peak intensity during 30 cycle coating with calix[4]res C11
This figure shows a summary of the data collected from tracking the intensity (top) and the wavelength (bottom) of 10 peaks.

As with the 15 cycles coating, there is a clear shift in the wavelengths of the peaks during the coating process. Additionally, there are signs of an overall reduction in the intensity of the transmitted light, although this is not visible in all tracked peaks. This intensity reduction

matches previous work with coated tapered fibres [109] and is not thought significant enough to reduce the sensitivity of the fibre to vapours.

This work demonstrated that, despite the poor coating obtained at a pressure of 30 mN m^{-1} in section Figure 10.1, there is consistent monolayer build up on the surface of the sensor at this pressure. It would have been interesting to expand this work. However, tapered sensors are very fragile due to their size, and frequent manipulation for multiple coating runs often causes defects and cracks to appear in the fibre structure creating artifacts in the results or even in some cases the breakage of the fibre. For example, after the work shown in Figure 10.9 the sensor broke whilst being cleaned. This fragility makes it hard to compare coatings without also factoring sensor-to-sensor variation in to the data. In order to avoid this problem all further coating work was carried out using LPGs, which have significantly increased tensile strength when compared to tapered sensors.

10.3.2. Coating LPG sensors

Unlike tapered fibre sensors, LPGs need refining to the particular application. As discussed in section 2.5, LPG sensors consist of a periodic modulation of the refractive index of the core of the optical fibre that promotes modes from the core to the cladding. The high attenuation of the cladding modes results in a series of attenuation bands in the transmission spectrum of the fibre. The period of the grating determines the cladding mode to which light is coupled, where each cladding mode has a different sensitivity to the surrounding enviroment. These first experiments in coating focused on determining the best LPG grating period to use in conjunction with the calix coating.

Previous work by Topliss *et al.* [1] used an LPG with period 180 μm, which produced a phase shifting effect in the transmission spectrum during coating. This phase shifting is not ideal in sensing applications as it can limit the maximum sensitivity of the sensor. In order to avoid this problem the first sensor chosen within this work had a period of 100 μm; this would act as a baseline from which the sensor could be fine-tuned in order to gain the greatest sensitivity.

The fibre and trough were mounted and prepared as discussed in sections 10.2 and 10.3.1. The fibre was then coated with 500 layers (250 cycles up and down through the monolayer) of calix[4]res C11 at a speed of 15 mm s^{-1}. During this coating process, the transmission spectrum of the fibre was recorded at the top (in air) and bottom (in water) of the dipping cycle. As in the previous experiments on tapered optical fibres only the spectra recorded

with the coated section in air were assessed. The data from this experiment was prepared into a grey scale plot shown in Figure 10.10.

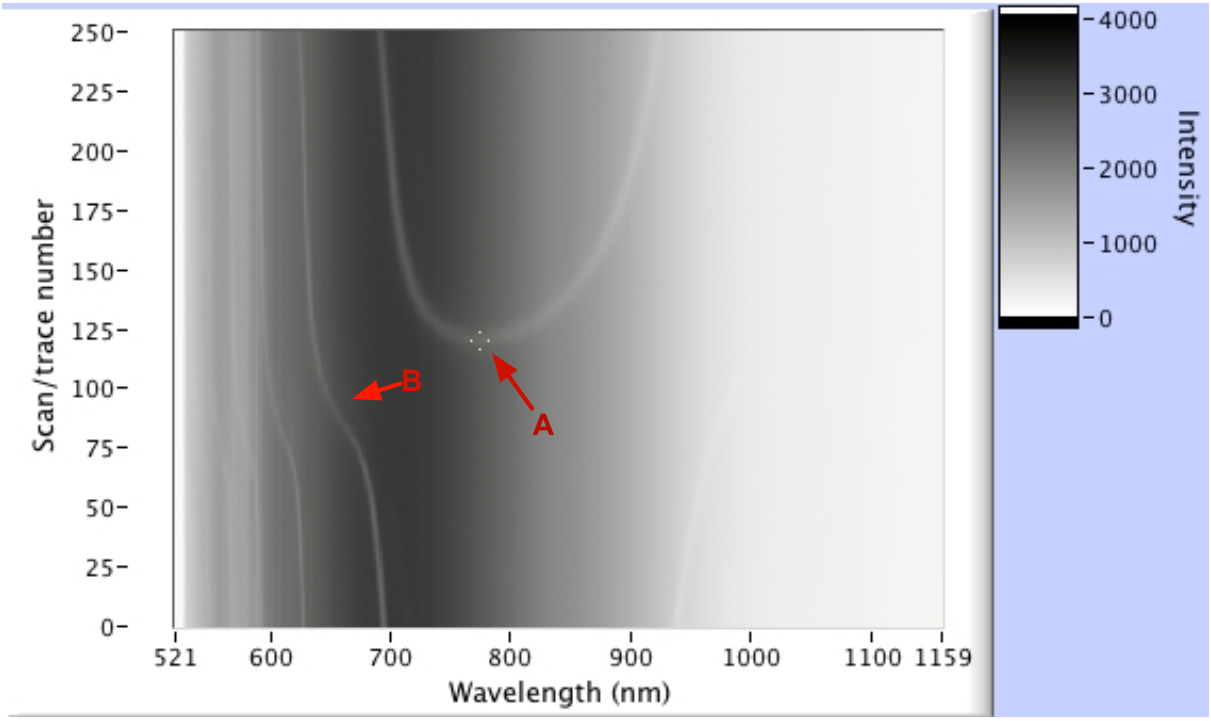

Figure 10.10: Gray scale plot of coating a100 µm LPG
A gray scale plot of the coating with calix[4]res C11 at 30 mN m^{-1} over 250 cycles (only the 'air' scans are shown). The yellow cross is positioned at the apex (A) of the modal change and is located at layer 120 (B).

The white bands in the above gray scale plot show the movement of the resonance bands in the LPG transmission spectrum in response to increasing coating thickness. The critical point for sensing is the point at which the two peaks appear and begin to separate, shown in this gray scale plot as the U shape that beings at layer 120 (figure calculated as described in 3.2.1). Ideally the coating process would be stopped at this start of this U shape (A in Figure 10.10) and any response of the film to external conditions would cause these peaks to move in a similar manner to continued coating. This is the same sensing method used by Topliss *et al.* [109] and numerous other LPG based sensors systems [120]. Ideally, the start of the U shape should correspond to the number of layers required for the mode change (B in Figure 10.10) seen in the secondary peak which starts at a wavelength of 780 nm when there was no coating on the LPG, before shifting to ~640 nm. Selecting the grating period that has the apex of the U associated with same layer, changes the shape of this feature, increasing the rate of peak formation relative to the change in the coating. In order to move the U, another set of fibres were prepared with LPG periods of 90 µm (Figure 10.11) and 97 µm (Figure 10.2).

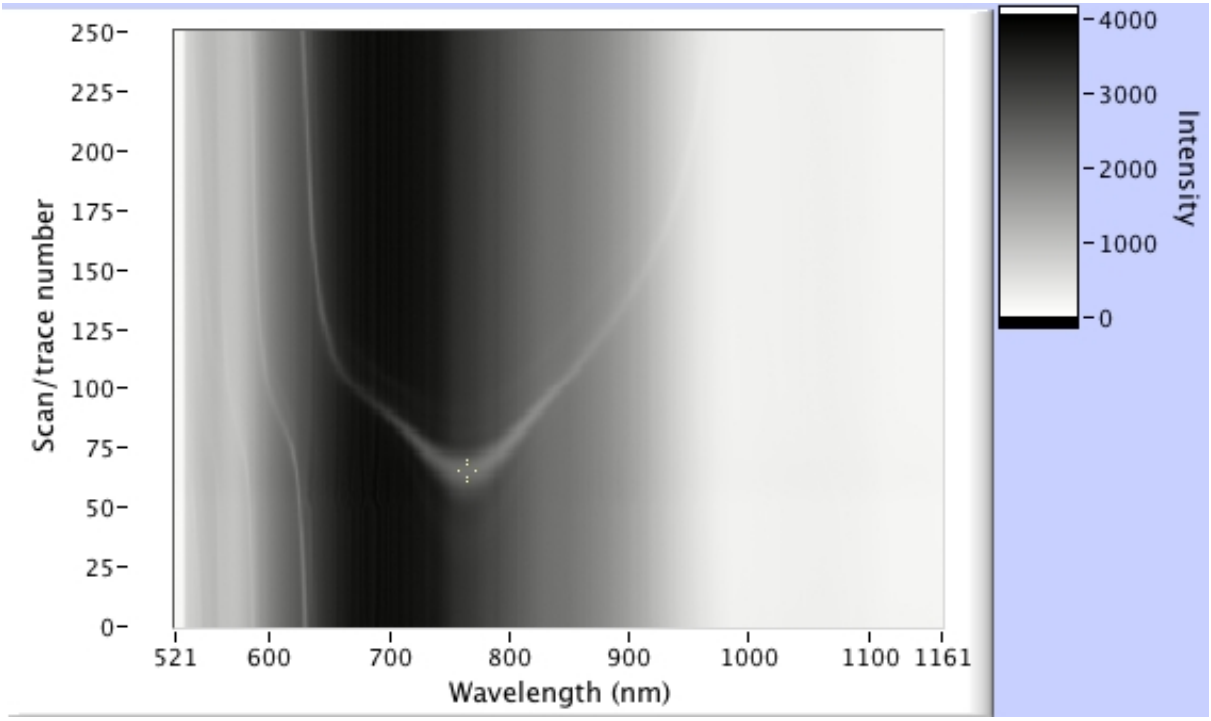

Figure 10.11: Gray scale plot using a 90 µm taper
A gray scale plot of the coating with calix[4]res C11 at 30 mN m^{-1} over 250 cycles (only the 'air' traces are shown). The yellow cross is positioned at the apex of the modal change and is located at layer 65.

The gray scale plot from a 90 µm LPG coated at 30 mN m^{-1} shows just how sensitive the fibres are to just a 10% change in the period of the crating. The U shape seen in Figure 10.10 has now altered into more of a V shape and the apex occurs earlier than the mode change in the secondary peak.

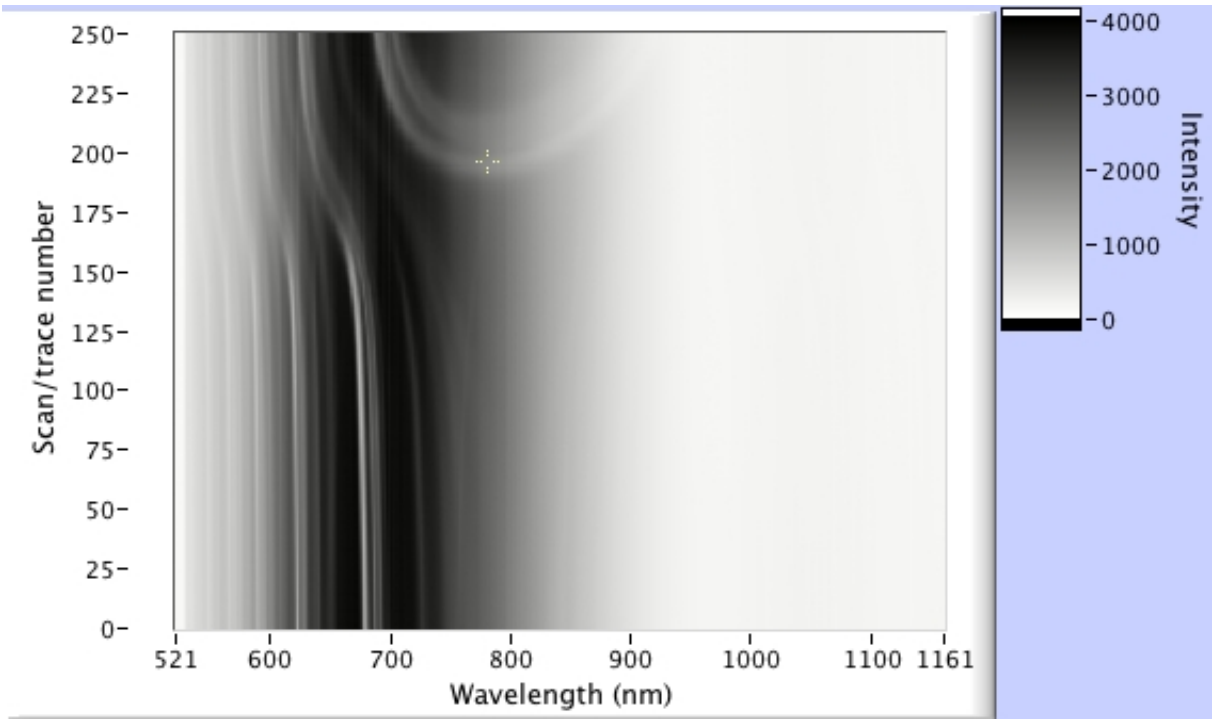

Figure 10.12: Gray scale plot of the coating a 97 µm LPG
A gray scale plot of the coating with calix[4]res C11 at 30 mN m-1 over 250 cycles (only the 'air' traces are shown). The yellow cross is positioned at the apex of the modal change and is located at layer 196.

Unfortunately due to a manufacturing error the 97 µm LPG the data shown in Figure 10.12 contains a phase shifted grating, which produce a series of ghost like shapes. This ghosting makes it hard to clearly identify the position of the coupled mode relative to the secondary mode. However, from looking at the shape of both features it becomes clear that they are closer together and occur at broadly the same layer, and this should confer the greatest sensitivity to the sensor. This coating process was repeated in order to confirm this positioning; the repeat gray scale plot is shown in Figure 10.13. Unfortunately, due to a power cut the experiment was prematurely cut short. However, it had run sufficiently to see the same feature.

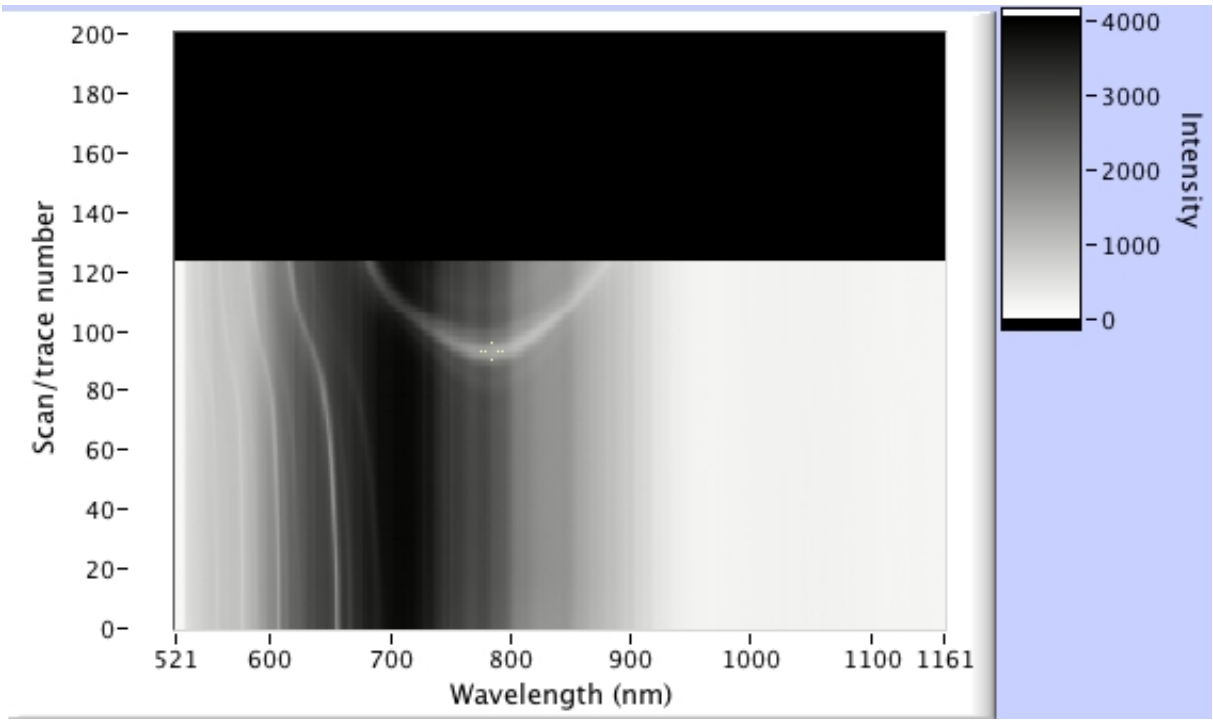

Figure 10.13: Gray scale plot of the coating a new 97 µm LPG
A gray scale plot of the coating with calix[4]res C11 at 30 mN m-1 over 200 cycles (only the 'air' traces are shown). The yellow cross is positioned at the apex of the modal change and is located at layer 93.5.

As is shown in Figure 10.13, at approximately layer 90 the coupling mode is more closely associated with the secondary mode transition. This confirms the coating show in in Figure 10.13 and provides confidence that this is an LPG period that will provide suitable sensitivity for use in future experiments.

10.4. LPG sensor coating

Following the initial coatings it was critical that the fibre was assessed further to determine the number of layers required in order to optimise the sensing potential of the fibre. As seen in the gray scale plots, an LPG sensor has high sensitivity to coating changes during the coupling of the modes; this is highlighted in Figure 10.14 where just three spectra from cycles 100, 101 and 102 of the data collected in the previous experiment (Figure 10.14) are shown.

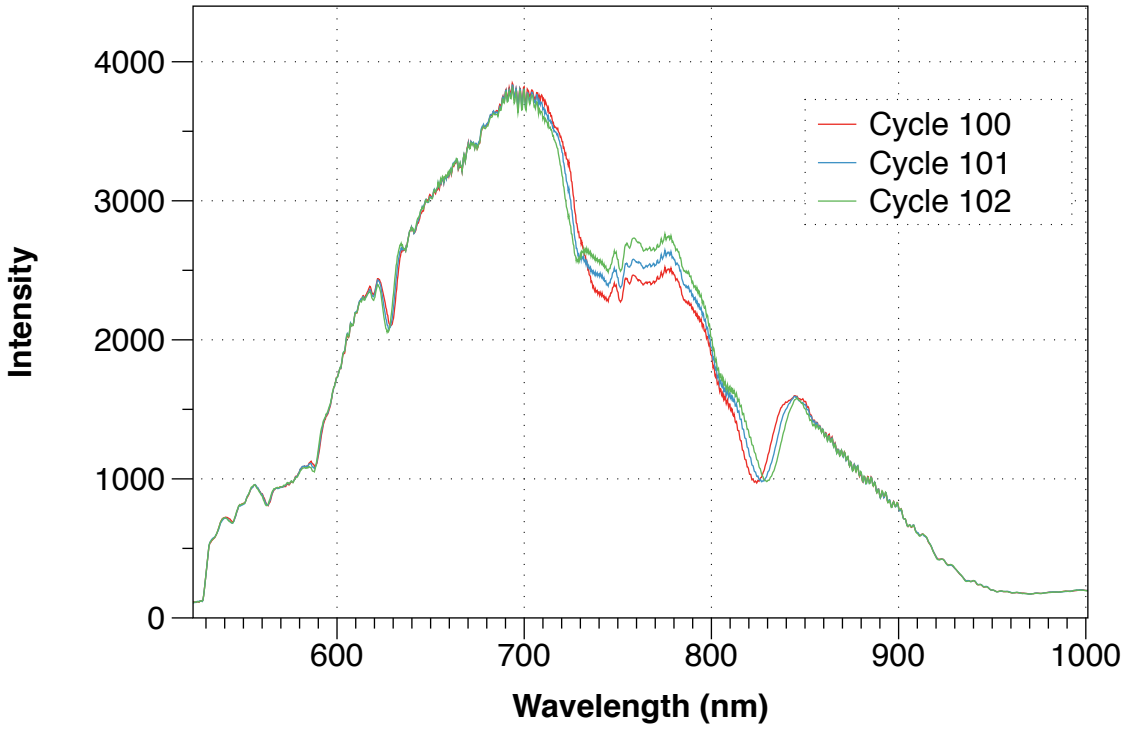

Figure 10.14: Peak separation just after the apex
Three plots of the transmission spectrum of a 97 µm LPG fibre during three successive layers of calix[4]res C11 coating at 30 mN m^{-1}

As shown in the example data in Figure 10.14 the peak separation area is a region of rapid spectral change, and single layers of calixarene produce nm order changes in spectrum features. Designing a sensor to work at this critical point ensures that any change in the coating via absorption of a secondary molecule is detectable in the transmission of the fibre. As discussed, the location (by coating number) of this critical point will vary with both the period of the grating (section 10.4.1) and also with the quality of the coating.

10.4.1. LPG sensor coating variation

The previous work was focused towards looking at the variation in the LPG period in just one coating condition (30 mN m^{-1}). As shown in section 10.1, calix[4]res C11 coats as a Z-Type monolayer at this surface pressure. It is not until higher surface pressures of 37.5 mN m^{-1} that Y-Type bi-layer Langmuir Blodgett coating is achieved. This coating difference should also be observable in the gray scale plots produced during LPG coating experiments. In order to demonstrate this difference the 97 µm taper used in section 10.3.2 was cleaned and recoated with calix[4]res C11 with surface pressures of 30, 35 and 37.5 mN m^{-1} spread on a 200mM EtOH subphase; this range was chosen as it includes the point at which the coating changes from monolayer to bi-layer. All three gray scale plots are shown in Figure 10.15, Due to a software error the coating at 37.5 mN m^{-1} was cut short at 96 cycles.

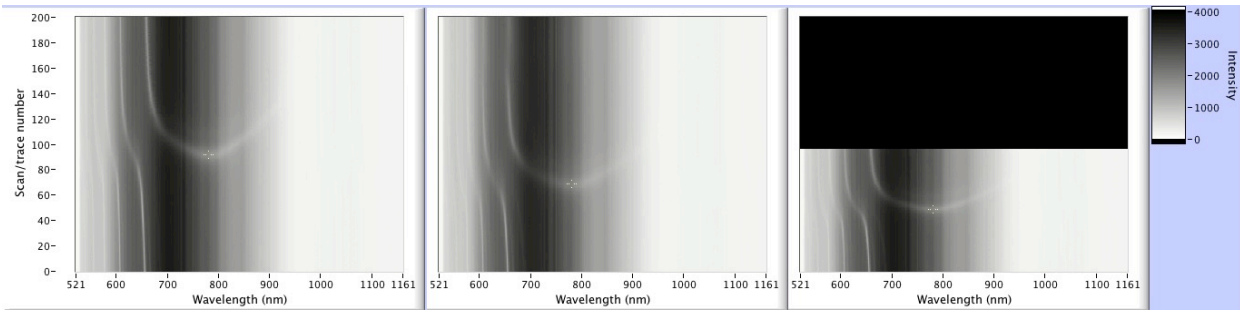

Figure 10.15: Gray scale plots of multiple coating pressures (200mM EtOH)
Three gray scale plots of the coating with calix[4]res C11 at surface pressures of 30, 35 and 37.5 mN m^{-1} on a 200mM EtOH subphase over 200 cycles (only the 'air' traces are shown).

The apex of the above plots have been summarised below in Table 10.1.

Table 10.1: Table of coupling location

Coating surface pressure (mN m-1)	Apex position (cycle number)
30	92
35	69
37.5	49

As the surface pressure increases, the position of the apex (summarised in Table 10.1) decreases in cycle number. This decrease is due the increase in the optical thickness of the coating with each cycle. This change in thickness is most likely the result of the shift of the coating from monolayer to bi-layer as discussed in section 10.1 and as is supported by the almost doubling in optical thickness of the coating when comparing 30 to 37.5 mN m^{-1}.

10.4.2. LPG sensor comparison to water

In order to further examine the influence of the alcohol-altered subphase, the coating experiment described in section 10.4.1 was repeated with a water-only subphase. The data obtained at a pressure of 30 mN m^{-1} had already been collected as part of the experiments described in section 10.3.2, this data is shown below in Figure 10.16 along side coating data for the same sensor at 35 and 37.5 mN m^{-1}.

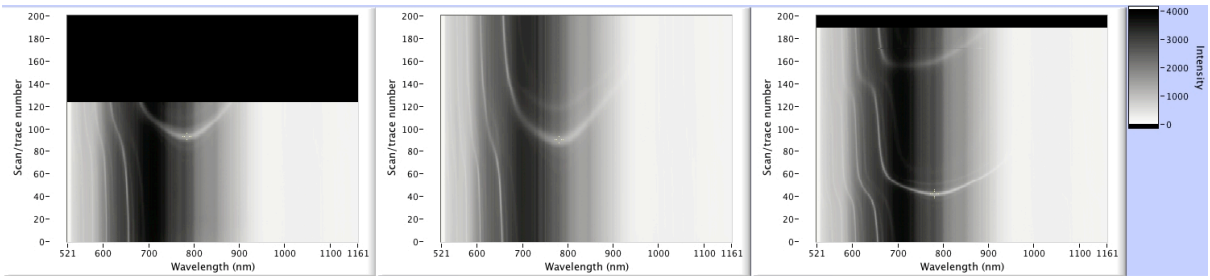

Figure 10.16: Grey scale plots of multiple coating pressures (water)
Three gray scale plots of the coating with calix[4]res C11 at surface pressures of 30, 35 and 37.5 mN m^{-1} on a water subophase over 200 cycles (only the 'air' traces are shown).

The position of the apex in each of the grey scale plots shown in Figure 10.16 has been summarised below in Table 10.2 along side the apex positions recorded when coating using a 200 mM EtOH subphase.

Table 10.2: Table of coupling location on two different subphases

Coating surface pressure (mN m^{-1})	Apex position (cycle number) with 200mM EtOH subphase	Apex position (cycle number) with pure water subphase
30	92	94
35	69	90
37.5	49	43

Again, the gray scale plots show the same relationship of increasing coating thickness with an increase in surface pressure. The pure water coating shows no significant improvement in the coating of the sensor until the surface pressure reaches 37.5 mN m^{-1}, whereas coating on a 200mM EtOH subphase shows some improvement at the lower 35 mN m^{-1} surface pressure. This transition is not the same as shown in section 10.1 but it is still indicative of the effect predicted by the isotherm changes in Chapter 9. It is not clear what might have caused the difference between this coating data and the capillary tube coating data, and it could be that the silica capillary tubes are not as chemically similar to the silica fibres as first assumed and so the coating conditions are not comparable. It is also worth noting that this is a small sample size and so we cannot say for sure if the effect observed is an accurate representation of the coating of the surface. Further work using multiple sensors is required to help explain this difference in the data.

One key difference between the two sets of data is that the features on the gray scale plots with an EtOH subphase are noticeable lighter (less intense) than those produced using a water subphase. Again it is not possible to produce a clear reason for this change; it implies

that there is a structural difference between the two coating methods that is not related to the optical thickness of the films. Only further study with multiple sensors would help explain this difference. However, for the purposes of future experiments within this project the stronger features seen in water subphase coated sensors will be easier to track and will produce a lower overall error in the feature tracking algorithms required when analysing sensor data. Therefore future sensor within this project work will use sensors coated using monolayers spread on a water subphase.

Chapter 11 Modelling sensor performance

Following the exploration of the improved coating methods described in Chapter 9, it was realised that the relationship between the coated surface and the surrounding vapour could be modelled to provide an indication of how further improvements might affect the performance of the sensor. It was hoped that this approach would indicate where future research should focus in order to produce optimal sensor characteristics.

The interactions of interest are those between the coated molecules and the target analyte. These interactions can be quantified using a series of common gas-modelling equations for determining the number of collisions on a surface within a given time frame. The quantification of the number of collisions can then be compared to the retention time of the sensitive surface molecules and the number of sensitive molecules spread across a given sensor surface.

11.1. Model development

As discussed in section 2.3.3, calixarenes interact with vapour molecules in two ways. At low vapour concentrations (e.g. <1kppmv for benzene) molecules of the vapour form gas state complexes with the calixarenes, whereas at higher concentrations the pore-like shape of the calixarenes allows for capillary condensation of the vapour. Previous work [1] has focused on higher concentrations of vapours (>1 kppmv), and therefore on capillary condensation effects. However, it is the formation of gas state complexes, which governs the ability of calixarenes to detect vapours in the concentration range of greatest interest (0-100ppmv) [30], identified in Chapter 1. This model will therefore only look at the interaction of vapour molecules in a 1:1 ratio with the calixarene when it forms a gas state complex.

11.1.1. Basic model

A fibre optic sensor can be viewed as an open ended cylinder coated with a single layer of material. This model provides a starting point to assess the interaction of the sensor surface with the surrounding gas. Typically, the sensitive section of the optical fibre has a length (***l***) of 20 mm and the optical fibre has a diameter (***D***) of 0.125 mm, which equates to a surface area of 9.42 mm^2 or $9.4x10^{-6}$ m^2. In Chapter 10 it was established that the surface pressure required to deposit a coating of a calixarene onto the surface of an optical fibre is approximately 40 mN m^{-1}, equivalent to a monolayer density (on a liquid subphase) of 1.7 nm^2 $molecule^{-1}$. The transfer ratio of a monolayer during coating is never 100% however, and while there will be small losses due to disinclinations and faults in the monolayer, overall the

density on the coated surface will be similar to that on the subphase. Thus for the purposes of this model it is assumed that the density of the coating and the density of the monolayer are the same. Using Equation 11.1, it is possible to combine the area per molecules and the surface area to determine the number of sensitive molecules presented to the surrounding medium as 5.54×10^{12}.

$$No.surface\ molecules = S_A/ApM$$

Equation 11.1: Number of surface molecules calculation

The next stage for the modelling of the interaction of the surrounding vapour with the sensor surface is to determine the composition of the bulk gas containing the analyte of interest. As discussed in section 2.1 1 ppmv is the current limit [3] for airborne exposure to benzene, making this the target for any benzene contamination sensor. 1 m^3 of air at 25 degrees celsius and 1 atmosphere is equivalent to 40.9 moles [121]. As 1 ppmv can be expressed as 1 µmol mol^{-1} of the bulk air sample, for a benzene concentration 1 ppmv, 1 m^3 of the bulk gas contains 40.9 µmol (or 4.09×10^{-5} moles) of benzene. Finally by multiplying by Avogadro's constant, it can be derived that this is equivalent to 2.46×10^{19} molecules of benzene per m^3 (n).

Despite being mixed with a complex bulk gas mixture, the benzene within the bulk can thought of as an ideal gas; which is to say it contains randomly moving, non-interacting particles. Ideal gas law allows us to separate out the benzene molecules from the bulk gas and model their interactions independently.

Given that benzene has a relative molecular mass of 78.118 g mol^{-1}, it can be determined, using Avogadro's constant, that each individual molecule as a mass (**m**) or 1.3×10^{-25} kg. Using the Boltzmann constant (k) and factoring the temperature (**T**), the mean square speed ($\overline{\boldsymbol{c^2}}$) of the molecules within the gas can be calculated using Equation 11.2 [121].

$$\overline{c^2} = 3kT/m$$

Equation 11.2: Mean square speed calculation

The mean square speed is then converted to mean speed using Equation 11.3 [121].

$$\bar{c} = \left(\frac{8 \times \overline{c^2}}{3 \times \pi}\right)^{0.5}$$

Equation 11.3: Mean speed calculation

However, the mean speed only provides information on the overall speed of the individual molecules, independent of direction. To model a fibre optic sensor, we need to know the velocity of the molecules that are moving towards the sensor surface. The direction independent mean square speed is the sum of the direction dependant velocity vectors, as shown in Equation 11.4 [121].

$$\overline{c^2} = \overline{v_x^2} + \overline{v_y^2} + \overline{v_z^2}$$

Equation 11.4: Mean square speed by vector calculation

By combining the Equation 11.4 with Equation 11.2 and Equation 11.3, it is then possible to calculate a single component of the mean velocity, as is shown in Equation 11.5 [121].

$$\overline{v_x} = \frac{8}{3 \cdot \pi}\left(\frac{k \cdot T}{m}\right)^{0.5}$$

Equation 11.5: Calculating a single vector velocity

For the given example, the equation 11.5 results in a mean velocity of 151.15 m s^{-1}. Finally, this velocity can be further converted into the number of impacts on a single sided surface with a given area, per second (Equation 11.6).

$$impacts/s = \frac{N \cdot A \cdot \overline{v_x}}{2}$$

Equation 11.6: Calculation for number of impacts per second

For the given example of benzene at 1 ppmv, this produces a value of 1.75×10^{16} impacts per second. This number of impacts per second is a useful figure but mis-represents the sensing interactions on the sensor surface. For a sensor to measure all the impacts within a given time frame, each impact would have to cumulatively add to the total number of impacts registered within that time frame. This is true of recognition elements such as antibodies, which essentially permanently bind their analyte of interest. However, as discussed in section 2.3.3, at low vapour concentrations calix[4]res C11 interacts reversibly with its analyte and is thus continuously absorbing and desorbing its analyte, benzene. This reversible binding is

best typified by the retention rate. The retention rate is the time taken for a sensitive molecule or structure to absorb and desorb a molecule of benzene. Retention rates vary, depending on the type of reversible interaction taking place. At the upper end of the scale enzymes typically retain their analyte for around 1 μs, whereas the chemical reactions occur over time scale on the order 1 ps [122,123].

Calix[4]res C11 has been shown to be reversible in all the sensor configurations it has been tested in. However, to date there is no published information on the retention time for its absorbance of benzene through the formation of gas state complexes. Previous studies of the benzene gas state complex formation of p-tert-butylcalix[4]arene have shown [124] that the interaction is low energy and transient - "…only weak dispersion forces are responsible for the complexation". There is no chemical reason why the relationship between calix[4]res C11 would be any more energetically favourable than that seen in p-tertbutylcalix[4]arene. For the purposes of modelling the interactions in calix[4]res C11, it is assumed that the gas state complex forms for 1 μs, this is a best-case value which allows us to model the theoretical limits of the sensor. Multiplying the impacts per second by the retention time allows the calculation of the number of impacts within the retention time of the sensitive molecule. For a retention time of 1 μs this produces a figure of 1.75×10^{10} impacts. As benzene is constantly being absorbed and desorbed, this number of impacts represents the maximum number of retained benzene molecules at any given time and thus the number of molecules that are being 'sensed' through their interaction with calix[4]res C11.

Finally, the number of impacts (within the retention time) is compared to the total number of sensitive molecules on the surface of the sensor as a percentage. This gives a final value of 0.3% of all available calix[4]res C11 molecules that are associated with a benzene molecule at any given time. The relationship between the percentage of occupied sites, based on this model, and the ppmv level of benzene is shown in Figure 11.1.

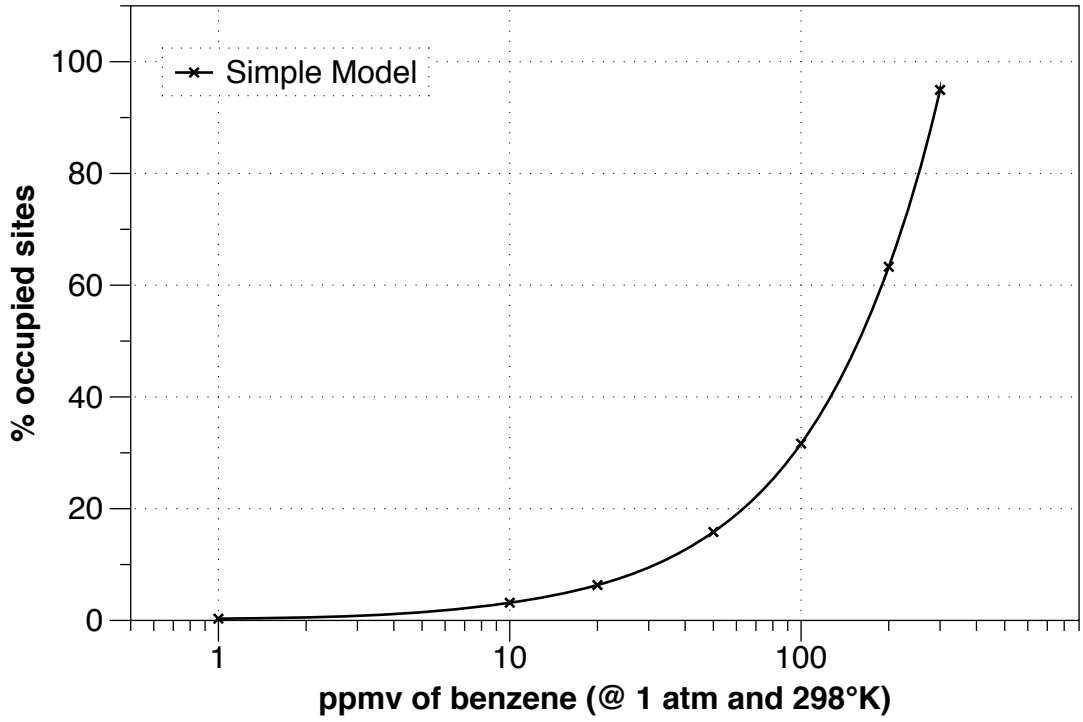

Figure 11.1: Simple model for benzene gas state complex formation
Percentage of occupied sites against the ppmv of benzene, as predicted by the basic model of calixarene vapour interactions

11.1.2. Impact model

The model described in section 11.1.1 shows how the vapour molecules interact with a calix[4]res C11 coated surface depending on the ambient vapour concentration. However, the data shown in Figure 11.1 has a critical flaw that results in an overestimation of the uptake of vapour by not accounting for the probability of a vapour molecule arriving at an already occupied site. The data assumes that every impact within the retention time results in the successful occupation of an available site. As the proportion of available sites decreases this cannot be true - given the random paths of the vapour molecules.

If we consider the sensor surface as being made up of a number of occupied sites (n_{oc}) and a number of vacant sites (n_{va}), with the total number of sites being n_{tot} , then the probability (p) of each vapour molecule arriving at the surface of hitting a vacant site is given by, Equation 11.7.

$$p = \frac{n_{va}}{n_{va} + n_{oc}} \quad \boldsymbol{or} \quad p = \frac{n_{va}}{n_{tot}}$$

Equation 11.7: Probability of a vacant site

As vapour molecules arrive at the sensor surface, the value of p changes from an initial value of 1 (no sites occupied) towards 0 (all sites occupied). Two methods were identified to adapt the model in order to solve this problem: individual impact modelling and rate equation balancing.

Impact modelling assesses the probability of each molecule impacting on a vacant site, and thus builds up a cumulative score for the number of impacts on vacant sites. Software was developed, using the Python programming language that allowed the modelling of all the interactions within the example used previously. A logic diagram for the modelling of a single impact is shown in Figure 11.2.

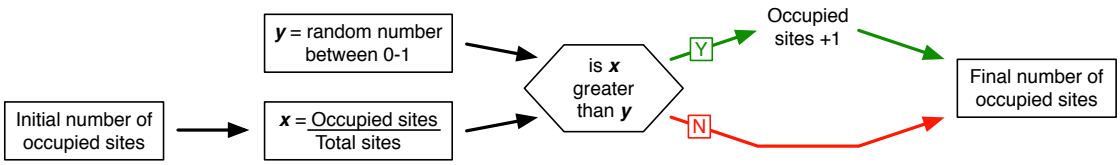

Figure 11.2: Logic diagram showing impact modelling
This logic diagram is for a modelling a single impact, this is looped for n impacts

The final result of the algorithm described in Figure 11.2 is the percentage of occupied sites, based on a constantly changing probability of an impact on a vacant site. As before, this logic loop was applied to a range of ppmv concentrations of benzene and is compared to the simple model in Figure 11.3.

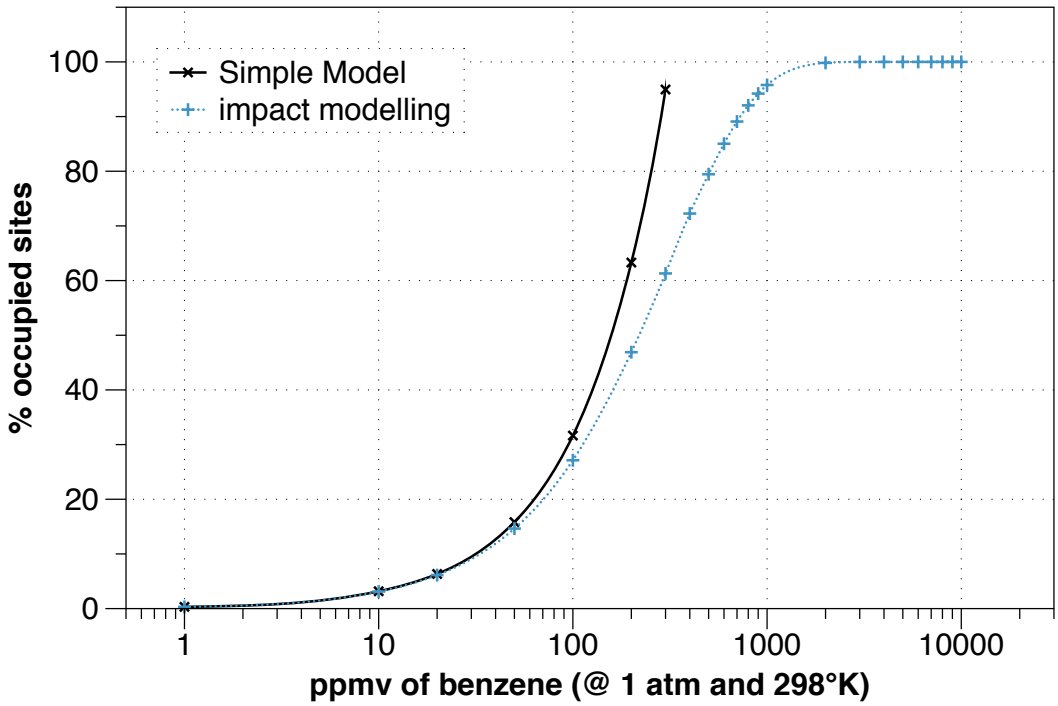

Figure 11.3: Comparison of the simple model to impact modelling
Modelling data calculated from a number of different ppmv levels for benzene at room temperature and pressure, on a logarithmic scale.

This algorithm produces a result that differs from the simplistic model at higher concentrations. The plateau at observed for concentrations > 2000 ppmv is expected, given the low availability of vacant sites. However, despite taking the occupancy of sites into account, this model is still incomplete. As shown in the logic diagram in Figure 11.2, the diagram assumes that the sensor surface begins with zero occupied sites, this figure then increases with successful impacts, modifying the probability of the next impact occurring onan unoccupied site. This model is true for the initial 1 µs time period of the sensor but it is not representative of the equilibrium state of the sensor. As the *initial impact model* starts with an empty surface. it will overestimate the equilibrium number of occupied sites at a given moment, as the initial impacts will have a high chance of occupying a site. Subsequent time periods don't start from this clean surface and the initial impacts have the same probability of occupation as the final impacts of the previous time period. It would be expected that over a number of subsequent time periods the number of occupied sites would find equilibrium.

The individual impact model was modified to run a number of iterations of the impact model. Each iteration (or generation) represented a period of 1 µs and each generation after the first took account not only of the impacts/µs but also the loss of the previous generation's occupied sites at a rate akin to their uptake in the previous generation. An example of how

the percentage of occupied sites evolves over model generations, at a single ppmv value, is shown in Figure 11.4.

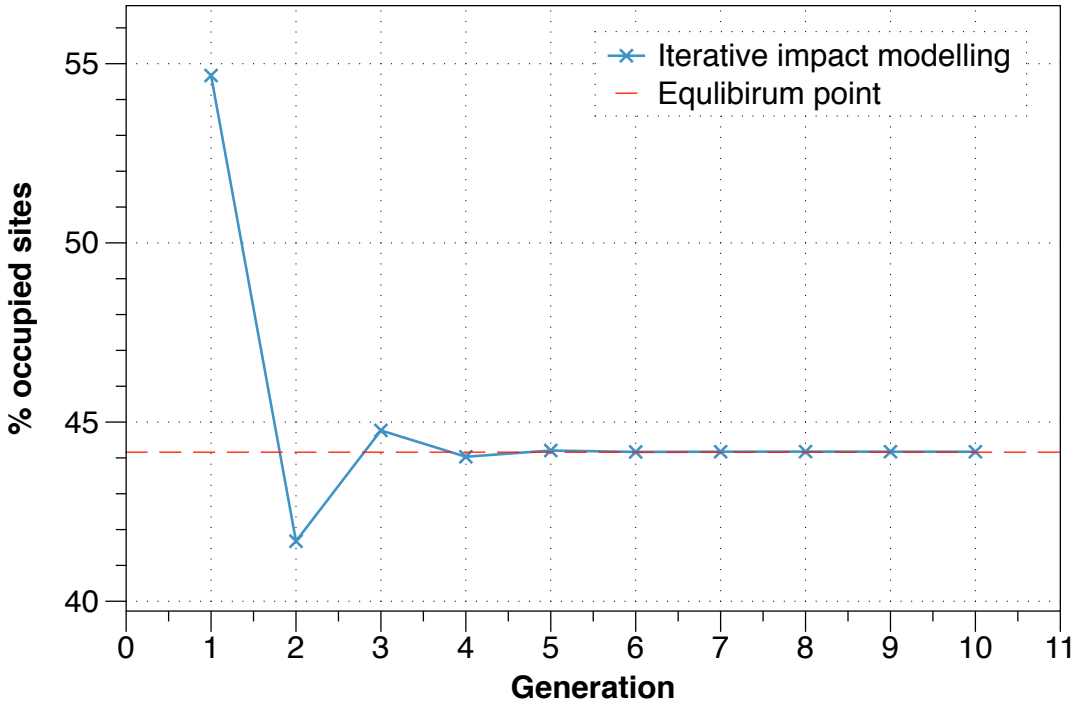

Figure 11.4: Evolution of the percentage of occupied sites over a number of generations
10 successive generations of the iterative impact model run using values for 250 ppmv benzene at room temperature and pressure.

The results of the iterative impact model in Figure 11.4 show how, as predicted, the initial generation overestimates the % of occupied sites by as much as 10%. In the example shown, a stable equilibrium is reach after 5-6 generations. Figure 11.5 shows the evolution of this iterative impact model for upto 10 generations for a range of ppmvs.

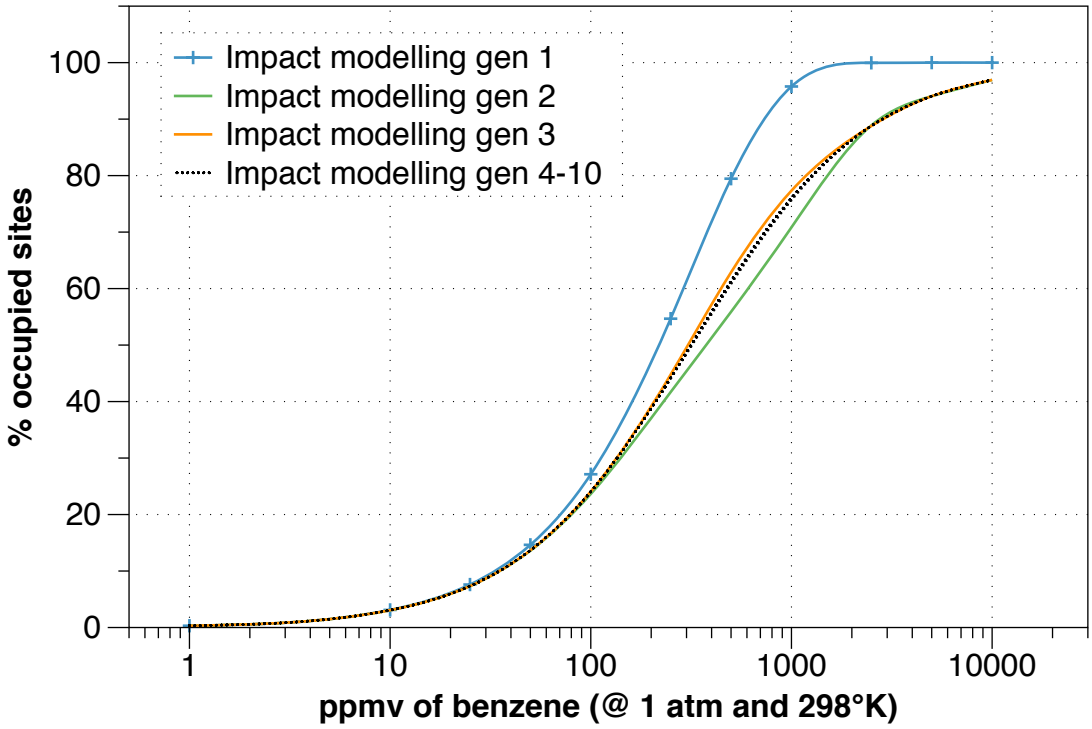

Figure 11.5: Iterative impact modelling
10 generations of iterative impact modelling. Generations 4-10 are visually indistinct as the average difference is less than 0.1% between generations

11.1.3. Balanced equation modelling

While effective, this iterative impact method of modelling was computationally intensive, with the modelling of a vapour concentration of 100 ppmv required the calculation of the outcomes of approximately 1 trillion impacts. In total, the data shown in Figure 11.5 required modelling sequentially around 100 trillion impacts, taking 48hrs to complete using a 2.66Ghz dual core processor. This reduces the utility of the model, as it would be highly time consuming to apply it to a range of conditions. In order to solve this problem, the original equations were re-examined to find a mathematical means of modelling the problem to solve for N-impacts rather than treating each impact individually.

As previously discussed, the number of occupied sites is equivalent to the impacts within a given time multiplied by the probability of each impact being on an occupied site (Equation 11.8(a). This is the combination of Equation 11.6 and Equation 11.7. By combining these two separate equations (Equation 11.8), we can see that by balancing the equation it is possible to derive the number of active sites.

$$n_{AC} = \frac{N \cdot A \cdot \overline{v_x}}{2} \cdot p \quad (a)$$

$$n_{AC} = \frac{N \cdot A \cdot \overline{v_x}}{2} \cdot \left(\frac{n_{VA}}{n_{tot}}\right) \quad \textbf{or} \quad n_{AC} = \frac{N \cdot A \cdot \overline{v_x}}{2} \cdot \left(\frac{n_{tot} - n_{oc}}{n_{tot}}\right) \quad (b)$$

$$n_{AC} = \frac{A \cdot N \cdot n_{tot} \cdot \overline{v_x} \cdot t}{2 \cdot n_{tot} + A \cdot N \cdot \overline{v_x} \cdot t} \quad (c)$$

Equation 11.8 a, b, c: Balancing the equation for the number of active sites

The simplified equation given in Equation 11.8c was again applied to a range of ppmv of benzene. The resulting proportion of occupied sites is compared to the *basic method* and the *iterative impact modelling* method in Figure 11.6.

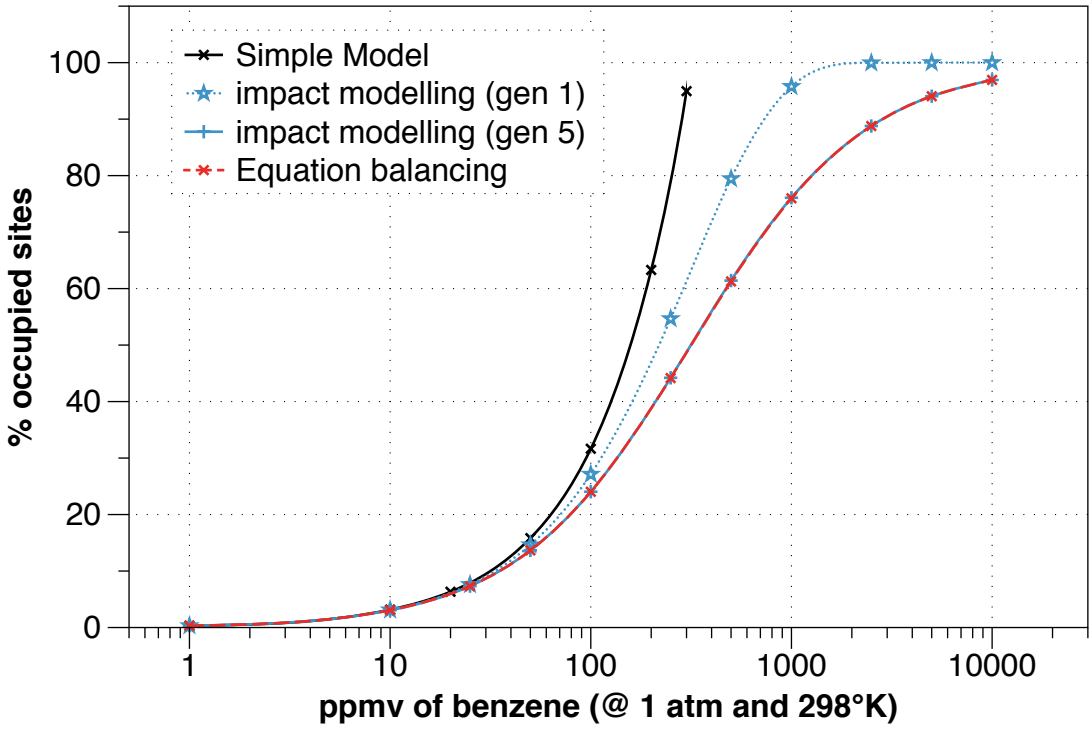

Figure 11.6: All models comparison
Comparison of all modelling methods. The results of impact modelling (gen 5) and the equation balancing model are similar and so are only visible as one line

.

The *iterative impact model* and the *balanced equation model* produce almost identical results across the range of ppmvs modelled. It is also important to note that the shape of the curves produced by the *iterative impact model* and the *balanced equation model* match data

obtained on similar calixarenes by previous groups [125,126]. As previously discussed, the target of this work is to produce a sensor that is capable of measuring vapours in the order of 1 ppmv. At this level, all three models give approximately a 0.3% occupancy rate for the sensor surface. Previous work by Hassan *et al.* [33] focused on measuring film reaction using sensitive elipsometry and SPR, both of these techniques are tuned to measuring film thickness and refractive index changes. While sensitive compared to many sensing techniques, the type of fibre optic sensors used in this project cannot match the sensitivity of elipsometry or SPR and will not be able to distinguish a change of this kind from background noise in the results. This potential limit indicates that any improvement for modifying the sensing capacity of the sensor system must focus on modifying one or more of the parameters of this model, in order to improve the % occupancy of the surface and therefore the theoretical limit of detection.

All further modelling and analysis was carried out using the *balanced equation model*. This allowed for a number of variable sets of data to be tested without the need for time-consuming *iterative impact modelling*.

11.2. Analysis of coating changes

As discussed in Chapter 9, modification of the functional coating by changing dipole-dipole interactions has the potential to alter the density of the coated materials on the sensor surface. This density shift will have two effects; firstly it will alter the density of the coated layers, reducing the number of available sites and secondly this decreased density will likely alter the porosity of the film to the vapour. At low concentrations of solvent it is only the first effect that is likely to have a significant impact on the properties of the sensing performance of the coating. Only as the concentration increases towards the capillary condensation point does the porosity of the film begin to have a marked impact on the absorption capacity, as Nabok *et al.* [30] showed, the mobility of the solvent though the film is a key force behind capillary condensation.

With respect to the change in the film density, the model described in section 11.1.3 can be tested with a number of different area per molecule values to show how this might affect the response of the sensor. As shown in Chapter 9, changes in the conditions used to deposit the coating can lead to a drop of 0.2 nm^2 in the surface area required for optimal coating of calixarenes. In addition, the work presented in Chapter 5 showed that the inclusion of surfactant groups can have an even greater effect, causing a change of 1 nm^2. In order to demonstrate the effect that this might have on the sensor, the model was run a number of

times for a range of values of the area per molecule (ApM). The results are presented in Figure 11.7a & b.

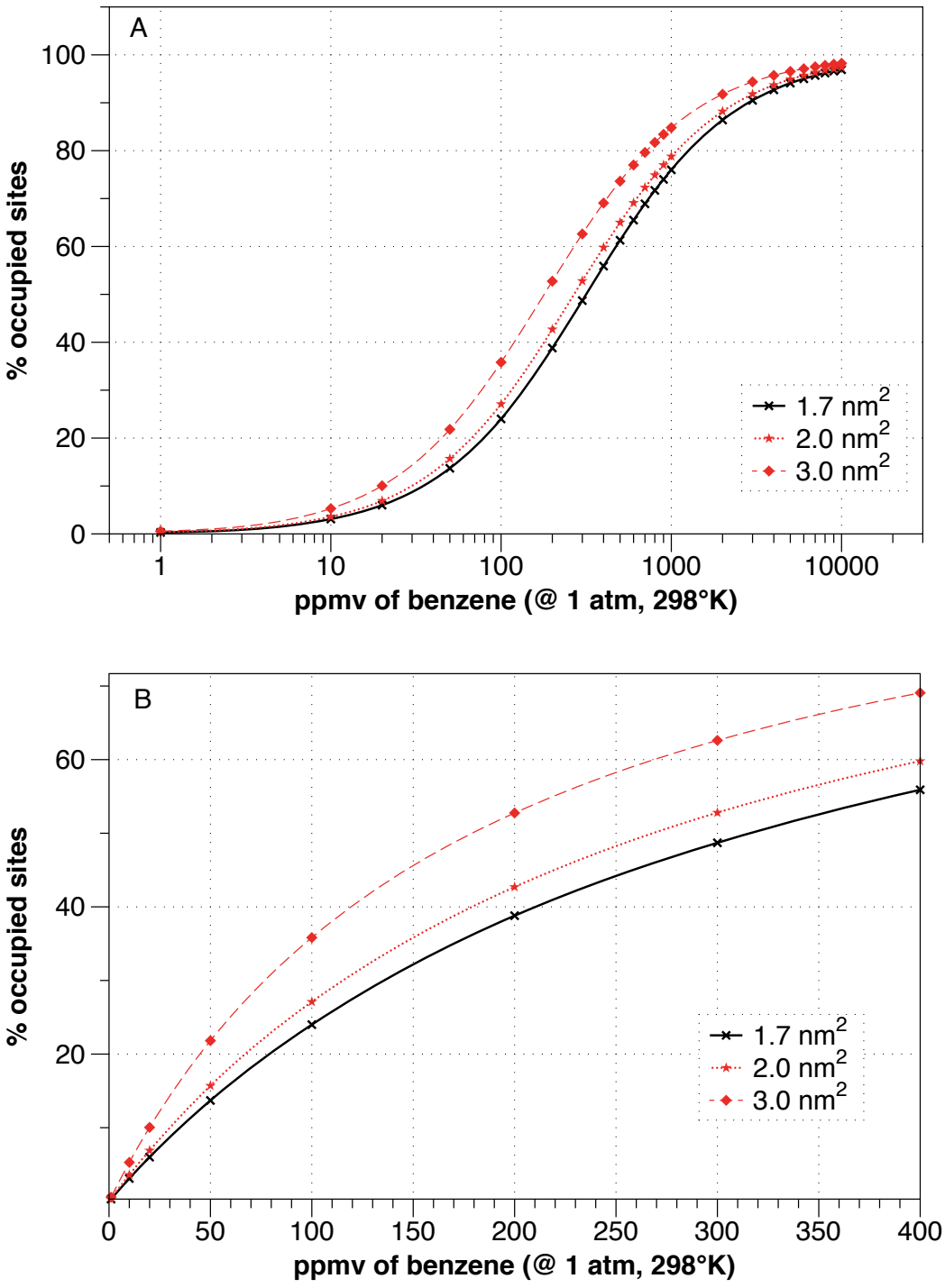

Figure 11.7a & b: ApM model change
a shows all the data modelled (plotted on a log scale), b is cropped data in the range 0-400ppmv plotted on a linear scale.

Figure 11.7a & b, show how a decrease in ApM, and therefore the number of available sites, can increase the equilibrium percentage of occupied sites. This assumes that, even at a low-

density state each molecule of calixarene is still capable of forming gas state complexes. It is suggested that the formation of gas state complexes is dependent on the shape and orientation of the calix[4]resorcarene, and this shape and orientation is strongly influenced by the packing of the molecules in the coated film [30]. In the case of the dipole-dipole modification method, the change in the density is relatively small and so conformational change that would impact the accuracy of this model are not expected. However, surfactant complexes induce a more significant change to the overall shape and function, due to the large packing requirements of the additional side chains. This has not yet been fully explored in the literature, but it is likely that this would have an adverse affect on the model.

Given the data presented in Figure 11.7, it is clear that the previously explored coating techniques will not significantly enhance the sensor limit of detection. However, from the model we can also examine what changes to the coating-vapour interaction will improve this relationship. For example, re-processing the data and assuming an increased surface area would allow the influence of larger sensor surfaces to be assessed. Such an analysis is shown to be of no practical value as the number of impacts increases linearly with the number of available sites, with the end result begin that the proportion of occupied sites remains the same. A more useful modification might be to look at molecules with alternative chemistry, which increases the retention time of the molecule to the solvent vapour. Several different retention times are plotted at a range of ppmvs in Figure 11.8 below.

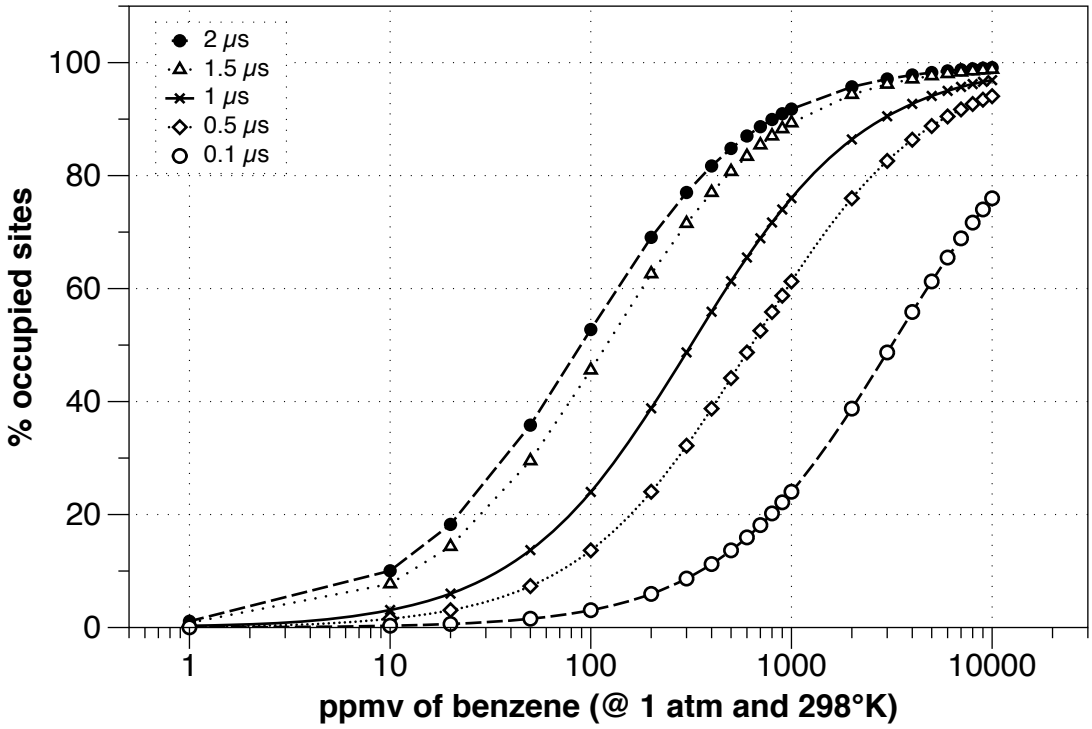

Figure 11.8: Modelled variation in retention time
Five versions of the balanced equation model, run with different molecule retention time

It can be seen in Figure 11.8 that increasing retention times initially makes a significant difference to the overall sensitivity of the molecules. As expected, a decrease in retention time quickly shifts the curve to the right. The value used in the original model (1 μs) produced data which matched quite closely with the limited work with low range ppmvs [126], however if a way could be found to increase this time, it is clear that there is a significant improvement in the sensitivity of the sensor to low ppmv concentrations of vapours. While this is beyond the scope of this project the model provides an indication that retention time modification should form a key part of any further development.

11.3. Outcome

Given the results of the modelling outlined above it became clear that the modified dipole-dipole coating would not be able to yield any significant improvements to the fibre sensor system. Taking in to consideration the sensing limits of the chosen fibre sensor, it is in fact unlikely that any modification of a calixarene coating could have a significant impact on the current limitations of the system.

While the model presented here matches with previously published data [33], this data has only explored the modelled effects using SPR and other sensor systems. While the coating conditions cannot enhance the sensing capacity of the fibre optic sensors, it is vital that data

is collected on this limit of sensitivity in order to validate fully the model. Consequently, rather than focusing on improving the coating conditions further, work will examine the lower range of the sensor system, an area that was not previously explored by *Topliss et al* [1].

Chapter 12 Fibre optic sensing

The final stage in this project was originally to be the coating and subsequent testing of a fibre optic vapour sensor using improved coating techniques. However, given the results of the modelling work described in Chapter 11 it is clear that these minor coating modifications will have little impact on the sensitivity of the sensor and its dynamic range for sensing in air. However, as discussed previously () the modelling only applied to gas sensing and does not hold for sensing in water.

The calix[4]res C11 molecule primarily used in this work and prior work has limited selectivity and has been shown to react to a wide range of aromatic hydrocarbons. It had been hoped that this poor selectivity could be corrected in future projects with pre-concentration stages or pre-filtration step upstream from the sensor. However, when used as a water sensor this poor selectivity can be a sensing advantage to detect oil spills. Crude oil comprises of 3 key groups of chemicals; naphthalenes, paraffins and aromatic hydrocarbons. The ratio of these three varies depending on the age of the crude oil [127] but, on average, crude oil contains around 30% aromatic hydrocarbons. Recent environmental disasters in the gulf [128] have highlighted the need to find new ways of tracking and monitoring the movement of oil spills, a large percentage of the oil leaked into the environment was trapped in the undersea currents and could not be tracked prior to washing up in nature reserve and beaches. Having a sensor system for finding these spills would be beneficial and would help reduce the environmental impact of such disasters. A fibre optic sensor coated with calix[4]res C11 is suitable for this work since firstly the fibre optic sensor and the calix can survive the highly variable conditions of use in the sea (temperature ranging from 2-15 degrees Celsius and high pressures at depth) , and secondly the semi-selectivity to aromatic hydrocarbonds in calix[4]res C11 makes it ideal for detecting the presence of mixes of aromatic hydrocarbons. The poor selectivity will in fact enable the sensor to detect the presence of crude oil at far lower concentrations due to the cumulative effect of the mixed aromatics in the oil. Finally, while calix[4]res C11 has poor selectivity between aromatic hydrocarbons, it has been shown to have little to no response to other possible contaminates such as alcohols, which may be more closely associated with organic decay.

12.1. Preparing a water sensor

The conclusions on the investigation of the coating properties described in sections 10.3 and 10.4 are the same for designing a water-based sensor as an air-based sensor. The performance of a water-based sensor can be easily assessed from the coating data already

collected in section 10.4. A coating cycle consists of an optical fibre moving out of and then into the subphase through the monolayer of interest. During this cycle transmission spectra are recorded at the top and bottom of the dipping cycle. The data shown in Chapter 10 was derived from the spectra recorded in 'air', as this was the focus of the project at the time, however data for the fibre taper sensor in 'water' were also recorded and the grey scale plot generated from this data is show below in Figure 12.1.

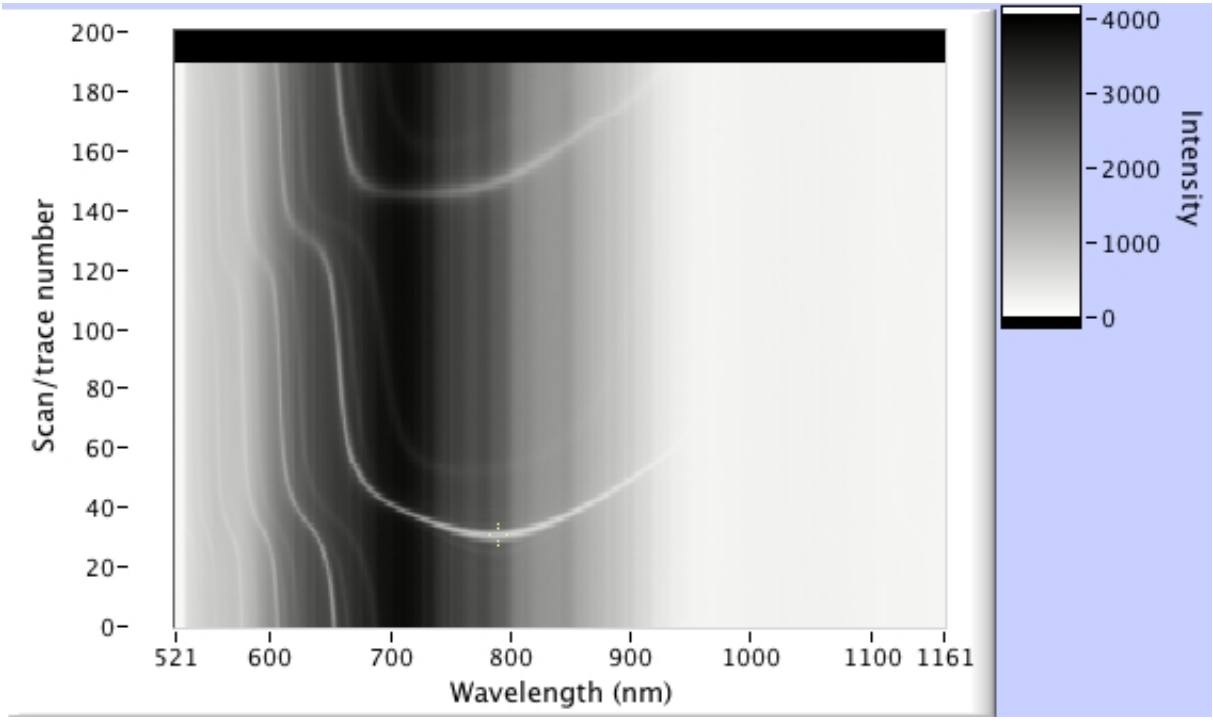

Figure 12.1: Grey scale plot of the coating a 97 µm LPG at a surface pressure of 37.5 mN m^{-1}
A gray scale plot of the coating with calix[4]res C11 at 30 mN m-1 over 190 cycles (only the 'water' traces are shown). The Apex of the 1st modal change and is located at cycle 30.

The key difference between the spectra recorded in air and water is the modal features occur earlier in the dipping cycles for water due to the higher refractive index of the surrounding medium. This is clear in the difference in the apex location between the two gray scale plots; 'air' shows an apex potion of cycle 42 whereas water is positioned at cycle 30. Preparing a sensor for use in water requires stopping the coating process ~12 cycles earlier than that for air sensing.

Using the same method as described in section 10.3, an LPG was coated from a calix[4]res C11 monolayer spread on a water subphase at a surface pressure of 37.5 mN m^{-1}. Unlike previous coatings, the process was stopped shortly after the apex seen in the gray scale plot. The identification of this point was judged by watching the change in the spectra develop over successive layers. The gray scale plot produced from this coating is shown below in Figure 12.2 and the final spectral trace is shown in Figure 12.3.

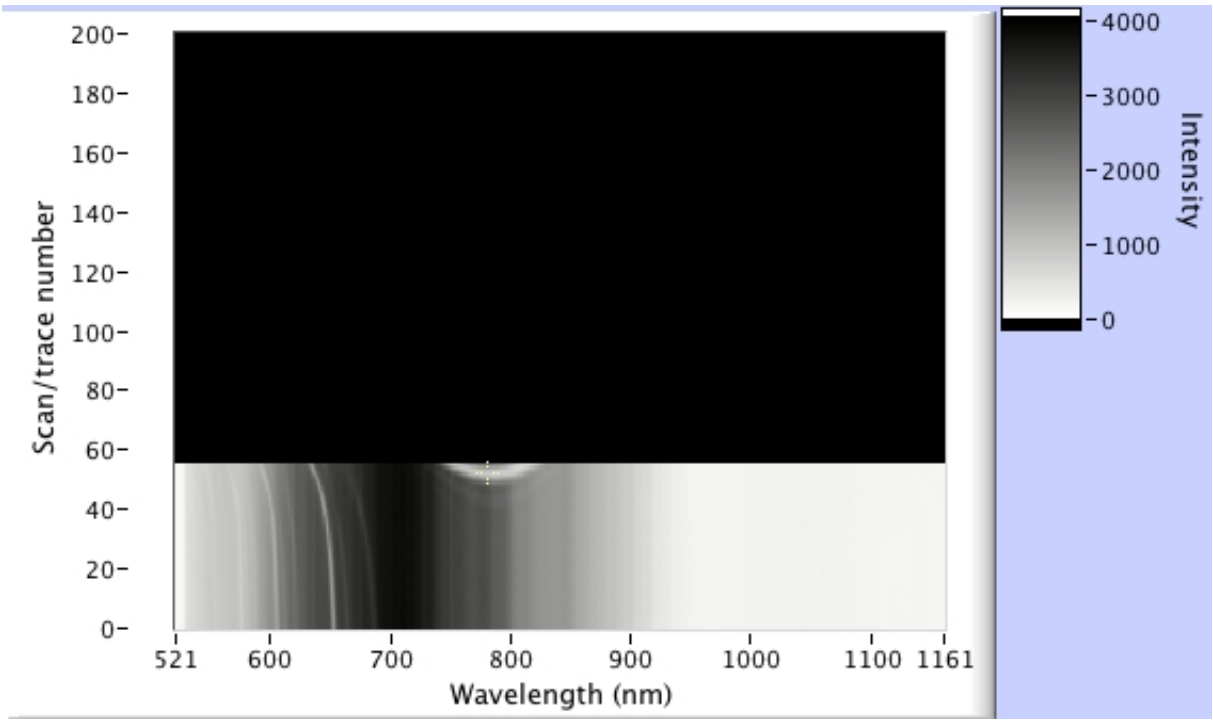

Figure 12.2: Grey scale plot of the coating of a 97um LPG fibre with calix[4]res C11

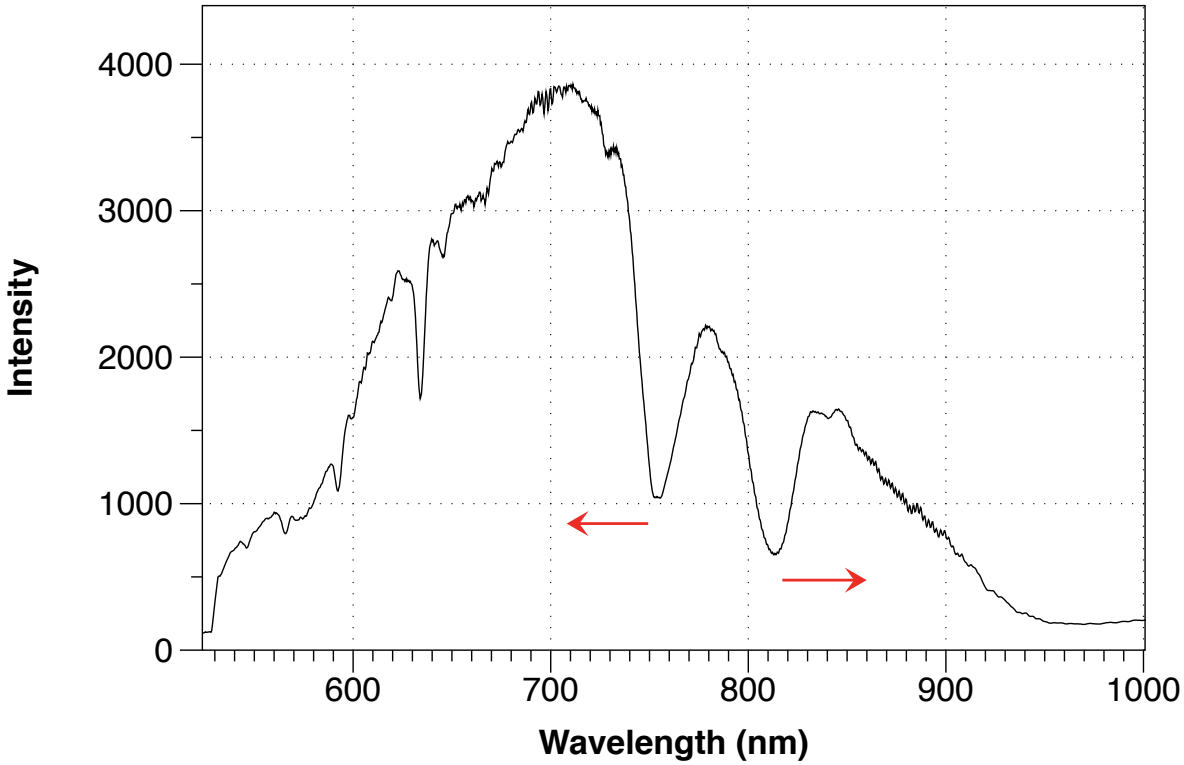

Figure 12.3: Final spectra from coating of 97um LPG with calix[4]res C11
This spectrum shows the two peaks that will be tracked during subsequent sensing experiments. Changes in the refractive index will cause these peaks to move in opposite directions as shown by the red arrows.

As discussed previously in section 10.4, this point just after the formation of two valleys in the spectrum is a sensitive region. Stopping the coating process at this point will give the sensor high sensitivity to the surrounding environment. Increases in the surrounding refractive index will cause the peaks to move apart as shown in the coating experiments. As toluene has a refractive index of 1.50 compared to water's refractive index of 1.33 it is expected that the sensors reaction to toluene will cause a sharp increase in this wavelength gap.

12.2. Initial sensitivity

As shown in previous work [1] calix[4]res C11 is sensitive to both toluene and benzene. However benzene is toxic and requires a number of safety precautions above and beyond normal laboratory safety provision. Therefore all testing of the sensors suitability was carried out using toluene. Initial characterisation was carried out using a solution of toluene at around 365 ppm (by mass) in deionised water (the maximum solubility of toluene). While still mounted in the trough, 5 ml of this toluene solution was poured into the dipping cavity in the trough over the sensor region of the fibre, which was already immersed in pure deionised water. The resulting valley separation recorded by taking a transmission scan every 400 ms and tracking the movement of the valleys is plotted below in Figure 12.4. In order to ensure that any reaction from the sensor was a true reaction to toluene, this experiment was also repeated with pure deionised water. Between the experiments the trough was emptied, cleaned and re-filled with pure deionised water. All experiments were carried out at 22.5 ℃ and the water temperature was confirmed prior to use.

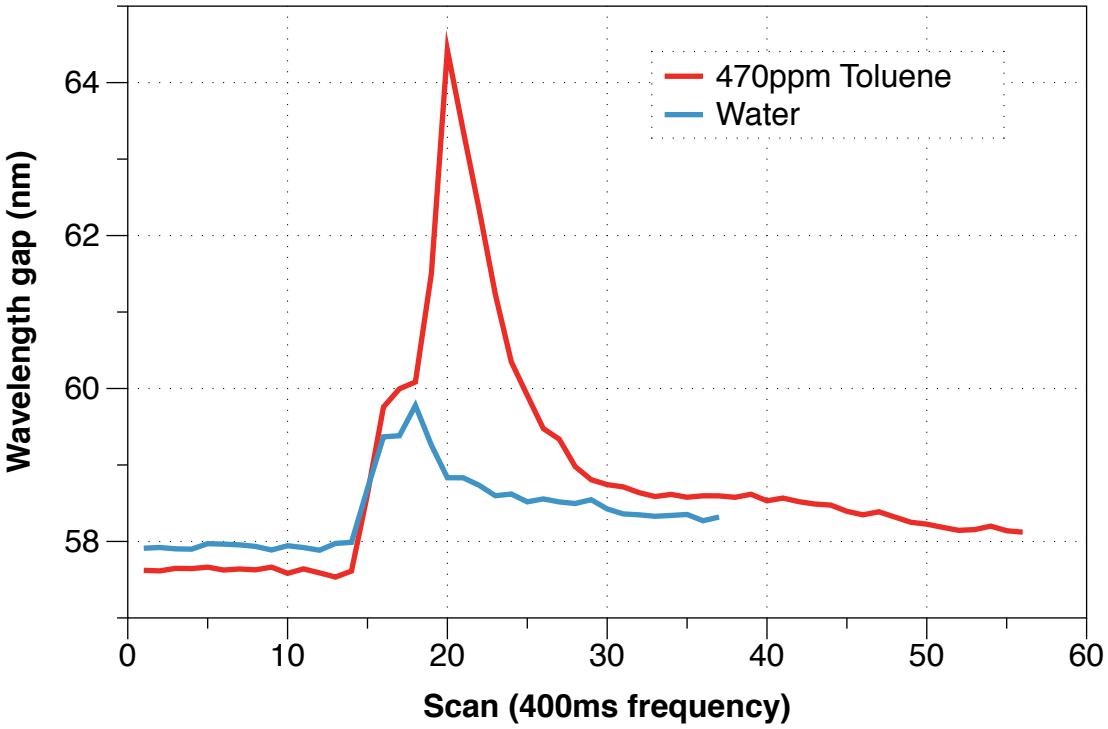

Figure 12.4: Change in wavelength gap during addition of 365 ppm by mass toluene solution
In both experiments the solution was poured into the vessel at scan number 15 (~6s)

The addition of the toluene-contaminated water produces a clear reaction in the sensor, followed by a sharp drop as the added toluene disperses into the surrounding solution and the disturbance to the solution settles down. This initial sensor reaction is likely the combination of both the toluene and localised disturbance of the surrounding liquid. This reaction to localised disturbance can be seen in the smaller peak produced by pouring deionised water over the sensor. This indicates that in this current embodiment the sensor has some sensitivity to currents within the test solution; this effect is also likely the cause of the slow return to base line seen after the addition of water.

In order to further examine the problems of fluid movement over the sensor as possibly identified above, a further experiment was run where the trough was filled with water and the spectra of the sensor was recorded every 1 minute for 4 hours (240 mins). The spectra were then processed and the wavelength gap for each was plotted on the graph in Figure 12.5.

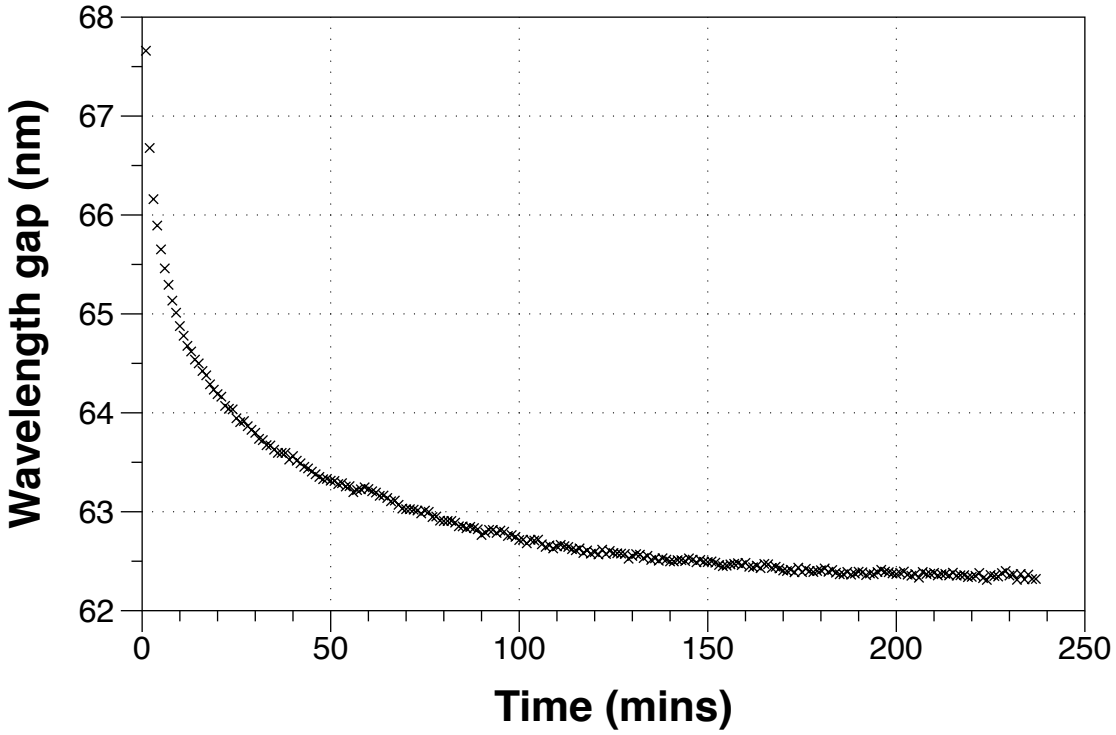

Figure 12.5: Slow stabilisation of the wavelength gap reading of a sensor in water
The wavelength gap between two valleys located at approximately 750 and 820 nm is plotted against time (mins). The wavelength gap was measured every 1 min.

The slow decrease in the wavelength gap over this 4 hour period suggest a slow reduction in the refractive in index of the surrounding water or the coated layer. Whilst it is known [129] that water can take many hours for the currents to become truly stable it is not clear why this would cause a significant refractive index change. It is also not clear why extreme currents (such as pouring water in around the sensor) caused an increase in the wavelength gap where as slow settling causes a slow decrease. This discord between the two sets of results could point towards an alternative theory that the sudden increase seen in Figure 12.4 is the result of the disturbance around the sensor where as the slow curve is simply the ingress of the water into the coated monolayer. It is known that the LB coating calix[4]res C11 is porous to a number of small molecules however, due to the amphiphilic nature of the molecule this process could be relativly slower with water. One final suggested cause is not that this is the impact of currents on the material but loss or damage to the material during its immersion.

In order to investigate the possibility of progressive damage of this immersion, a series of experiments were performed where the sensor was washed multiple times with water over a period of three days. For each reading the trough was filled with deionised water and a transmission spectra was recorded immediately; the trough was then emptied ready for the next reading. This was repeated ~5 times each day for three days in order to determine if

constant 'washing' of the sensor would degrade the performance over time as would be expect from monolayer damage. The results of this experiment is shown in Figure 12.6.

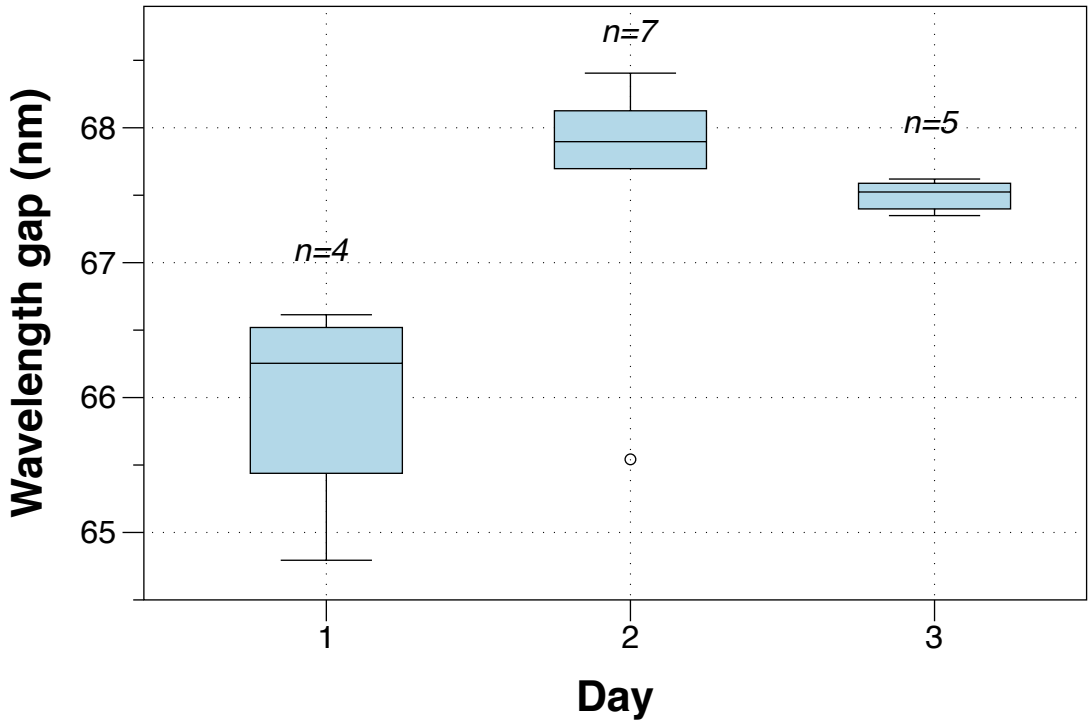

Figure 12.6: Box and whisker plot of repeat measurement of pure water.
Plot showing the variation in water only readings over three days, variable repeat number is due to experimental limits on the amount of deionised water avaliable.

The results shown in Figure 12.6 show no overall trend in the readings from one day to the next. The average position and variation on each day is consistent with what would be expect by chance. This indicates that there is no significant change in the sensor with successive washes/uses.

Following this work it was assumed that the most likely reason for this slow change in the sensor readings is related to the interaction through ingress of the surrounding water into the monolayer. At this stage it is not possible to prevent or alter this slow change, so for the purposes of all experiments with the sensor, all readings were taken within 1 min of the vessel being filled.

12.3. Toluene sensing

Following the investigations of the basic sensor functionality described in section 12.2, the sensor was exposed to a range of toluene dilutions (0, 40, 75, 150 and 300 ppm by mass). These dilutions were made by adding small volumes of pure toluene to deionised water; the

combined solution was then shaken vigorously and sonicated for 30 s to ensure that the toluene had dissolved in the water. As with previous experiments, the toluene solutions were then poured into the vessel surrounding the fibre and the spectra was immediately recorded. A cropped version of the spectra between 720 and 845nm is shown in Figure 12.7. The fibre was not moved in between experiment and as before the water/toluene mix around the fibre was changed between each experiment.

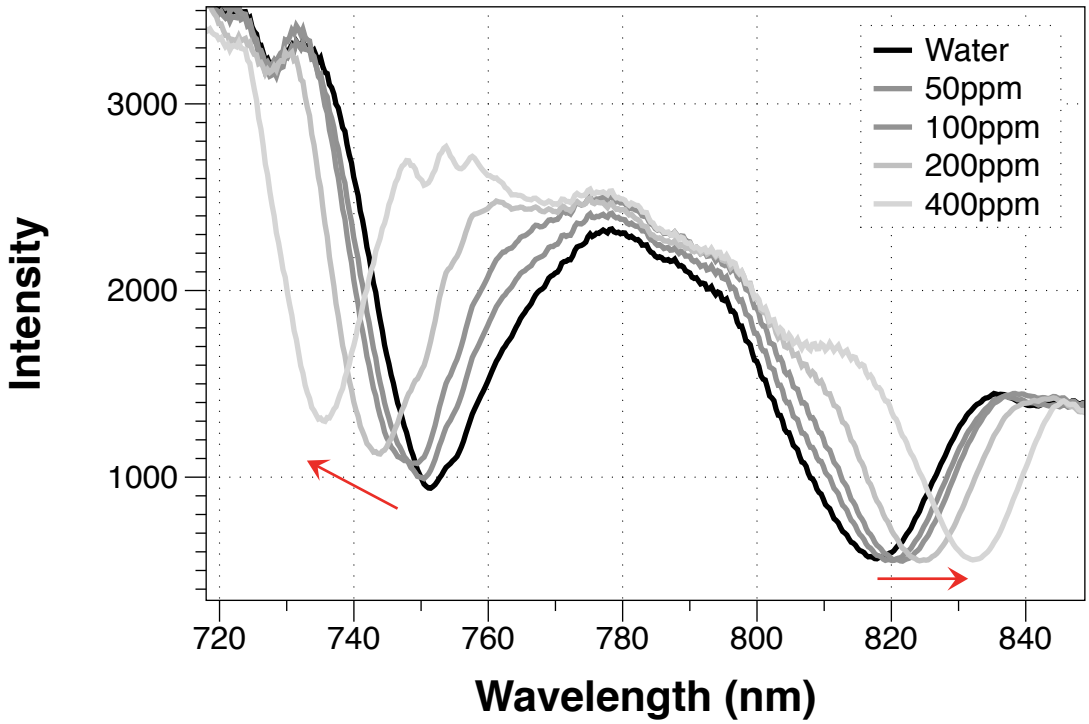

Figure 12.7: Toluene dilution spectra
5 spectra from a series of toluene dilutions overlaid. The red arrows represent the direction of movement in the peak position

The spectra shown in Figure 12.7 show the reaction of the LPG sensor to the presence of toluene. The calculated wavelength gap between the features shown in Figure 12.7 data is plotted against the concentration of toluene in solution in Figure 12.8.

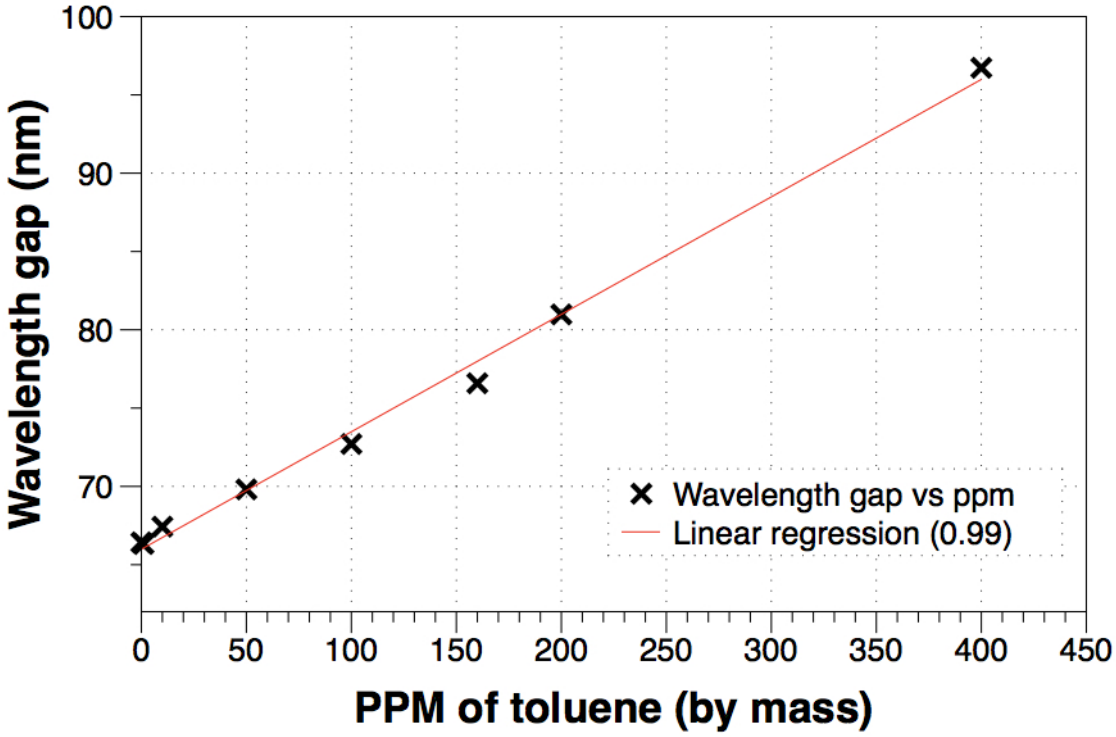

Figure 12.8: Toluene dilution curve

The dilution curve in Figure 12.8 shows a linear relationship between the sensor reading (wavelength gap) and the concentration of toluene across this range. This linear relationship is encouraging for the first prototype of a water based sensor and indicates that the sensor has potential for further use. The final stage in this assessment is to expand the work to assess the error on a particular reading. Work in the section 12.2 outlined the variation inherent in a blank water sample but this error is likely different from the error in prepared samples. In order to compare the error, several repeat (n=6) measurements were taken for a 100 ppm toluene solution were measured. As with the water repeats the trough was emptied and re-filed with a fresh solution between each run. The measured wavelength gap data is compared to the combined water data from Figure 12.6.

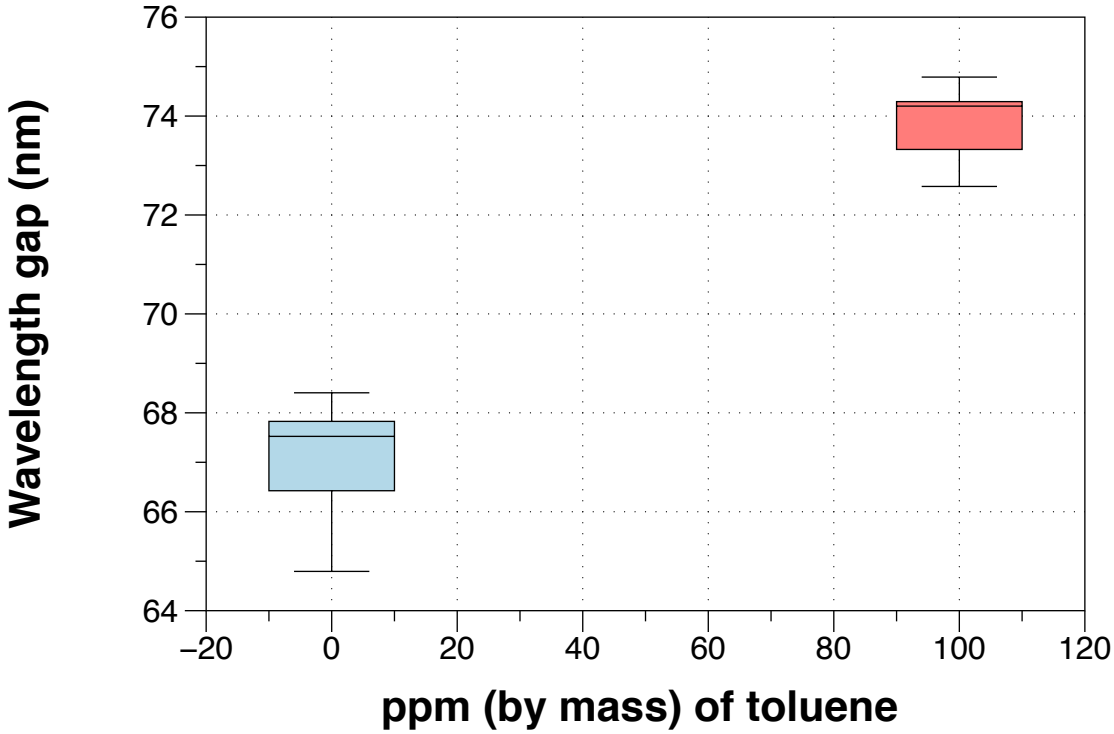

Figure 12.9: Box and whisker plot of 0 to 100 ppm comparison
The blue box represents the collected water day from 3 runs over 3 days, the red box represents 100ppm toluene repeated 6 times over one day.

As shown in Figure 12.9 the variation between a blank and 100 ppm is similar the standard deviation of water and 100 ppm toluene is 1 and 0.8 respectively. This variance is within the expected variation cause by the spectrophotometer, which only has a resolution of around 0.5 nm.

12.4. Conclusions

Within this chapter a water based toluene sensor based on calix[4]res C11 and an LPG fibre sensor has been demonstrated. This sensor is capable of linear sensing across the range 50-400 ppm. As discussed, this sensor is designed for finding oil within seawater and this preliminary work only shows the potential of the sensor for this application. However, given that the aromatic-hydrocarbon concentrations around oil spills are expected to be in the order of hundreds of ppm by mass this sensor is already capable of sensing within the target range. Further work will need to focus on possible cross-reactive species and improving the variance of the system.

Chapter 13 Summary of conclusions and suggestions for future work

The original aims of this project were to improve the Langmuir Blodgett coating methods used in previous work with an end goal of improving the limits of detection of the fibre optic vapour sensor system. It was also hoped that the project could devise a rapid method for testing a large panel of calixarene molecules for possible vapour sensitivity.

In order to produce improved coatings the project initially focused on better understanding three particular features; the Langmuir Blodgett coating equipment, monolayer measurement and monolayer modification.

The work on the Langmuir Blodgett coating equipment produced, among other improvements, an immediate benefit in the solving of the slow drift in sensors readings when initially setup. This work has been examined by several other LB groups and many now use the suggested pre-soaking method in order to increase the through put of their troughs. In the future it would be useful to expand this work with additional experimental data in order to build a comprehensive study of Wilhelmy plate variation.

Following on from this studies on the monolayer parameters with existing Langmuir equipment, produced sufficient data in order to propose a newly discovered calix[4]resorcarene monolayer structure. This knowledge of monolayer calix[4]res structure will be vital in any further development of a sensor system. Additionally it is hoped that future work will expand this work to include other structurally similar molecules in the hope of expanding our knowledge of these monolayer structures. This work led on to the subphase-monolayer dipole-dipole modification technique, which was developed as a potential way of modifying the shape of the isotherm of a given material and therefore the coating properties. The results presented on six materials show the significant changes in isotherm shape with the addition of materials into the subphase. It is hoped that this work can be expanded further with additional measurement of the surface potential, which will allow for further development of a mathematical model to help understand this effect.

In addition to existing Langmuir equipment several other monolayer experimentation techniques were tested in order to better understand the materials interaction with the subphase and their possible coating properties. The first of these additional studies was the development of a simple low cost BAM using readily available equipment (section 3.3). This

small project achieve good results considering it's makeup and design and a number of other groups and BAM manufacturers have shown interest in it's development. While not developed further as part of this project it is hoped that further development will result is a fully functional prototype for use in a wide range of projects. One particular area where the BAM would have useful is expanding the work on the correlation of vortex ring propagation to monolayer property. As identified in section 3.3.2 while the work produced a wealth of new data on the technique from a perspective not previously studied this would have benefitted from the ability to test correlation of the formation of vortex ring to more monolayer properties. Ultimately the work carried out as part of this project was not sufficient to develop this in to a usable technique but with additional work and equipment as discussed, it may be possible to answer some of the unknown aspects of vortex ring formation. One significant development regarding monolayer parameter measurement within this project was the design and development of the curved fibre optic surface pressure sensor. This sensor has the potential to be an accurate new tool in our understanding of the monolayer-subphase interface. The results demonstrated as part of this project have led the filing of a patent [130] and this work is now being carried further in a dedicated PhD project here at Cranfield University.

Monolayer modification primarily focused on optimisation of the coating method beyond the primary work carried out by Steve Topliss. This work quickly showed that the coating method previously adopted was not producing the results that had been assumed and a simple increase of surface pressure was seen to produce a significant increase in the coating quality. This work was then expanded further to include the isotherm modification method as demonstrated in Chapter 5 in order to give greater flexibility over the coating conditions. As suggested by the change in isotherm shape the coating properties were altered by the inclusion of alcohols in the subphase. By weakening the subphase-monolayer dipole-dipole force the materials tested coated at lower surface pressures. Further work is needed to understand the effect this has on the coating morphology and the techniques utility for improving sensor quality. In the short term this work would benefit greatly from more coating data with a wide range of subphase additives both on glass substrates and sensor surfaces.

Prior to the product of a vapour sensor it was seen vital to understand the possible reactions and limits of the sensor in order to understand what parameter would be most likely to improve a particular aspect (e.g. sensitivity) Chapter 8. A model was developed for a simplistic fibre optic sensor, which demonstrated a number of limitations on any possible improvements. The model showed how improving the overall LB coating would have little impact on the sensing limits of the system as a whole and until the fibre could be made more

sensitive it was unlikely any of the outlined methods would have a significant impact on the limits of the sensor. However, this work is only accurate for a particular type of fibre optic sensor and future work should focus on developing porous structures, which will take up more target analyte, these do not share the same limitations of the model demonstrated. However, as discused these possible improvements went beyond the scope of this project and so the project was changed from being targeted at vapour sensing to looking at water based contamination sensing where the same limits do not apply.

As shown in Chapter 12 a water based toluene sensor demonstrated high sensitivity to dissolved toluene down to ppm levels. This sensor shows that as a proof of principle a LB coated fibre optic sensor is suited to contamination detection in water in conjunction with an appropriate coating. The work presented here shows sensitivity of toluene down to around 40ppm; this is obviously higher than the WHO suggested limit for drinking water (0.7 ppm) [131] however, it is expected that with finer tuning of the sensor this limit could be reached. For example in the work presented the key focus was on the separation of the two coupled valleys that move in conjunction with changes in the coating however, if the sensor was re-coated in order to tune the sensitivity not to the peak separation but to the initial formation of the two peaks, this could provide higher sensitivity. This range of 0.1 to 1 ppm also represents the range on interest [132] for oil spill detection and tracking which was one of the suggested applications for this sensor system.

Chapter 14 References

1. Topliss S, James SW, Davis F, Higson SPJ, Tatam RP. Optical fibre long period grating based selective vapour sensing of volatile organic compounds. Sensors and Actuators: B. Chemical. 2010;143(2):629–34.

2. Korposh S, Batty W, Kodaira S, Lee SW, James SW, Topliss SM, et al. Proceedings of SPIE. Fourth European Workshop on Optical Fibre Sensors. SPIE; pages 76531D–76531D–4.

3. European-Union. Directive 2008/50/EC on ambient air quality and cleaner air for Europe. 2008. pages 1–44.

4. Hecht J. City of Light. Oxford University Press, USA; 2004.

5. Tatam RP, Jones J. Optical Fibre Sensors 17 (OFS-17). Meas Sci Technol. 2006;17(5):–.

6. David Gutsche C. Calixarenes: an introduction. 2nd ed. Stoddard FJ, editor. Cambridge: Royal society of Chemistry; 2008.

7. Kato T, Ohshima K. Defect-Free LB Films by the“ Isobaric Thermal Treatment” of Barium Arachidate Monolayers. Japanese Journal of Applied Physics. 1990;29(11):L2102–4.

8. Lesieur P, Barraud A, Vandevyver M. Defect characterization and detection in Langmuir-Blodgett films. Thin Solid Films. 1987;152(1-2):155–64.

9. Bibo A, Peterson I. Defect annealing rate in monolayers displaying a smectic-L phase. Thin Solid Films. 1992;210(1-2):515–8.

10. Inczédy J, Lengyel T, Ure AM. Compendium of analytical nomenclature. Blackwell Science Inc; 1998.

11. Agency for tocix substances and disease registry.

12. Rasooly A, Herold KE. Biosensors and Biodetection- methods and protocols : electrochemical and mechanical detectors, lateral flow and ligands for biosensors. New York: Humana Press; 2009.

13. Rasooly A, Herold KE. Biosensors and Biodetection -Methods and Protocols Vol 503: Optical-Based Detectors. 1st ed. New York: Humana Press; 2009. pages 1–452.

14. Pearce TC, Schiffman SS, Nagle T, Gardner J. Handbook of machine olfaction: electronic nose technology. Darmstadt: Wiley-VCH; 2003.

15. Grant S, Davis F, Law K, Barton AC, Collyer SD, Higson SPJ, et al. Label-free and reversible immunosensor based upon an ac impedance interrogation protocol. Analytica Chimica Acta. 2005;537(1-2):163–8.

16. Erdem A, Ariksoysal D, Karadeniz H, Kara P, Sengonul A, Sayiner A, et al. Electrochemical genomagnetic assay for the detection of hepatitis B virus DNA in polymerase chain reaction amplicons by using disposable sensor technology. Electrochemistry Communications. 2005;7(8):815–20.

17. Morus IR. When physics became king. Chicago: University Of Chicago Press; 2005.

18. Penner SS. Quantitative molecular spectroscopy and gas emissivities. Boston: Addison-Wesley Pub. Co; 1959.

19. B M Schasfoort R, J Tudos A. Handbook of surface plasmon resonance. Cambridge: Royal Society of Chemistry; 2008.

20. Liedberg BO, Nylander C, Lundstrom I. Surface-plasmon resonance for gas-detection and biosensing. Sensor Actuator. 1983;4(2):299–304.

21. Potyrailo R, Hobbs SE, Hieftje G. Near-Ultraviolet Evanescent-Wave Absorption Sensor Based on a Multimode Optical Fiber. Anal Chem. 1998;70(8):1639–45.

22. Peshko I, Cherry O, Rutkevich T, Hockley B, Rubtsov V. Long-period gratings in optical fibres for chemical sensor applications. Meas Sci Technol. 2005;16(11):2221–8.

23. Baekeland LH. Method of making insoluble products of phenol and formaldehyde. US Patent Office; 1907.

24. Zinke A, Ziegler E. Zur Kenntnis des Härtungsprozesses von Phenol-Formaldehyd-Harzen, X. Mitteilung. Ber. dtsch. Chem. Ges. A/B. 1944 Apr 26;77(3-4):264–72.

25. Benco J, Nienaber H, McGimpsey W. A sodium ion sensor based on a covalently-linked aminorhodamine B-calix[4]arene chromoionophore. Sensors and Actuators: B. Chemical. 2002;85(1-2):126–30.

26. Lee MH, Quang DT, Jung HS, Yoon J, Lee C-H, Kim JS. Ion-induced FRET on-off in fluorescent calix[4]arene. J Org Chem. 2007;72(11):4242–5.

27. Robert P, Lamartine R, Perrin M. The potential industrial applications of calixarenes. Pure Appl Chem. 1993;65(7):1549–59.

28. Iki N, Kabuto C, Fukushima T, Kumagai H, Takeya H, Miyanari S, et al. Synthesis of p-tert-butylthiacalix[4]arene and its inclusion property. Tetrahedron. 2000;56(11):1437–43.

29. Gutsche CD, Dhawan B, No K, Muthukrishnan R. Calixarenes. 4. The synthesis, characterization, and properties of the calixarenes from p-tert-butylphenol. Journal of the American Chemical Society. 1981;103(13):3782–92.

30. Nabok AV, Hassan AK, Ray AK. Condensation of organic vapours within nanoporous calixarene thin films. Journal of materials chemistry. 1999;10(1):189–94.

31. Nabok A, Lavrik N, Kazantseva Z, Nesterenko B, Markovskiy L, Kalchenko V, et al. Complexing properties of calix [4] resorcinolarene LB films. Thin Solid Films. Elsevier; 1995;259(2):244–7.

32. Erdoğan M, Çapan R, Davis F. Swelling behaviour of calixarene film exposed to various organic vapours by surface plasmon resonance technique. Sensors and Actuators: B. Chemical. 2010;145(1):66–70.

33. Hassan AK, Nabok AV, Ray A, Lucke A, Smith K, Stirling C, et al. Thin films of calix-4-resorcinarene deposited by spin coating and Langmuir-Blodgett techniques: determination of film parameters by surface plasmon resonance. Materials science & engineering. C, Biomimetic materials, sensors and systems. 1999;8:251–5.

34. Rubio JEF, Arsuaga JM, Taravillo M, Baonza VG, Cáceres M. Refractive index of benzene and methyl derivatives: temperature and wavelength dependencies. Experimental Thermal and Fluid Science. 2004 Oct;28(8):887–91.

35. Colladon. La Fontaine Colladon. La Nature. 1884;584:325–6.

36. Wheeler W. Apparatus for light dwelling or other strucutres. US Patent Office; 1881.

37. O'Reilly JJ. Telecommunication principles. Wokingham: Routledge; 1989.

38. Smith DD. Surgical Lamp. US patent Office; 1899. pages 1–4.

39. Strutt G. Charles Vernon Boys 1855-1944. Notice of Fellow of the Royal socity. 4(13):19.

40. Jackson D, Jones J. FIbre optic sensors. Optica Acta. 1986;33(12):1469–503.

41. Hocker GB. FIbre-optics sensing of pressure and temperature. Applied Optics. 1979;18(9):1445–8.

42. Butter CD, Hocker GB. Fiber optics strain gauge. Applied Optics. 1978;17(18):2867–9.

43. Sensa Technology Principles [Internet]. Sensa; [cited 2012 Apr 18]. Available from: http://sensa.org/technology_principles.aspx

44. Leung A, Shankar P, Mutharasan R. A review of fiber-optic biosensors. Sensors and Actuators: B. Chemical. 2007;125(2):688–703.

45. Hill KO, Malo B, Bilodeau F, Johnson D, Albert J. Bragg gratings fabricated in monomode photosensitive optical fiber by UV exposure through a phase mask. Applied Physics Letters. 1993;62(10):1035–7.

46. James SW, Tatam RP. Optical fibre long-period grating sensors: characteristics and application. Meas Sci Technol. 2003;14(5):49–62.

47. López-Higuera JM. Handbook of Optical Fibre Sensing Technology. New York: John Wiley & Sons; 2002.

48. Hale ZM, Payne F, Marks R, Lowe C, Levine M. The single mode tapered optical fibre loop immunosensor. Biosens Bioelectron. 1996;11(1-2):137–48.

49. Anderson GP, Golden J, Ligler FS. A fiber optic biosensor: combination tapered fibers designed for improved signal acquisition. Biosemors & Bioelectronics. 1993;8:249–56.

50. Zibaii MI, Latifi H, Karami M, Gholami M, Hosseini SM, Ghezelayagh MH. Non-adiabatic tapered optical fiber sensor for measuring the interaction between α-amino acids in aqueous carbohydrate solution. Meas Sci Technol. 2010 Sep 2;21(10):105801.

51. Lee CT, Wu ML, Sheu LG, Fan PL, Hsu JM. Design and analysis of completely adiabatic tapered waveguides by conformal mapping. Lightwave Technology, Journal of. IEEE; 1997;15(2):403–10.

52. Jian F, Ying-Ying X, Shao-Fang T, Yang L, Shuo S. Transverse Multimode Evolution in Non-Adiabatic Optical Micro/Nanofiber Tapers. Chinese Phys. Lett. 2010 Jan 14;27(1):014202.

53. Pacetti SD. Spin coating apparatus and a method for coating implantable devices. Advanced cardiovascular systems inc., editor. US; 2008. pages 1–7.

54. Bunkoed O, Davis F, Kanatharana P, Thavarungkul P, Higson SPJ. Sol-gel based sensor for selective formaldehyde determination. Analytica Chimica Acta. 2010;659(1-2):251–7.

55. C Petty M. Langmuir-Blodgett films: an introduction. Cambridge: Cambridge university press; 1996.

56. Langmuir I. The consitution and fundamental properties of solids and liquids. Journal of the American Chemical Society. 1916.

57. Baoukina S, Monticelli L, Risselada HJ, Marrink SJ, Tieleman DP. The molecular mechanism of lipid monolayer collapse. Proc Natl Acad Sci USA. 2008 Aug 5;105(31):10803–8.

58. Hatta E. Sequential Collapse Transitions in a Langmuir Monolayer. Langmuir. 2004 May;20(10):4059–63.

59. Blodgett K. Films built by depositing successive monomolecular layers on a solid surface. Journal of the American Chemical Society. 1935;57(6):1007–22.

60. Clemente-León M, Coronado E, Delhaes P, Gómez-García C, Mingotaud C. Hybrid Langmuir-Blodgett films formed by alternating layers of magnetic polyoxometalate clusters and organic donor molecules-towards the preparation of multifunctional molecular materials. Advanced Materials. 2001;13(8):574–7.

61. Hansma HG, Gould S, Hansma PK, Gaub H, Longo M, Zasadzinski J. Imaging nanometer scale defects in Langmuir-Blodgett films with the atomic force microscope. Langmuir. 1991;7(6):1051–4.

62. Parris R, Knowler R. OVG-4 User guide. Owlstone Ltd; 2009 Aug.

63. Owlstone. Generating Calibration Gas Standards with OVG-4 and Permeation Tubes. 2010 Jul pages 1–11.

64. Jain VK, Kanaiya PH. Chemistry of calix[4]resorcinarenes. Russ. Chem. Rev. 2011 Mar 4;80(1):75–102.

65. Kurihara K, Ohto K, Honda Y, Kunitake T. Efficient, complementary binding of nucleic acid bases to diaminotriazine-functionalized monolayers on water. Journal of the American Chemical Society. ACS Publications; 1991;113(13):5077–9.

66. Hassen WM, Martelet C, Davis F, Higson SPJ, Abdelghani A, Helali S, et al. Calix [4] arene based molecules for amino-acid detection. Sensors and Actuators: B. Chemical. 2007;124(1):38–45.

67. Sugden M, Richardson T, Davis F, Higson SPJ, Faul CFJ. Langmuir and LB properties of two calix [4] resorcinarenes: Interactions with various analytes.

68. Davis F, Faul CFJ, Higson SPJ. Calix [4] resorcinarene–surfactant complexes: formulation, structure and potential sensor applications. Soft Matter. 2009;5(14):2746–51.

69. Ozbek Z, Çapan R, Göktaş H, Şen S, İnce FG, Özel ME, et al. Optical parameters of calix[4]arene films and their response to volatile organic vapors. Sensors and Actuators: B. Chemical. Elsevier B.V; 2011 Nov 15;158(1):235–40.

70. Hogberg S. Stereoselective Synthesis and DNMR Study of Two 1,8,15,22-Tetraphenyl[14]metacyclophan-3,5,10,12,17,19,24,26-octols. Journal of the American Chemical Society. 1980 Sep 6;102:6046–50.

71. Gaines GL. Insoluble monolayers at liquid-gas interfaces. New York: John Wiley & Sons; 1966.

72. Supian FL, Richardson TH, Deasy M, Kelleher F, Ward JP, McKee V. Interaction between Langmuir and Langmuir–Blodgett Films of Two Calix[4]arenes with Aqueous Copper and Lithium Ions. Langmuir. 2010 Jul 6;26(13):10906–12.

73. Wilhelmy LF. Ueber die Abhängigkeit der Capillaritäts-Constanten des Alkohols von Substanz und Gestalt des benetzten festen Körpers. Annalen der Physik. 1863;195(6):177–217.

74. Lapham G, Dowling DR. In situ force-balance tensiometry. Experiments in Fluids. 1999;27:157–66.

75. Hibbs DE, Hursthouse MB, Malik KMA, Adams H, Stirling CJM, Davis F. Tetraundecylpentacyclooctacosadodecaenoctol Tetraethanol Solvate, (I), and Tetraundecylpentacyclooctacosadodecaenedodecol Hydrate 2.5-Ethanol Solvate, (II). Acta Crystallogr C Cryst Struct Commun. International Union of Crystallography; 1998 Jul;54(7):987–92.

76. Kurihara K, Ohto K, Tanaka M, Aoyama Y, Kunitake T. Molecular Recognition of Sugars by Monolayers of Resorcinol Dodecanal Cyclotetramer. Journal of the American Chemical Society. 1991;113(2):444–50.

77. Davis F, Lucke A, Smith K, Stirling C. Order and Structure in Langmuir– Blodgett Mono- and Multilayers of Resorcarenes. Langmuir. 1998;14(15):4180–5.

78. AHUJA RC, CARUSO PL, Mobius D. Counterion Specific Interactions in Dioctadecyldimethylammonium Bromide Monolayers at the Monolayer Subphase Interface. Thin Solid Films. 1994;242:195–200.

79. Manabe O, Asakura K, Nishi T, Shinkai S. Diazo-Coupling with a Resorcinol-Based Cyclophane. A New Water-Soluble Host with a Deep Cleft. Chemistry Letters. 1990;19(7):1219–22.

80. Hassan AK, Nabok AV, Ray AK, Davis F, Stirling C. Complexation of metal ions with Langmuir-Blodgett films of novel calixarene azo-derivative. Thin Solid Films. 1998. pages 686–9.

81. He PS, Fang K, Zou G, Peltonen J, Rosenholm J. Elasticity of Langmuir monolayer detected by dynamic oscillation method. Colloid Surface A. 2002;201:265–73.

82. Akhmentov D. Vortex Rings. Berlin: Springer; 2009.

83. Esmailizadeh L, Mesler R. Bubble Entrainment with Drops. J Colloid Interf Sci. 1986;110(2):561–74.

84. Blanchette F, Messio L, Bush JWM. The influence of surface tension gradients on drop coalescence. Phys. Fluids. 2009;21(7):072107.

85. Chapman D, Critchlow P. Formation of vortex rings from falling drops. Journal Fluid Mech. 1967;29(1):177–85.

86. Gilet T, Mulleners K, Lecomte JP, Vandewalle N, Dorbolo S. Critical parameters for the partial coalescence of a droplet. Phys Rev E. 2007;75(3):–.

87. Pikhitsa P, Tsargorodskaya A. Possible mechanism for multistage coalescence of a floating droplet on the air/liquid interface. Colloid Surface A. 2000;167(3):287–91.

88. Blank M, Lucassen J, Van Den Tempel M. Elasticities of Spread Monolayers of Bovine Serum Albumin and of Ovalbumin. J Colloid Interf Sci. 1970;33(1):94–&.

89. Alonso C, Zasadzinski JA. A Brief Review of the Relationships between Monolayer Viscosity, Phase Behavior, Surface Pressure, and Temperature Using a Simple Monolayer Viscometer †. J. Phys. Chem. B. 2006 Nov;110(44):22185–91.

90. Rein M. Phenomena of liquid drop impact on solid and liquid surfaces. Fluid Dynamics Research. 1993;12:61–93.

91. Cresswell R, Morton B. Raindrops in the sea II -Experimental studies of vortex ring generation. Proc. 11th Australasian Fluid Mech. Conf., University of Tasmania, Hobart. 1992;:615–8.

92. Saylor JR, Grizzard NK. The effect of surfactant monolayers on vortex rings formed from an impacting water drop. Phys. Fluids. 2003;15(10):2852–63.

93. Henderson DM. Effects of surfactants on Faraday-wave dynamics. Journal of Fluid Mechanics. 1998;265:89–107.

94. Mohamed-Kassim Z. Drop coalescence through a liquid/liquid interface. Phys. Fluids. 2004;16(7):2170–81.

95. Gaines GL. Insoluble monolayers at liquid-gas interfaces. John Wiley & Sons Inc; 1966.

96. Davis F, Higson S. Macrocycles. Sussex: Wiley; 2011.

97. Río O, Neumann A. Axisymmetric Drop Shape Analysis: Computational Methods for the Measurement of Interfacial Properties from the Shape and Dimensions of Pendant and Sessile Drops. J Colloid Interf Sci. 1997 Dec 15;196(2):136–47.

98. Saylor JR. The fate of soluble and insoluble surfactant monolayers subjected to drop impacts. Experiments in Fluids. 2003 May 1;34(5):540–7.

99. Saylor JR, Szeri AJ, Foulks GP. Measurement of surfactant properties using a circular capillary wave field. Experiments in Fluids. 2000;29:509–18.

100. Cinbis C, Khuri-Yakub BT. A noncontacting technique for measuring surface tension of liquids. Review of scientific instruments. 1992;63(3):2048–50.

101. Joos FM, Anders AK. Apparatus for measuring viscosity or thickness, surface tension and surface and surface dilational elasticity. Eastman Kodak Company, editor. US Patent Office; 1997. pages G01M3/08.

102. Garrett WD, Zisman W. Damping of Capillary Waves on Water by Monomolecular Films of Linear Polyorganosiloxanes. J Phys Chem-Us. 1970;74(8):1796–805.

103. Daillant J, Bosio L, Benattar J, Meunier J. Capillary Waves and Bending Elasticity of Monolayers on Water Studied by X-Ray Reflectivity as a Function of Surface Pressure. Europhysics Letters. 1989;8(5):453–8.

104. Khaliq S, James SW, Tatam RP. Fiber-optic liquid-level sensor using a long-period grating. Optics Letters. 2001;26(16):1224.

105. Imae T. Advanced chemistry of monolayers at interfaces. Academic Press; 2007.

106. Xiaowei D, Ruifeng Z. Detection of liquid-level variation using a side-polished fiber Bragg grating. Opt Laser Technol. 2010;42(1):214–8.

107. Zhang W, Grice S, Sugden K, Bennion I. Tilted Fiber Bragg Grating for Direct Liquid Level Sensing. 11th European Quantum Electronics Conference (CLEO/EQEC). IEEE; 2009. pages 1–1.

108. Jarzebinska R, Cheung CS, James SW, Tatam RP. Response of the transmission spectrum of tapered optical fibres to the deposition of a nanostructured coating. Meas Sci Technol. 2009 Feb 4;20(3):034001–6.

109. Jarzebinska R, Cheung CS, James SW, Tatam RP. Response of the transmission spectrum of tapered optical fibres to the deposition of a nanostructured coating. Meas Sci Technol. 2009 Feb 4;20(3):034001.

110. Jarzebinska R. Tapered optical fIbre sensors employing nanostrucutred coatings. School of Engineering, Cranfield University; pages 1–181.

111. Hoenig D. Direct visualization of monolayers at the air-water interface by Brewster angle microscopy. The Journal of Physical Chemistry. 1991;95:4590–2.

112. Tronin A, Strzalka J, Krishnan V, Kuzmenko I, Fry HC, Therien M, et al. Portable UV-visible spectrometer for measuring absorbance and dichroism of Langmuir monolayers at air-water interfaces. Rev Sci Instrum. 2009 Mar;80(3):033102.

113. Richmond G. Structure and bonding of molecules at aqueous surfaces. Annual Review of Physical Chemistry. 2001;52:357–89.

114. Moore FG, Richmond GL. Integration or Segregation: How Do Molecules Behave at Oil/Water Interfaces? Accounts of Chemical Research. 2008 Jun;41(6):739–48.

115. Oliveira ON, Taylor DM, Lewis TJ, Salvagno S, Stirling CJM. Estimation of group dipole moments from surface potential measurements on Langmuir monolayers. J. Chem. Soc., Faraday Trans. 1:. 1989;85(4):1009.

116. Smith R. The collapse of surfactant monolayers at the air--water interface. J Colloid Interf Sci. 1980;74(1):273–86.

117. Vazquez G, Alvarez E. Surface tension of alcohol+ water from 20 to 50 C. Journal of chemical and engineering data. 1995;40:611–4.

118. Kampf J, Frank CW, Malmström E. Adaptation of bulk constitutive equations to insoluble monolayer collapse at the air-water interface. SCIENCE. 1999;283:1730–3.

119. Langmuir I, Schaefer VJ. The effect of dissolved salts on insoluble monolayers. Journal of the American Chemical Society. ACS Publications; 1937;59(11):2400–14.

120. Rees N, James SW, Tatam RP, Ashwell G. Optical fiber long-period gratings with Langmuir—Blodgett thin-film overlays. Optics Letters. 2002.

121. Flowers BH, Mendoza E. Properties of matter. 1st ed. New York: John Wiley & Sons; 1970.

122. Gruebele M, Zewail AH. Ultrafast reaction dynamics. Physics Today. American Institute of Physics; 1990;43(5):24–33.

123. Roberts G. Femtosecond chemical reactions. Philos T Roy Soc A. 2000;358(1766):345–66.

124. Benevelli F, Khimyak YZ, Klinowski J. 13C and 2D WISE NMR Studies of the Host Mobility in Two Aromatic Complexes of p-Tert-Butyl-Calixarene. Journal of Inclusion Phenomena. 2004;49(3/4):211–8.

125. Hassan AK, Ray A, Nabok A, Wilkop T. Kinetic studies of BTEX vapour adsorption onto surfaces of calix-4-resorcinarene films. Applied surface science. Elsevier; 2001;182(1-2):49–54.

126. Hassan AK, Ray A, Nabok AV, Davis F. Spun films of novel calix [4] resorcinarene derivatives for benzene vapour sensing. Sensors and Actuators: B. Chemical. 2001.

127. Hyne NJ. Nontechnical Guide to Petroleum Geology, Exploration, Drilling, and Production. PennWell Books; 2001.

128. Barstow D, Saul S. Deepwater Horizon's Final Hours. The New York Times. 2010 Dec 25.

129. Finney J. Molecular and mesoscale structures in hydrophobically driven aqueous solutions. Biophysical Chemistry. 2003 Sep;105(2-3):391–409.

130. Jarzebinska R, Partridge M. *Fibre Optic Sensor*. EU patent office.

131. Toluene in drinking water. World Health Organisation; 2004 Jul pages 1–17.

132. González JJ, Viñas L, Franco MA, Fumega J, Soriano JA, Grueiro G, et al. Spatial and temporal distribution of dissolved/dispersed aromatic hydrocarbons in seawater in the area affected by the Prestige oil spill. Marine Pollution Bulletin. 2006 Jan;53(5-7):250–9.

Chapter 15 Appendices

Appendix 1 – Publications resulting from this project

Conferences

- European Conference on Organized Films 12 (presenting author)
    - *Theoretical interactions between monolayer materials and the subphase through complex hydrogen bonding;* M Partridge, M Collins, F Davis, S P J Higson, S W James and R P Tatam
    - The *formation of fast moving vortex rings beneath a monolayer surface*; M Partridge, M Collins, F Davis, S P J Higson, S W James and R P Tatam
    - *A fixed fibre optic surface pressure sensor*; M Partridge, R Jarzebinska, S P J Higson, F Davis, S James and R P Tatam
- IEEE Sensors 11 (presenting author)
    - Presentation: *Curved tapered optical fibre surface pressure sensor*; M Partridge, R Jarzebinska, S P J Higson, F Davis, S James and R P Tatam

Journal Papers

- *Monolayer behavior of calix-4-resorcinarenes and their surfactant complexes*: M Partridge, F Davis, S W James, R P Tatam, C F J Faul and S P J Higson. Thin Solid Films 520 (2012) 6989–6993
- *Altering monolayer to subphase dipole-dipole interactions*: M Partridge, M Collins, S W James, F Davis, R P Tatam and S P J Higson. Colloids and surfaces (under consideration)
- *The effect of surface pressure modification on the speed of vortex rings*: M Partridge, F Davis, S W James, R P Tatam and S P J Higson. Physics of fluids (under consideration)

Other materials

- Patent
    - 1108004.1 *Fibre Optic Sensor*, Inventors: Matthew Partridge, Renata Jarzebinska, Filing Date: 16/05/2011

- Software
    - OVG-4 live control software, sold to Owlstone Ltd.
    - Nima Remote control interface, released open source to other groups using Nima equipment.